Characterization of Surface Defects Produced with Focused Ion Beams and Exploration of Applications for Controlled Growth of Nanostructures

Dissertation

Zur Erlangung des Doktorgrades der Naturwissenschaften

der Fakultät Physik der Technischen Universität Dortmund

vorgelegt von

Farhad Ghaleh

Dezember 2008

I. Index of Contents

1 Introduction 1

2 Basics 3

2.1 Clusters and their properties 3
2.2 Patterning methods 4
2.3 Graphene 5
2.4 Graphite oxidation 8

3 Experimental methods and setup 9

3.1 Focused Ion Beams 9
3.1.1 Liquid Metal Ion Source 9
3.1.2 The ionLiNE tool 10
3.1.3 Ion dose definitions 13
3.1.4 Origin of the defect distribution or structure width 15
3.2 Scanning Tunneling Microscopy 16
3.2.1 Principles 16
3.2.2 LT-System 17
3.2.3 RT-System 18
3.2.4 Data analyzing 19
3.3 Scanning Tunneling Spectroscopy 21
3.4 Photo Emission Electron Microscopy 22

4 Sample preparation 23

4.1 Substrate properties 23
4.2 Nano-pit fabrication 24
4.3 Cluster fabrication 27

5 Results and Discussion 29

5.1 Ion dose dependence 29
5.2 Patterning with low ion dose 31
5.2.1 Nano-pits 31
5.2.1.1 Nano-pit patterns 31
5.2.1.2 Distance dependence 33
5.2.1.3 Influence of the pit size 35
5.2.1.4 Beam characterization using nano-pits 35
5.2.1.5 Finding patterns 39
5.2.2 Cluster growth 41
5.2.2.1 Silver cluster patterns 42
5.2.2.2 Lead layer patterns 47
5.2.2.3 Lead cluster patterns 50
5.3 Patterning with high ion dose 59
5.3.1 Nano-cavities 59
5.3.1.1 Nano-cavity patterns 59
5.3.1.2 Penetration depth of gallium ions 61
5.3.1.3 Beam characterization using nano-cavities 62
5.3.1.4 Graphene nano-structures 63

5.3.2 Island growth ... 67
5.4 Cluster properties ... 70
5.4.1 Gold clusters ... 70
5.4.2 Silver clusters ... 70
5.4.2.1 Cluster height ... 71
5.4.2.2 Cluster facet ... 72
5.4.2.3 Cluster stability ... 74
5.4.3 Lead clusters ... 74
5.4.3.1 Cluster height ... 75
5.4.3.2 Cluster facet ... 81
5.4.3.3 STS measurements ... 84
5.4.3.4 Cluster stability ... 85
5.4.4 Discussion ... 88
6 Monte Carlo Simulations ... 91
6.1 Ion impact ... 91
6.1.1 About TRIM ... 92
6.1.2 Simulation results ... 92
6.2 Oxidation ... 98
6.2.1 Algorithm ... 98
6.2.2 Characterization ... 99
6.2.3 The physical background ... 106
6.2.4 Simulation results ... 108
6.2.4.1 Oxidation process ... 108
6.2.4.2 Random defects ... 110
6.2.4.3 Defect groups ... 111
7 Summary ... 115
8 Outlook ... 117
9 References ... 119
10 Glossary ... 135
11 Acknowledgements ... 139

II. List of Abbreviations

AFM ..... Atomic Force Microscope
Ag ..... Silver
Ar ..... Argon
Au ..... Gold
BNC ..... Bayonet Nut Connector
C ..... Carbon
CF ..... CONFLAT Flange of company Varian
EC-STM ..... Electro Chemical STM
EFM ..... Evaporator with integral Flux Monitor
FBMS ..... Fixed Beam Moving Stage
FIB ..... Focused Ion Beams
FWHM ..... Full Width of Half Maximum
Ga ..... Gallium
GDSII ..... Graphical Design Station II
Hg ..... Mercury
HOPG ..... Highly Oriented Pyrolytic Graphite
HOQS ..... Highest Occupied Quantum State
IGP ..... Ion Getter Pump
ionLiNE ..... ion beam lithography, nanofabrication and engineering workstation (Raith Tradename)
LHe ..... Liquid Helium
LMIS ..... Liquid Metal Ion Source
LN2 ..... Liquid Nitrogen
LOQS ..... Lowest Unoccupied Quantum State
LT ..... Low Temperature
MC ..... Monte Carlo
ML ..... Monolayer
Nano-cavity ..... Nanometer sized cavity
Nano-FIB ..... Tradename of Raith for FIB
Nano-pit ..... Nanometer sized pit
Nano-groove ..... coalesced nano-pits in a line
Pb ..... Lead
Pb(111) ..... (111) oriented lead crystal
PEEM ..... Photo Emission Electron Microscope
PES ..... Photo Electron Spectroscopy
Point ..... Localized group of defects or nano-pits
O ..... Oxygen atom
O_2 ..... Oxygen molecule
QW ..... Quantum Well
QWS ..... Quantum Well State
RT ..... Room Temperature
SEM ..... Scanning Electron Microscope
Si ..... Silicon
SiC ..... Silicon Carbide
SPM ..... Scanning Probe Microscope
SP-STM ..... Spin Polarized STM
SRIM ..... Stopping and Range of Ions in Matter
STM ..... Scanning Tunneling Microscope

TEM ..... Transmission Electron Microscope
TMP.....Turbo Molecular Pump
TRIM..... Transport Range of Ions in Matter
TU..... Technische Universität
UHV ..... Ultra High Vacuum
UPS.....Ultraviolet Photoelectron Spectroscopy
WD .....Working Distance
WSxM ..... free Program for SPM data analyzing
XPS.....X-ray Photoemission Spectroscopy

III. List of Variables

$\langle v_{O2} \rangle$ ..... mean velocity of O_2-molecules
$\hbar$ .....the reduced Planck constant (= 1.054×10^{-34} Js)

Γ, Δ

Γ ..... effective coverage
Γ_{total} ..... total effective coverage
Δt.....deposition duration
Δt_{ox} ..... oxidation duration

H, K, Λ

η.....sticking probability of O_2-molecules
κ .....calibration constant for EFM
λ_{diff} ..... diffusion length before desorption for metal atoms

P, T, Φ

ρ_{limit} ..... vacancy density needed for a layer oxidation
ρ_{norm} ..... normalized vacancy density
ρ_o.....density of O-atoms striking on surface (simulation)
ρ_{O2} .....density of O_2-molecules striking on surface (real)
τ.....time constant of a capacitor
$\tilde{\tau}$ .....ratio of two time constants of capacitors
Φ ..... work function

A, C

A..... area
a_{C60} .....lattice constant of C_{60}
a_{HOPG}..... lattice constant of graphite
A_{min}.....smallest facet detectable
A_{point} .....area of an exposed point
A_{sheet} .....size of the graphene sheet (simulation)
c ..... light velocity ($\approx 2.998 \times 10^8$ m/s)

D

D ..... Diffusivity
D_{area}.....area dose
d_{area}.....area step size
d_{C60} .....monolayer height of C_{60}
d_{ca}..... diameter of the capture area
D_{dot}..... dot dose
d_{HOPG}.....layer distance in HOPG
D_{line} .....line dose
d_{line} ..... line step size
d_{max}.....maximal penetration depth of gallium ions
D_{pa}.....point area dose
d_{peak} ..... peak distance in the height distributions
D_{point}..... point dose
d_{point}..... point to point distance
d_{pit} .....pit diameter

E

e ..... elementary charge (= 1.602×10^{-19} C)
E_a ..... activation energy for oxidation
E_b ..... lattice binding energy
E_d ..... displacement energy
E_{diff} ..... activation energy for diffusion
$E_{F,sample}$ ..... Fermi level of the sample
$E_{F,tip}$ ..... Fermi level of the tip
E_s ..... surface binding energy
E_v ..... vacuum level

I

I_{em} ..... emission current
I_{FIB} ..... ion current of the FIB
I_{flux} ..... flux current

K, L

k_B ..... Boltzmann constant (= 1.38×10^{-23} J/K)
l_{diff} ..... diffusion length before desorption for O_2 (real)
l_o ..... diffusion length before desorption for O-atoms (simulation)

M, N

m ..... mass
m_{O2} ..... mass of an O_2-molecule
n ..... correction factor for pit perimeter in simulations
N_{ion} ..... number of incident ions
N_o ..... number of O-atoms (simulation)
N_{O2} ..... number of O_2-molecules
n_{O2} ..... density of O_2-molecules
N_{Vac} ..... number of vacancies

P, Q

P ..... perimeter
p_{O2} ..... pressure of O_2
p_{ox} ..... oxidation probability (simulation)
q ..... charge

R, T

R ..... gas constant (= 8.31 J/(mol K))
T ..... Temperature
t_{diff} ..... diffusion time
t_{dwell} ..... dwell time
T_{ox} ..... oxidation temperature
t_w ..... settling time

U, V, Z

u ..... atomic mass unit (= 1.66×10^{-27} kg)
$V_{1,2}$ ..... capacitor voltages
V_a ..... acceleration voltage in deposition process
v_{diff} ..... diffusion velocity
z ..... target depth

1 Introduction

Humankind always explored the nature, first what one could feel and see and then what avoided direct perception. Instruments were developed starting with simple lenses to microscopes and telescopes for observation of features at the both ends in the length scale. Today, there are instruments for investigation of features which can not be observed with the visible light spectrum. For example there are x-ray telescopes for exploration of astronomical objects such as black holes, and particle accelerators for exploration of subatomic particles. For the investigation of structures in the atomic scale range *scanning probe microscopy* (SPM) opens the door for many new applications in particular in surface physics. With this instrument the surface morphology can directly be observed and analyzed.

One interesting subject which can be investigated with SPM are clusters on substrates. Generally *cluster* is the name of an ensemble of objects. These objects can be everything, e.g. stars or computers. In this work clusters consisting of atoms are investigated. Many studies reported a difference between cluster and bulk properties. Hence, the cluster properties can not be directly deduced from the bulk properties and they have to be investigated separately resulting in a new research field called *cluster physics*.

In the last decades the miniaturization of electronic devices made enormous progress. One of the fields most visible in the daily routine is the computer technology where, e.g., computer memories or processors become smaller, faster and provide more memory. Every year many new useable technologies come into the market. In order to satisfy this hunger for higher information densities, the structures have to become smaller and smaller. Consequently the study of small particles such as metal clusters becomes more important.

One aspect for industrial usage of clusters, e.g. in electronics, is their controlled fabrication, e.g. in a pattern. That was performed in several experiments before using the interaction between the clusters and the surface and using the natural superstructure of a certain surface. However, these methods have limits concerning production because they depend on the cluster and surface material. For a selective patterning of any cluster or surface material high resolution fabrication tools such as scanning electron microscope or focused ion beams have to be used. That is the main topic of this work.

The idea was to combine two structuring methods for the production of nanostructures. For this purpose a new collaboration was launched between the TU Dortmund and the company Raith GmbH, supplier of nanofabrication tools. The first method is the fabrication of nanometer sized pits on graphite which was performed in our group before. These pits were used to produce metal clusters with a narrow size distribution. The second method is the fabrication of predefined structures with a beam of focused gallium ions. With this almost any pattern can be structured on any sample. The tool used here for this purpose is a new development of Raith (Raith 'ionLiNE').

Within this thesis the applicability of this method was tested and new applications were found. The fabrication of nanostructures with feature sizes smaller than 50 nm is presented (see section 5). These nano-structures were then used for the controlled growth of metal clusters. New and special properties of the metal clusters (silver and lead) were observed. Another topic in this work is the structuring of graphite layers, called graphene. In the last years the interest in this material arose particularly because of its special electronic properties. It will be shown that we are able to produce corresponding structures with our method. The experiments are combined with Monte Carlo simulations to understand the results.

2 Basics

In this chapter the basic elements of the investigated structures and used methods are discussed. The main purpose of this work is the investigation of metal clusters. The item clusters and their special properties will be discussed in the first section. The following section gives an overview about patterning methods for the fabrication of nanostructures. An interesting material which is intensively investigated in the last decades is graphene. Actually the graphite substrate is a stack of graphene layers. Hence with the structuring of graphite also graphene can be manipulated. In the third section the graphene is treated in detail to understand why it is an interesting material. Finally the last section gives a short insight into the chemical processes during the oxidation of graphite.

2.1 Clusters and their properties

Cluster physics is a relatively new topic in the solid state physics and is investigated in many studies [3-5]. *Cluster*s are nanometer sized particles containing few to several of thousands atoms. According to the number of atoms the clusters are classified in four groups as listed in table 2-1. The size of the clusters lies between the atomic and bulk scale. Single atoms have quantized electronic states and bulk materials have electronic band structures. The clusters exhibit an electronic structure which lies between these two extremes. They can be modeled with two methods. Either atoms can be composed to a cluster or a bulk material can be split down to the size of a cluster. These are called ‘bottom-up’ and ‘top-down’ approach.

micro clusters	3 -13 atoms
small clusters	14 - 100 atoms
large clusters	100 - 1000 atoms
micro crystallites	> 1000 atoms

TABLE 2-1: Classification of clusters by their size.

For metal clusters the atoms are bound by metallic bonds. For this bond type the valence electrons are delocalized among the lattice atoms. The metal can be regarded as a lattice of ions imbedded in a sea of electrons [6]. Theoretically the electronic structure of metal clusters can be described with the so called *Jellium-Model* [7-9]. It proceeds on a smeared out jelly-like background of the positive charge of the lattice atoms. The system properties only depend on the shell electrons.

The behavior of metallic clusters is interesting concerning e.g. electric, magnetic or optical properties. For example silver oxide particles can be optically activated with a laser [10,11]. Iron or cobalt clusters have very interesting magnetic properties [12-14]. Novel metal clusters like silver or gold clusters have an interesting electronic structure [15,16]. Palladium, platinum and iridium clusters exhibit catalyst properties mostly in respect of CO oxidation [17]. It is also known that noble metal clusters are catalytically active, too [18,19]. Most of these properties are strictly size dependent, which makes the production of well-defined cluster sizes important.

Experimentally the electronic and geometric structure of clusters was investigated in free beam experiments [20-22]. It has been shown that for the electronic structure ‘every atom counts’. One atom more or less can change the properties of a cluster. This behavior implicates a large spectrum of cluster properties. The problem is that this behavior brings a large number of experimental parameters into play which makes the investigation of clusters a field which needs a lot of time and equipment. Consequently many groups are working on different topics of cluster physics.

For almost any possible application the clusters have to be located at surfaces. The surface also influences the properties of clusters. The experimental group in Dortmund is specialized in investigations of the morphology and electronic structure of metal clusters, mainly noble metal clusters, at surfaces.

2.2 Patterning methods

There are different methods for patterning of structures on surfaces. The most used method is the structuring with a SEM (*scanning electron microscope*) which uses a beam of accelerated electrons [23]. Defect production can be performed by transfer of the electron energy to the substrate. However the probability of defect production is very small due to the small electron mass and it needs a high electron energy and intensity which influence the resolution of the SEM-tool. Nevertheless there are special molecules used as resist layer which are very sensitive to electron beams. The electron irradiation changes the bonds in the molecular structure. Thus either for a *negative resist*, initially soluble molecules become insoluble or for a *positive resist* the molecules change in the reverse direction. The soluble part can be removed by a solvent (called *developer*). The rest of the resist acts as a mask for a subsequent etching or evaporation step [24-26]. Then the resist can be removed completely, if necessary. This method is often used and yields good results. Instead of electrons, photons can also be used. In both methods the patterning is performed using a resist. That means they are reasonable for experiments which are not very sensitive to the surface properties or contaminated by ambient air.

For the conventional production of nano- or micro-structures masks or stamps are often used. Both are pre-structured for example with SEM. In the first case the mask is positioned between the evaporator and the substrate. Thus the evaporated material arrives only the areas with a free path to the substrate which builds the pattern of the mask on the substrate [27]. In the second case the material is evaporated on a stamp and then it will be mechanically transferred on the substrate. Principally it works like a printing machine [28].

Both methods are reasonable for patterning of a large number of micro- or nano-structures at short time scales.

At very small scales atoms or molecules can be moved by the tip of an STM (*scanning tunneling microscope*) or an AFM (*atomic force microscope*) [29-31]. With this technique atom corrals could be formed in order to visualize electron standing waves. This method is very time consuming since every atom has to be moved separately in a complex procedure. Hence, it is reasonable for local investigation of fundamental physics.

Another patterning method is the direct writing with focused ion beams (FIB). With this method the pattern is directly fabricated by damaging the surface with ion impacts. That originates from the larger mass of the ions and the stronger interaction with the surface in contrast to electrons. This method can be also combined with a resist supposed patterning [32,33]. However the direct patterning provides a preparation method of surfaces without contaminations which appear usually by the usage of resist layers [34-36]. That method is used in the present studies in combination with the oxidation of the surface, which replaces the etching process.

2.3 Graphene

Graphene is a two dimensional material which contains carbon atoms in a honey comb lattice as illustrated in figure 2-1a. The carbon atoms have four valence electrons which take three sp^2-hybridized σ-bonds to their neighbored atoms. Every C-atom is surrounded by three other atoms (figure 2-1b). The σ-bond is the strongest type of covalent bonds. Thus it makes the graphene layer a very stable material which is inert to many preparation methods. Additionally the carbon atoms exhibit weak π-bonds vertical to the graphene plane (figure 2-1b). This bond type makes the two dimensional existence of the graphene layer difficult in despite of its weakness. It interacts with atoms on the same or on other graphene layers and initiate the formation of different carbon structures as illustrated in figure 2-2. The illustration shows that stacking of a graphene layer leads to graphite, rolling up to a nano tube and wrapping to a fullerene.

Graphene has two types of edges; the armchair edge and the zigzag edge each in three available directions (cf. figure 2-1a).

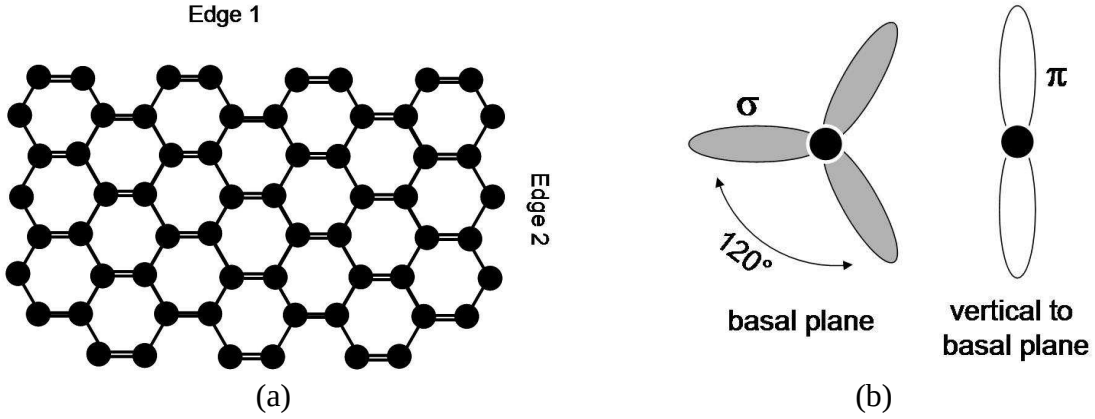

FIGURE 2-1: **(a) Illustration of the crystalline structure of graphene. Carbon atoms are localized in a hexagonal lattice. Graphene has two stable edge types (armchair and zigzag edge) labeled with 1 and 2. (b) Bond types of carbon atoms imbedded in graphite. In the basal plane the atoms have sp^2-hybridized σ-orbitals and vertical to it non-hybridized π-orbitals.**

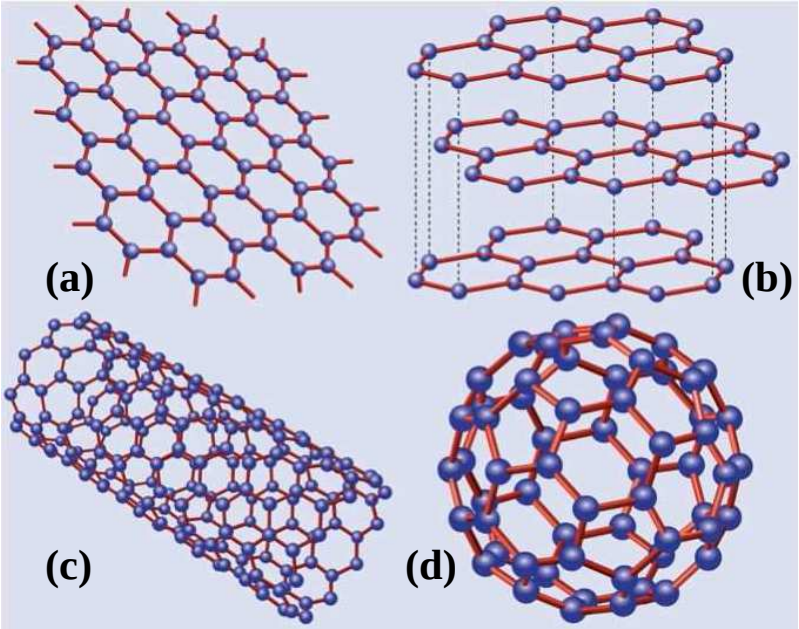

FIGURE 2-2: Different forms of graphene based materials (from [39]). (a) A freestanding graphene layer which is only stable on a substrate. (b) Graphite consists of a stack of graphene layers. (c) A carbon nano tube is formed by rolling up of a graphene sheet. (d) A fullerene (C_N) emerges by wrapping of a graphene layer with introduction of pentagons.

Graphene is an interesting material considering its electronic structure which is deduced from a tight binding approximation [40]. An illustration of the band structure is shown in figure 2-3. The electronic band structure has a conical shape at the so called *Dirac point*. At zero temperature there are no electrons in the conductance band. At higher temperature this band is filled by excitation of electrons from the valence band. Materials with this behavior are called zero-gap semiconductors.

Near these crossing points, the electron energy is linearly dependent on the wave vector. That is comparable with massless relativistic particles like photons which exhibit a linear dispersion relation with $E = c\hbar k$ with the light velocity c and the wave vector k. Consequently, electrons near the Dirac point can be treated as quasi massless particle and behave like relativistic particles which can be described by the Dirac equation (which describes relativistic quantum particles with spin ½) and not by the non-relativistic Schrödinger equation. Thus the electrons have a constant velocity at this point [41,42].

The electrons in graphene move ballistically and not by scattering at lattice phonons as usual for conductive materials. The evidence for this is that the carrier mobility is nearly independent on the temperature [43,44]. It is known that the scattering at lattice phonons dominates for higher temperatures and disappears for temperatures near zero. At these low temperatures scattering will only occur at defects. If the temperature does not play a role which is the case for graphene the electrons are only scattered at defects even at room temperature. Due to the very low defect density in comparison with the lattice atom density the mean free path becomes very large. Consequently the carrier mobility is very high. Indeed many experiments have shown a very good conductivity of graphene. Chen et al. have obtained a mean free path of 2 µm and a maximal mobility about 200000 $cm^2\ V^{-1}\ s^{-1}$ [44].

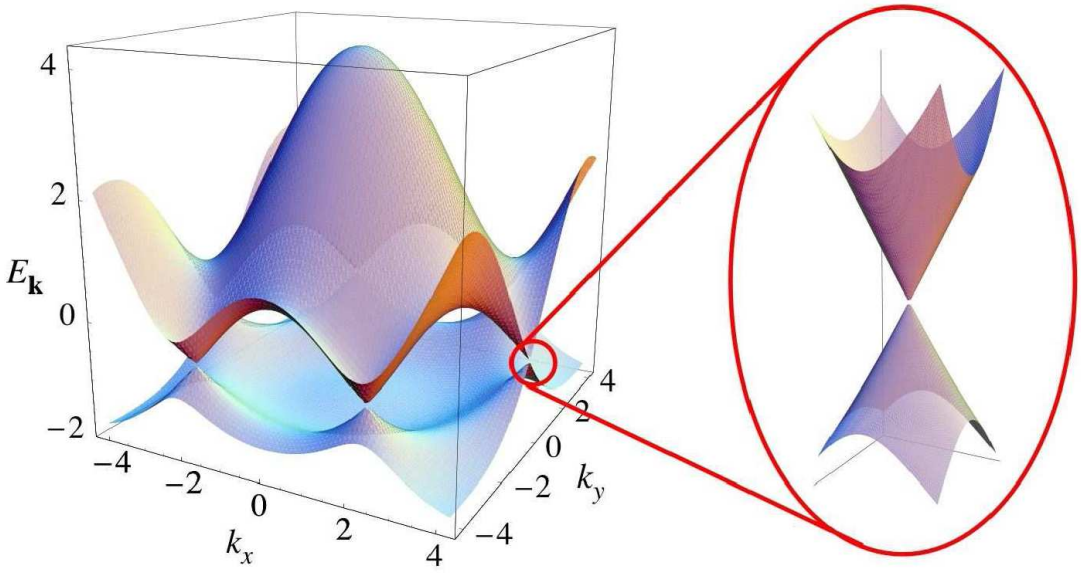

FIGURE 2-3: Band structure of graphene. The conductance band touches the valence band at the K and K' points (from [38]).

Graphene is an important material for further miniaturization of devices due to two main reasons:

- The enhanced stability in the graphene plane caused by strong σ-bonds enables the fabrication of very small stable structures.
- The high mobility in the 2D structure allows the construction of a high variety of electronic devices. For example one application is the production of devices based on ballistic transport phenomena.

Experimentally a graphene layer was first produced by Novoselov et. al. [45]. They used a mechanical exfoliation (repeated peeling) of an HOPG sheet for graphene production. Another newer fabrication method is the epitaxial growth on SiC samples. By annealing of the SiC surface above 1150 °C graphene layers can be obtained. The annealing temperature determines the layer thickness [46]. However in both cases beside the single layer also graphene multi-layers are obtained. The electronic behavior of e.g. bilayers differs from single graphene layers. Its band gap at the Dirac point is asymmetric [47,48]. The increase of the number of layers changes the electronic properties of the graphene. Single layer graphene is a zero gap semiconductor while graphite shows a semi-metallic behavior [49,50]. Additionally the electronic structure of graphene can be manipulated, e.g. by doping with foreign atoms [51].

2.4 Graphite oxidation

The pit production method is based on the oxidation of a graphite surface as it will be presented in 4.2. The graphite substrate can react with many gases like O_2, H_2, H_2O, CO_2, NO and Cl_2. Chu and Schmidt investigated the reaction with NO, H_2, H_2O and CO_2 in experiments [52] and Bennett et al. theoretically described the chemisorption of H, C, N, O and F on graphite [53]. The reaction of oxygen and graphite is investigated experimentally by Olander et al. [54] and theoretically by Blyholder et al. [55].

Especially for the graphite-O_2 reaction Olander et al. showed that the oxidation process can not be described only with a simple O_2 adsorption and CO desorption like equation 1 [56]. This first order reaction is only observed for higher temperatures (>1200 K). As reported by other studies there are two types of active sites on graphite namely site A, a more reactive, and B, a less reactive type [55-58]. In support of this hypothesis Olander et al. developed a two-site model of the oxidation process as depicted in equation 2. It implies that the oxygen molecule chemisorbs only on A-type sites (S_A) with the sticking probability η to form a bound CO and at the same time releases the partner oxygen atom. The oxygen atom migrates over the surface (labeled with k) and finds a B-site (S_B) with which it reacts and forms a bound CO. In both cases the CO molecule desorbs (labeled with k_d). In order to provide a net generation of A sites Olander et al. assumed that upon release of CO from B site, a fresh A site may be created. They could explain their experiments with this model.

$$O_2(g) + C \rightarrow 2CO(ads) \rightarrow 2CO(gas) \tag{1}$$

$$O_2(g) + S_A \xrightarrow{\eta} \begin{cases} CO(ads) \xrightarrow{k_d} CO(g) + S_A \\ O(ads) + S_B \xrightarrow{k} CO(ads) \xrightarrow{k_d} CO(g) + S_A \text{ or } S_B \end{cases} \tag{2}$$

Furthermore they showed that the rate of the oxidation to CO_2 is two orders of magnitude smaller than the oxidation to CO. Hence this reaction process can be neglected.

3 Experimental methods and setup

In this chapter the experimental equipment and methods are described. For sample preparation a focused beam of gallium ions is used, which enables the fabrication of patterned structures on a surface. With an ion sputter gun defects in a given intensity but at random positions can be prepared. The samples are investigated mainly with a scanning tunneling microscope. A part of them is investigated with tunneling spectroscopy and photoemission electron microscopy.

3.1 Focused Ion Beams

The *focused ion beam* (FIB) facility was developed by the company Raith and the NanoFIB partners [59]. The system structure and its usage are very important for the experiments. Hence, this facility is described in more detail. An important aspect is the fabrication of a stable beam of singly charged ions. That will be discussed in subsection 3.1.1. In the next subsection the facility including the FIB-column and important parts of the exposure sequence are presented. In the last subsections some properties of the ion beam are treated in detail.

3.1.1 Liquid Metal Ion Source

The LMIS (*Liquid Metal Ion Source*) is described very well in reference [60]. A liquid forms in a strong electric field a roughly conical shape, called *Taylor-Gilbert-cone*. It was first reported by Gilbert [61] and mathematically described by Taylor [62]. Taylor showed that a cone with a half-angle of 49.3°, called *Taylor-angle*, is in mechanical equilibrium with the surface. An LMIS produces ion emission from the apex region of a liquid-metal Taylor-Gilbert-cone. The cone can be made with two methods. Either the liquid metal flows through a narrow-bore capillary tube to the apex [63,64] or the cone is made by

wetting of a needle with the liquid metal. The needle type is more usual and it is used for the FIB-facility here. In both cases the liquid flow is assisted by capillary forces caused by roughness in the needle surface [65]. During operation the end of the cone pulls out into a cusp. The resulting radius of the emitting apex is typically 1.5-3 nm. From the apex ion emission occurs by field evaporation which happens if ions escape from the liquid surface [66-68]. They simultaneously ionize and break the atom-surface bonds. These ions can be used for the further processes.

The reasonable material for LMIS was investigated in many experiments (see [64] and the references in it). The most investigated materials are cesium and gallium. With gallium a high emittance and more stability was obtained [63,69,70]. Furthermore it has many useful properties. It is liquid at a temperature slightly above room temperature. Hence, it does not need a heating if it is once started. It produces mainly single charged ions and has a low vapor pressure. Due to these properties gallium is used for most of the LMIS-investigations and facilities.

The LMIS used in the present studies is developed and made by Gierak et al. [71,72]. It has gallium as source material. The gallium source is located within a looped wire which is crossed by a tungsten tip (figure 3-1a). The tip apex which is wetted with gallium is shown in figure 3-1b. The shape of the Gilbert-Taylor-cone and the emission area were observed with *transmission electron microscopy* (TEM) (figure 3-1c). In contrast to many other LMIS this source does not need a heating stage. Primarily it is featured for its long term stability.

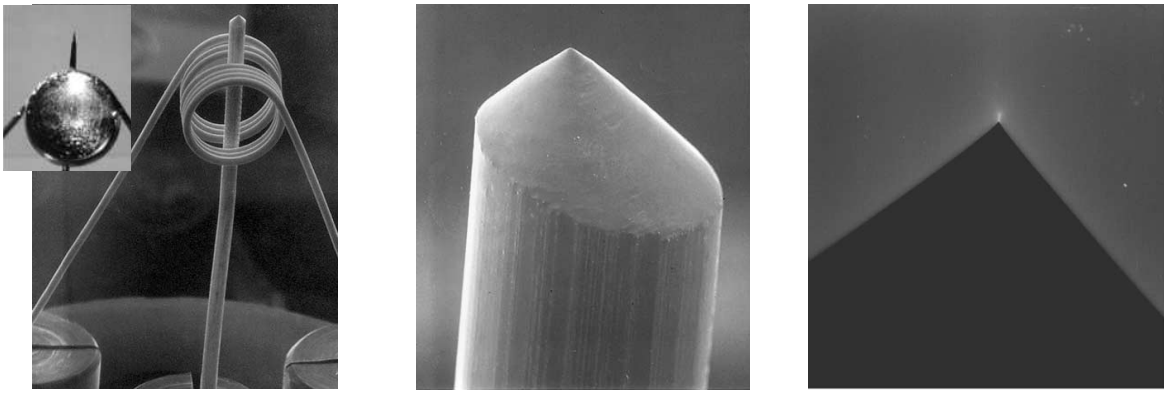

(a) (b) (c)

FIGURE 3-1: Images of the gallium LMIS developed by Gierak et al. (all images are taken from [71]). (a) shows the complete geometry of the LMIS without (large SEM-image) and with gallium (inset). (b) SEM-image of the tungsten tip shows the shape of the tip apex wetted with gallium. (c) TEM-image of the Gilbert-Taylor-cone. The emission area at the cone apex is clearly visible.

3.1.2 The ionLiNE tool

The first FIB facility was developed by Seliger et al. [73]. The FIB-column as used here is treated in references [74,75] in more detail. A schematic illustration of the FIB system is shown in figure 3-2. The ion beam produced with the gallium LMIS passes the *extractor* to the Nano-FIB system. After crossing an aperture the beam is focused with the *condenser* lens and corrected by the *stigmator*. There is a *blanker* between them to drive the gallium beam out of the microscope axis, if necessary. Before the beam passes the objective lens it can be deflected in lateral direction (*scanning*). This enables the exposure of pre-

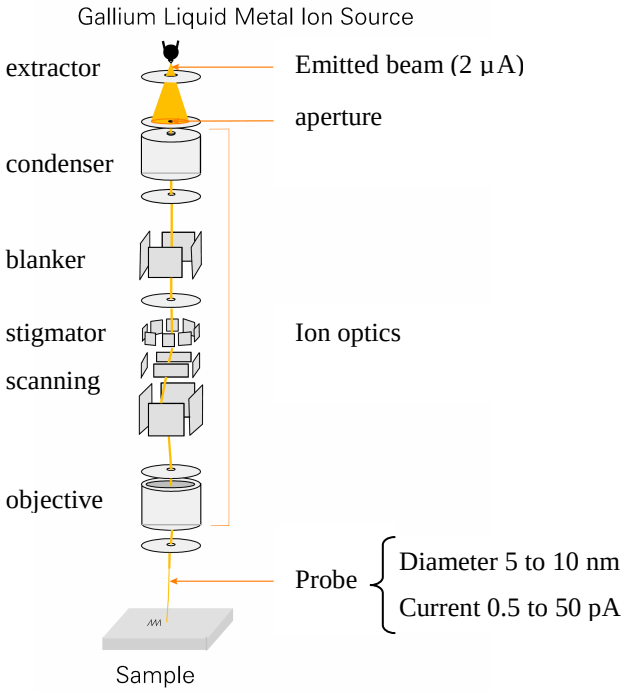

FIGURE 3-2: Schematic illustration of the Nano-FIB column (from [74]).

programmed nano patterns on a substrate. Actually the main architecture is an improved version of the Seliger FIB-facility and provides many functions in combination with a powerful software, a precisely movable stage and other helpful features. The main and most important part of the Raith patterning technique is the *pattern generator* which analyses and translates the patterns created with the computer software in the matching voltage values for the x- and y-deflectors.

An overview of the Raith nanofabrication tool, named ionLiNE (*ion beam lithography, nanofabrication and engineering workstation* [77]) is shown in figure 3-3. The Nano-FIB column is mounted on a high vacuum chamber which is separately pumped with an ion getter pump. Thus the column pressure during operation is about 5×10^{-8} mbar. This chamber is coupled to the main vacuum chamber which is pumped with a turbo molecular pump and has a pressure better than 10^{-7} mbar. In this chamber the sample stage and the *laser interferometer* are housed. The laser interferometer in combination with piezo elements guarantees a high accuracy and repeatability in nanometer range for the motion of the sample stage. The stage itself can host wafers up to 6 inch. A secondary electron detector is mounted in an angle about 45° relative to the FIB-column. The ionLiNE-tool provides two optical cameras for sample or position imaging on the stage. The pattern generator is housed together with the remote computer and other control panels in a control cabinet.

The FIB-column is designed for high resolutions and low ion currents. The resolution is obtained by using high acceleration voltages of 30 kV and above. The calculated lowest available resolution (FWHM) of the column amounts to 5 nm at 40 kV. Experimentally a probe diameter evaluated from etching of points and lines in thin SiC membranes down to 8 nm was observed [78]. The ion current is first determined by the extraction voltage. It increases with the voltage. After passing the extractor lenses the current is limited by an aperture. With an aperture diameter of 5 µm a beam current down to 0.5 pA can be achieved (cf. table 3-1). The capability for low ion dose patterning is very important for a number of experiments in this work, since they are based on single ion events. The

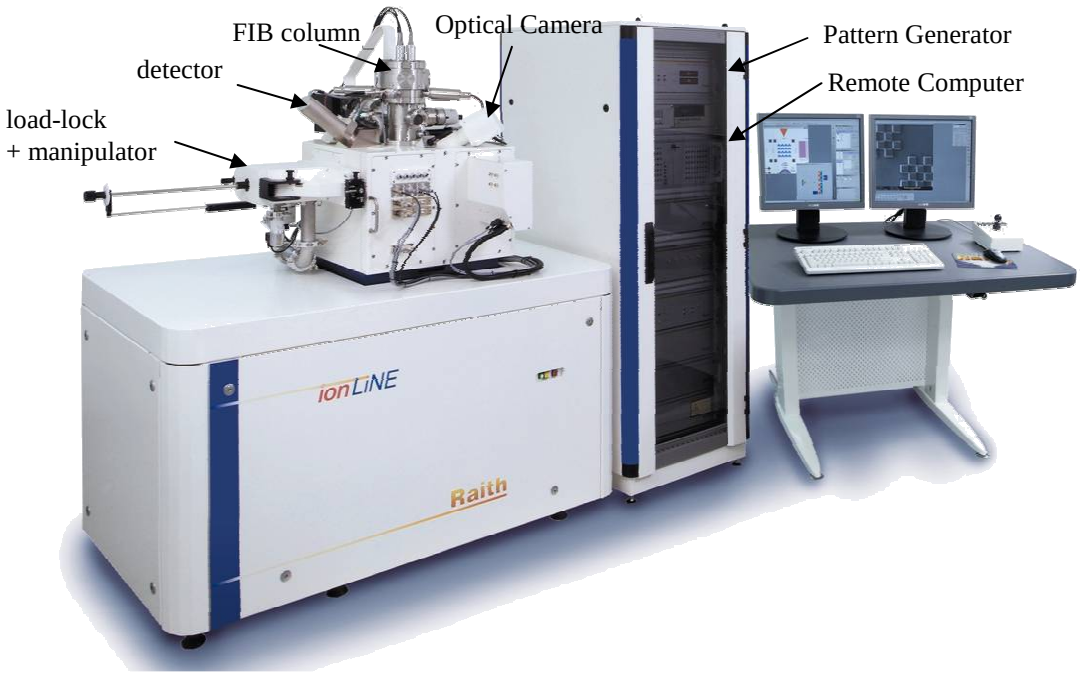

FIGURE 3-3: The ionLiNE lithography tool of the company Raith [77].

aperture	ion current
5 µm	0.5 – 5 pA
10 µm	3 – 8 pA
20 µm	6 – 20 pA
50 µm	> 40 pA

TABLE 3-1: The current of the ion beam for different apertures. It depends on the column architecture and aperture.

aperture also improves the resolution due to a cutting of the ion beam in the angular distribution. Furthermore the *working distance* (WD) influences the resolution. The best working distance is about 5 mm as calculated in reference [78]. The field of view is about 250 µm for a beam energy of 30 keV and a WD of 10 mm. An advantage of the FIB-facility is that it provides long time beam current stability as required for advanced and automated patterning.

The Nano-FIB facility is used for many applications like fabrication of quantum dots [74,75], patterned gold cluster aggregates [72], FIB sculpted membranes [79], connections in nanometer range [80] and modification of different magnetic layers [81-84]. All these experiments have shown very good performance of the FIB tool. The direct patterning of graphite substrates opens a new application of the FIB tool which tests the limits for very low ion intensities and high resolutions.

The exposure procedure includes the following steps:

- Pattern design: The pattern is designed in the GDSII-program module, which provides graphic tools for design editing. The designed elements are then placed in a position list which forwards the pattern, its position and the ion dose to the pattern generator.
- Aperture setting: The ionLiNE provides an *aperture changer* containing 5 apertures mostly with different sizes. Their position is saved in the ionLiNE software and can be driven automatically. This is very helpful e.g. for the

reduction of the exposure time and to save the small apertures for low ion doses. So in this work for structures which only define the pattern borders and do not need a high resolution larger apertures are used. The higher ion current results in a shorter exposure duration. For the main patterns which need a high resolution and low ion intensities the smaller apertures are used.

- Focusing: The focus of the ion beam can be adjusted with three parameters. The *focus* changes the voltage of the objective lens, the asymmetric probe shape can be corrected by the *stigmator* and the *fine movement of the aperture*, which adjusts the centricity of the beam.
- Position adjustment: There are two coordinate systems in the software. The *global system* defines the absolute position on the sample stage. The *local system* is defined by the user. It provides origin, angle and 3-points correction. The origin is mostly set near the region to be patterned.
- Ion current measurement and dose adjustment: The ion current can be measured with a Faraday cup on the stage. With this value and the planned ion dose the dwell time is calculated.
- Write field alignment: A large deflection of the ion beam causes a distortion of the pattern to be exposed. In order to avoid this effect the pattern is divided into smaller areas, called *writefields*. In this case the stage movement replaces the beam deflection. For this the stitching areas have to be combined as precisely as possible. That is the purpose of the write field alignment. It ensures that a point in the middle of the area has the same position if the beam is deflected to the border of the writefield and the stage is driven exactly in the opposite direction at the same time.

3.1.3 Ion dose definitions

The ion dose is determined by the waiting time of the ion beam on one point, called *dwell time* t_{dwell}, and the constant ion current I_{FIB}. For the correlation of ion dose and ion current the rule of thumb is that ***1 pA makes 6 ions/µs***. The ionLiNE software provides three types of ion dose specifications: *dot dose* D_{dot} given in pAs, *line dose* D_{line} given in pAs/cm and *area dose* D_{area} given in µAs/cm². All three are evaluated from ion current and dwell time as visible in the following equations:

$$D_{\mathrm{dot}} = I_{\mathrm{FIB}} \times t_{\mathrm{dwell}} \tag{3}$$

$$D_{\mathrm{line}} = \frac{D_{\mathrm{dot}}}{d_{\mathrm{line}}} \tag{4}$$

$$D_{\mathrm{area}} = \frac{D_{\mathrm{dot}}}{\left(d_{\mathrm{area}}\right)^2} \tag{5}$$

where d_{line} and d_{area} are the corresponding *line* and *area step sizes*. All structures even those consisting of areas or lines are written with dots. The ionLiNE software provides another writing mode, called FBMS (*Fixed Beam Moving Stage*), which is based on the writing of a continuous line by driving the sample stage. This mode is new and was not used in the experiments presented here. The ion dose is often adjusted by a multiplier called *dose factor* in the ionLiNE software.

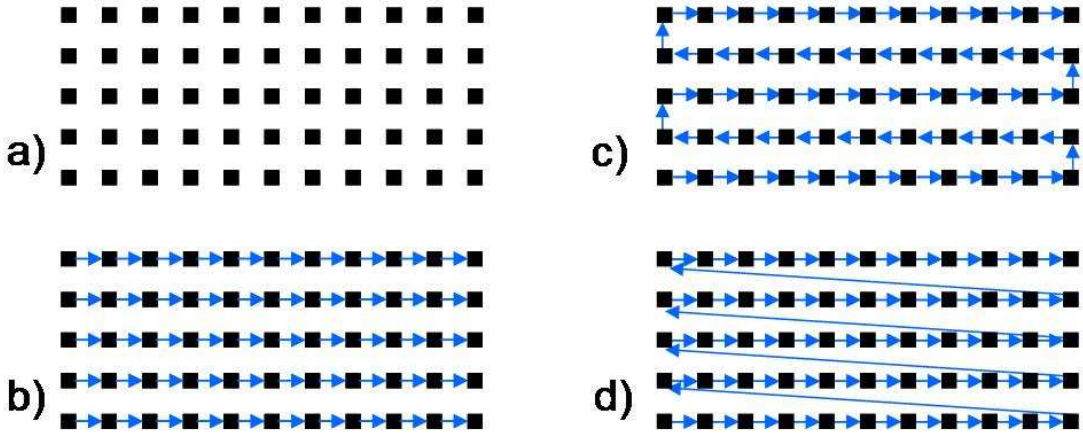

FIGURE 3-4: Four exposure modes of the ionLiNE tool demonstrated for a dot array: (a) dot mode with beam blanking, (b) line mode with beam blanking between the lines, (c) area meander mode and (d) area line mode, both without beam blanking.

The mean difference of these dose parameters is the writing process as illustrated in figure 3-4. In dot mode every dot is written independently and between them the ion beam is blanked. In line mode the beam is blanked only between the lines and in area mode the beam is not blanked (in the normal configuration). In the case of relative high ion currents about 10 pA the beam driving between the points would also make defects. Thus in many experiments lines are observed instead of dot arrays (cf. 3.1.3). Additionally the ionLiNE offers two kinds of area modes which distinguish in the change between the lines (the method is called *direct Gaussian beam vector scan*). In *area meander mode* the next line is written in the opposite direction of the writing direction of the previous line. In *area line mode* the lines begin every time at the left side and are written to the right. The ionLiNE tool provides also other writing modes which are not of interest here.

In the case of dot mode every point has its own position parameters. That noticeably reduces the writing speed. In contrast the area mode is defined with few parameters and is much faster. Principally it is possible to switch on the beam blanking for the area mode and use it instead of the dot mode, for a periodic point pattern with the advantage of a higher writing speed.

Most of the patterns exposed in the present studies are lattices of *points* (dots in the software). Since the ion doses are very small, they are mostly given in counts of ions per point. This ion dose specification is named *point dose* D_{point}. Thus the different results can be compared. This dose specification neglects the writing mode. Assuming single charged ions it can be calculated with:

$$D_{\text{point}} = D_{\text{dot}} / e \tag{6}$$

where e is the elementary charge of 1.602×10^{-19} As.

As it will be discussed in 5.3.1.1 the experiments have shown that different structures emerged with the same D_{point} and the same pattern. The reason for this are different focus conditions. In order to compare results with different focus conditions another dose specification is needed, named *point area dose* D_{pa} given in ions/cm². It can be evaluated from:

$$D_{\text{pa}} = D_{\text{point}} / A_{\text{point}} \tag{7}$$

where A_{point} is the area of the irradiated region. The value of A_{point} can be estimated from the shape of the exposed area in case of high ion dose. However A_{point} is not sharply defined and its determination is quite inaccurate. But it yields a rough value for qualitative comparisons.

The point dose is determined by I_{FIB} and t_{dwell}. These parameters are given by the FIB exposure. It is the adjustable dose parameter. In contrast the point area dose is dependent on the point dose as well as on the ion focus size, i.e., for the same point dose a better focus results in a higher point area dose. It is the crucial parameter for the distribution of the defects and the point shape after oxidation. It is not simple to choose D_{point} for an aimed D_{pa} since the range of the irradiated area is unknown before exposure. The best way for comparable results is to find the best focus and use the same D_{point} [1].

One further parameter in the ionLiNE software is the waiting time after exposure and before changing to the next pattern point, called *settling time* t_w. If t_w is too small the shape of the exposed point can be deformed.

3.1.4 Origin of the defect distribution or structure width

The defect distribution or the width of the exposed area is mainly influenced by the beam profile. The probe diameter is estimated to be about 10 nm. The ion beam resolution is given by the full width at half maximum (FWHM) of the ion distribution, assumed to be e.g. a Gaussian (figure 3-5a). Not only the ions within the 10 nm region but also the ions at the distribution onset contribute to defect production. Hence the produced structure is larger than the probe diameter. However the beam profile alone can not explain the width of the structures. Another reason for a larger exposed area is the existence of recoil atoms which are created by the scattering process (figure 3-5b). They form defects at a certain distance from the main impact point which could be far away from the origin ion distribution. The number of recoils increases when increasing the ion dose. Finally, the structure can be enlarged by the oxidation process (figure 3-5c).

The lateral size of the pits can be compared with the simulations without the oxidation process in reference [72] and own simulations in section 6.1.2, which show that an ion beam of 8 nm FWHM produces defective areas with a diameter of about 20 nm. That is in good agreement with the measurement (diameter of the ‘nano-cavities’ up to 30 nm, cf. 5.3.1.1). It shows that the oxidation process does not drastically increase the ‘cavity’ diameter. We assume that the main process which causes the larger width of the exposed structures is the recoil of carbon atoms.

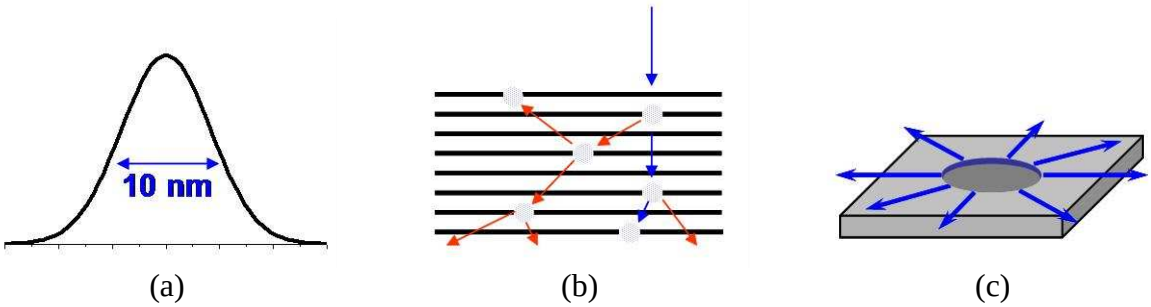

FIGURE 3-5: Origins of the structures width after FIB exposing and oxidation. (a) Gaussian curve with FWHM of 10 nm representing the ion distribution in the focused beam. (b) Ion and atom trajectories in a graphite substrate. Blue arrows illustrate the path of the impacted ion and the red lines the recoiled carbon atoms. (c) Oxidation process. The arrows illustrate the progression direction of the etching process.

3.2 Scanning Tunneling Microscopy

The samples are measured in *ultra high vacuum* (UHV) with a *Scanning Tunneling Microscope* (STM). STM has been developed 1982 by G. Binnig and H. Rohrer [86,87]. For this development they got the Nobel Prize in physics together with E. Ruska in 1986. Today the STM is one of most important tools for investigation of conductive surfaces like metals or semiconductors down to atomic resolution. Its most important advantage is the ability for local investigation of periodic as well as non-periodic structures. The main analysis topic is the visualization of the surface topography but recently it found more applications like surface manipulation. STM tools exist in many variants each specialized for an application. For example there are STM with a magnetic tip to investigate magnetic surfaces (SP-STM, [88]), electrochemical STM (EC-STM, [89]), and video STM for real time observations [90].

The used STM apparatus here can be operated at low temperatures. It is embedded in a low temperature UHV surface analyzing system (LT-system). An overview is given in 3.2.2. Additionally another UHV-system (RT-system) containing an STM operated at room temperature is set up for further investigations of nano-pits. It is described in 3.2.3.

3.2.1 Principles

STM is based on the *tunneling effect* that arises from quantum mechanics. It was used for explanation of α decay of radioactive nuclei [91-93]. In classical mechanics electrons can not flow between two conductors separated by a gap, even if a voltage is applied. In quantum mechanics there is a probability that electrons can tunnel through the potential barrier which represents the space between the conductors. That can be described with a simple model as shown in figure 3-6. Assuming that the work functions Φ of tip and sample are equal and the sample bias is small ($eV \ll \Phi$) the following equation applies for tunneling current.

$$I \propto \exp\left(-2d\sqrt{2m(\Phi - E)/\hbar^2}\right) \tag{8}$$

where $\hbar$ is the reduced Planck constant, m the electron mass, d the distance between tip and surface, and E the binding energy of the electron related to the Fermi level of the substrate. The essential aspect is the exponential dependence of the tunneling current on the distance d. Thus a small variation of d results in a large variation of I.

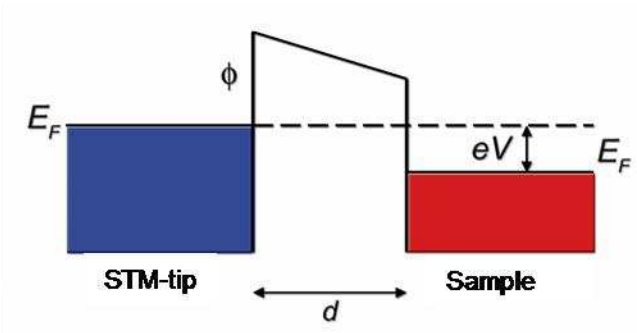

FIGURE 3-6: Band model of a one dimensional potential well for the case that the work function Φ is equal for tip and sample.

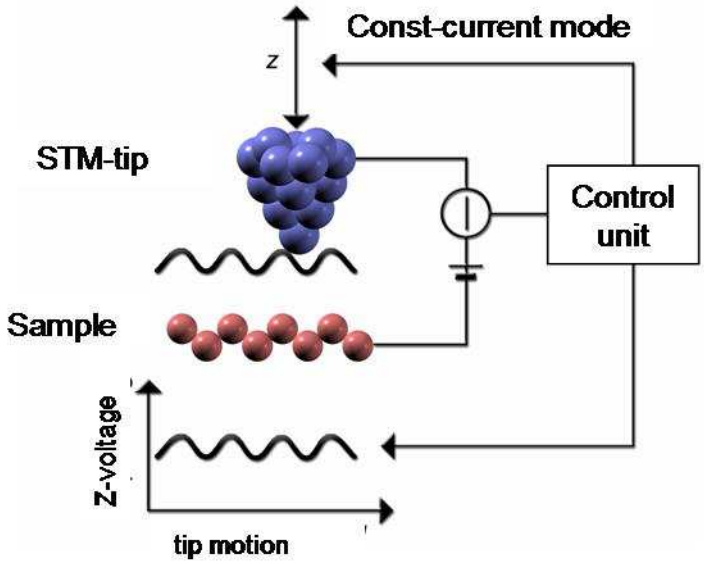

FIGURE 3-7: Illustration of the basic setup of an STM.

The basic setup of an STM is displayed in figure 3-7. The STM is operated in the so called *constant-current-mode* which is used for the present experiments. In this operation mode the distance *d*, and with this the tunneling current *I* (called *set point*), is kept constant using a *feedback loop*. During scanning the tip follows the structure of the surface. The tip motion in *z*-direction is measured and combined with the tip motion in *x*- and *y*-direction first to line profiles and then to an STM image. The motion of the tip is realized e.g. by applying voltages on three piezoceramic elements each for one direction (here a tube scanner). For high resolution as needed here the probe diameter should be smaller than the investigated subject. That is achieved by using a carefully electrochemically etched tungsten tip. The apex of this tip contains few atoms. Thus the tunneling current, which mainly flows through this region due to the exponential dependence as explained above, is laterally confined resulting in a high resolution. The other operation mode is the *constant-height-mode* where the *z*-position is kept constant and the tunneling current is measured. This operation mode is attended with danger of collisions. Hence, the constant-current-mode is favored for most of measurements. For more details see reference [94].

An STM image does not exactly display the surface morphology. Actually a surface with a constant *local density of states* (LDOS) at the sample surface is imaged in STM and not the geometric shape. This is theoretically described by Tersoff and Hamann [95] based on the studies of Bardeen [96]. The density of states differs for different materials. Adsorbates or vacancies have other LDOS as their surrounding surface. Depending on the sample bias both can be imaged either as holes or hills [97,98].

3.2.2 LT-System

The sample preparation and STM measurements were mainly performed in an UHV surface analysis system of the company Omicron Nanotechnology GmbH [99] which is capable of working at low temperatures down to 5 K. It is described in detail in reference [100]. A schematic illustration with the main parts labeled is shown in figure 3-8. The facility provides good vacuum conditions with pressures down to 10^{-11} mbar. It is

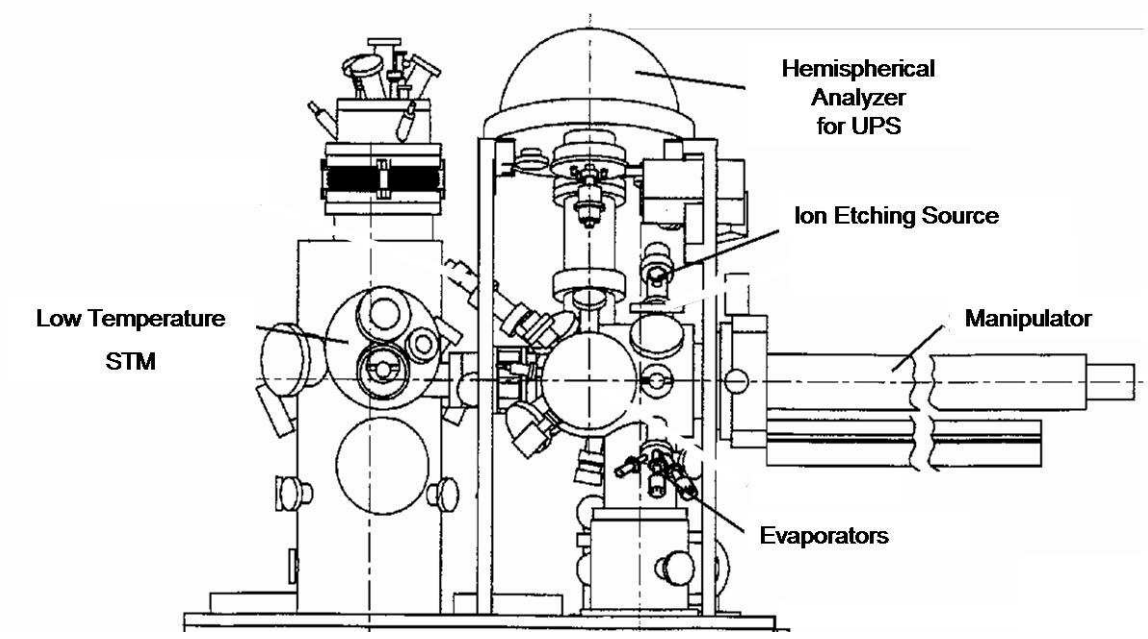

FIGURE 3-8: Schematic illustration of the UHV low temperature system [100].

composed of two chambers. The left chamber contains the low temperature STM (the analysis chamber). With liquid nitrogen (LN_2) and/or liquid helium (LHe) temperatures of 77 K or 5 K can be achieved. For a stable imaging the present STM measurements are mostly performed at 77 K. The right chamber (preparation chamber) provides apart from analysis methods such as *UPS* (*ultraviolet photoemission spectroscopy*) many instruments for sample preparation. The sample holder located on the manipulator provides heating up to 800 °C and cooling down to 15 K. With the ion etching source argon ions can be accelerated to the sample for sample sputtering. It is also used for defect production as needed for nano-pit production. The metal deposition for cluster formation is performed with *evaporators with integral flux monitor* (*EFM*). The deposition process and the determination of the deposited coverage are described in reference [101] in detail.

3.2.3 RT-System

For investigation of nano-pit patterns (as will be discussed in 4.2) often low temperature measurements are actually not needed. In order to make measurements faster and more frequently, an existing STM apparatus is extended to fulfill the needed requirements. It is intended for further experiments and was used only infrequently in the present study. Hence it is described here only shortly. For detailed descriptions see references [102-104].

The investigated areas cover only a small part of the sample (mostly 250 µm × 250 µm). In order to localize this area in STM with an optical camera markers are placed on the sample. These markers can be observed with a face-to-face positioned observation and lightening with an angle of at least 25° relative to the sample surface. For this the front flange was replaced by a new flange with two angled view ports and the STM stage was lifted upwards with a CF-spacer [103] (figure 3-9a). Instead of the face-to-face positioning an angled mirror within the STM was installed in such way that one view port can be used for camera observation and the other one for lightening. Additionally a new camera was acquired for a reasonable enlargement. Another extension is a new sample storage for 5 samples in the STM stage [103].

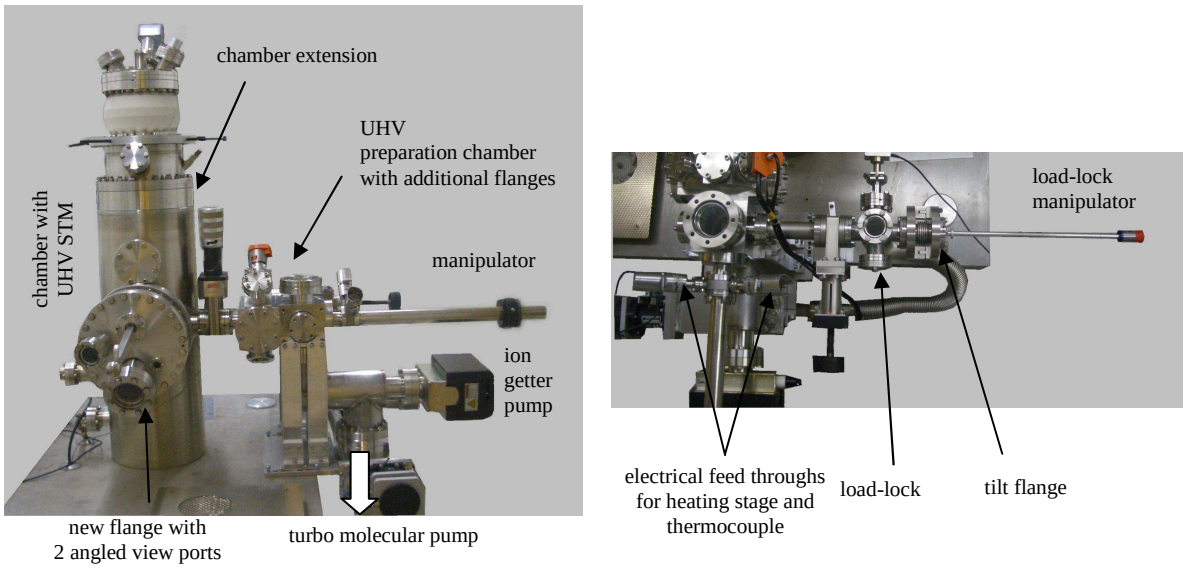

FIGURE 3-9: (a) The room temperature UHV system with STM (called RT-System) in side view. (b) The preparation chamber and load-lock in top view.

The STM apparatus was investigated and improved in respect of vibration reduction [102,104]. Thus the noise in the STM measurements could be reduced at least by a factor two. For sample preparation a new chamber was constructed which also provides a number of flanges for further applications like evaporators, optical measurements or wobblestick installation. It provides UHV conditions with a pressure down to 10^{-10} mbar using a turbo molecular pump and an ion getter pump. The sample transfer is performed with the load-lock extension (figure 3-9b). The transfer is realized with a linear/rotary feedthrough and a tilt flange [102].

3.2.4 Data analyzing

With line profiles the height and width of the imaged structure can be measured. These values should be treated carefully since the shape of the imaged structure is influenced by the tip shape. In following two example cases are treated since both appear in the analysis of STM images.

"Cluster Imaging"

The first case is the measurement of clusters as illustrated in figure 3-10. This illustration is simplified in that way that the tunneling current only flows between the nearest points. That is of course a good approximation due to the exponential dependence as discussed in 3.2.1. During the movement over the cluster the tunneling current can flow not only through the tip apex but also through the tip sides. That and the non ideal shape of the STM tip causes a broadening of the imaged cluster as visible in the illustrated line profile. The important aspect is that the width of the cluster is broadened. It also hinders to image the three dimensional shape of clusters. That is exemplary demonstrated by three fictional cluster shapes on the right side. All three would be in agreement with the STM line profile. Independent from the lateral shape of the clusters the cluster height can be measured. Usually a spherical shape or an octahedron for faceted clusters is assumed [105]. For a facet the lateral size can be evaluated. The faceted area is another measurable value since it is not deformed by the STM tip.

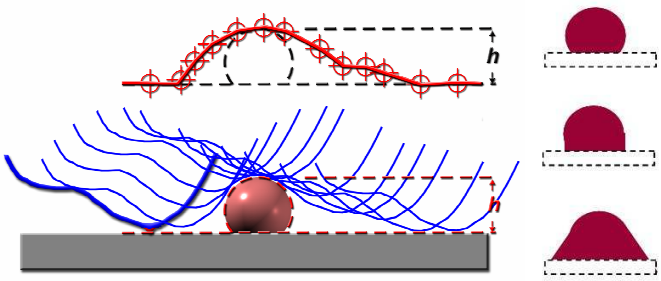

FIGURE 3-10: **Influence of the tip on the STM image for a cluster. (bottom) The STM tip has a non ideal shape. The movement of the tip over the cluster is illustrated with this tip. The tunneling current can also flow through tip sides. This results in a broadening of the cluster shape. (top) The resulting line profile. (right) Three possible shapes, if the real shape is unknown.**

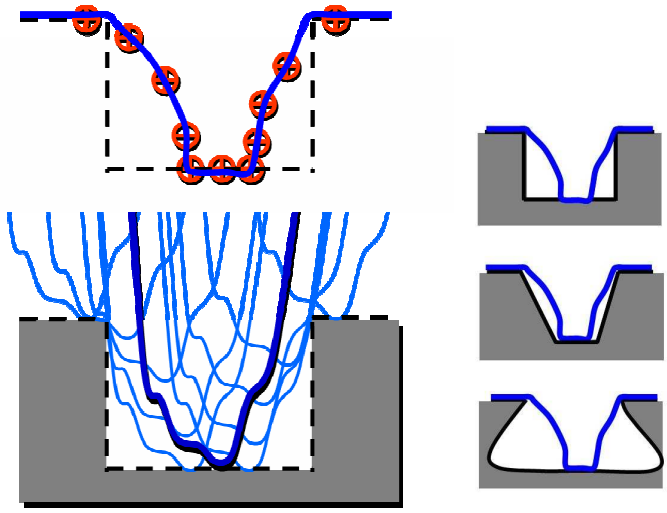

FIGURE 3-11: **Influence of the tip on the STM image for a large pit. (bottom) Similar to the cluster imaging the tip moves over the pit. The pit shape and the flowing current through the tip side result in a narrowing of the width within the pit. (top) The resulting line profile. (right) Three possible pit shapes, if the real shape is unknown.**

This analysis of the STM images was performed with the WSxM program [106] developed by Nanotec [107]. Also the STM images are prepared with this program. The cluster height is measured by the difference of the cluster top and the surface level directly at the cluster onset. The cluster facet is measured by cutting of the cluster top slightly (< 1 atomic layer) below the top side. This analyzing method is described in reference [101]. In the present study many clusters were analyzed to obtain good statistics for analysis. That is performed with a program, named *Clusterizer*, developed by Grönhagen [104]. The program was tested and compared with many STM images and yields good results.

"Pit Imaging"

The other case is the measurement of deep pits as illustrated in figure 3-11. Similar to the cluster imaging the tunneling current can not only flow at the tip apex but also at the tip sides during the movement. This time the tip has to move within the pit. Thus the tip shape primarily determines the imaged pit shape. However the measured width on the surface is correct. Also the pit depth can be measured if the pit is broader than the entered part of the tip. The real 3D shape of the pit can not be determined with STM as illustrated with three fictional pit shapes at the right side in figure 3-8. All three will result in the same line

profile in STM. For the modeling of the pit shape Monte Carlo simulations were used as it will be presented in section 6.1.

3.3 Scanning Tunneling Spectroscopy

Electronic properties of the sample can be investigated with many spectroscopic methods. But most of these methods can only measure a large area of the surface which results in averaging over this area. A method for local investigation of the electronic structure is the *scanning tunneling spectroscopy* (short STS) which can be performed with an STM tool. It is a useful tool for the investigation of clusters at surfaces.

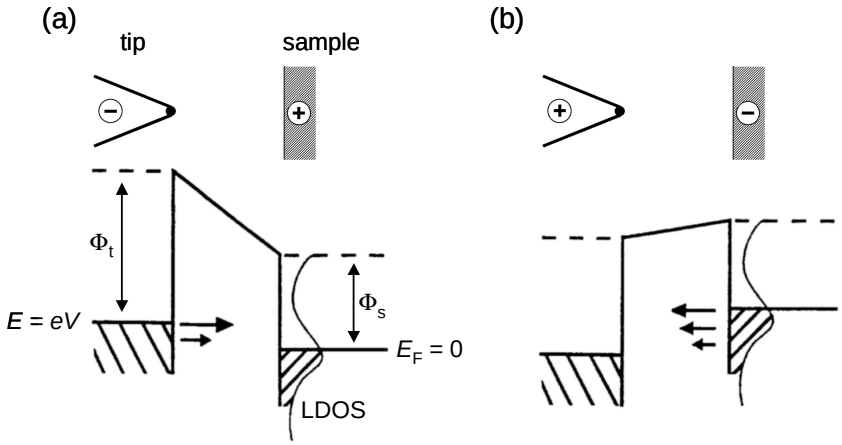

FIGURE 3-12: Schematic illustration of the tip-surface system for (a) positive and (b) negative sample bias voltages. The shape of the potential barrier between tip and surface depends on the respective work functions Φ_t and Φ_s. The different polarity of the bias voltages results in tunneling either into unoccupied states or out of occupied states of the sample.

The idea of STS is the measurement of the tunneling current *I* in dependence on the sample bias voltage *V* (figure 3-12). During measurement the tip position is kept constant. If the sample bias voltage is positive electrons tunnel from occupied states of the tip into the unoccupied states of the surface. A negative voltage results in the tunneling from the occupied states of the surface into the unoccupied states of the tip. Assuming a constant tip DOS and low voltages the differential conductivity *dI/dV* is directly proportional to the *local density of states* (LDOS) of the sample surface [108]. The set point (*I*,*V*) before starting the spectroscopy procedure determines the signal amplitude.

3.4 Photo Emission Electron Microscopy

The *photo emission electron microscope* (PEEM) is based on the photo emission of electrons as used for photoelectron spectroscopy methods (short PES, e.g. UPS, XPS) [109-111]. Electrons in the sample are excited with light. The emitted electrons are accelerated with a high electric field towards the PEEM-equipment in which the image is magnified by electric and magnetic lenses. Finally a detector (CCD-camera) records the image and forwards it to a computer. PEEM directly images surface areas emitting electrons without scanning in contrast to SEM. Thus the image appears in real time. With PEEM the photoelectron spectroscopy is improved to a local measurement method. Since it includes PES it does not only measure the surface topography. It also makes chemical, electronic and magnetic properties of the surface and their distribution visible.

The used PEEM is a part of an UHV facility of the AG Aeschlimann, TU Kaiserslautern (figure 3-13). It is described in reference [2] and the PEEM is described in reference [112]. The optimum resolution of the used PEEM is < 40 nm. As excitation source a mercury lamp or a laser can be used. The different sources enable different chemical contrast in the imaging. The sample can be prepared in-situ and also measured with STM or AFM.

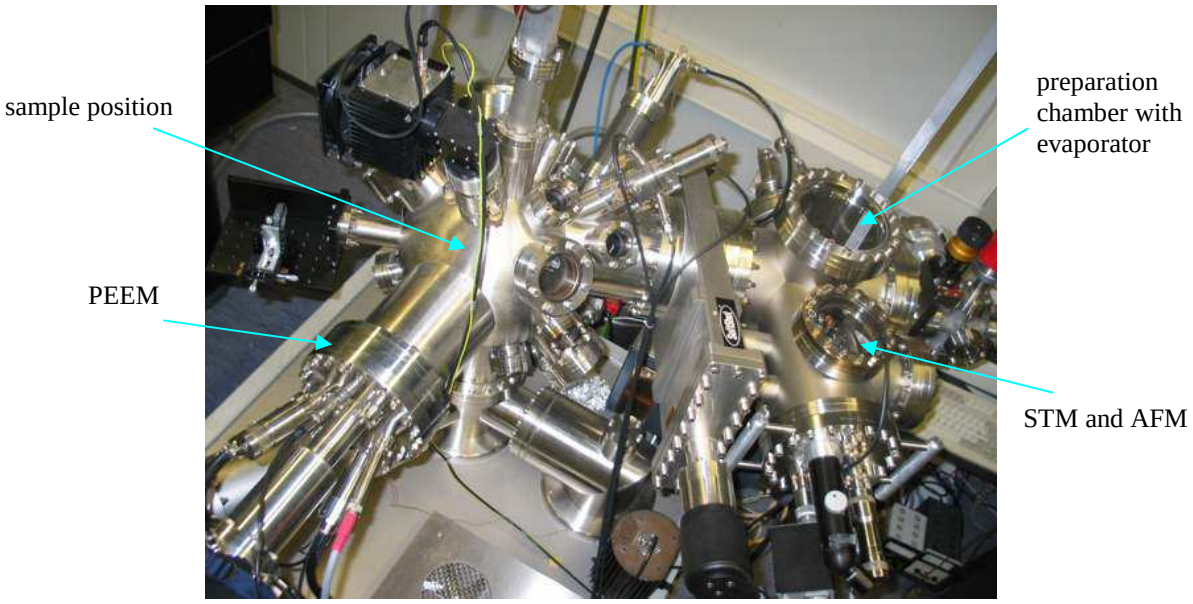

FIGURE 3-13: PEEM UHV-tool at TU Kaiserslautern [113].

4 Sample preparation

The investigated structures are metal nano particles on a graphite substrate. Due to its special properties, such as weak interaction with metallic particles, graphite is often used in experiments. Thus these samples are good model systems for further developments. For the production of metal structures with a narrow size distribution or in a given pattern nanometer-sized pits act as anchor sides. The production of these pits opened new options for applications. With different sizes and shapes of the pits different structures can be obtained. Hence the description of the pit production method is as important as the formation of metal clusters and is also treated in this section in detail.

4.1 Substrate properties

The used substrate for all experiments is a *highly oriented pyrolytic graphite* (HOPG). It has a polycrystalline structure with crystals of varying sizes, typically several μm, and it exhibits high chemically inertness. The mentioned crystals provide a large flat surface only interrupted by graphite atomic edges. The weak cluster-substrate coupling makes HOPG to a reasonable substrate for investigating metal clusters, which is the main topic of our group.

Graphite consists of stacked graphene layers which were discussed in section 2.3 in detail. The hexagonal structure is shown in figure 2-2b. The atomic distance along the σ-bonds is 0.142 nm. The honey comb structure of the graphene layers can be described with a two atomic basis and a lattice constant of $a_{\mathrm{HOPG}} = 0.246$ nm. The distance between the graphene layers is $d_{\mathrm{HOPG}} = 0.335$ nm [114,115].

The weak cluster coupling on the surface is also a disadvantage, since the clusters are very mobile on the surface. Therefore, in order to fabricate and investigate clusters on HOPG, ‘nano-pits’ serve as nucleation centers (see next section). They also enable a stable imaging with the STM.

Due to the weak interaction between the graphene layers HOPG can be cleaved parallel to the layers. This is performed with a commercial tape in ambient conditions. The freshly cleaved surface is used as substrate surface for experiments. After the fabrication of pits

the sample is introduced into vacuum, annealed at 600 °C and metal atoms are deposited. Between these preparation steps STM measurements have been performed.

4.2 Nano-pit fabrication

"Growth Mechanism"

The existence of large circular pits on HOPG was observed with the technique of etch-decoration transmission electron microscopy in 1964 [116,117]. In later experiments the pits were investigated with STM [118,119]. The kinetics of the oxidation process, especially oxidation of defects were investigated in many studies experimentally [117,120-123] as well as visualized by simulations [124,125].

The diameter of the pits is uniform and given by the oxidation parameters such as substrate temperature T_{ox}, oxygen partial pressure p_{O2} and duration of the oxidation process Δt_{ox}. The temperature of the oxygen gas does not affect the oxidation process as reported in reference [54]. Adjusting these parameters, pits in the range of a few nanometers for the smallest pits and up to several hundred nanometers (*molecule corrals* [126,127]) can be achieved. The diameter of the pits d_{pit} corresponds to the formula:

$$d_{\text{pit}} = C\, p_{\text{O}_2} t_{ox} \times e^{-E_a/RT} \tag{9}$$

where R is the gas constant and $E_a = 1.27 \times 10^5$ J mol^{-1} the activation energy for the monolayer etching with O_2 [119]. The constant C is of the order of 10^4 nm mbar^{-1} s^{-1}. It is dependent on the pit density [117,128].

"Fabrication"

The experimental sequence of the pit production consists of the defect production and the oxidation process. The defects are produced with ion bombardment performed either by sputtering with argon ions [128,129] or by FIB exposure [130]. The latter method enables the production of given defect patterns. Afterwards these defects are oxidized in an oven which can be floated with different gases. The oven is heated at 1000 °C using a nitrogen atmosphere to remove impurities, in particular water, before inserting the sample. Then the oven is cooled down to a well defined temperature. After that the gas is changed to an Ar/O_2-mixture (2% oxygen) and the HOPG sample is inserted. A constant flow rate is maintained across the oven to keep the oxygen density constant and avoid entering air from outside. The oxidation temperature and time are known from previous experiments for fabrication of pits with reasonable depth and diameters [16]. The used parameters for oxidation as well as for defect production are listed in table 4-1.

The fabrication principle is illustrated in figure 4-1. At the temperature used in the present studies the graphite surface (not the defects) would not oxidize since the σ-bonds in the lateral direction are very strong. That happens only at temperatures above 700 °C [118]. Consequently the oxidation process occurs only at step edges and surface defects where the σ-bonds are broken. The density of natural defects on the HOPG surface is very low. It amounts to approximately 1 defect/μm² as reported in references [128,131]. With the mentioned ion bombardment the defect density can be controlled. In former studies, using Ar ions with 1 keV kinetic energy, it was estimated by comparison of the ion dose and the number of nano-pits that surface defects in the first graphite monolayer occur approximately for every 10th incident ion. The decisive point of pit fabrication is the layer structure of the HOPG substrate. If the layer under the surface layer does not exhibit

defects only the first monolayer starting at the surface defects oxidizes [52]. Thus the resulting pit is only one atomic layer deep. These atomic pits which exhibit diameters about a few nanometers are called nanometer-sized pits, short *nano-pits*.

In reality defects occur also in the inner graphite layers. The probability for uncovering of an inner defect during the surface oxidation increases with the defect density given by the ion dose and layer location relative to the surface. That means the rate of the *multilayer pits* increases with the ion dose. Zhu et al. observed that these pits oxidize faster than the one monolayer pits [132]. If the ion dose is very high a volume full of defects is produced. This volume oxidizes completely. These very deep pits are called *nano-cavities*. Nano-cavities can also be produced by the impingement of clusters onto the surface and subsequent oxidation [133,134].

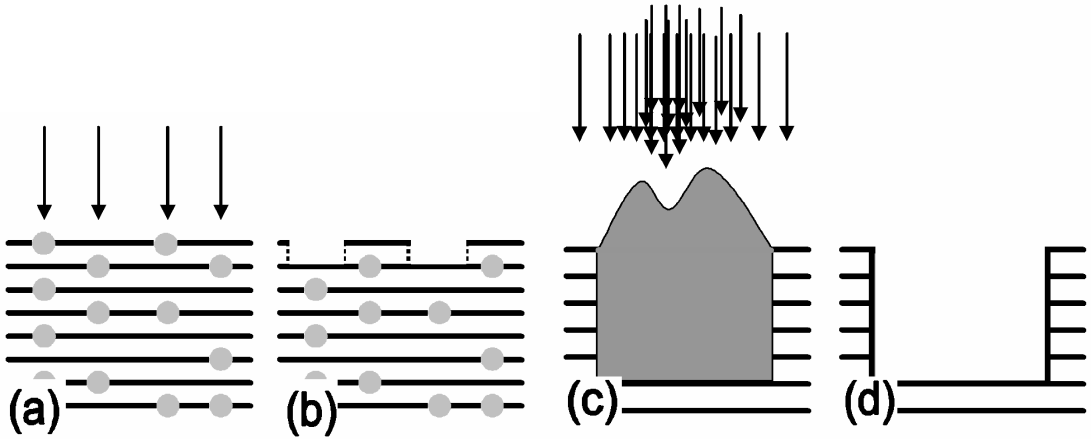

FIGURE 4-1: Schematic representation of the defect formation and oxidation process. (a) For low ion dose each incident ion causes a few defects arranged in a line inside the sample. (b) Only the defects in the first graphite layer oxidize and grow to nano-pits. (c) For high ion dose the ions produce a volume full of defects. (d) The whole volume is removed after the oxidation and a nano-cavity is formed. The depth of the nano-cavity is equal to the maximal penetration depth of the incident ions (c.f. 5.3.1.2).

FIB patterned samples							
Sample	Δt_{ox} [min]	T_{ox} [°C]	I_{FIB} [pA]	writing mode	aperture [µm]	laboratory notation	main purpose
SAMPLE 1	200	540	6	area	20	HOPG_R02	ion dose variation
SAMPLE 2	200	540	1.7	area & dot	--	HOPG_R04	writing mode
SAMPLE 3	200	540	6	dot	--	HOPG_R08	writing direction vs. ion dose
SAMPLE 4	200	540	1.9	line	10	HOPG_R11	distance dependence of oxidation
SAMPLE 5	200	540	5	dot	--	HOPG_R05	finding pattern
SAMPLE 6	200	540	11	dot	--	HOPG_R03	distance reducing
SAMPLE 7	200	540	3-4.4	dot	--	HOPG_R07	large 4 mm² area
SAMPLE 8	200	500	2.3	line	10	HOPG_R20	cluster rows
SAMPLE 9	200	450	0.5	area	5	HOPG_R18	single cluster pattern, distance test
SAMPLE 10	300 200	450 500	0.55	area	5	HOPG_R19	single cluster pattern, ion dose test
SAMPLE 11	200	540	1.1 & 9,5	dot & area	5 & 20	HOPG_R10	distance reducing
SAMPLE 12	200	540	13-14.5	area	10	HOPG_R22	graphene structures

argon sputtered samples							
Sample	Δt_{ox} [min]	T_{ox} [°C]	I_{sample} [nA]	p [10^{-7} mbar]	$t_{sputter}$	laboratory notation	main purpose
SAMPLE A1	200	540	0.56	2.1	8 min	HOPG_85	silver clusters
SAMPLE A2	150	540	0.55	2.9	8 min	HOPG_100	lead clusters

TABLE 4-1: Parameters for the defect production and oxidation processes. 12 samples are patterned with FIB and 2 samples are sputtered with argon ions.

4.3 Cluster fabrication

The metal clusters are grown by self organization of atoms at nano-pit edges. The mechanism of cluster growth is shown in figure 4-2. A *nucleation center* for the cluster growth is a nano-pit, a step edge or another surface defect. It is in this case a nano-pit. It is assumed that clusters do not nucleate on the pristine surface of HOPG due to the weak interaction with the surface [135]. These aggregates would move on the surface until they arrive at a nucleation center.

The growth is dominated by two mechanisms. The first one is the direct impingement of atoms. In the second case the atoms are at first adsorbed on the surface and then they diffuse between the clusters performing a random walk. After a *mean diffusion length before desorption* λ_{diff} they desorb except they are captured by an existing cluster or a nucleation center. Anton et al. reported a diffusion length before desorption of a few nanometers for gold on graphite at 350 °C [137].

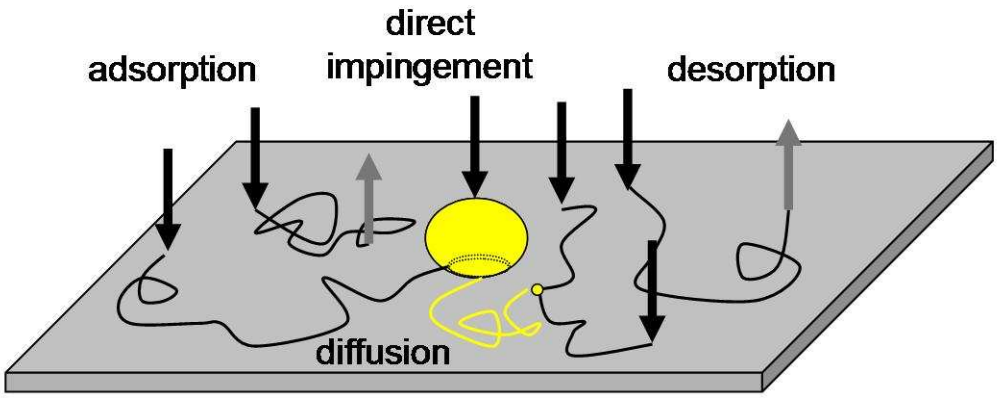

FIGURE 4-2: Schematic illustration of cluster growth mechanism (cf. [5] and [138]).

The atoms are evaporated with the EFM mentioned in 3.2.2. The electrons emitted from a filament (with the *emission current* I_{em}) are accelerated with a voltage V_{a} to a crucible filled with the cluster material. Thus the material is heated and vaporized. The evaporation rate is measured with the *flux monitor*. It measures the fraction of the atoms which are ionized by I_{em}. The measured current I_{flux} is mainly dependent on the material and I_{em}. The effective coverage Γ given in atomic monolayer (ML) can be evaluated from:

$$\Gamma = \kappa \cdot \frac{I_{\mathrm{flux}}}{I_{\mathrm{em}}} \cdot \Delta t \tag{10}$$

where Δt is the evaporation time and κ the calibration constant given in ML/s. The calibration method is described very well in reference [101]. The value of κ for three materials used in this study is listed in table 4-2. The parameters used for the metal atom deposition and the calculated material coverages are listed in table 4-3.

Material	κ [ML/s]
Ag	311
Au	30.64
Pb	131

TABLE 4-2: Calibration constants of the evaporator for different materials.

Sample	n	Material	I_{flux} [nA]	I_{em} [mA]	V_a [V]	Δt [s]	T	Γ [ML]	Γ_{total} [ML]
SAMPLE 1	1	Ag	*	*	*	*	RT	0.4	0.4
	2	Au	41000	51	800	1180	350°C	30	30
SAMPLE 3	1	Pb	10	2.5	800	103	RT	0.05	0.05
	2	Pb	10	2.5	800	120	RT	0.07	0.12
	3	Pb	20	3	800	160	150°C	0.07	0.07[1)]
	4	Pb	30	3	800	540	RT	0.7	~0.8
SAMPLE 6	1	Ag	*	*	*	*	RT	2.6	2.6
	2	Ag	*	*	*	*	RT	2.6	5.2
SAMPLE 7	1	Ag	*	*	*	*	RT	2	2
	2	Ag	*	*	*	*	RT	2	4
SAMPLE 8	1	Pb	20	3	800	80	150 K	0.07	0.07
	2	Pb	20	3	800	320	150 K	0.28	0.35
SAMPLE 9	1	Pb	20	3	800	160	RT	0.14	0.14
SAMPLE 10	1	Pb	20	3	800	160	RT	0.14	0.14
	2	Pb	20	3	800	1560	RT	1.36	1.5
	3	Pb	100	3.3	800	360	RT	0.48	1.98
	4	Pb	20	3	800	294	0°C	0.3	2.28
SAMPLE 11	1	Pb	20	3	800	160	55°C	0.14	0.14
SAMPLE A1	1	Ag	12	8	610	140	56°C	0.07	0.07
	2	Ag	12	8	610	420	57°C	0.20	0.27
	3	Ag	12	8	610	1680	57°C	0.78	1.05
SAMPLE A2	1	Pb	20	3	800	150	40°C	0.14	0.14
	2	Pb	20	3	800	150	50°C	0.14	0.28
	3	Pb	20	3	800	150	50°C	0.14	0.42
	4	Pb	20	3	800	150	50°C	0.14	0.56

TABLE 4-3: Parameters for the deposition process.
1) This sample was annealed at 600 °C before this deposition step. The vapor pressure for lead at 600 °C amounts to 10^{-3} mbar [136]. That corresponds to a vaporization rate of about 10^3 ML/s. With this the whole Pb coverage is removed after annealing.
***) These depositions were performed at the TU Kaiserslautern in collaboration with M. Rohmer et al.**

5 Results and Discussion

In this chapter the results of the experiments are presented and discussed. First the results of an experiment with different ion doses are discussed. Based on this experiment the results are divided into two groups. The first group is structured with low ion doses and includes nano-pits and metal clusters. The second group is structured with high ion doses and includes nano-cavities and metal islands. These structures and their application are presented in the sections 5.2 and 5.3. In section 5.4 the grown clusters are analyzed in respect of height, facet and stability.

5.1 Ion dose dependence

To figure out the dependence of the ion dose on the nano-pit growth 16 areas exposed with 35 keV gallium ions were placed on a sample in a first experiment (SAMPLE 1). The exposed pattern for each area was a lattice of defect points with a pitch of 300 nm. The ion dose was doubled by the transition from area to area. Thus we have 16 areas with very different ion doses. The corresponding values are summarized in table 5-1. In optical microscopy images (see [1]) the areas exposed with the highest ion doses were visible due to the significant surface damage. In this experimental run the ion beam instrument was operated in a defocused mode, which resulted in feature sizes of about 150 nm and an irregular triangular shape. Results with high resolution are presented in 5.2.2.3 and 5.3.1.1.

Of special interest are the results for very low and very high ion doses. The production of the defects and their expected influence on the formation of nano-pits are discussed in section 4.2 (figure 4-1). An incident ion produces defects in the sample up to the maximal penetration depth d_{max}. In the case of low ion intensity each incident ion causes a few defects arranged in a line inside the sample (cf. figure 4-1a). The defects on the surface affect only a few atoms and are not visible in large-scale STM images. The defect density is too small to cause a coalescence of defects or nano-pits formed after oxidation. For these areas only the defects in the first monolayer oxidize and form nano-pits [120], which are visible in the STM images (cf. figure 4-1b). The defects in inner layers do not oxidize and are not visible in the STM images. We emphasize that the nano-pits are caused by

area	D_{point} [ions/point]	D_{pa} [ions/cm²]	pits/point	ions/pit
1	$3.0 \cdot 10^{1}$	$2.1 \cdot 10^{11}$	4	8
2	$6.0 \cdot 10^{1}$	$4.1 \cdot 10^{11}$	14	4
3	$1.2 \cdot 10^{2}$	$8.2 \cdot 10^{11}$	20	6
4	$2.4 \cdot 10^{2}$	$1.7 \cdot 10^{12}$	85	3
5	$4.8 \cdot 10^{2}$	$3.3 \cdot 10^{12}$	110	4
6	$9.6 \cdot 10^{2}$	$6.6 \cdot 10^{12}$	110	9
7	$1.9 \cdot 10^{3}$	$1.4 \cdot 10^{13}$	160	12
8	$3.8 \cdot 10^{3}$	$2.8 \cdot 10^{13}$	180	21
9	$7.7 \cdot 10^{3}$	$5.5 \cdot 10^{13}$	~ 300	26
10	$1.5 \cdot 10^{4}$	$1.0 \cdot 10^{14}$	~ 200	77
11	$3.1 \cdot 10^{4}$	$2.1 \cdot 10^{14}$	~ 100	307
12	$6.1 \cdot 10^{4}$	$4.1 \cdot 10^{14}$	----	----
13	$1.2 \cdot 10^{5}$	$8.2 \cdot 10^{14}$	----	----
14	$2.5 \cdot 10^{5}$	$1.7 \cdot 10^{15}$	----	----
15	$4.9 \cdot 10^{5}$	$3.4 \cdot 10^{15}$	----	----
16	$9.8 \cdot 10^{5}$	$6.9 \cdot 10^{15}$	----	----

TABLE 5-1: Comparison of ion dose and pit density for areas in SAMPLE 1. One point corresponds to a 300 nm × 300 nm area. The point dose D_{point} has been calculated from the dot dwell time and the constant current of I_{FIB} = 6 pA. t_{dwell} amounts to 800 ns per point for the first area and has been doubled for each of the following areas. For the last area it amounts to 26 ms. The point area dose D_{pa} given in ions/cm² is calculated for the number of ions impacted in the triangular shape of the impact point. The value pits/point shows qualitatively the change of the pit density for increasing ion dose. For areas with high ion dose one deep pit and a few one monolayer deep pits are formed, thus it is not reasonable to give a value for the pit density. The column ions/pit is calculated by division of ions/point and pits/point.

single ion defects and reflect the distribution of incident ions. In table 5-1 the comparison of ion dose and pit density is given as the ratio ions/pit. In the case of the areas structured with low ion doses (area 1 to 7) this ratio is comparable with previous results using the random impact of Ar ions [128] and amounts to approximately 10 ions/pit. The scatter of this parameter for the different areas is due to the limited statistics. Thus the areas 1 to 7 comprise the reasonable ion dose range for the production of separated nano-pits.

A high point dose causes a high defect density per point. For very high ion doses as used in the areas 13-16 the incident ions produce a volume full of defects (cf. figure 4-1c). The damaged volume is oxidized completely and a deep pit is formed as measured with STM (cf. figure 4-1d), similar to the results for the impact of C_{60} ions [139]. There are no entries for the pit density in table 5-1 for the areas 12-16 because one deep pit and a few smaller pits per point are observable and it is not reasonable to count the pits in that case.

For areas between the two extremes low and high ion doses (2000 to 60 000 ions/point) a continuous transition from one monolayer deep pits to several ten nanometers deep pits is observed. First a few multilayer deep pits emerge. With increasing ion dose these pits coalesce and build wider and deeper pits. In area 12 the pits are 10 nm deep and 50 nm

wide. Doubling the ion dose for area 13 the depth increases to 50 nm as mentioned above. Before and after the oxidation we observed for areas 7 to 12 a hill shape of the impact region with a height of a few nanometers, probably caused by integration of incident gallium ions into the inner layers. For more details about these results see the references [103,131].

In further experiments two ion dose ranges are used for patterning and further investigations. The first one is the ion dose used for areas 5 and 6. In these areas nano-pits are observed and the impact region does not indicate a hill shape. This is especially interesting for the production of cluster patterns. The results for patterning with low ion doses are presented in 5.2. The second interesting region is the ion dose used for areas 13 and 14. In this case deep pits are emerged at the impact point. They can be used to investigate the ion beam profile as well as the penetration depth of ions. Also they can be used to grow particles larger than 50 nm called *island*s to distinguish them from clusters whose sizes are smaller than 20 nm. The results for patterning with high ion doses are presented in 5.3. Note that the important parameter is the point area dose D_{pa} and not the point dose D_{point}. The ion dose has to be adapted to the beam focus. That means that the point dose has to be smaller for a better focusing.

5.2 Patterning with low ion dose

The patterning with low ion dose and the subsequent oxidation results in nano-pits. These nano-pits could be produced in rows as well as in a point lattice. Other experiments showed that the point pitch and the size of pits in surroundings influence the shape and size of the nano-pits. These effects are discussed for two samples. Additionally two exemplary applications of the nano-pits are presented. These results are presented in section 5.2.1. After metal deposition patterns of clusters (rows or two dimensional lattices) and thin lead layer patterns are produced as presented in section 5.2.2.

5.2.1 Nano-pits

5.2.1.1 Nano-pit patterns

"Nano-pit Rows"

For areas structured with low ion doses of 100 to 1000 ions per lattice point on SAMPLE 1 the results are comparable to previous experiments for the production of nano-pits [128]. Before oxidation no defects were visible in the STM images for areas structured with ion doses lower than 2000 ions/point. After oxidation we observed in the areas 1 to 3 an increase of the nano-pit density but no special pattern. For the next areas an arrangement of nano-pits emerges. Especially areas 5 and 6 exhibit nano-pits arranged in rows with a distance of 300 nm (figure 5-1a). These rows have a width of 150 nm. They are due to the writing process (no blanking between the pattern points). A magnification of the image (figure 5-1b) shows the pattern of the nano-pits in detail. Almost no nano-pits are visible between the rows. The STM images show that the nano-pits are only a few nanometers wide and a line profile shows the shape of a few nano-pits. Most of them are only one monolayer (0.34 nm) deep (figure 5-1c). Their shape is comparable with the nano-pits produced in previous experiments [128].

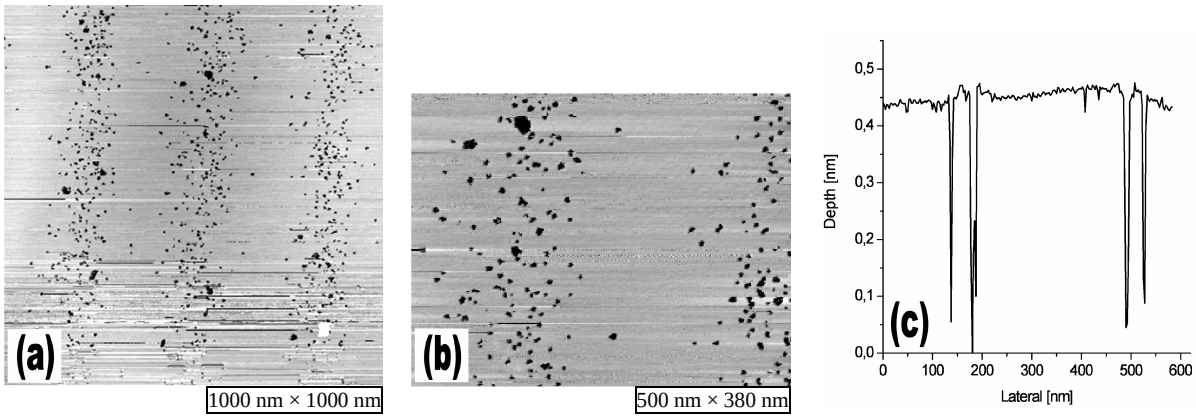

FIGURE 5-1: **(a) STM image shows area 5 structured with D_{point} = 500 ions/point on SAMPLE 1 after oxidation. At this ion dose several rows of nano-pits are formed. The distance between the rows amounts to 300 nm. Image (b) is a magnification of image (a). The space between two rows remains almost free of nano-pits. The nano-pits are a few nanometers wide. Also the line profile (c) reveals that they are only one monolayer (≈ 0.34 nm) deep.**

"Nano-pit Groups"

Using improved focus conditions of the FIB-tool nano-pits can be structured as well separated groups (SAMPLE 2, figure 5-2). The pattern is the same as for SAMPLE 1. The diameter of the nano-pit group amounts to approx. 100 nm. The point shape seems to be elongated. This may be an effect of a too short settling time. This seems to be the physical limit of the patterning of one atom deep nano-pits at this time (cf. section 3.1.4). In contrast for deeper pits smaller diameters down to 20 nm could be obtained (cf. section 5.3.1.1).

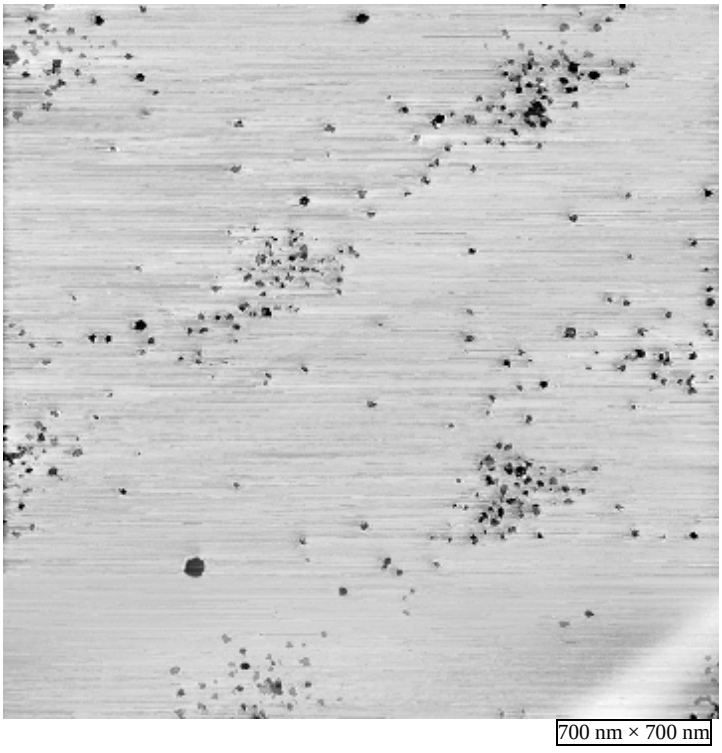

FIGURE 5-2: **STM image of an area on SAMPLE 2 structured with the ion dose 800×10^{-19} C (D_{point} = 500 ions/point) using an improved focus condition. The point pitch amounts to 300 nm. The nano-pit groups are well separated.**

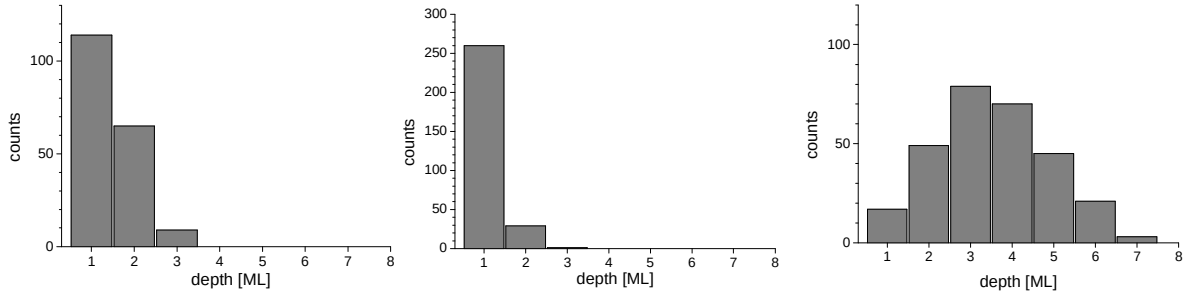

FIGURE 5-3: Distribution of nano-pit depth for (a) an Ar sputtered sample (SAMPLE A2), (b) SAMPLE 1 (figure 5-1b) and (c) SAMPLE 2 (figure 5-2).

In the image in figure 5-2 approximately 70 nano-pits per point can be counted. In contrast to SAMPLE 1 the nano-pits are concentrated on one point. This leads to a higher point area dose of $D_{pa} = 9.5 \times 10^{12}$ ions/cm² which is comparable with area 7 in SAMPLE 1. In figure 5-3 the distribution of the nano-pit depth is compared for both samples with an Ar sputtered sample. For SAMPLE 2 the nano-pits exhibit a broad depth distribution. The pits with 4 ML depth dominate. For other both samples the 1 ML nano-pits dominate. That is a result of the higher D_{pa} for SAMPLE 2 which results in deeper nano-pits.

5.2.1.2 Distance dependence

An important aspect for the oxidation process is the distance between the surface defects. Figure 5-4a illustrates a simplified model for the oxidation process. The oxygen molecules can reach a defect in two ways: directly or by adsorption and subsequent diffusion on the surface. Indeed the second way is more probable and more important for the oxidation process. In this model a circular area with the diameter d_{ca} (named *capture diameter*) marks the *capture area* of oxygen molecules around the defect comparable with the capture area of gold clusters for gold atoms in reference [140]. That means that the most of the oxygen molecules involved in the oxidation of the defect come from this area. In reality the adsorption and diffusion processes are more complex. However this model should be reasonable for a qualitative discussion.

In particular for the FIB structured samples a number of defects are concentrated in a small area. Figure 5-4b shows this for three defects. The defects have to share their capture area and cause a reduction of d_{ca}. Thus, the middle defect in this illustration gains less oxygen and oxidizes slower. This effect causes that for an accumulation the defects do not oxidize well. The defects in the inner region would be smaller than the ones in the outer region.

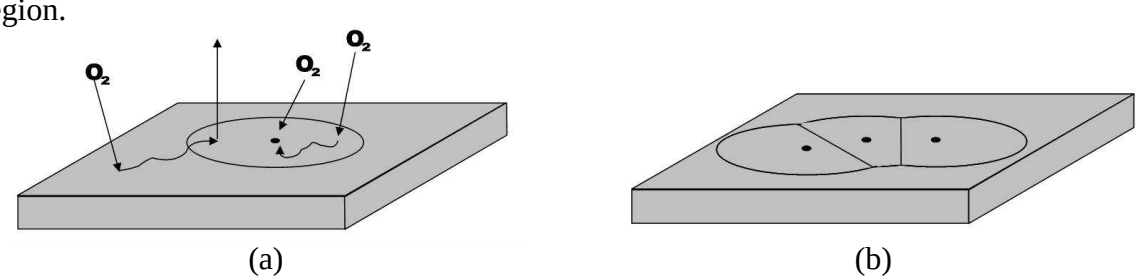

FIGURE 5-4: (a) Circular model of the oxidation process. The oxygen molecules, which can reach the defect, come mostly from the circle around the defect (oxygen capture area). (b) Several defects have to share their oxygen capture area. Thus the middle defect has a smaller capture area and oxidizes slower.

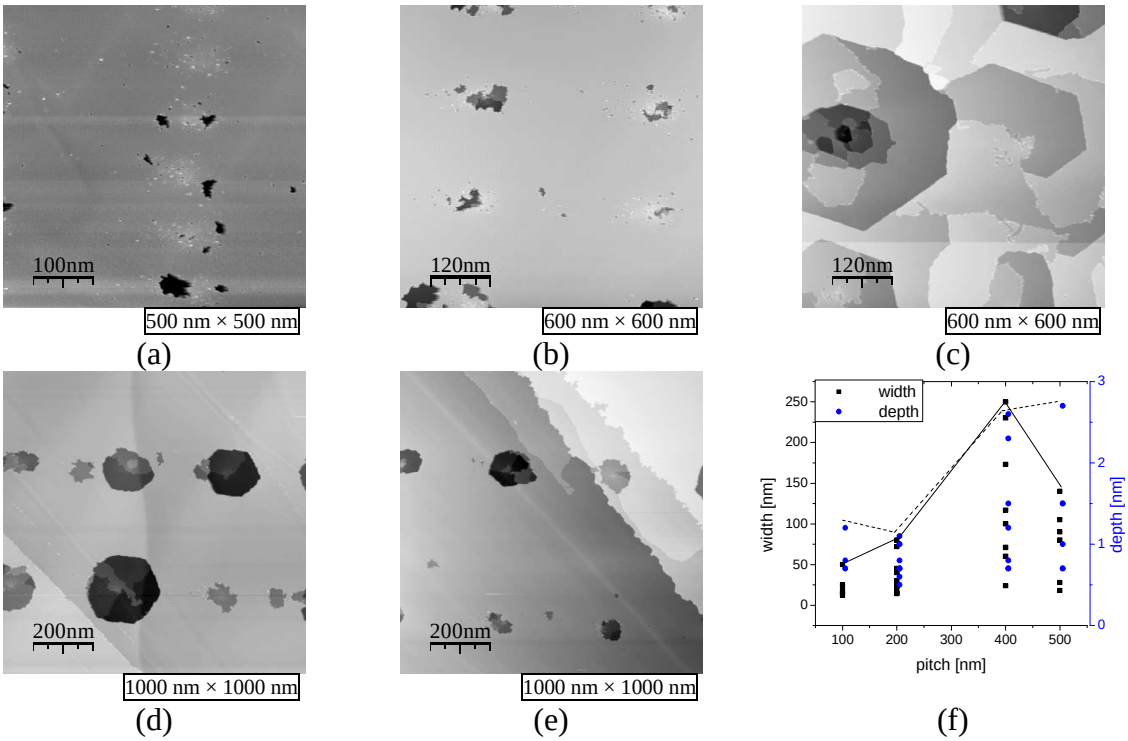

FIGURE 5-5: STM images of 5 areas on SAMPLE 4. The ion dose is 8×10^{-5} pAs (D_{point} = 500 ions/point). The horizontal distance is 300 nm for all areas. The vertical distances are (a) 100 nm (b) 200 nm (c) 300 nm (d) 400 nm and (e) 500 nm. (f) Width and maximal depth of larger pits in previous images.

Patterns of defects can be used to measure the capture diameter. The ideal case is the production of single defects in a pattern with a well-defined pitch between them. However, the experimental realization is not possible yet. Instead, groups of defects arranged in well-defined distances to each other can be obtained. This idea is realized in SAMPLE 4, where 5 areas with vertical defect-group pitches between 100 and 500 nm were structured (figure 5-5). The horizontal pitches are constant and amount to 300 nm. Thus the problem is reduced to one dimension. Similar to the capture area of defects a capture area of defect groups can be considered if $d_{ca} >> d_{pit}$. All patterned areas are located on one sample, so they are structured and oxidized at the same conditions.

The oxidation process is influenced by other surface defects, too. Figure 5-5c shows the STM image of one area, where not the defects but other features on the surface are oxidized. In figure 5-5e the pit growth is influenced by step edges, so that the pit diameters are smaller as the pits in figure 5-5d, where the pit pitch is larger.

Figure 5-5a makes the influence of the capture area visible. In the nano-pit groups only the nano-pits at the left or right side are enlarged and coalesced. The inner nano-pits remain unaffected due to a very small capture area. Increasing the point distance the pits become wider and deeper, because the overlapping region of the capture area of defect-groups becomes smaller.

If the pitch is much larger than d_{ca} the pit size approaches its final limit. The critical pitch yields the capture diameter d_{ca}. A coalescence of the nano-pits in the experiment can be observed from figure 5-5a to b. In contrast the pits do not become wider from image d to e. Unfortunately the threshold regime should be in the area shown in image c, where the measurement had failed. That leads to an inaccuracy of the measurement and the threshold pitch of the pit-groups can be determined between image b and d.

The dependence of the pit width and depth on the point pitch is visualized in figure 5-5f. The larger pits are more of interest. Hence, the lines connecting the highest values can be discussed. Between the pitch values of 200 nm and 400 nm the highest slope can be observed. The decrease between 400 nm and 500 nm is caused by surface steps in image e. Thus the capture diameter can be roughly fixed to d_{ca} = 150 nm.

The effect discussed in this caption is an important part of production of nano-pit patterns. Considering this effect the oxidation parameters should be separately adjusted for different pit pitches. As a result of this effect it is not possible to produce similar pits with different distances on the same sample if the pit pitch is comparable or smaller than d_{ca}.

5.2.1.3 Influence of the pit size

If a lot of nano-pits have a common capture area as explained in 5.2.1.2 they have to share the oxygen in this volume. Therefore a higher pit density results in smaller nano-pits. Another indication for this effect provides the observation of the nano-pit density in the region between two points in areas structured on SAMPLE 1 (figure 5-6). In contrast to the points the ion dose of these regions should either remain nearly constant for all areas because they are caused by driving of the ion beam to the next point, or they should increase with increasing ion dose if they are caused by the tails of the ion distribution.

However in the STM images a decrease of the nano-pit density with increasing ion dose can be observed. This indicates that the oxidation is supported by an oxygen reservoir adsorbed on the surface [117]. The oxygen consume of nano-pits increases with the pit size due to more available open bindings. So the large pits in the areas exposed with higher ion doses consume the oxygen in their surroundings. Thus there is less oxygen for the small defects which can not oxidize completely and do not become visible in the STM image.

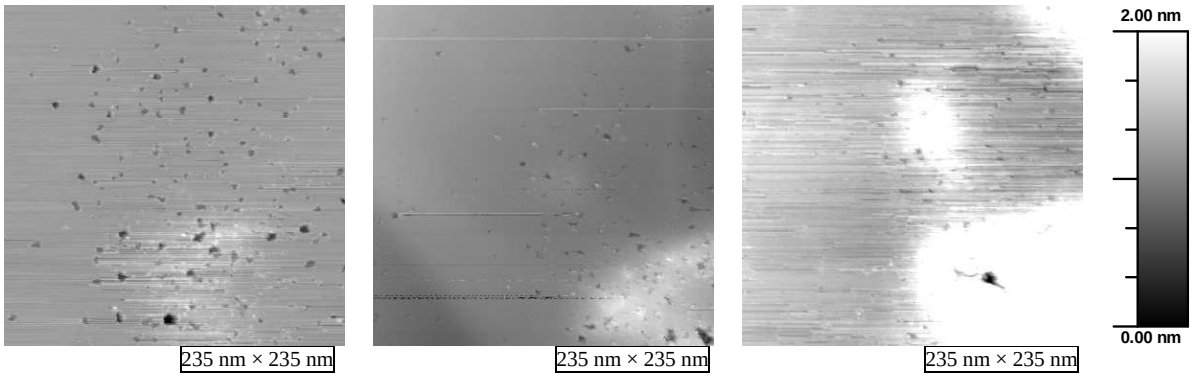

FIGURE 5-6: STM images of (a) area 8 (b) area 9 and (c) area 11 on SAMPLE 1. The grey scale of all three images corresponds to a height of 2 nm, thus the visibility of small pits is equal. These images show the dependence of the pit density on the ion dose for the region between two points. In this region the nano-pit density decreases with increasing ion dose.

5.2.1.4 Beam characterization using nano-pits

Since nano-pits on an HOPG surface are caused by ion impacts they can be used as a detection tool for single ion events. It is helpful to examine the beam properties for low ion intensities which are useable for the production of nano-pit patterns. In the following the examination of beam blanking in a preliminary version of the FIB column will be discussed as an application example.

To determine the influence of beam blanking 6 areas were exposed with two writing directions and three different distances between the points (figure 5-7). In the horizontal writing direction no influence of the beam blanking is visible because the blanking and writing direction are the same. In the vertical writing direction the beam blanking causes a diagonal trace of nano-pits. This distribution was caused by simultaneous beam drive in the vertical direction and beam blanking in horizontal direction. Since the beam blanking power is always the same the different nano-pit distribution for different point pitches is due to the point to point movement of the ion beam.

That can be described with a simple model of two capacitors (figure 5-8). In this model the beam blanking in *x*-direction is performed with the capacitor 1 and the scanning in the *y*-direction with capacitor 2. The deflection in a linear electric field within the capacitors can be described with:

$$\begin{aligned} x &= \frac{q}{2m} V_1 t^2 \quad \text{for } 0 < z < l_1 \\ y &= \frac{q}{2m} V_2 t^2 \quad \text{for } l_1 + a_1 < z < l_1 + a_1 + l_2 \end{aligned} \tag{11}$$

where m is the mass and q the charge of the ion and $V_{1,2}$ the applied capacitor voltage. Between the capacitors the beam performs a linear motion. During beam blanking and scanning, which occur in this case at the same time, the capacitors perform a voltage change which can be described by the charging equation of a capacitor assuming a start voltage of 0 V:

$$V_{1,2} = V_{01,02}\left(1 - e^{t/\tau_{1,2}}\right) \tag{12}$$

where V_{0i} is the charging voltage and τ_i the time constant of the capacitor i. With this and the assumption that $a_1, a_2 \gg l_1, l_2$ the deflection in *y*-direction can be expressed as a function of the deflection in *x*-direction:

$$y = A_2\left(1 - \left(1 - \frac{x}{A_1}\right)^{\tilde{\tau}}\right) \tag{13}$$

with the ratio of the time constants $\tilde{\tau}$, kinetic energy of the ion v_0 and the deflection constants A_1 and A_2:

$$\begin{aligned} \tilde{\tau} &= \frac{\tau_1}{\tau_2}, E = \frac{1}{2} m v_0^2 \\ A_1 &= \frac{q}{2E} V_{01} \cdot \left(l_1 a_1 + l_1 a_2\right) \\ A_2 &= \frac{q}{2E} V_{02} \cdot \left(l_2 a_2\right) \end{aligned} \tag{14}$$

In the expression for A_2 only the parameters of the capacitor 2 are present. Hence, it represents directly the point distance. V_{02} and therefore A_2 are created with the pattern generator. The expression A_1 represents the beam blanking in the simplified model which is followed by other electric optics in the real configuration. Hence the parameters A_1 and $\tilde{\tau}$ including τ_1 can not be directly compared.

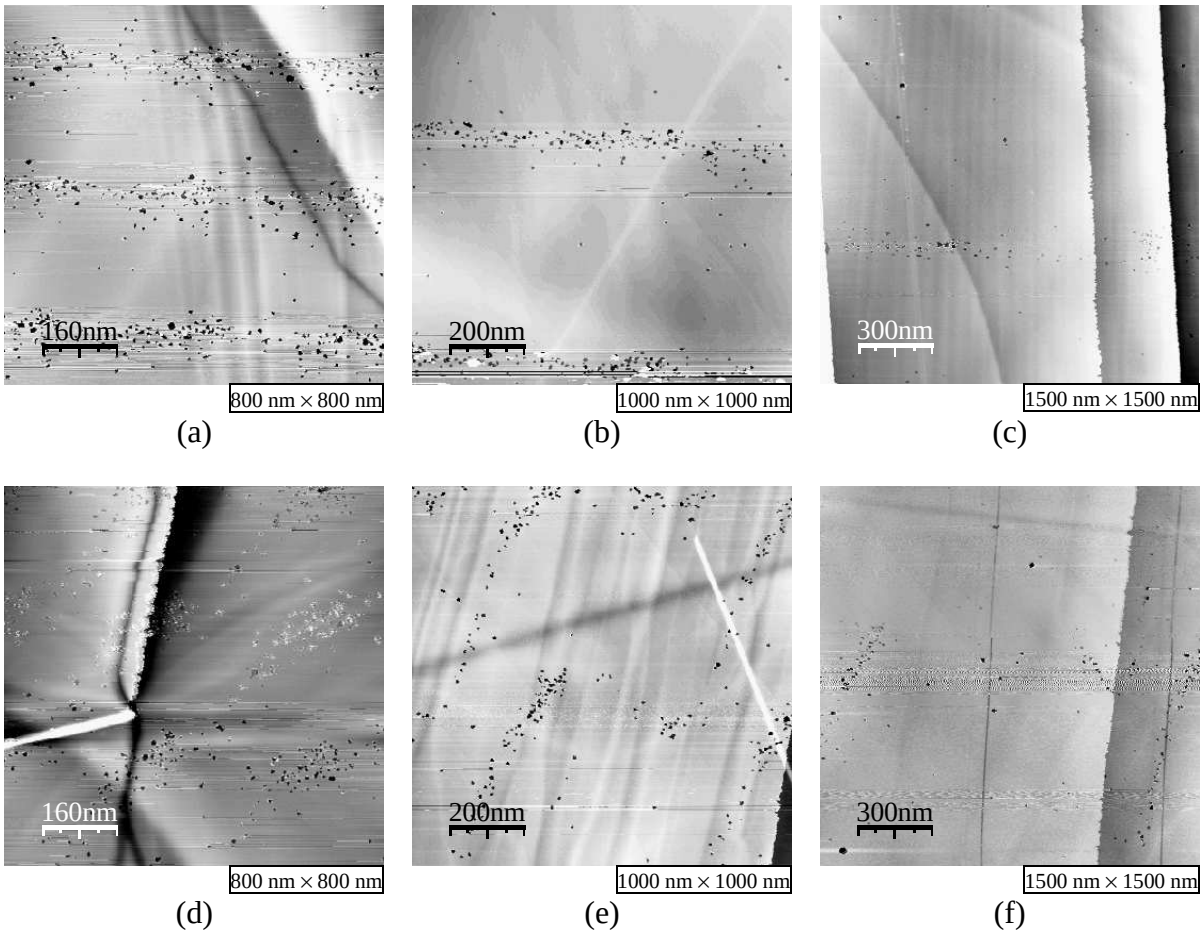

FIGURE 5-7: **STM images of areas structured with an ion dose of 800 × 10^{-19} pAs (D_{point} = 500 ions/point) on SAMPLE 3 using beam blanking. The point pitch is (a, d) 300 nm (b, e) 600 nm (c, f) 1200 nm. The writing direction is horizontal for images a-c and vertical for images d-f. The blanking direction is horizontal for all images.**

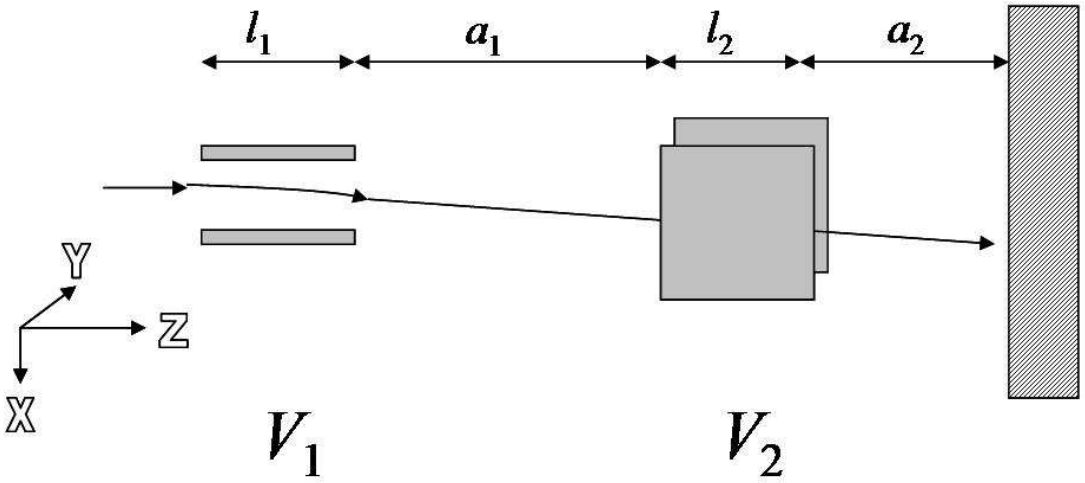

FIGURE 5-8: **Beam path in a simplified model of the FIB-column with two capacitors.**

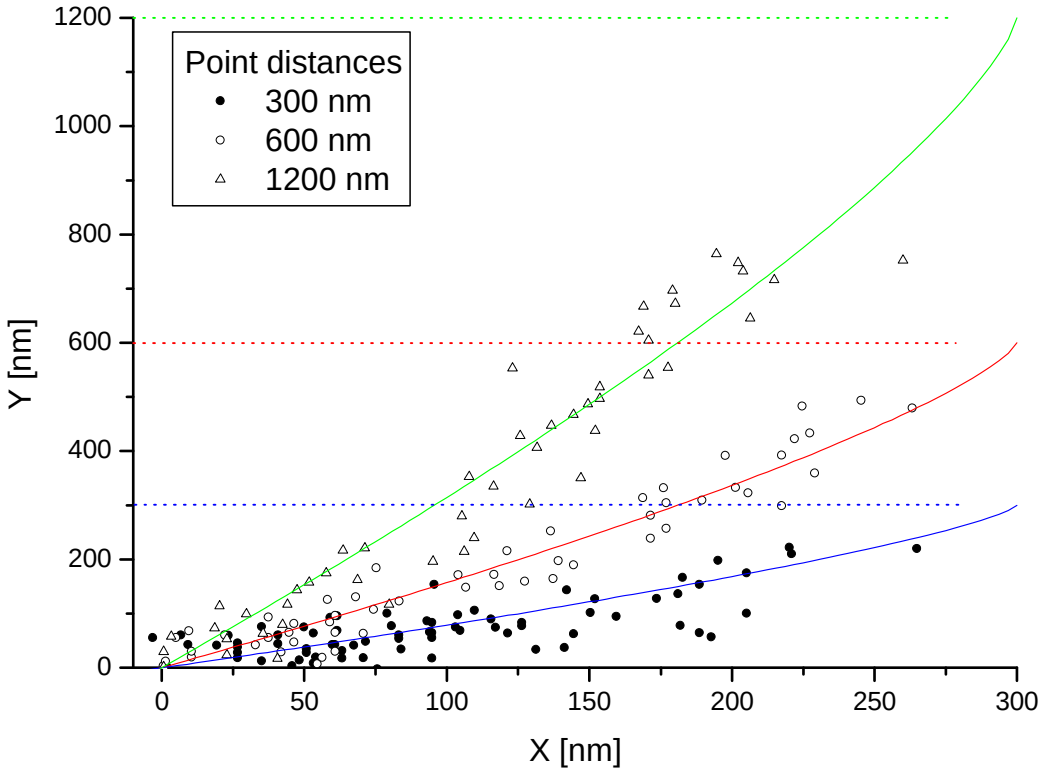

FIGURE 5-9: **The graph shows the nano-pit distribution for three point pitches. The origin represents the position of the point. Horizontal lines mark the different point pitches. The distribution in *x*-direction is caused by beam blanking and the distribution in *y*-direction is caused by point to point movement of the ion beam.**

The nano-pit distribution in the experiment is shown in figure 5-9. The horizontal lines mark the point pitch for the three cases. For 300 nm pitch the pits are distributed in *y*-direction to 300 nm, for 600 nm pitch to 500 nm and for 1200 nm pitch to 800 nm. That is the beam is not completely blanked for 300 and 600 nm pitch before arriving the next pattern point. Only for a large pitch of 1200 nm the beam is blanked completely before arriving the next pattern point. With this feature the nano-structuring of nano-pits becomes difficult. The fits in figure 5-9 are performed with formula 13 using the same parameters for all three cases since they are exposed with the same FIB-column. The best parameters are A_1 = 300 nm and $\tilde{\tau}$ = 0.75. Although this fits have a high uncertainty they show that it is possible to make a statement about the electric lens system of the FIB-column using the distribution of the nano-pits which are a result of single ion defects as mentioned before.

For a conventional use of FIB with higher ion doses the ion impact during the blanking would not be important. And only with the oxidation of the single ion defects to nano-pits they get visible with STM.

Meanwhile the beam blanking process and the beam movement of the ionLiNE are improved. The faster beam movement led to better results (see figure 5-2, figure 5-27 and figure 5-32).

5.2.1.5 Finding patterns

A problem of the investigation of structures smaller than 100 nm is that the local investigation of the same particle is mostly difficult or impossible to realize because the particle is undiscoverable after a sample or tip manipulation (in STM). This problem can be solved by using the nano-structuring of the particles in order to realize a finding pattern. However some physical and technical limits make the nano-structuring difficult as mentioned in the following:

- STM has a limited scan range, e.g. LT-STM at 77K has a scan range about 3 μm.
- The STM scan velocity has to be chosen small to resolve the nano-particles. This results in long scan times for each image, which causes drift effects and distorts the dimensions in the STM image. That is, the position of a particle has to be identified in small STM images.
- The structuring process is limited by the ion distribution. Therefore it is not possible to write characters/symbols in small dimensions.
- The tip position can only be observed with a camera. In order to find the structured region it should be a large area. It is known by experience that an area about 200 μm × 200 μm can be localized with the used camera.

To use the nano-structuring for navigation and localization on the sample a design is needed which has to fulfill the following points:

- The design elements have to be simple and small.
- The position of each element should be deducible from STM images with a maximal size of 1000 nm × 1000 nm.
- The size of the designed pattern has to be about 200 μm × 200 μm.

The simplest design is a pattern of points. The easiest pattern is a pattern based of a dual system. However this pattern brings many problems, since it has to be completely imaged for identification. Thus in the method presented here the distance to the next points is used to find the point position. A sequence of point to point distances emerges as listed in table 5-2. This sequence is split into 13 parts with nearly equal length. It is chosen in a way that the sequence of two distances occurs only one time. To simplify the sequence ciphers are used in table 5-2. For example the cipher combination 12 represents 3 points with distances of 100 and 200 nm. With this method only two distances are needed to identify the position of one point in the patterned region.

Combination of two sequences (one row × one column) leads to 169 areas (notation is ‘area (row nr., column nr.)’) each with nearly 5 × 5 μm². Additionally a distance between the areas of 5 μm is chosen to enlarge the patterned region. Thus the whole pattern covers an area of 130 μm × 130 μm. A part of this pattern is shown in figure 5-10a.

In the experimental realization the pit shape and the orientation in the imaging process influence the identification of the sequence code. Hence, a calibration area with a distinct pattern on the same sample is needed. In this case a distance sequence of (123456 × 2468) is chosen. The STM image of the calibration area indicates the point shape consisting of

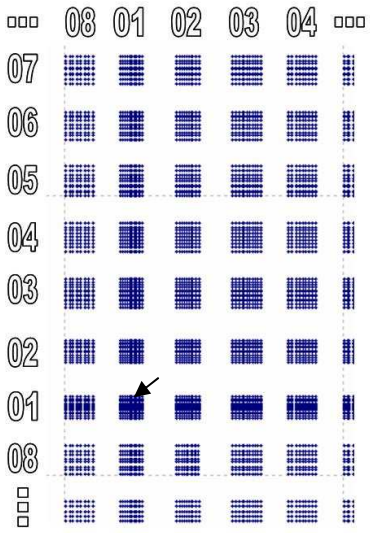

(a)

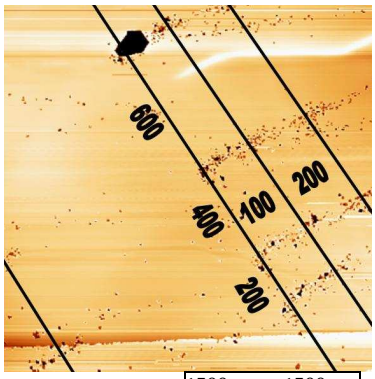

(c)

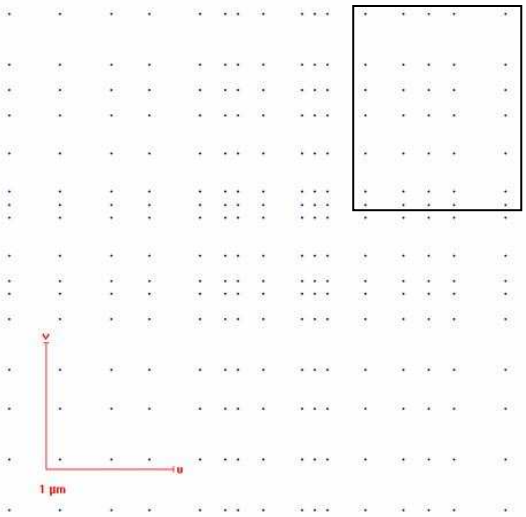

(b)

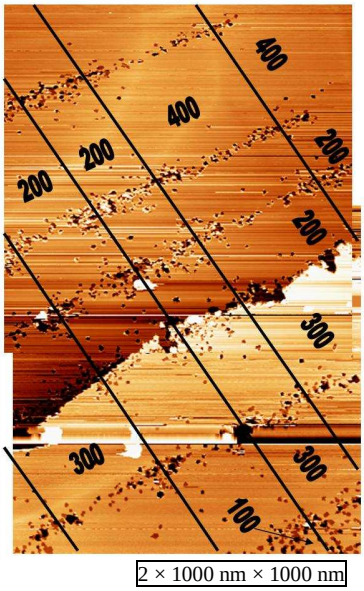

(d)

FIGURE 5-10: **(a) A clipping of the GDSII file in Raith software illustrates the point distribution on the sample. The numbers mark rows and columns as mentioned in table 5-2. (b) Close up of area (01,01) which is marked in (a) with an arrow. (c) STM image of the calibration area within SAMPLE 5. The distances between the rows/columns are given in nm. (d) STM image of an area identified as area (01, 01). The distance sequence for this area is (443421231133224 × 443421231133224). This region is marked with a square in (b).**

row/ column	distance sequence	Length [nm]
01	443421231133224	3900
02	5545352515	4000
03	661626364146	5100
04	77675657	5000
05	727374788	5300
06	85868717	5000
07	818283848	5000
08	9495969	5100
09	979899	5100
10	91929390	5200
11	070809	5400
12	0405060	5500
13	00102030	5600

cipher	Distance [nm]
1	100
2	200
3	300
4	400
5	500
6	600
7	700
8	800
9	900
0	1000

TABLE 5-2: Distance sequences for nano-pit addressing. Each cipher in the sequence represents a distance between two points as shown in the right table. The sequences are numbered to mark rows or columns.

nano-pits (figure 5-10b). In this case a line of nano-pits chain the points to each other due to preliminary status of the blanking system. This makes the identification of the pattern difficult. However the points can be identified as an accumulation of nano-pits. The calibration area indicates also the orientation of the pattern. Figure 5-10c shows an STM image of an area patterned with the finding structures. On the basis of distances in the image the location on the sample can exactly be identified.

This method roughly fulfills the requirements mentioned above. It is fitted to the available structuring at this time. However it was hindered by the following problems:

- The point identification is not easy. This problem is solved for other experiments with improved focus and blanking conditions.
- The structured area is not as large as needed.
- The space between the areas hinders the searching in the STM.

Regarding the results in 5.3.1.1 it is possible to use distances down to 50 nm which enables the use of more and smaller distances for the sequence creation. This could lead to an enlargement of the structured area and solve the mentioned problems.

5.2.2 Cluster growth

The most important application of nano-pit patterns is the growth of clusters in a given pattern. Usually the clusters are formed by deposition of atoms on the sample. It is known that the growth of clusters in nano-pits is favored. The question is whether the clusters grow only on the nano-pits or not. That is essential for the growth of clusters in nano-pit patterns. Additionally it is to figure out whether this behavior is dependent on the deposited material and the ion dose. In the following the growth of cluster patterns with two different materials is presented.

5.2.2.1 Silver cluster patterns

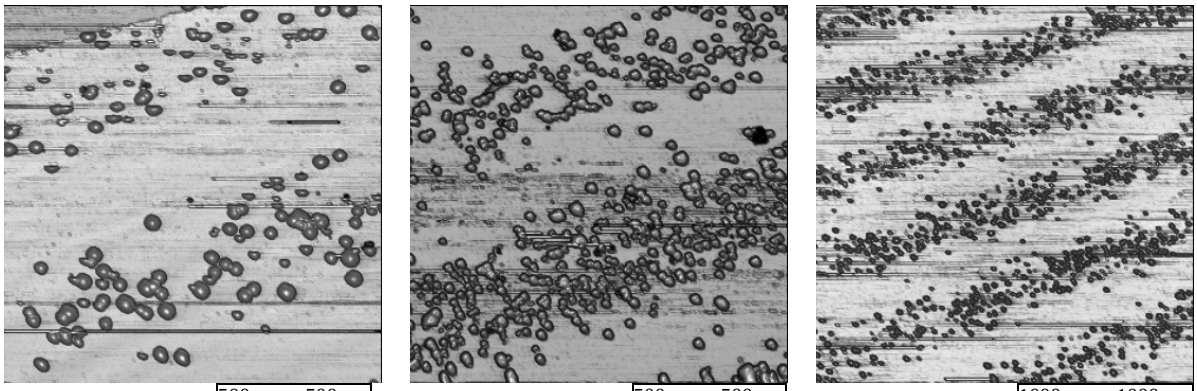

FIGURE 5-11: STM images of cluster patterns grown on SAMPLE 1 after room temperature deposition of 0.4 ML silver. They show (a) area 4 structured with 240 ions/point, (b) area 5 structured with 480 ions/point and (c) a larger frame of area 5.

"STM Measurements"

On SAMPLE 1 0.4 ML silver were deposited at room temperature in UHV. After a short air contact and transport in a desiccator it was investigated with STM. On this sample a cluster pattern is formed equal to the nano-pit pattern as shown in figure 5-1 (figure 5-11). It is interesting that only a small number of these clusters are grown between the rows. They are only grown in the nano-pits. Figure 5-11c indicates that this growth behavior pertains for larger areas, too. That enables the building of clusters in pre-defined patterns. At a closer look into figure 5-11c the location of the points in the pattern can be found as places with higher cluster density.

The cluster height changes with the ion dose for areas structured with ion doses smaller than 4000 ions/point (c.f. figure 5-12a). It varies from 3 nm to 6 nm. The cluster height decreases up to the ion dose of 480 ions/point then it increases again. For higher ion doses it does not increase anymore. The nano-pit density is the reason for this effect. For lower ion doses the nano-pits have large distances to each other and the nano-pit density is small. With increasing ion dose the nano-pit density increases. This is directly reflected in the cluster density which increases with increasing ion dose until 480 ions/point (figure 5-12b). This is also visible by comparing figure 5-11a and b. With this, the same coverage of silver is now divided into more nucleation centers if the ion dose is increased. Consequently the clusters are larger for a lower pit density and smaller for a higher pit density.

For ion doses higher than 960 ions/point the nano-pit production is in equilibrium with the nano-pit coalescence which results in a nearly constant nano-pit density. Another reason for this is the coalescence of the clusters due to small distances to neighbored clusters. This behavior is also visible in the cluster density which is decreased from 480 ions/point to 960 ions/point. Due to poor statistics this analysis is not performed for higher ion doses.

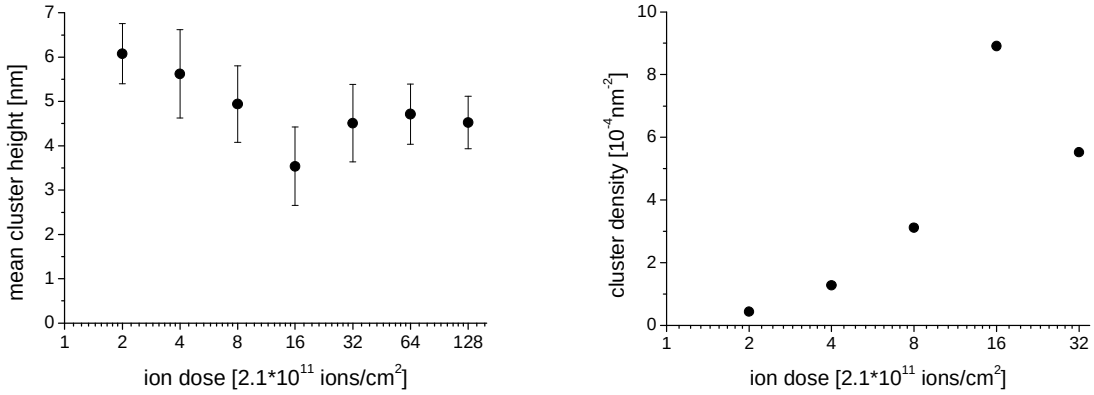

(a) (b)

FIGURE 5-12: (a) Mean height of the silver clusters grown on SAMPLE 1 depending on the ion dose. The smallest cluster height is in the area 5 written with D_{point} = 480 ions/point (D_{pa} = 3.3 × 10^{12} ions/cm²). (b) Cluster counts in the STM images for an area of 100 × 100 nm². The cluster density increases with increasing ion dose up to D_{point} = 480 ions/point (D_{pa} = 3.3 × 10^{12} ions/cm²) and decreases for higher ion doses.

The interesting point is that the cluster height and density are directly influenced by the ion dose. This could be used for the production of different cluster sizes on the same sample. It has the advantage that the clusters are produced and investigated always at the same conditions such as temperature, deposition rate, vibration and other environmental effects. This method can be tuned by changing the focus (i.e. wider focus) and thus control the pit density in larger areas. Since the interesting height variation appears for lower ion doses this attempt could result in a higher variety of cluster heights.

"PEEM/SEM Measurements"

In collaboration with TU Kaiserslautern silver cluster patterns were investigated with PEEM and SEM [2].

Figure 5-13 shows an STM image before and an SEM image after the silver deposition onto an area structured on SAMPLE 6. The structured nano-pits do not exhibit a visible pattern. Evaporation of 4 monolayers of silver at room temperature results in the condensation of silver clusters on the native HOPG and in the nano-pits. For silver evaporated at room temperature on native HOPG surfaces it is well known that a stable STM imaging of the surface is not possible due to the small binding energy and the corresponding high mobility of the silver clusters [141,142]. In order to compare the structured and non-structured regions SEM is used in addition to STM for high resolution imaging of the clusters. The pattern periodicity of 150 nm is well resolved in the SEM image after silver evaporation in spite of non visible pattern of the nano-pits in the STM image before silver evaporation. The region to the right as well as an interstitial area interrupting the nano-structured regions correspond to the cluster decorated native HOPG.

High Resolution SEM allows quantifying the cluster size, cluster size distribution (figure 5-15) and cluster density. For the cluster decoration of the nano-structured areas the cluster density amounts to 800/μm^2, dominated by cluster diameters between 12 and 7 nm. In contrast in the native HOPG areas the cluster density is smaller and amounts to 200/μm^2 from 20 nm diameter to sizes below the resolution limit of the SEM.

Figure 5-14 shows an STM (SEM) image for another area structured with higher ion dose of 480 ions/point and a larger point pitch of 300 nm before (after) silver deposition. For this area a clear periodic structure is visible in the STM image, which is caused by the line by line scan of the ion beam at a periodicity of 300 nm during the writing process. Similar to SAMPLE 1, the SEM image exhibits the same pattern for clusters. Furthermore, steps of the HOPG substrate decorated with silver clusters (see lines labeled with A, B and C) are clearly visible in the SEM image. The analysis of high resolution SEM images shows that in this region the nano-structured areas exhibit a cluster size distribution between 10 and 8 nm at a density of $1300/\mu m^2$. In contrast native HOPG areas exhibit a cluster size up to 20 nm at a density of $200/\mu m^2$.

PEEM measurements of the surface before the silver deposition show a slightly increased (however, overall very small) photoemissivity from the nano-structured areas in comparison to the native HOPG. The photoemissivity from both areas (nano-structured as well as native) after silver evaporation has increased by orders of magnitude in comparison to the undecorated surface. It is that the photoemission signal originates dominantly from the silver clusters and not from the HOPG substrate. A limitation in the PEEM resolution arose from the reduced extractor voltage that could be applied between the sample and the entrance lens of the PEEM in this experiment (maximal 5 kV as opposed to 15 kV in the optimum case). For voltages higher than 5 kV, leakage currents due to field emission from macroscopic defects in other regions of the HOPG prevented the imaging of the sample. Thus it was not possible to resolve the 150 nm periodicity in the PEEM experiments.

Clearly resolved are steps of the HOPG in the native areas, which are decorated by silver clusters. The 300 nm periodicity of the patterning is also resolved in the PEEM image (figure 5-16). The graphite step edges are decorated with silver clusters and are distinctly visible in the PEEM image (figure 5-16b). Within the patterned area the step edges are not visible. The nano-structuring is not always influenced by natural surface defects. Indeed STM measurements have shown that the step edges are not decorated with more clusters than the structured nano-pits. Hence, the cluster pattern prevails due to the high density of the structured nano-pits. It would be helpful for fabrication of nano-structures if the natural defects on the surface can be neglected.

Continuous time resolved PEEM measurements indicate that life-time maps and histograms are different for structured and non-structured regions (for more details see reference [2]). This makes the cluster pattern interesting for investigations of their optical properties.

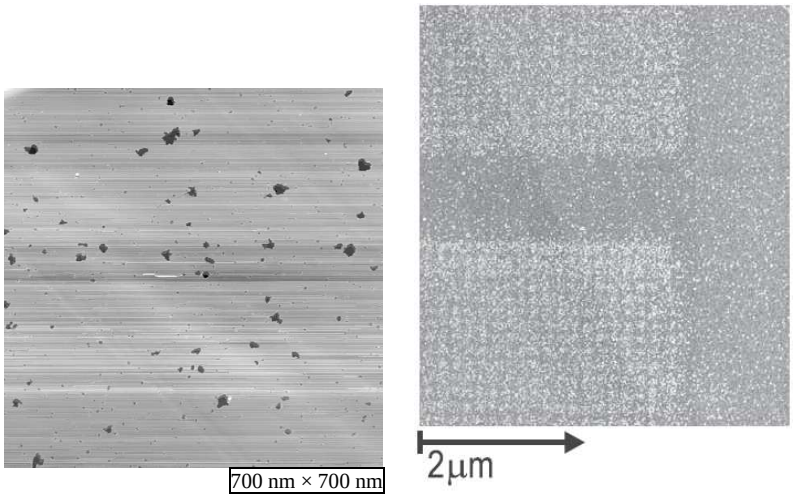

FIGURE 5-13: **(a) STM image of nano-pits within area 3 on SAMPLE 6 written in a point pattern with 150 nm periodicity exposed with D_{point} = 480 ions/point. It exhibits two characteristic pit sizes. Pits in the size regime between 5 nm and 20 nm diameter appear at a density of 100/µm^2, pits with a diameter below 5 nm appear at a density of 900/µm^2. (b) SEM image of the border region of area 3 after cluster condensation. The nano-patterned area corresponds to the two regions at the top left and bottom left of the image.**

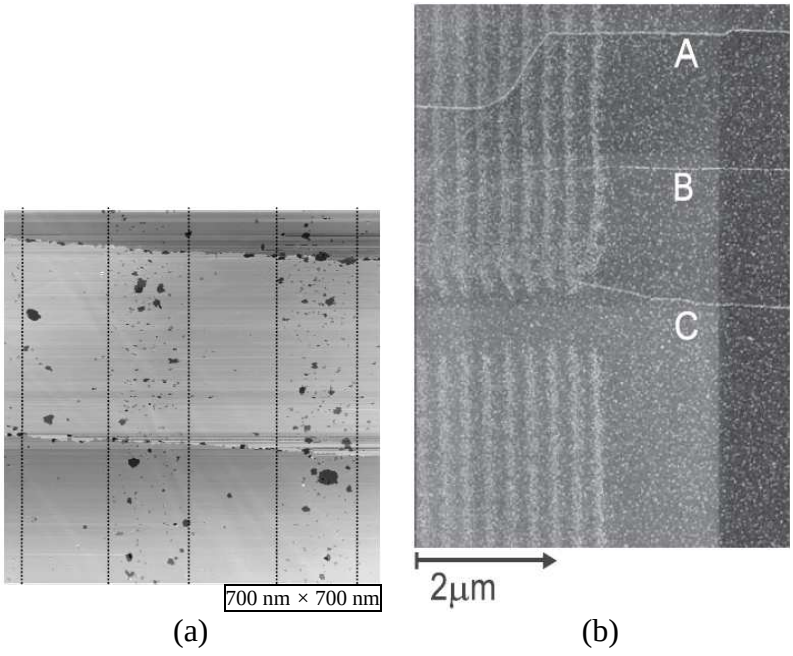

FIGURE 5-14: **(a) STM image of nano-pits in area 4 of SAMPLE 6 structured with D_{point} = 240 ions/point. The lines that have been written with a periodicity of 300 nm in the initial FIB process are clearly visible as areas of increased pit density. These lines have a width of about 150 nm and exhibit two characteristic pit sizes similar to area 3. The large pits are found at a density of 400/µm^2, the small pits are found at a density of 1500/µm^2. The depth of the pits varies between 1–3 ML. (b) SEM image of the border region of area 4 after cluster condensation. Clearly visible are the lines written in the FIB process with a periodicity of 300 nm. A, B, and C label steps in the HOPG substrate.**

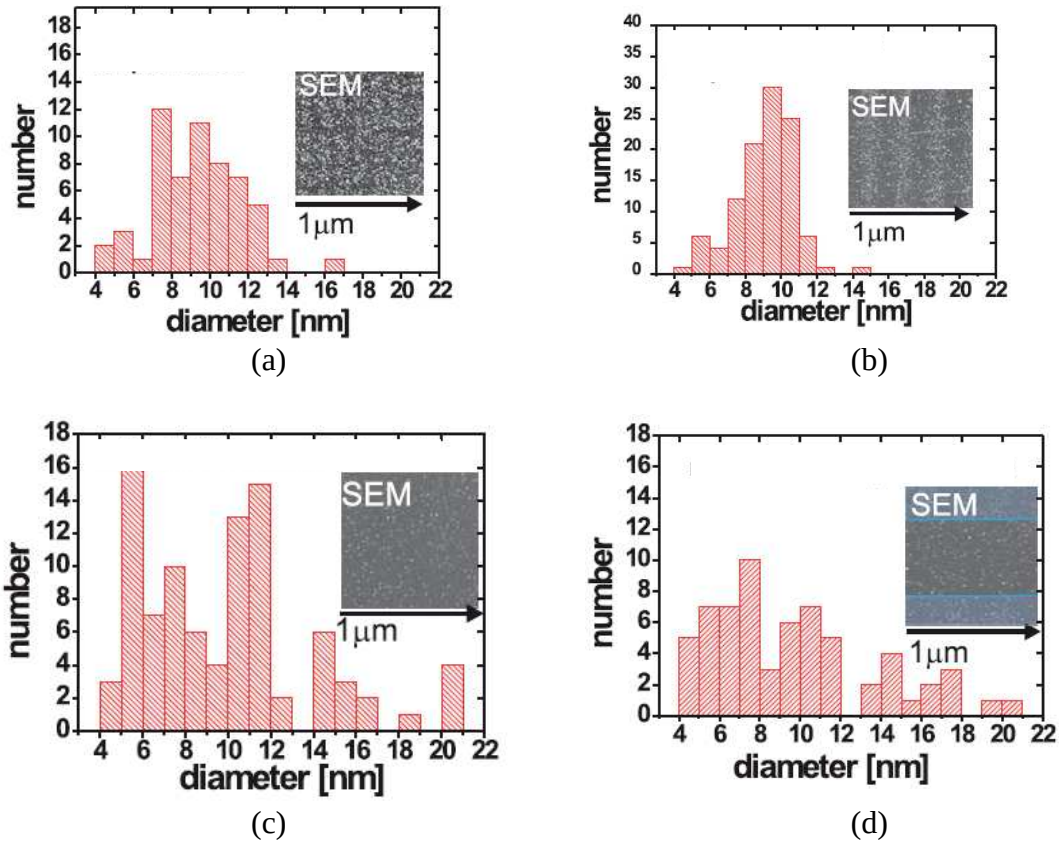

FIGURE 5-15: **Size distribution of the clusters deduced from SEM images at (a) the patterned region of area 3 on SAMPLE 6, (b) patterned region of area 4 on the same sample, (c) native HOPG substrate (d) interstitial region (the blue lines mark the boarder to the patterned region).**

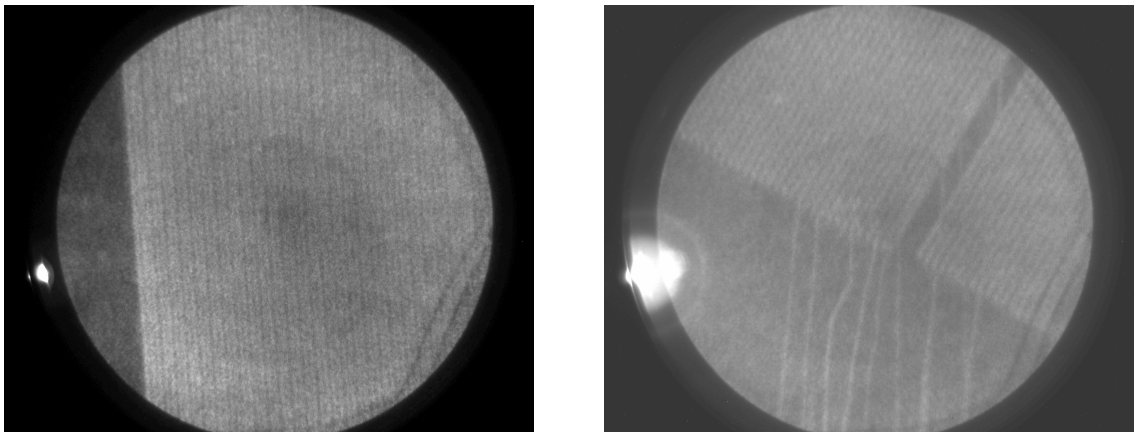

FIGURE 5-16: **(a) PEEM image of area 5 structured on SAMPLE 6 shows a pattern of silver clusters after deposition of 4 ML silver. The area was pre-structured with a nano-pit pattern which was exposed with D_{point} = 480 ions/point. The point pitch amounts to 300 nm. The PEEM measurement was performed with a 420 nm laser (200 mW). (b) PEEM image of a border region structured on SAMPLE 7 shows cluster patterns after deposition of 2 ML silver. The point pitch amounts to 300 nm and the ion dose is D_{point} = 1870 ions/point. For this PEEM measurement an Hg-lamp was used.**

5.2.2.2 Lead layer patterns

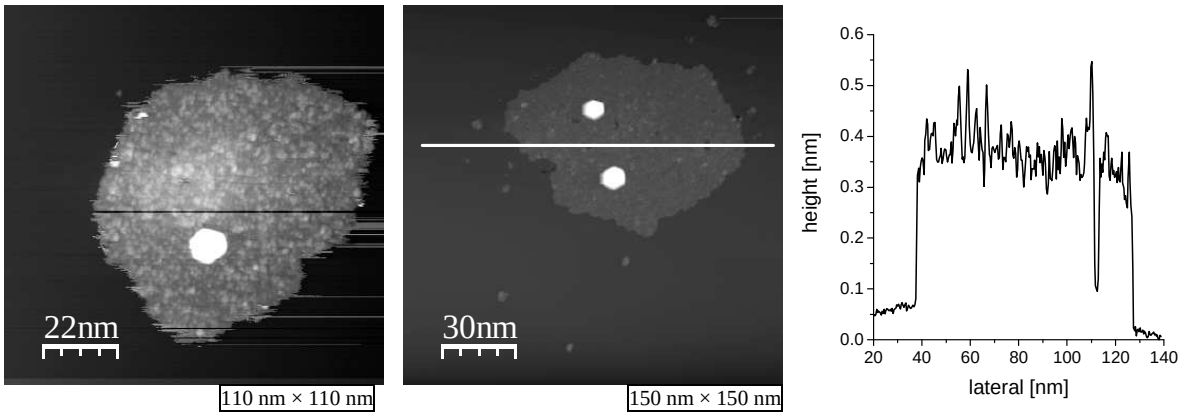

FIGURE 5-17: High resolution STM images show two points structured with an ion dose of 7×10^{-5} pAs within two different areas on SAMPLE 9 after room temperature deposition of 0.14 ML lead. (a) The structure of the lead wetting layer surrounding a faceted lead cluster is well visible. It does not indicate any crystalline structure. (b) Lead wetting layer surrounding two faceted lead clusters. Nano-pits are visible within the lead layer. (c) Line profile of image b (white line) shows the structure of the lead layer in detail. The minimum within the lead layer is a nano-pit.

Lead atoms tend to build a wetting layer. Henzler et al. observed electric conductivity for layers thicker than one monolayer and superconductivity for layers thicker than 4 ML at a temperature about 1 K [143-145]. In spite of the existence of nano-pits the atomic layer is very mobile on the surface. Hence its imaging with STM is not simple. The STM imaging of the lead layer is strongly dependent on the tunneling parameters as well as the tip shape. Mostly the layer is removed without any trace in the STM image.

Principally the layers can be produced by room temperature deposition (cf. figure 5-25 and figure 5-27). SAMPLE 9 is particularly capable for this application since the nano-pits are not completely oxidized. The incompletely oxidized defects are ideal candidates to support the growth of lead layers. Figure 5-17 shows high resolution STM images of two points decorated with lead layers. There are one or more faceted clusters within the points with a height of 1-3 nm. However the wetting layer does not seem to be influenced by the clusters or nano-pits but rather by the defect rich region (c.f. figure 5-17b). A closer look on the layer structure does not indicate any crystalline structures (figure 5-17a). The layer could be an aggregation of smaller lead particles like dimers or trimers. The line profile shows that the layers are between 0.3 to 0.4 nm high (figure 5-17c). Peak to peak distances of a few nanometers are too large for atomic structures.

For production of lead layers in a pattern a high density of weakly oxidized defects as anchor points is needed. The oxidation process can not be left out because the sputtered carbon atoms have to be removed. They could influence the layer growth or heal the defects during the routine heating of the bare substrate. SAMPLE 8 is an applicable substrate for this purpose. On this substrate 0.07 ML lead was deposited at 150 K. The reduced temperature should reduce the atom mobility on the surface and hinder them to build clusters. The purpose was to obtain lead layers structured in a line pattern. Best results were obtained for an ion dose of 2×10^{-5} pAs as shown in figure 5-18. Lead layers can be observed only in a few areas. They are interrupted by clusters and well oxidized nano-pits (figure 5-18a). Apparently the density of weakly oxidized defects is too low for a layer

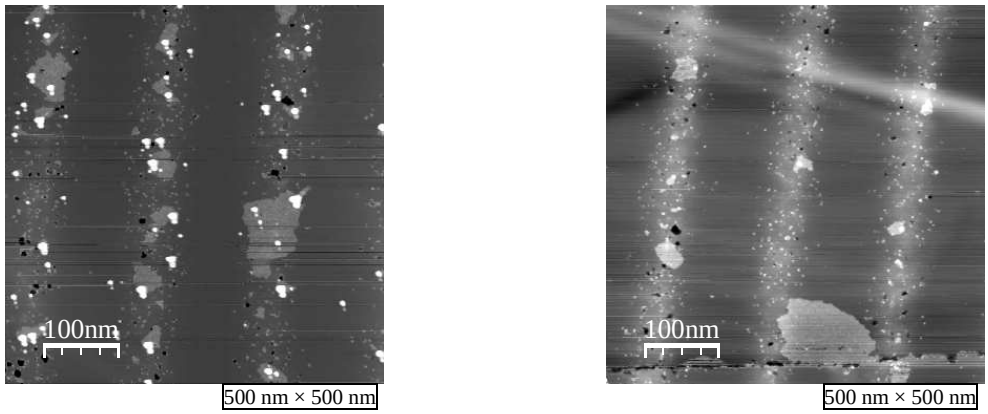

FIGURE 5-18: STM images show the same area structured with 2×10^{-5} pAs on SAMPLE 8 after deposition of 0.07 ML lead at 150 K. The used pattern is shown in figure 5-20. The light gray regions are covered with a lead layer. The cluster shapes in image (a) are deformed by the tip shape. In image (b) no clusters are visible, and a lead layer is grown at the step edge in the bottom.

growth. In that case cluster growth is more favored. Also natural defects like graphite step edges influence the layer growth (c.f. figure 5-18b). The growth at step edges seems to be more favored than at defects.

Increasing the ion dose to 3.5×10^{-5} pAs leads to very different results. The lead layers do not grow on the defected structure but between them. This may seem a strange behavior because in these regions no defects or other anchor structures exist. The reason for this becomes clearer by regarding the STM image in figure 5-19a. In this image a natural defect (called carbon ridge in the following) with a height of 4 nm crosses the structured lines. The lead layers are grown at the carbon ridge up to a maximum height of 2.5 nm. It is interesting that the lead layers are separated by the structured lines. Consequently it can be concluded that there must be a common property of the structured lines and the carbon ridge which causes the growth of lead layers. It is known that the exposure of graphite with high ion doses results in hill structures. These hills are in this case 0.5 nm high. That could be the reason for this growth behavior.

A similar example with step edges acting as anchor points is shown in figure 5-19b. The step edge is 3 nm high. The length of the lead layers starting at the step edge is limited to a few 100 nm. A detailed image of one layer grown at a 3 nm high step edge is shown in figure 5-19c. The 200 nm long lead layer is in this case not homogeneous. The vacancies in the layer may have been caused by a tip interaction. An indication for a tip interaction is the exactly horizontal oriented vacancy line in the layers top side since its orientation is equal to the scanning direction. In contrast the layers in figure 5-19d are grown homogenously and they are interrupted by the structured lines. The step height is in this case approximately 0.4 nm which corresponds to one monolayer graphite. The line profile shows the shape of the lead layers. The onset of the structured hills is clearly visible. At this point the Pb layer starts and ends at the neighbored hill onset. The lead layers are 0.3 to 0.4 nm high. The hills are at most 0.1 nm higher.

The lead atoms can not break through the potential barrier at the hill flank and reach the nano-pits. Since diffusion is the main process for the cluster growth they can not grow on the hills. It seems that there is no attractive interaction between the hills onset and the lead atoms that is strong enough to support the layer growth. A further increase of the ion dose could change this and enable the nano-structuring of lead layers in different well controlled shapes.

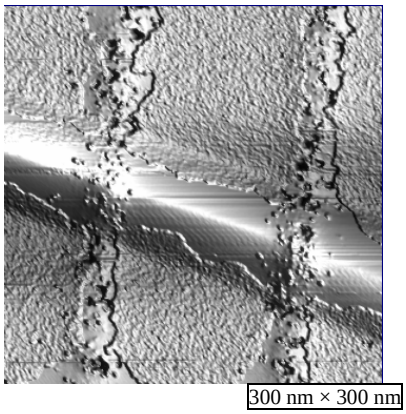

(a)

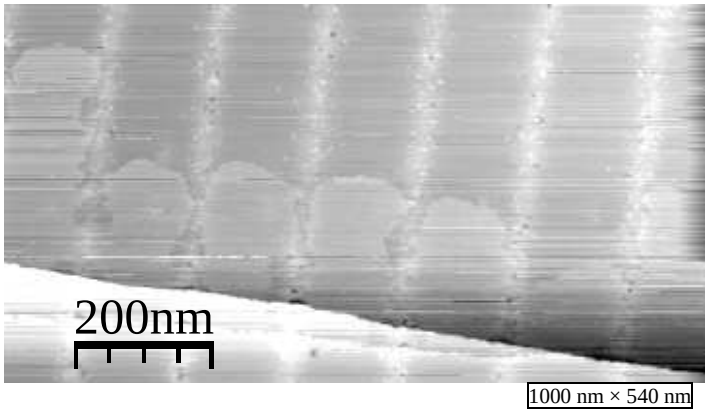

(b)

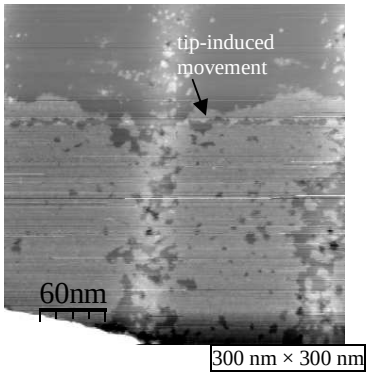

(c)

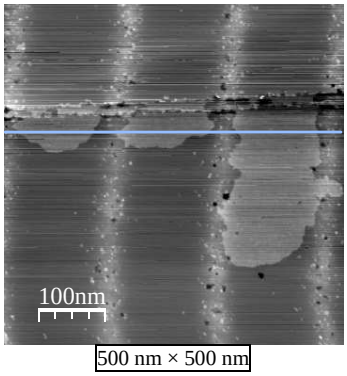

(d)

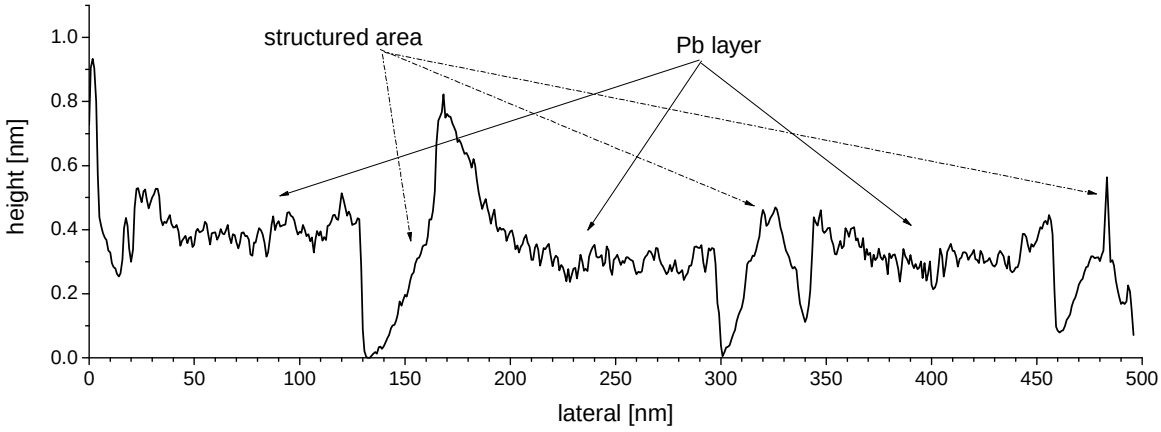

(e)

FIGURE 5-19: STM images show an area structured with 3.5×10^{-5} pAs on SAMPLE 8 after the deposition of 0.07 ML lead at 150 K. (a) A natural defect on HOPG with a height about 4 nm crosses the nano-pit lines from the left to the right. The lead layers are anchoring at this defect and oriented in the direction of the nano-pit lines. The lines have a hill shape with a height about 0.5 nm decorated with nano-pits. For a better display the image is rendered in 3D shading. (b) A large scale image shows lead layers grown at a graphite step edge. The nano-pit lines separate the lead layers. (c) The image shows the lead layers in detail. In the upper part of the image a tip-induced movement of the lead layer is visible. (d) In contrast to the previous image the lead layers are coherent. (e) Line profile of image (d). The lead layers abruptly end at the structured lines. The onset of the hill shape is well visible. The lead layers have nearly the same height as the hills.

5.2.2.3 Lead cluster patterns

"Cluster Rows: Fabrication"

On SAMPLE 8 a pattern of lines with a 150 nm pitch was structured. To produce a continuous line the point distance in the lines was set to 20 nm. In order to investigate the influence of the structuring process on the cluster growth 8 areas are exposed with an ion dose of 10^{-6} pAs/point multiplied with the dose factors 1, 5, 10, 15, 20, 25, 30 and 35 for every area. The STM images in figure 5-20 show that the lines and the contained nano-pits are well separated. The lines exhibit the typical hill shape with a width of about 80 nm. The first deposition of 0.07 ML lead atoms at 150 K results in very small clusters which can not be imaged well due to their small sizes. In addition lead wetting layers were observed, as described in section 5.2.2.2.

The deposition of additional 0.28 ML at 150 K (total coverage of 0.35 ML) and the subsequent annealing at room temperature resulted in larger faceted lead clusters as shown in figure 5-21a for one area. The clusters are grown in the pre-structured lines. The line width amounts to 50 nm in this case. Beside the clusters and the nano-pits smaller particles are visible as white points in the image. They could be either smaller aggregates consisting of several atoms or non-oxidized defects which become visible by electronic effects. The line profiles in figure 5-21b show typical shapes of lead clusters with typical heights (concerning this see section 5.4.3.1). The clusters distinctly exhibit large facets. Mostly the clusters with smaller heights have larger facets.

"Cluster Rows: Height & Density Analysis"

The dependence of the cluster heights on the ion dose is shown in figure 5-22a. The height distribution reaches its maximum of ca. 2 nm for an ion dose of 2×10^{-5} pAs. The same behavior is observed for the faceted area as shown in figure 5-22b. The largest mean cluster facet is 25 nm².

The cluster density increases with increasing ion dose and then remains nearly constant for ion doses higher than 2×10^{-5} pAs (figure 5-23). That can be explained with the cluster growth mechanism. The probability of atom capture is higher for larger clusters. That entails that larger clusters grow faster than their smaller neighbors. At a certain cluster density these clusters do not allow the growth of more clusters. Consequently the cluster density remains constant.

One may expect that larger cluster sizes should result in a lower cluster density because the clusters share the same coverage of deposited material. But for ion doses higher than 2×10^{-5} pAs the cluster sizes decrease although the cluster density does not change. That can be explained as follows. The high density of nano-pits in these areas causes that the defects do not oxidize completely as discussed in 5.2.1.2. These weak oxidized nano-pits and the well oxidized nano-pits near a large cluster do not support the growth of clusters. Instead smaller aggregates are formed, visible as small white points in the STM images. Thus less material remains for the cluster growth. Additionally the high defect density may suppose the formation of lead layers as discussed in 5.2.2.2. These effects finally result in smaller cluster sizes.

The sample was annealed at room temperature, first for a short time of 45 minutes and then for a long time of approximately 3 days. A comparison of STM images before and after annealing is presented in figure 5-24 for three representative ion doses. The images show the variation of the cluster density depending on the ion dose and the annealing process. The cluster density decreases about 67% for the short annealing interval and there is only a small additional change for the long annealing interval (cf. figure 5-23).

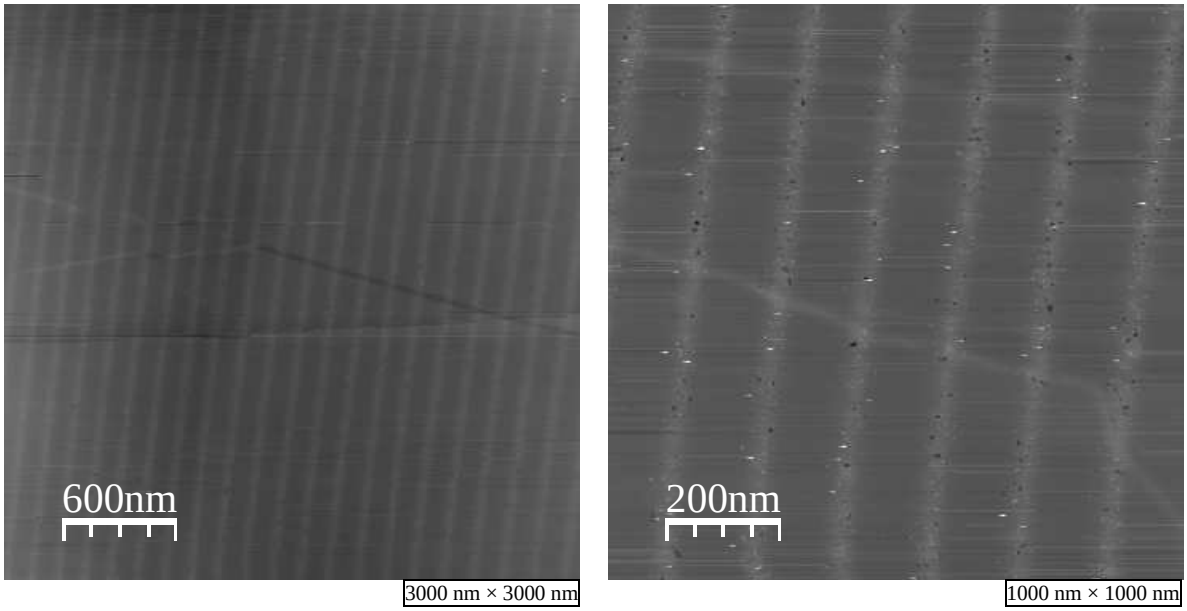

(a) (b)

FIGURE 5-20: **(a) STM image of an area on SAMPLE 8 structured with an ion dose of 3.5×10^{-5} pAs/point after deposition of 0.07 ML lead at 150 K. The nano-pits are patterned in lines with a 150 nm pitch. The point pitch in the lines amounts to 20 nm to get a continuous line. The clusters are too small to become visible in this image. Some other defects are also visible. In the center of the image a graphite atomic step is visible. (b) Inset of another region shows the nano-pit pattern in details. In addition to the nano-pits non oxidized defects are visible as small white points and some smaller clusters. The ion bombardment causes a hill shape of the lines with a width of about 80 nm.**

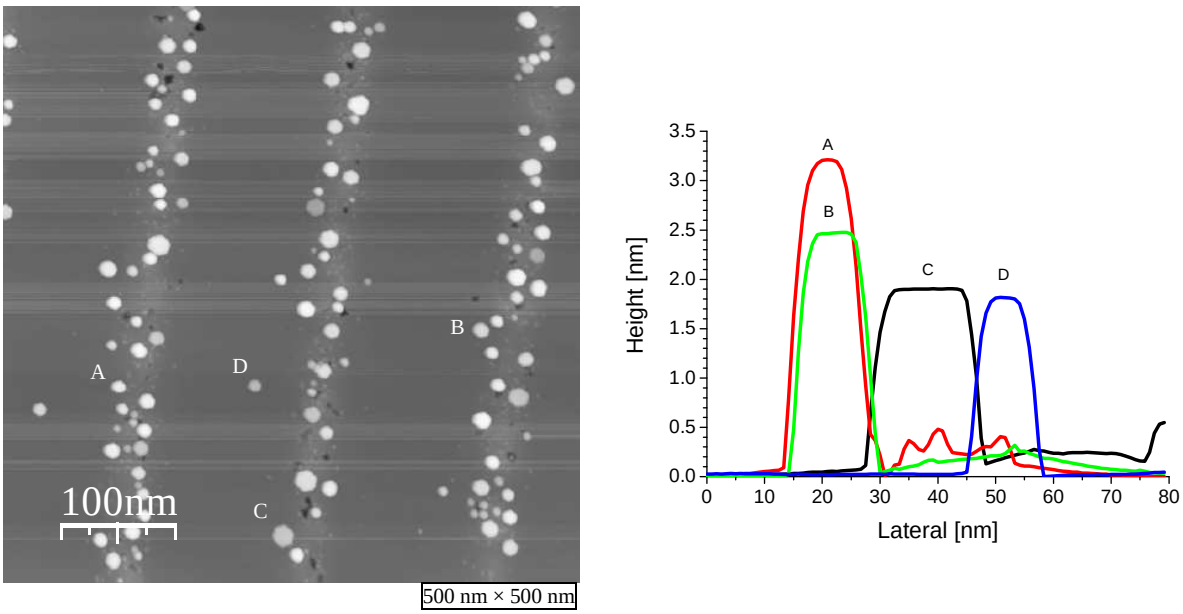

(a) (b)

FIGURE 5-21: **(a) STM image of an area on SAMPLE 8 structured with an ion dose of 2.5×10^{-5} pAs/point after deposition of 0.35 ML lead at 150 K and the subsequent annealing at room temperature for 3 days. The faceted lead clusters are patterned in lines. (b) Line profiles of 4 typical clusters in the image (a) labeled with A, B, C and D. These clusters represent the three most favored cluster heights in this image.**

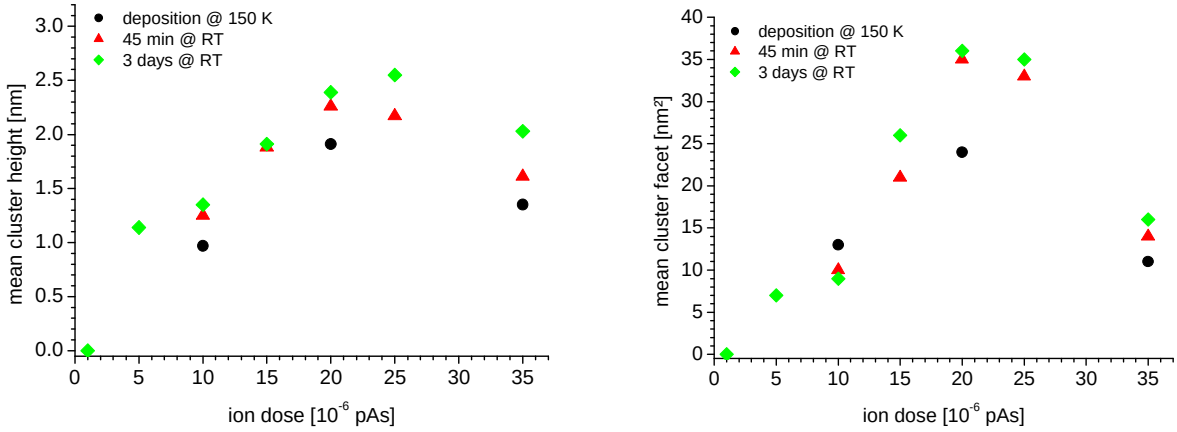

(a) (b)

FIGURE 5-22: Distribution of (a) mean cluster height and (b) mean cluster facet versus the ion dose. These statistics are derived from STM images such as the images shown in figure 5-21 and figure 5-24. The cluster size increases with increasing ion dose. The maximum is reached at app. 2.5 × 10^{-5} pAs (corresponds to a line dose of 12.5 pAs/cm). After this the cluster sizes especially the cluster facets decrease. Notice that only particles larger than 0.6 nm are considered.

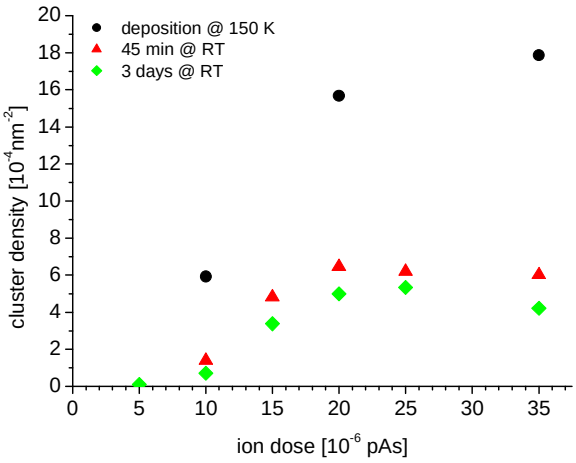

FIGURE 5-23: The density of the lead clusters grown on areas within SAMPLE 8 depending on the ion dose. The cluster density is determined for a 100 nm × 100 nm area. It increases with the ion dose until 2 × 10^{-5} pAs and remains nearly constant for higher ion doses. The annealing process results in a lower cluster density. Notice that only particles larger than 0.6 nm are considered.

The cluster heights increase about 17 % after the first annealing interval (cf. figure 5-22a). Larger clusters are formed via Ostwald ripening (see below for a detailed discussion). After the long annealing interval the cluster heights do not change for ion doses below 2 × 10^{-5} pAs. Above this value the Ostwald ripening process continues and the clusters become higher. Also the cluster facets become larger. The deviation for 10^{-5} pAs may be a statistical effect.

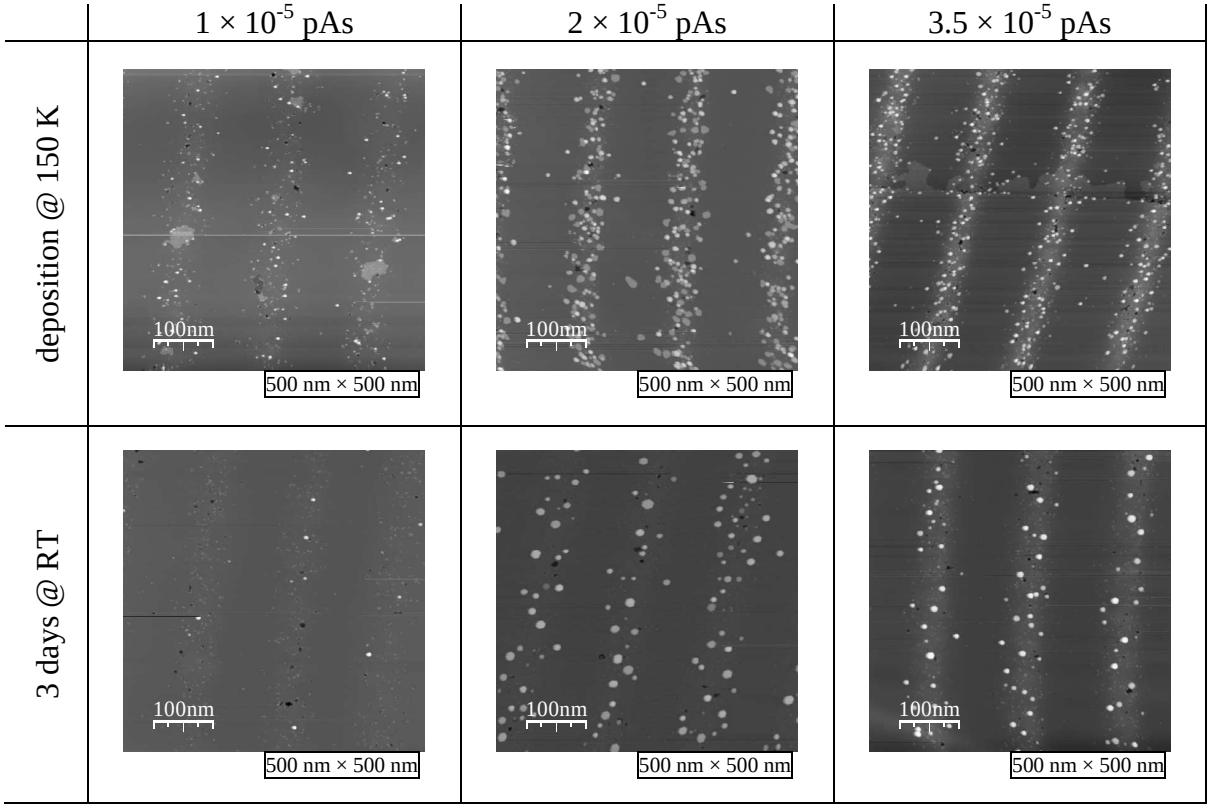

FIGURE 5-24: STM images show three areas structured with different ion doses on SAMPLE 8 after deposition of 0.35 ML lead (top) and after annealing at room temperature for approximately three days. The pattern is the same as discussed in figure 5-21. The lead clusters are grown on nano-pit rows in a 150 nm pitch.

"Single Cluster Patterns: Fabrication"

The challenge of cluster patterning is the production of single clusters in a pattern. Therefore patterns of single nano-pits are necessary. It is known that every 10^{th} ion produces a defect on the surface which can oxidize and build a nano-pit. Neglecting that the pit production is a random process it should be possible to produce single nano-pits with an ion dose of about 10 ions/point. This corresponds to a dot dwell time of 4 µs using the lowest available ion current of 0.5 pA. This approaches the limit of the ion beam tool ($t_{dwell,min}$ = 100 ns). Apart from this, patterning with such low ion doses underlays physical limits. The ion beam profile and the given resolution are defined for a large number of ions. That means for single ions that the impact location is determined more by the noise of the Gaussian distribution as by the distribution itself. Also recoils play a decisive role for the nano-pit distribution since the surface defects produced by recoils are far away from the beam impact point. For the oxidation process all defects (patterned or accidentally emerged) are equivalent. For this reason only groups of nano-pits can be produced in a pattern.

Nevertheless the variation of the oxidation process can be used to produce a pattern of clusters. The idea is to fabricate a pattern of defect groups and then oxidize the sample at lower temperatures which causes a reduction of the oxidation rate. Usually that would not lead to the growth of nano-pits but the high density of surface defects would cause a coalescence of them at a low oxidation rate. Thus more ions are needed to produce one nano-pit and the recoils would only play a minor role for the nano-pit production.

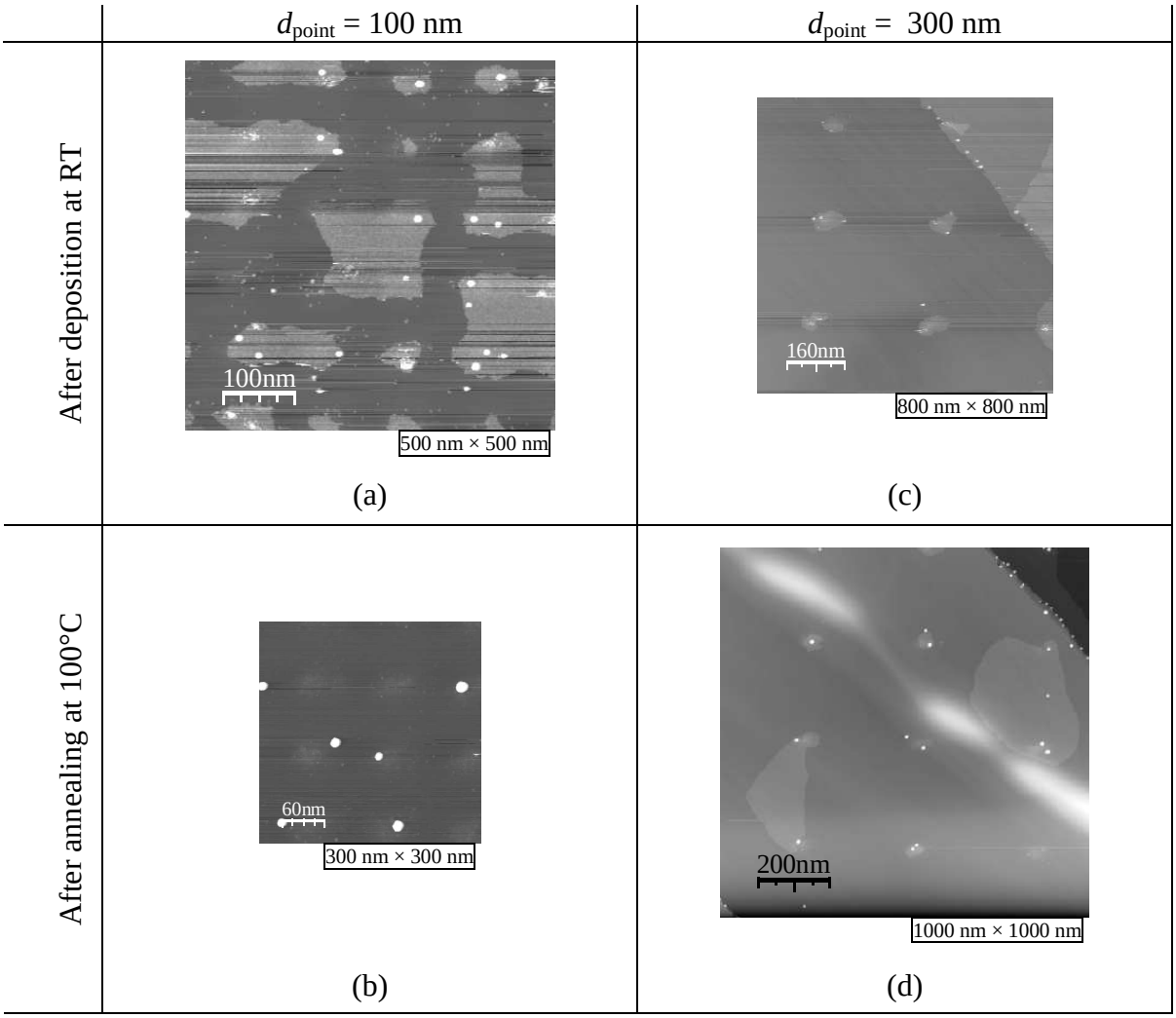

FIGURE 5-25: STM images show two areas with different point pitches structured on SAMPLE 9 after room temperature deposition of 0.14 ML lead and after annealing at 100°C. The ion dose amounts to 7×10^{-5} pAs for both areas. Around the clusters grown on the points lead layers are visible in most of the images. Most of these layers shrunk or disappear after annealing. Images (a) and (b) as well as images (c) and (d) are scaled in a way that both images have the same magnification.

This idea was realized in SAMPLE 9. On this sample five areas were structured with different point pitches from 100 to 500 nm in 100 nm steps. The ion dose amounts to 7×10^{-5} pAs for all areas. After the oxidation at a reduced temperature of 450 °C for 200 minutes the sample was transferred to UHV and covered with 0.14 ML lead at room temperature.

The results for two areas with 100 and 300 nm pitches are presented in figure 5-25. The high defect density in the exposed region causes a lateral aggregation of the lead atoms which form a wetting layer around the point and hinder the cluster formation. In order to obtain clusters the sample is annealed at 100°C. After this the wetting layers shrunk indeed but not always disappeared. The interaction of the wetting layer with the defects seems to be strong. However several larger clusters are formed on the points.

Another effect is the movement and coalescence of the wetting layers. After annealing large areas (c.f. figure 5-25d) or stripes (c.f. figure 5-27b) of the wetting layer are formed. This effect is observed in all areas and indicates that the lead atoms are very mobile on the surface. The region of coalescence seems to be at random positions.

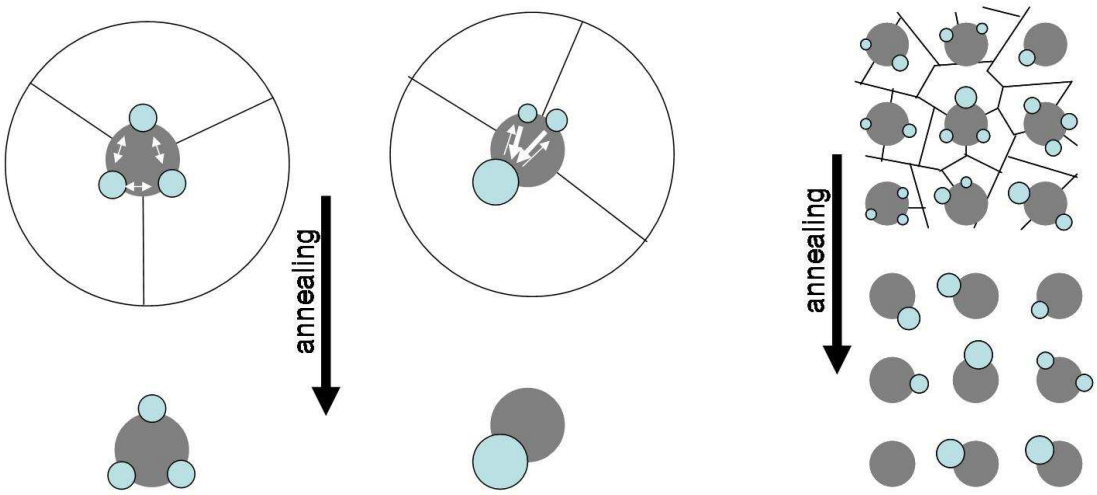

FIGURE 5-26: Illustrations for the understanding of the Ostwald ripening around a point. (a) illustrates the case $d_{point} > d_{ca}$. The gray circle represents the lateral extension of a point which could contain nano-pits or defects. The large circle represents the mean atom capture area of the point which is divided for three nucleation centers. The clusters grown on them are the smaller blue circles. The arrows show the material exchange between the clusters during annealing process. The distribution of the clusters around the point determines the strength of the ripening process. (b) illustrates the case $d_{point} < d_{ca}$. Lines separate the capture areas which determine the clusters size. The ripening process occurs not only at the points but also between the points.

"Single Cluster Patterns: Ostwald Ripening"

The idea of the annealing process was to tune the cluster pattern by Ostwald-ripening [146]. Every cluster is releasing and receiving atoms at the same time. However atom positions on the surface of larger clusters are more favored than on smaller clusters since smaller clusters result in a lowering of the binding energy per atom due to a lower contribution of the surface energy for a smaller surface to volume ratio. Thus the probability for atom desorption is higher for smaller clusters. This causes a movement of lead atoms from smaller clusters to larger clusters. This cluster growth is well visible in figure 5-25a and b. After metal deposition lead layers are grown connecting the points. Also some points are decorated with smaller clusters. These layers and clusters disappear after annealing. Only the larger clusters remain which are not necessarily exactly positioned on the point.

The ripening process does not always result in a single cluster per point. The reason for this can be explained with the illustrations in figure 5-26. If an atom adsorbed on the surface finds a defect during its diffusion time on the surface it can contribute to the growth process. Otherwise it desorbs to the vacuum. Hence, every point can be associated with a mean capture area which depends on the diffusion length of the lead atoms (comparable with the capture area of O_2 molecules as discussed in section 5.2.1.2).

If the point pitch d_{point} is larger than the diameter of the capture area d_{ca} the capture area is only divided between the nucleation centers at the point edges (figure 5-26a). The cluster size depends on the size of its capture area fraction (and of course on the deposited coverage of lead atoms). That means a nearly equal distribution of the nucleation centers around the point would roughly result in equal cluster sizes. In the other case the cluster

sizes would be very different. By Ostwald ripening larger clusters get material from smaller clusters. So, different cluster sizes are needed for the ripening process. That is not the case for an equal distribution of the clusters around the point. In this case the ripening process does not occur efficiently.

If d_{point} is smaller than d_{ca} the nucleation centers would have very different and smaller capture areas since they are influenced by the neighbored points (figure 5-26b). Thus an equal distribution of nucleation centers at a point would not necessarily result in equal cluster sizes. Equal cluster sizes at a point become rarer. Consequently only the highest clusters remain on the point. In this case the growth of single clusters per point dominates. However points with more than one cluster or without clusters remain unavoidable. This effect also results in different cluster sizes after the ripening process as illustrated in figure 5-26b. In order to produce clusters with uniform sizes they have to be positioned exactly in the center of the points. That is of course an experimental challenge.

"Single Cluster Patterns: Analysis"

Large scale STM images of areas structured with 100 and 200 nm pitch and covered with 0.14 ML lead are shown in figure 5-27 after annealing. Ostwald ripening supported by a reduced point pitch of 100 nm results in a pattern of single clusters. In fact not every point is decorated with one cluster. There are points with two, three or without clusters but the number of single clusters is higher. For d_{point} = 200 nm there are points with one cluster but the points with two and more clusters dominate. In this case all points are decorated with clusters.

The mean cluster/point depending on the point pitch is shown in figure 5-28. It is abruptly increased for a pitch of 200 nm and rises linear for higher point pitches. It shows that the single cluster patterning can be only obtained for a point pitch of 100 nm. Indeed the success of the single cluster patterning evolves from a complex combination of a number of parameters such as ion dose, point pitch, oxidation temperature, deposition temperature and annealing process.

Another question is controlling the cluster size with patterning. The height distribution of the clusters for two point pitches before annealing is shown in figure 5-29. The maximum is located at 2 nm. Due to poor statistics no statements with respect to the pitch dependence of the cluster height can be made here. The cluster height distribution for all point pitches after annealing is shown in figure 5-30. The maximum is located between 3.25 and 3.5 nm after annealing (marked with a dashed line for all histograms). The cluster heights are clearly enlarged which is an indication of the Ostwald ripening effect. The cluster heights do not change with the variation of the point pitch. The main reason for this effect is the increased cluster density (per point) for larger point pitches. But the overall cluster density remains nearly constant which results in an equal height distribution.

Furthermore the clusters have a narrow height distribution but not better than clusters grown on a non-structured sample. This is due to the reason explained above (discussion of Ostwald ripening) and due to the deviation from the ideal case with one cluster/point which causes a non-equal distribution of the deposited material on clusters resulting in a broadening of the height distribution. This is visible in figure 5-25b. The clusters on the top right and bottom are larger than the cluster in the center because it lost material to the neighbored cluster on the left side.

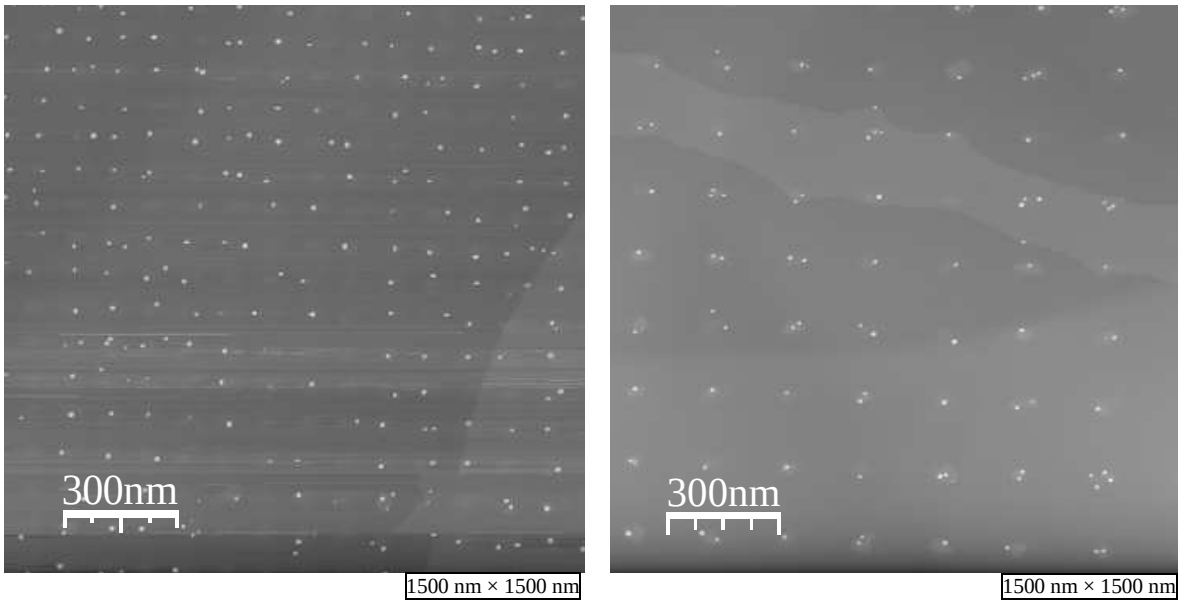

(a) (b)

FIGURE 5-27: STM images show clusters grown in patterns within two areas structured on SAMPLE 9 after deposition of 0.14 ML lead and subsequent annealing at 100°C. The ion dose amounts to 7 × 10^{-5} pAs for both areas and the point pitch amounts to (a) 100 nm and (b) 200 nm. The brighter area at the bottom right of image (a) is a graphite step edge (h = 0.34 nm). Also a few regions decorated with lead layers are visible at the bottom. In contrast the stripe at the top of image (b) is a large lead monolayer (h = 0.24 nm) connecting the points to each other. Also almost every point is decorated with a lead layer.

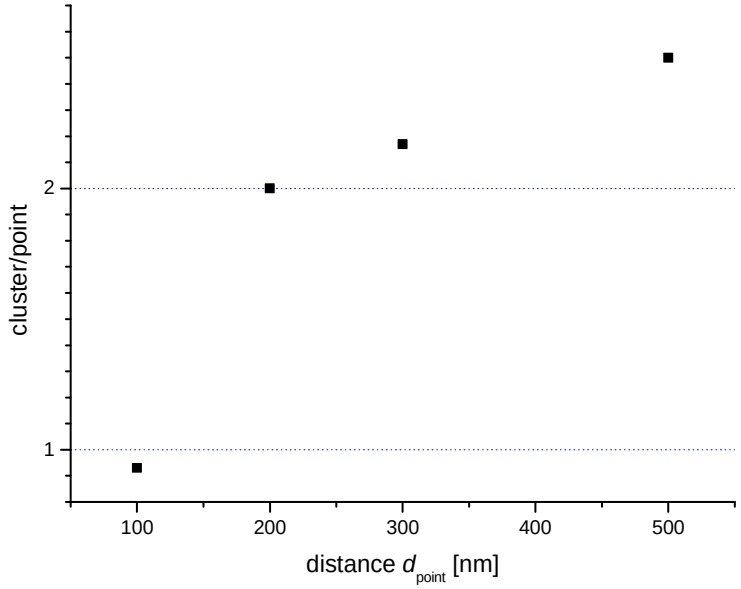

FIGURE 5-28: Mean cluster density per point depending on the point pitch for SAMPLE 9. The higher the point pitch is the more clusters are grown on the points.

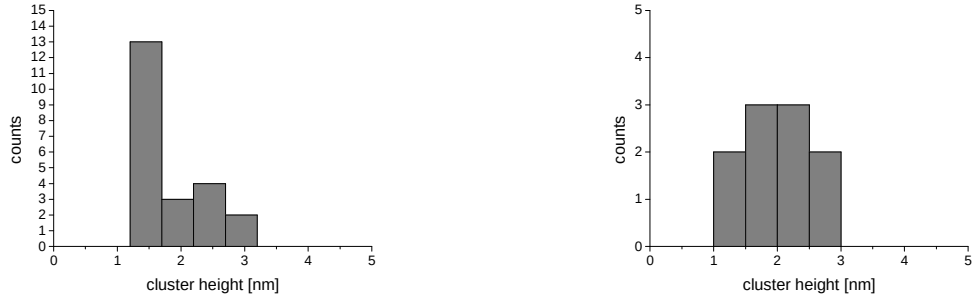

(a) d_{point} = 100 nm (b) d_{point} = 200 nm

FIGURE 5-29: Height distribution of lead clusters on SAMPLE 9 before annealing for two point pitches. The mean cluster height is about 2 nm.

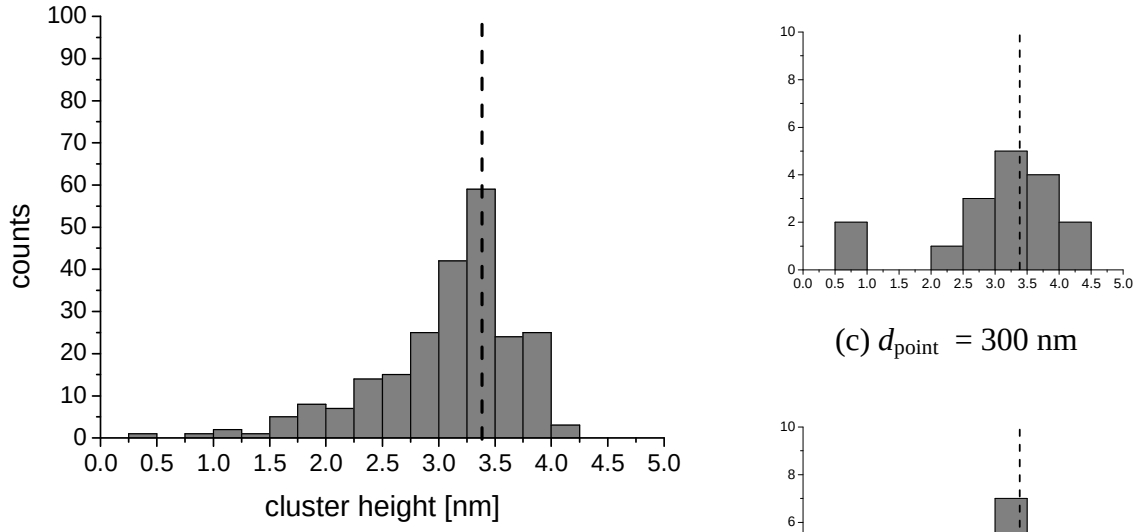

(a) d_{point} = 100 nm

(c) d_{point} = 300 nm

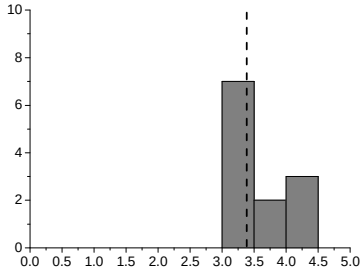

(d) d_{point} = 400 nm

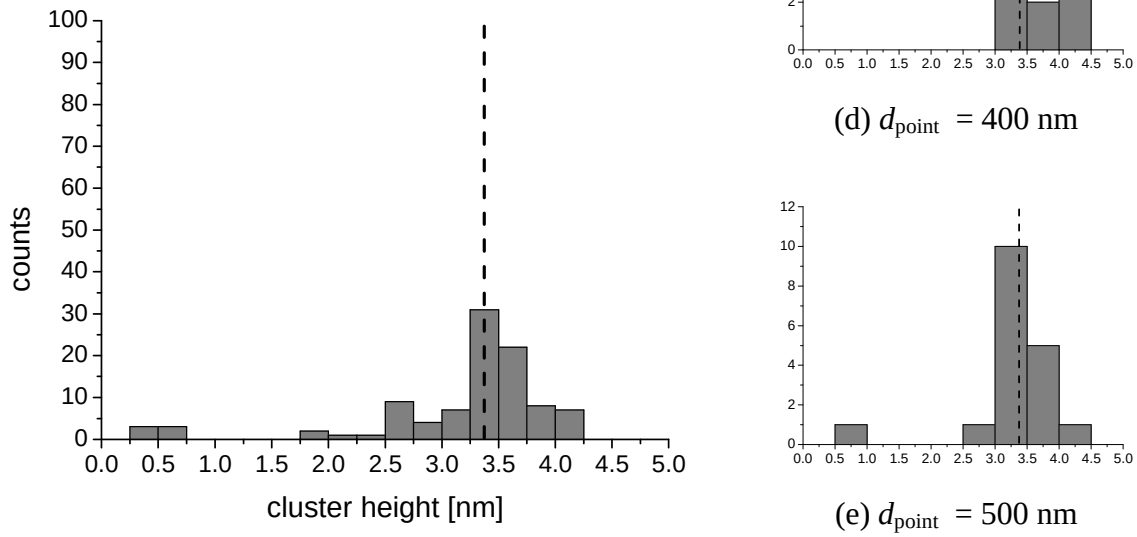

(b) d_{point} = 200 nm

(e) d_{point} = 500 nm

FIGURE 5-30: Height distributions of lead clusters for different point pitches d_{point} after annealing. The corresponding STM images are displayed in figure 5-27a, figure 5-27b and figure 5-25d for histograms a, b and c. Most of the clusters have a height between 3 and 3.5 nm. The dashed line marks the same height in all histograms.

5.3 Patterning with high ion dose

In contrast to the nano-pits which are produced by single ion events a higher ion dose can be used to produce deeper pits, called nano-cavities. Nano-cavities are defined here as pits deeper than 3.4 nm (this corresponds to 10 ML HOPG). In the following, first the patterning of nano-cavities and then their application for the beam characterization will be discussed. In section 5.3.2 the growth of metal islands on the nano-cavities after metal deposition is presented.

5.3.1 Nano-cavities

5.3.1.1 Nano-cavity patterns

"Broad Nano-Cavities"

In the areas on SAMPLE 1 which were structured with high ion doses over 100 000 ions/point a volcano shape is observed at each pattern point before oxidation (figure 5-31a), which is comparable with earlier studies [72]. The carbon atoms are displaced out of their crystalline lattice position and incident gallium ions are incorporated. One can estimate that 10^7 carbon atoms are located in a volume of $(50\ \text{nm})^3$. For the areas with high ion dose starting at area 8, 10^3 to 10^6 gallium ions have impinged on the substrate for one point. Hence, more space is needed due to the almost equal number of gallium atoms compared to the carbon atoms. In addition, voids in the defective structure may increase the volume. Electronic effects in STM imaging also cannot be excluded. Thus a hill shape of the surface with a height up to 7 nm emerges. For the highest ion doses the sputtering of atoms in the center of the point results in a volcano shape.

The subsequent oxidation process forms deep broad cavities (inset in figure 5-31a). Their depth amounts to approximately 50 nm for the areas 13 to 16. The nano-cavities are 100 to 200 nm wide for the areas 13 to 15 and become wider for area 16 where they coalesce. Figure 5-31b displays representative for these areas a 3D-image of a nano-cavity in area 14 after oxidation. It has an unusually steep border. Due to the properties of graphite one may expect for deep structures oxidized on graphite a staircase shape like a cascade of surface steps. But in contrast the experimental results suggest that the complete defect filled volume is oxidized. That can be compared to the formation of pits two or more monolayer deep as observed in other studies [52]. Also the bottom of the nano-cavities is very smooth, probably due to a sharp limit for the penetration depth of the ions (cf. 5.3.1.2).

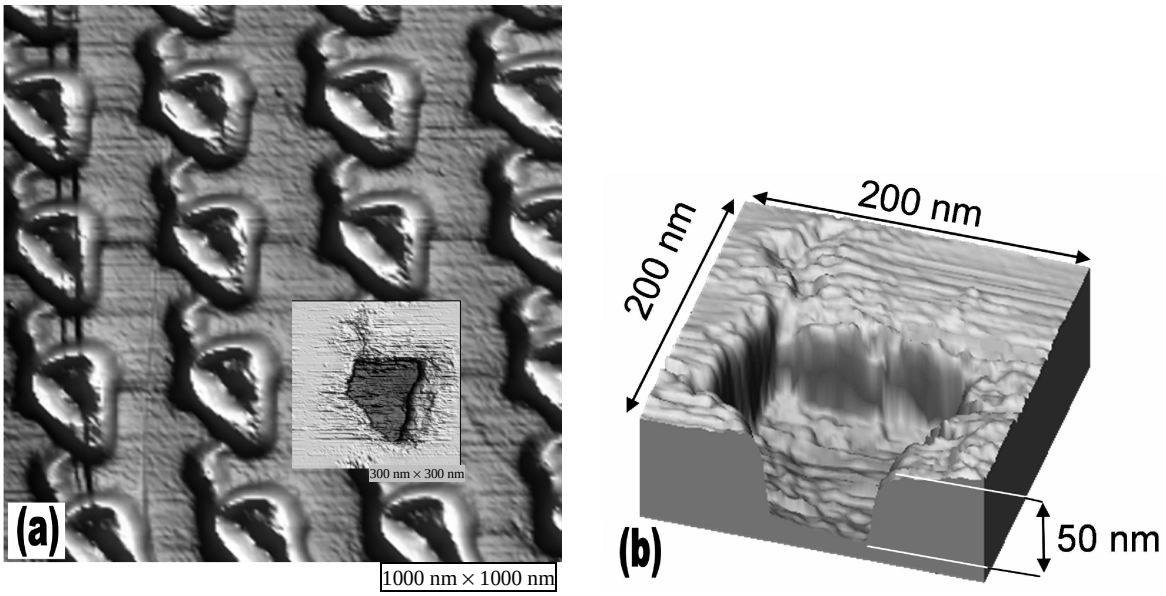

FIGURE 5-31: (a) STM image of area 13 in SAMPLE 1 before oxidation. The irregular shape of the impact points and the line between two points emerge due to a distorted focus of the ion beam. The rearrangement of carbon and gallium atoms around the impact point causes the volcano shape. For a better display of the height differences the image is rendered in a 3D-shading. The inset shows an STM image of a nano-cavity within area 14 after oxidation. (b) A 3D image showing the cavity shape, in particular the steep walls and the flat bottom. The nano-cavity is 50 nm deep and 100 to 150 nm wide.

"Optimized Nano-Cavities"

A measurement with optimized focus of the ion beam (with a diameter of approximately 10 nm and beam blanking between the single points) reveals the resolution power of the FIB tool (figure 5-32a). The ion dose was chosen to 1870 ions/point based on the results of the experiments discussed in section 5.1. In this experimental run the ion energy was reduced to 16 keV. However this does not observably change the results. The STM image shows an array of nano-cavities with a distance of 300 nm which is orientated at approximately 45° due to the orientation of the sample in the STM. Two natural defects of the HOPG sample are also visible. The white line is due to a subsurface defect which is not oxidized, and the black vertical line results from a surface defect, probably a grain border, which is oxidized. In the magnified image (figure 5-32b) nano-pits are visible around the cavities. They show the distribution of single ions whose origin is not yet known. The suspect is that, although beam blanking is used, they are caused by scattered ions or atoms which are of course unimportant for almost any other application. The single ion defects only become visible after oxidation. The line profiles show that the nano-cavities are 20 to 30 nm wide and 5 nm deep. The true depth may be larger due to the finite STM tip size (cf. section 3.2.4).

We repeated the experiment with the same parameters but with 35 keV gallium ions and a reduced point to point distance of 50 nm (figure 5-32d). The nano-cavities, with the same dimensions as above, are clearly separated and they have an irregular shape formed by the oxidation process. The nano-pits around them are more visible than in figure 5-32a and b due to the smaller image size.

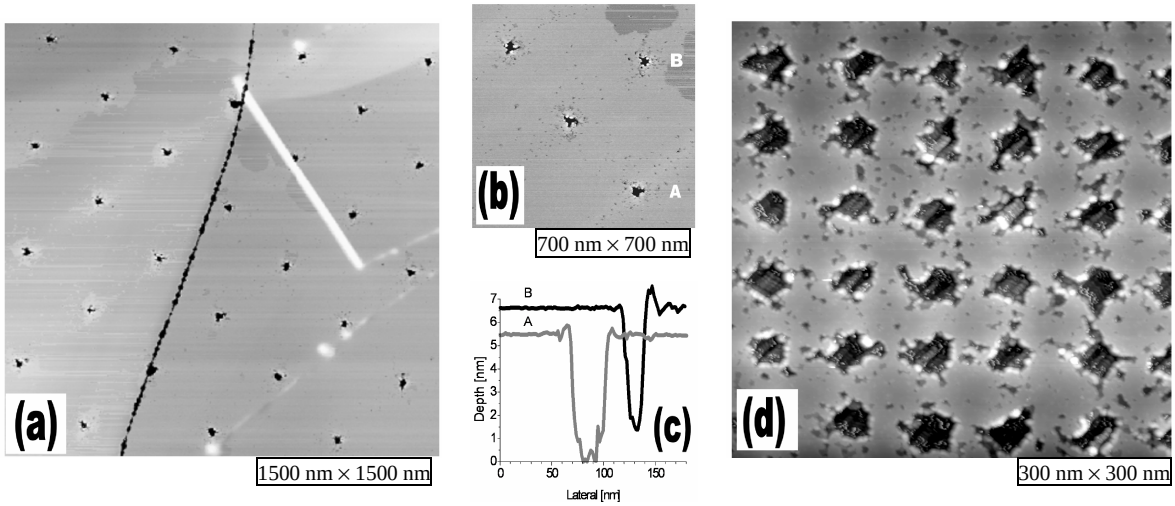

FIGURE 5-32: (a) STM image of an area structured with an optimized FIB focus on SAMPLE 2. Nano-cavities arranged in a lattice with 300 nm pitch. Each point is at least 5 nm deep and 20 to 30 nm wide. (b) Magnified image showing the patterned nano-cavities and a number of one monolayer nano-pits around them. (c) Exemplary line profiles of the two nano-cavities A and B in (b). (d) STM image of an area on SAMPLE 3 for which the distance between the nano-cavities was reduced to 50 nm.

The point area dose for these samples amounts to 4×10^{14} ions/cm² (assuming a defective area with a diameter about 25 nm). This is comparable to area 12 on SAMPLE 1 where indeed up to 10 nm deep cavities were observed. Considering the size of the ion focus, which has a diameter of approx. 10 nm, the area dose could be higher and achieve a value above 10^{15} ions/cm² where the maximal penetration depth could be measured for the broad ion focus (see 5.3.1.2). However it is not possible to make a quantitative statement for the cavity depth of the samples shown in figure 5-32, due to influence of the STM tip (see figure 3-11).

5.3.1.2 Penetration depth of gallium ions

The measurement of the nano-cavity depth (cf. figure 5-31) yields the *maximal penetration depth* d_{max} of the gallium ions. Gierak et al. obtained a value of ca. 25 nm for the penetration depth by simulation of 30 keV gallium ions into graphite [72]. This value is smaller than the cavity depth of about 50 nm measured here. The reason for this deviation is that the needed defect density for oxidation of a graphite layer is smaller than the main ion track area as presented by a usual color coding of the simulation results. Gierak´s group neglected this small number of vacancies (for a detailed discussion see section 6.1.2). However, the maximal penetration depth is defined here as the depth of nano-cavities, in the limit when they do not noticeably get deeper increasing the ion dose. The measured depth of the cavity is increased to a value of about 50 nm for an ion dose of about 10^{15} ions/cm² (10^5 ions/point) and remains nearly constant for a higher ion dose (c.f. figure 5-33). At this ion dose all layers down to the maximal penetration depth are defect-rich enough to be oxidized and uncover the next layer which will be oxidized, too.

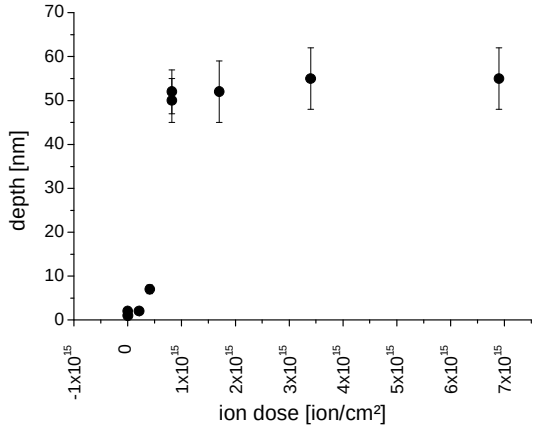

FIGURE 5-33: Depth of nano-cavities on SAMPLE 1 depending on the ion dose. For ion doses higher than 10^{15} ions/cm² the nano-cavities are oxidized completely and the depth does not change considerably.

The method of oxidation to measure the penetration depth was used in other studies, e.g. for size-selected silver clusters [134] or cesium ions [132]. Böttcher et al. observed a depth of about 50 nm in SEM images for an ion energy of 30 keV [148]. That shows the independency of the measured depth on the different preparation and observation methods. So, it makes sense to establish the maximal penetration depth of 35 keV gallium ions into HOPG to (50 ± 5) nm. In 6.1 the vacancy distribution will be discussed by simulations.

5.3.1.3 Beam characterization using nano-cavities

The shape of a nano-cavity can be used to investigate the beam profile of the FIB-tool. The lateral shape of the nano-cavity represents the distribution of the ions in the beam. In order to determine the localized ion intensity the depth of the nano-cavity should be smaller than the maximal penetration depth d_{max}, because otherwise the cavity depth is equal for the whole oxidized volume which would result in the same cavity shape for areas exposed with different local ion doses. Furthermore it has to be considered that the measured profile is influenced not only by the beam profile but also by the ion dose, oxidation process and measurement method.

The variation of the ion dose for SAMPLE 1 is a good method to find the best parameters for this measurement. Figure 5-34 shows two points exposed with different ion doses. Indeed both have the same triangular shape. However the ion beam profile is more visible in image (b). For image (a) the local ion intensity is not sufficient to build clearly visible nano-cavities with the chosen oxidation parameters. It is possible to discuss details of the beam profile with image (b). In this case the beam is split into 3 main beams marked with 1 in the image. All cavities are about 50 nm wide and 5 to 8 nm deep caused by a defocused beam. The real beam profile should be narrower than the cavity shape. The regions marked with 2 consist of many multilayer pits, which could be an indication for an adjustment of the stigmator lenses in one direction. Additionally the region marked with 3, which also consists of multilayer pits, could be an indication for another beam part with clearly lower ion intensity than the three main beams. This knowledge could be used to identify the critical points of the FIB tool and help its improvement.

For comparison figure 5-34c shows points exposed with optimized beam focus. The round shape and the constant distribution of nano-pits around them are indications for a good adjustment of focus and stigmator lenses.

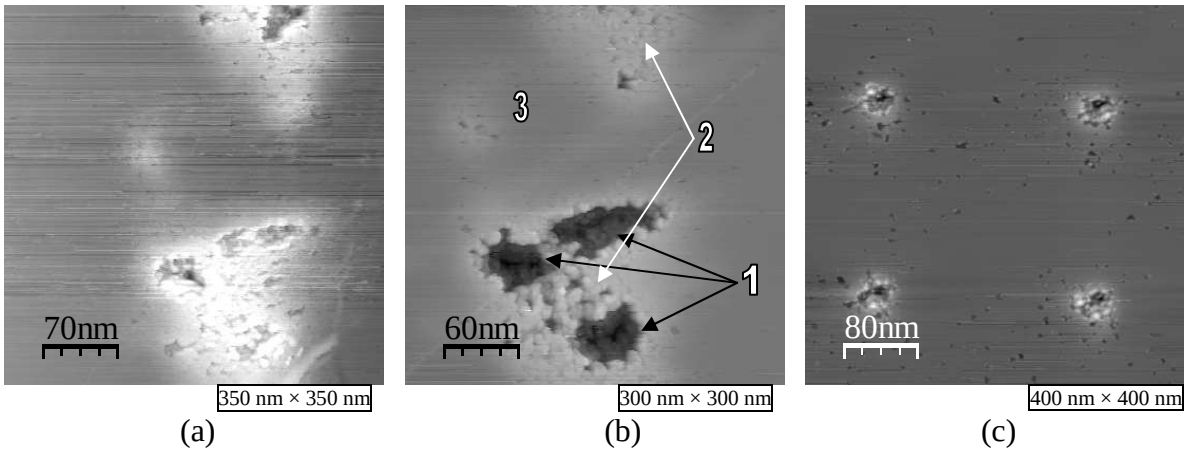

FIGURE 5-34: (a,b) STM images of two points on SAMPLE 1 (area 11 and 12) exposed with (a) 3.1×10^4 and (b) 6.1×10^4 ions/point. Both structures are produced at the same conditions. (c) STM image of points on SAMPLE 3 exposed with optimized beam focus. The used ion dose is 1870 ions/point.

5.3.1.4 Graphene nano-structures

"Fabrication"

In the last sections the high ion doses were used for patterning of nano-cavities but the same process can also be used to fabricate other structures. The graphite substrate is a stack of graphene layers. Using the nano-patterning of FIB in combination with oxidation a 'mesa-structure' can be divided from the surrounding graphite. Thus several free standing graphene layers can be isolated if they are separated in all lateral directions (figure 5-35a). Since the conductivity in the vertical direction is weak a patterning of these layers could enable nano-electronics based on graphene without preparation of single layers. Other groups are working on the transfer of graphene layers to other substrates. This is indeed not simple. The mean challenge is to find a matching stamp for which the attraction to graphene is higher than the interlayer attraction in graphite and furthermore the attraction stamp-graphene should be weaker than the substrate where it is transferring to. Liang et al. used glue like layers combined with temperature variation to manipulate the attraction ratios [149].

Here two exemplary devices are produced (figure 5-35b and c). Such *wave guide cross junctions* were investigated by Knop et al. [150,151] but for GaAs nano-structures. The idea is to use these structures for the ballistic transport of electrons, resulting in so called *ballistic electronic devices*. Since graphene layers support ballistic transport of electrons at higher temperatures (see 2.3) it would be the ideal material for this purpose. In the following these structures are calling X- or Y-structures for better reading. The ion energy for this experiment was 30 keV and the ion current was 13 pA which increased to 14.5 pA during exposure. The dwell-time for dose factor 1 amounts to 0.01 ms. The structures are exposed in area mode with an area step size of 20 nm. Four areas containing these structures are exposed with dose factors 10, 1, 3, and 7. The sequence represents the exposure chronology.

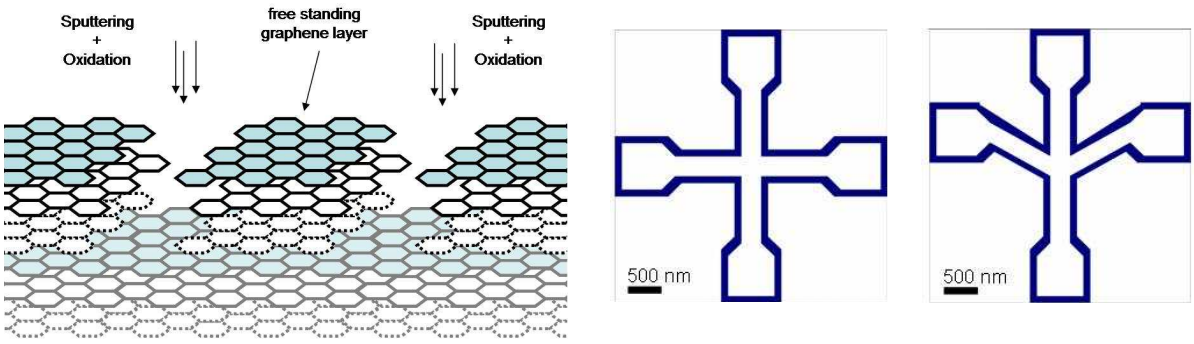

FIGURE 5-35: Schematic illustration for fabrication of free standing graphene layers. The sputtering and oxidation processes separate the middle part from the rest. (b-c) Graphical illustrations from FIB software for two structures (X and Y-structure) which are used as examples for graphene nano-structures. The filled area will be exposed with FIB. The width of this area is 100 nm. The width of the wave guides is 300 nm. The squares at the structure ends are provided for electrical connections.

"Ion Dose Dependence"

The results for two dose factors are displayed in figure 5-36. The biggest difference can be found between the different ion doses. For comparison the same X-structures exposed with different ion doses are shown in figure 5-37. The width of the wave guides for dose factors 1 and 3 are comparable. It amounts to 140-170 nm. For dose factor 7 it is decreased to 10-50 nm. In this case the wave guide is shrunken to a carbon wire. That is more visible in the high resolved SEM image in figure 5-38b. It shows untouched regions of the graphite surface and the etched region within the structure with a very high surface roughness. The very narrow carbon wire is not closed. However it shows the possibility of fabrication of carbon nano-wires.

For dose factor 10 both cases are observed. For some structures the width amounts to 80-100 nm and for others down to 10 nm. The reason for this is the change of the ion current during exposure which was caused by damaging of the used aperture with high number of gallium ions. Since this area was exposed first the areas exposed with other dose factors are written with the higher ion current. Consequently the effective dose for dose factor 7 is higher than for dose factor 10. However for all dose factors the width of the wave guides are smaller than the programmed one which was 300 nm. The width of the oxidized areas is about 200, 250 and 400 nm for dose factors 3, 4 and 10, respectively. This is a factor 2-4 more than the programmed width of 100 nm. That can be explained by a high ion dose and the subsequent oxidation.

"Roughness"

Another interesting aspect is the roughness of the waveguides. That is a very important point for a possible ballistic transport of electrons which is based on reflections at the side walls. In the case of a smooth wall more electrons would be reflected, but in the case of a rough side wall there will be an increased rate of backscattered electrons. The edge dependence of the electronic behavior is investigated by Akola et al. which have shown that the edge type (zigzag or armchair) or the edge roughness changes the DOS of a graphene layer [152,153].

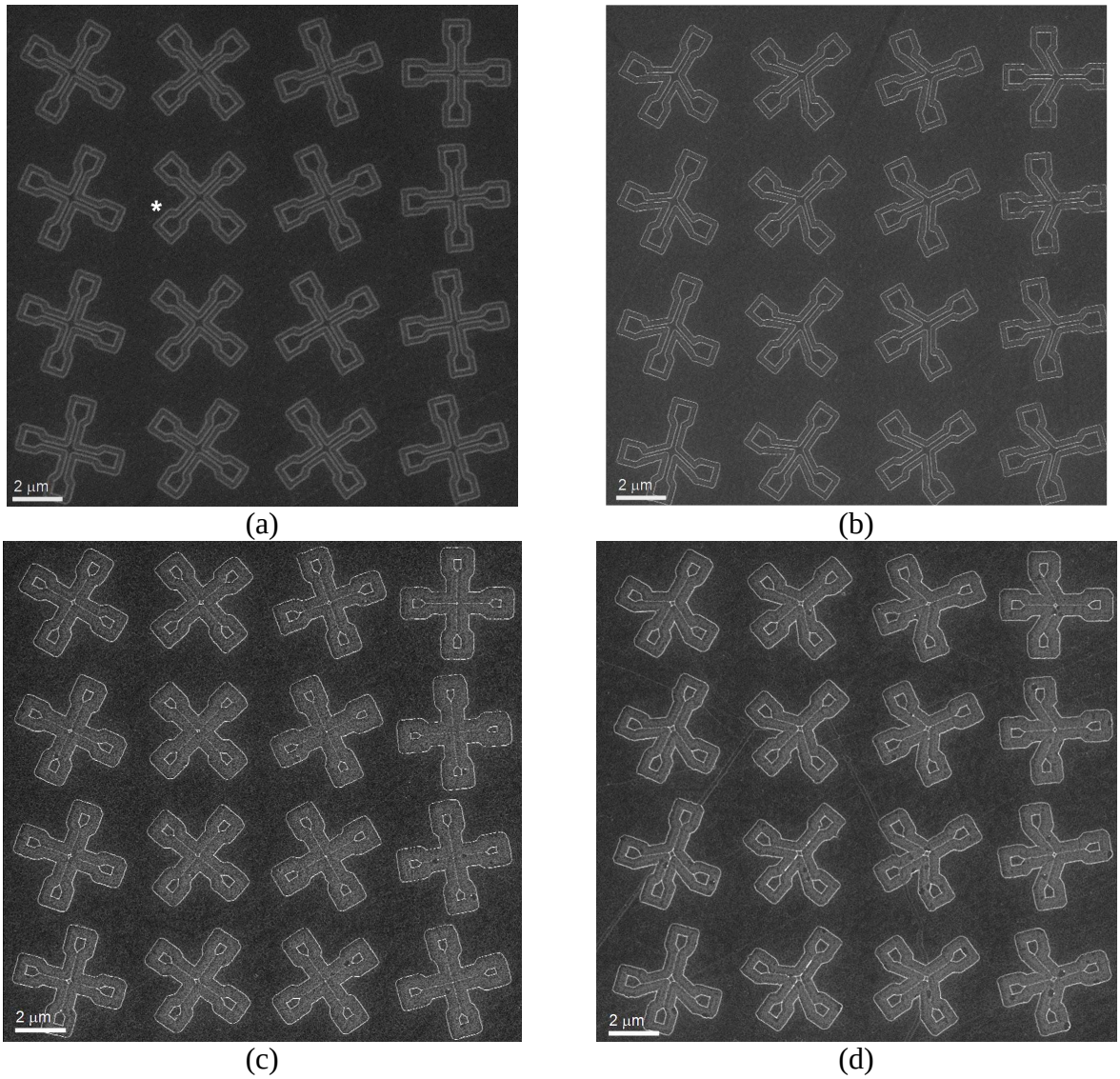

(a) (b)

(c) (d)

FIGURE 5-36: SEM images of SAMPLE 12 for both X and Y structures exposed with the dose factor 1 (a-b) and dose factor 7 (c-d). The structures are rotated in 5°-steps in order to investigate the dependence on the crystalline structure of the substrate.

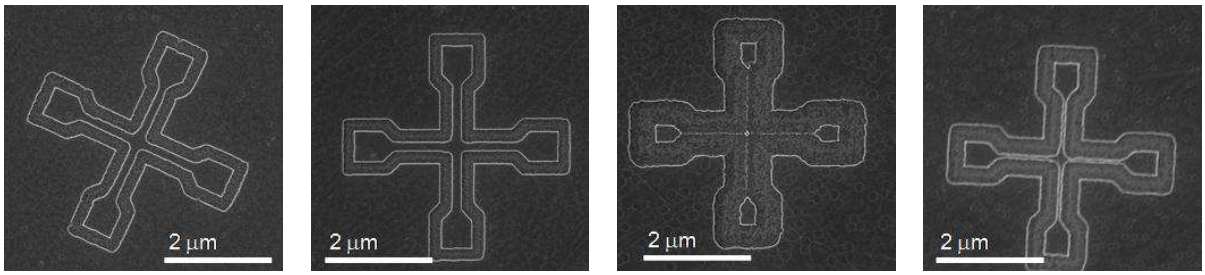

(a) (b) (c) (d)

FIGURE 5-37: SEM images of X-structures for the dose factors 1, 3, 7 and 10, respectively.

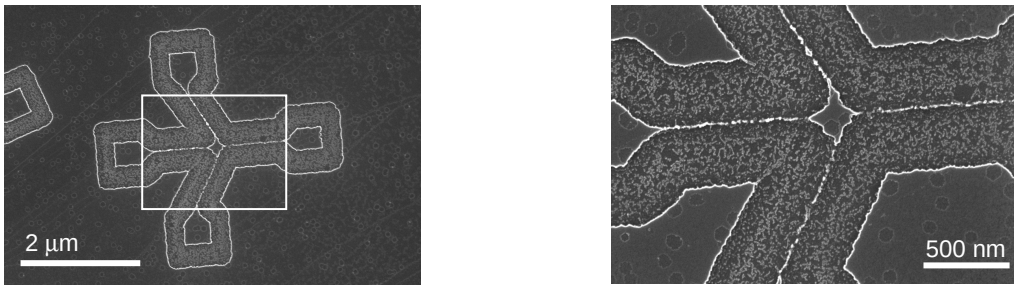

(a) (b)

FIGURE 5-38: (a) SEM image of a Y-structure written with a dose factor of 10. (b) is a high resolution SEM image of the middle part of the image (a). It shows the carbon lines in detail.

In the case of the structures produced here a very small roughness is observed for dose factor 3 (cf. figure 5-37). For dose factor 1 the roughness is less, too, but not as good as for dose factor 3. The sides of the structures written with dose factor 10 are very rough. Hence, dose factor 3 seems to be the best parameter for fabrication of structures with nearly smooth side walls.

The roughness is caused by two factors. Firstly the defect distribution at the structure borders which is caused by the ion distribution in the beam contributes to the roughness. For a high ion dose also the ions in the tails of the ion focus contribute. These ions do not exactly follow the pattern of the structure. Secondly the oxidation occurs at the defects and progresses circularly. A high defect density would result in a common frontline of the cycles. Thus the border side would be smoother. The roughness of the border sides is a result of the combination of these two counteracting effects. The dose factor 3 seems to be a good compromise.

"Substrate Dependence"

The X- and Y-structures in figure 5-36 are rotated in 5° steps to investigate the dependency of the crystalline structure of graphite on the etching process. That was previously reported by Böttcher et al. [154]. In the overview SEM images the structures seem to be equal. But some wave guides are slightly broader. As an example one of them is labeled with '*' in figure 5-36a. The limb at lower left side is broader than the others. This effect is proceeding to the upper X-structure. The reason for this is the parallel orientation of the wave guide and the six available directions of the graphite step edges (cf. figure 2-1). In this case the oxidation probability is lower due to the more stable bindings.

Furthermore the crystalline structure of graphite influences the roughness of the structure side borders. That is visible comparing the two X-structures labeled with (a) and (b) in figure 5-39. The wave guide along the arrow 1 exhibits a rough side border with a staircase like shape. In contrast the wave guide along arrow 3 is smoother. It is also parallel to the graphite step edges which are visible as thin white lines crossing the image. The orientation of step edges indicates the orientation of one of the six available stable crystalline orientations.

The step edges themselves are mostly not considered in the etch process, but sometimes they change the etch behavior. One of these locations is labeled with '*' in figure 5-39. The etch process proceeded along the step edge and has made a convexity in the structure. The reason for that could be the change of the orientation of the step edges which happens accidentally for this step edge in that region. The transition orientation may be not a stable one and promotes the oxidation process.

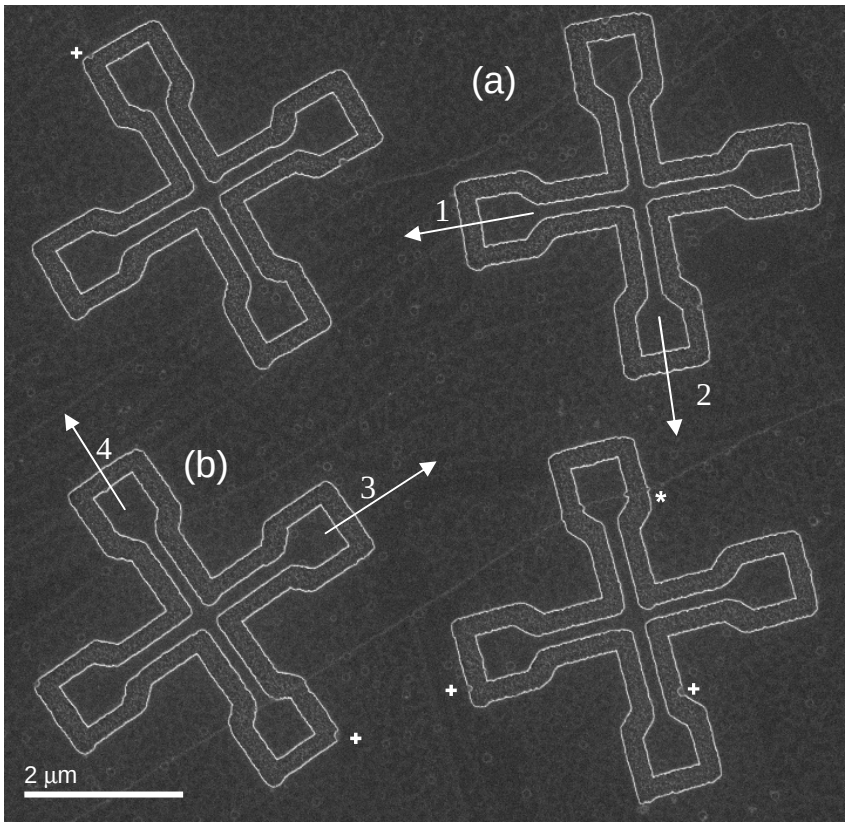

FIGURE 5-39: Four X-structures with different orientations. These structures are exposed with a dose factor of 1.

Furthermore some other defects seem to hinder the oxidation process and as result they make concavities in the structure. Some of these not rare concavities are labeled with '+' in figure 5-39. The origin of these defects is unknown. Probably they are impurities in the graphite substrate.

In summary graphene nano-structures with steep border sides can be produced using an *inverted patterning* and the oxidation method. The production of wave guides and carbon nano-wires is demonstrated. It is shown that the ion dose plays an important role not only for structure dimension but also for the structure roughness. Measurements of the electronic properties of such graphite mesa-structures are planned.

5.3.2 Island growth

In order to investigate the growth of larger structures in nano-cavities 30 ML gold was deposited on SAMPLE 1 at a temperature between 300 and 370°C. This effective coverage was estimated to fill the nano-cavities in area 14. The sample was covered with 0.4 ML silver for other experiments before (5.2.2.1). However, this small coverage can be neglected in comparison to the gold coverage.

Figure 5-40a shows the island growth on a free area without defects. The same behavior (figure 5-40b) shows area 5 structured with nano-pits (structured with low ion dose, cf. section 5.2.1.1). In both cases large gold islands are grown on the sample without any observable pattern. Figure 5-41 shows that the faceted areas of the clusters are distributed in a wide range. The height distribution shows the same behavior. Note that the height of the islands is given in absolute height, which is defined as difference between the highest

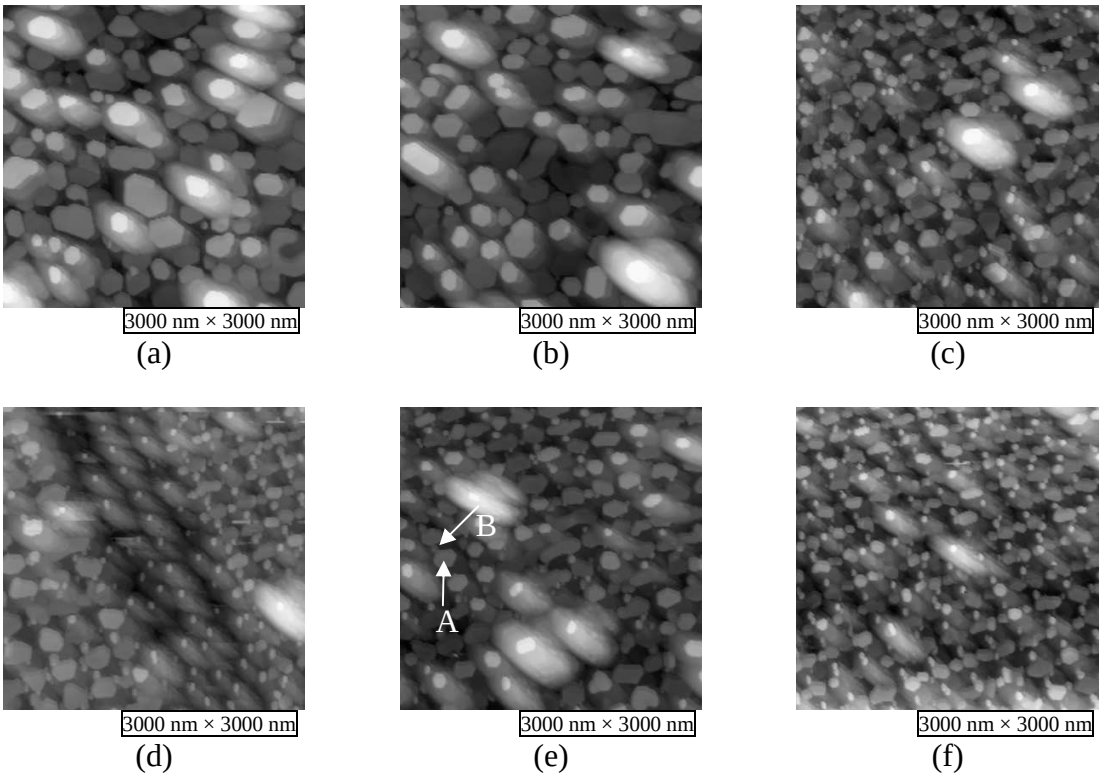

FIGURE 5-40: STM images of SAMPLE 1 after deposition of 30 ML gold. The images correspond to (a) free area, (b) area 5, (c) area 14, (d) area 15, (e) area 15, (f) area 16. The corresponding ion doses are listed in table 5-1. They show the dependence of island growth on the surface structure.

point on the gold island and the deepest point in the STM image. This analysis method is necessary, because it is not possible to determine the surface-level in the images due to few free spaces between the islands. This causes a maximum inaccuracy of a few nanometers.

Figure 5-40c shows the island growth on nano-cavities in area 14, which is structured with $D_{point} = 2.5 \times 10^5$ ions/point. In this area a pattern of gold islands can be observed. With increasing ion dose this pattern becomes clearer (figure 5-40d-f). Every point in the pattern consists of several islands. As shown in figure 5-31 the nano-cavities do not have a perfect shape. They consist of a main large cavity and a smaller one on the upper left side. The gold islands have the same pattern. The larger islands (labeled with A) are neighbored with smaller islands on the upper left side (labeled with B). Comparing the position of islands A relative to islands B with the corresponding nano-cavities it can be deduced that the islands are directly grown on the nano-cavities.

With this the island growth can be imagined as follows. First gold islands grow on the cavity edges and then they coalesce over the cavity and build a common island. Below this island a hollow could exist. An indication for this supposition is that, in comparison with the deposited gold coverage, the islands are larger as expected. That can be explained by comparison of the deposited gold coverage with the gold coverage needed to fill all nano-cavities up to the surface level. The latter value can be estimated from the oxidized volume of a nano-cavity. It yields a coverage of 35 ML gold for area 14. The calculated effective gold coverage for the islands yields 12 ML. Thus only 18 ML gold is located inside the nano-cavities assuming a sticking probability of 1.

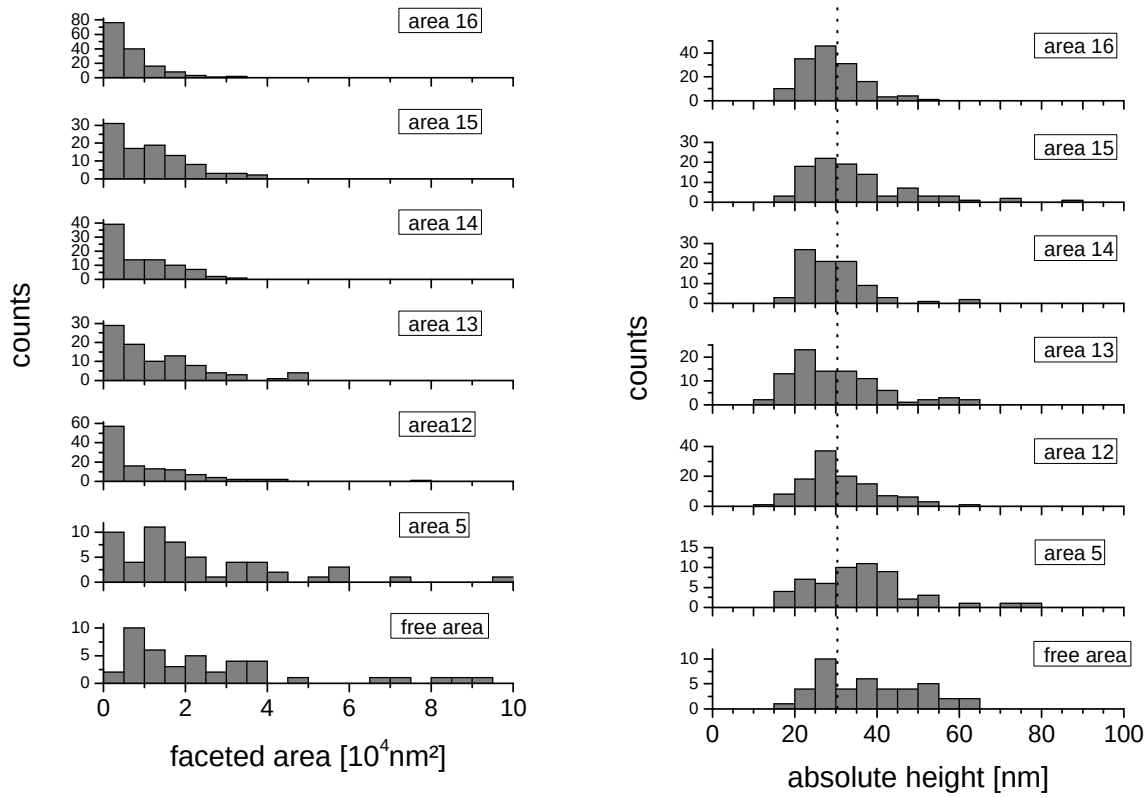

(a) (b)

FIGURE 5-41: Distribution of the faceted area and height of gold islands grown on SAMPLE 1 for the selected areas (compare with table 5-1). The height of the islands is given in absolute height, which is defined as difference between highest point on the gold island and the deepest point in the STM image.

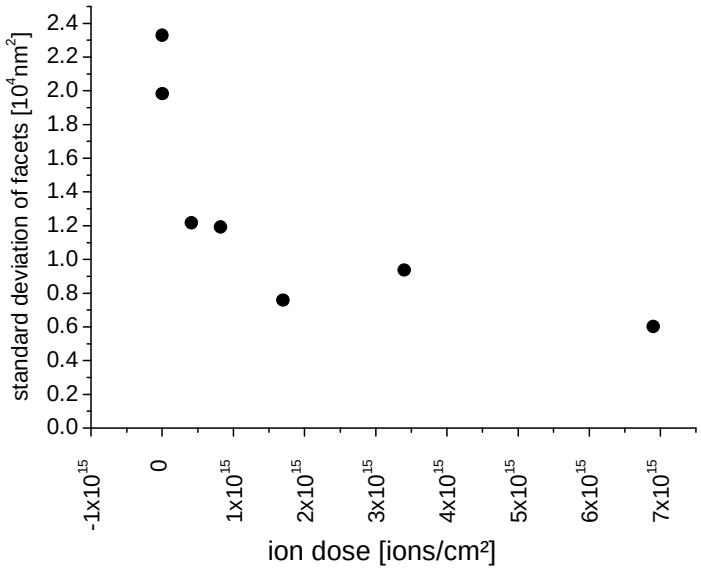

FIGURE 5-42: Standard deviation of the faceted areas deduced from the histogram in figure 5-41a. The reduction of the standard deviation is an indication for a narrower size distribution.

With increasing ion dose the faceted area becomes smaller and more uniform. This is visible in STM images and in the corresponding histograms in figure 5-41a. The trend of the distribution width can be extracted from standard deviation as shown in figure 5-42a. The standard deviation decreases for low ion dose below 10^{15} ions/cm². For a higher ion dose it does not change distinctly. Furthermore the width of the height distribution is smaller for the higher ion dose (figure 5-41b). The mean island height is about 30 nm for area 12 to 16 (dashed line).

These results clearly show that the patterning influences the size of the islands.

5.4 Cluster properties

An important aspect for structuring of nano-particles is the deposited material and its special properties. They influence the particle growth. Important aspects are surface diffusion, temperature dependence, desorption temperature and surface energy. These result in different particle properties, e.g. shape, particle mobility, stability in respect of temperature, air contact or a measuring probe like an STM tip, facet building or height distribution. A few of these points will be discussed in the next sections. The material investigated most extensively in this work is lead which will be discussed in more detail. The lead clusters are investigated concerning the height distribution, facet formation and their stability. Additionally silver clusters are investigated concerning the height distribution, facet formation and reactivity. Gold clusters will be discussed, too, but in less detail.

5.4.1 Gold clusters

Gold clusters were investigated in other studies [105]. It is a material which is very comfortable to handle. It is inert and does not oxidize. A sample covered with gold can be transferred in air without a great damage of the nano structures. Furthermore the grown clusters are stable concerning their interaction with the STM tip which results in a stable imaging.

Due to the high desorption temperatures of gold atoms, the deposition can be performed at higher temperatures leading to a larger diffusion length before desorption. That means a large range of temperatures is available to tune the cluster growth. Gold atoms form hexagonal faceted clusters. The cluster facet emerges for clusters higher than 1 nm. Standing waves were observed on these facets in STS maps [155]. Gold is especially suitable for production of larger particles as used for the experiments presented in 5.3.1.4. In order to force gold atoms into nano-cavities the sample can be annealed at temperatures up to 600°C.

5.4.2 Silver clusters

Silver is a very interesting material with respect to its electronic structure. It is a good approximation for a free electron metal. In many studies the electronic structure of silver clusters was investigated concerning their size. Silver has also very interesting optical properties. Therefore the patterning of silver nano-structures offers interesting perspectives for future applications.

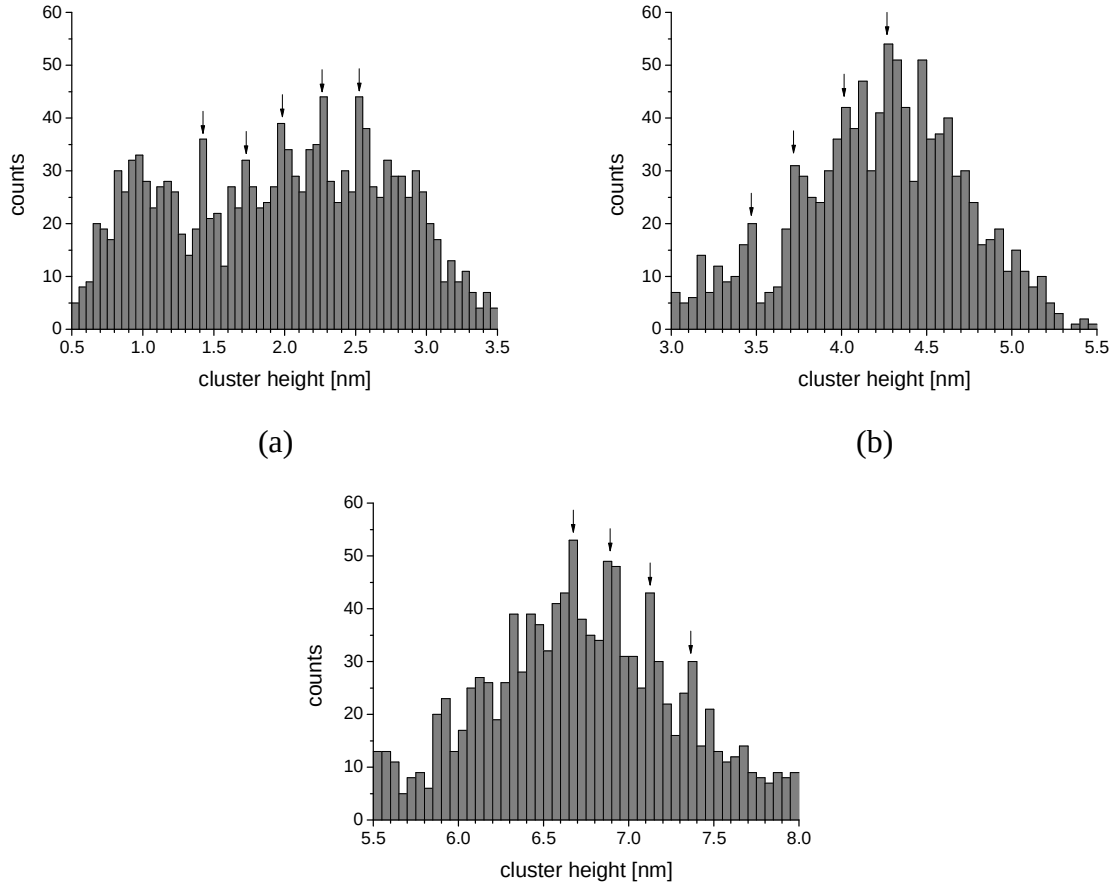

FIGURE 5-43: Height distribution of silver clusters after deposition of (a) 0.07 ML, (b) 0.27 ML and (c) 1.05 ML silver on SAMPLE A1 at 56 °C. The height distributions indicate peaks in the histograms. The peak distance is evaluated from the peaks marked with an arrow.

A sample structured with argon ions (without patterning) is used to investigate the growth properties of silver clusters. The silver atoms were deposited on SAMPLE A1 at 56 °C. The silver material was deposited in three steps as listed in table 4-3. The total coverage is 0.07, 0.27 and 1.05 ML, respectively. Additionally the results are compared with the results of SAMPLE 1 which was patterned with FIB and covered with 0.4 ML silver at room temperature. As mentioned before, this sample was transferred to the LT-System for STM measurements after a short air contact and transport in a desiccator.

5.4.2.1 Cluster height

The height distribution of silver clusters grown on SAMPLE A1 is shown in figure 5-43. The silver deposition and the investigation with the STM were performed in UHV. The heights have a Gaussian distribution as a global shape. The mean cluster height amounts to 2, 4.3 and 6.2 nm for the corresponding deposition steps. At a closer look many peaks are visible in the distributions. Indeed the peaks mostly are not much higher than the noise of the Gaussian distribution, but they can be identified as periodical peaks. To distinguish the peaks from the statistical noise the peak counts have to be about $2\sigma = 2\sqrt{N}$ higher than the bins beside the peak, e.g. a peak with 40 counts has to be 13 counts higher. Thus the peak exists with a probability of 95.45%. The most prominent peaks are marked with an arrow in the histograms. They can be used to determine the peak pitch d_{peak} using the formula 15.

$$d_{peak} = \frac{h_{last} - h_{first}}{N_{peaks} - 1} \tag{15}$$

For example, in figure 5-43a there are 5 peaks between 1.425 and 2.525 nm. That results in a mean peak distance of 0.28 nm. The same calculation results in 0.27 nm and 0.23 nm for histograms in figure 5-43b and c, respectively.

5.4.2.2 Cluster facet

The shape of the silver clusters is observed in the STM images shown in figure 5-44a-c. To measure the cluster facet, the cluster is cut at a height 0.143 nm below the cluster top. This value is estimated to be smaller than the height of one monolayer silver and high enough to get the whole faceted area. Thus only the last atom layer on the top of the cluster contributes to the measured area. This area corresponds to the cluster facet. The corresponding histograms are shown in figure 5-44d-f.

After deposition of 0.07 ML silver, clusters are grown on nano-pits or at step edges (figure 5-44a). Many nano-pits are covered with silver particles with a height of a few monolayers. No cluster facet can be observed in this image. Hence, the facet distribution exhibits a large peak around 0 nm².

99% of the facets are smaller than 10 nm². This value is a result of the tip influence on the cluster shape. It indicates that the computed facet area is only relevant for values higher than the *smallest facet detectable* A_{min} = 10 nm².

A deposited silver coverage of 0.27 ML results in higher clusters but mostly without a facet. The fraction of cluster facets > A_{min} is 3%. Only for a silver coverage of 1.05 ML the clusters are truly faceted with areas up to 80 nm² (figure 5-44f). They have a hexagonal shape which is typical for a (111)-facet. The fraction of cluster facets > A_{min} reaches 50%.

In figure 5-45 the mean faceted area is calculated in dependence on the cluster height for all silver clusters. In this image only facet areas over A_{min} are relevant. This value is reached for a height of about 5 nm. The maximum is between 6 and 7 nm, which equals to the maximum in the height distribution for 1.05 ML Ag. Then the cluster facet becomes smaller since the clusters with a height larger than 9 nm do not have enough material to build a large facet.

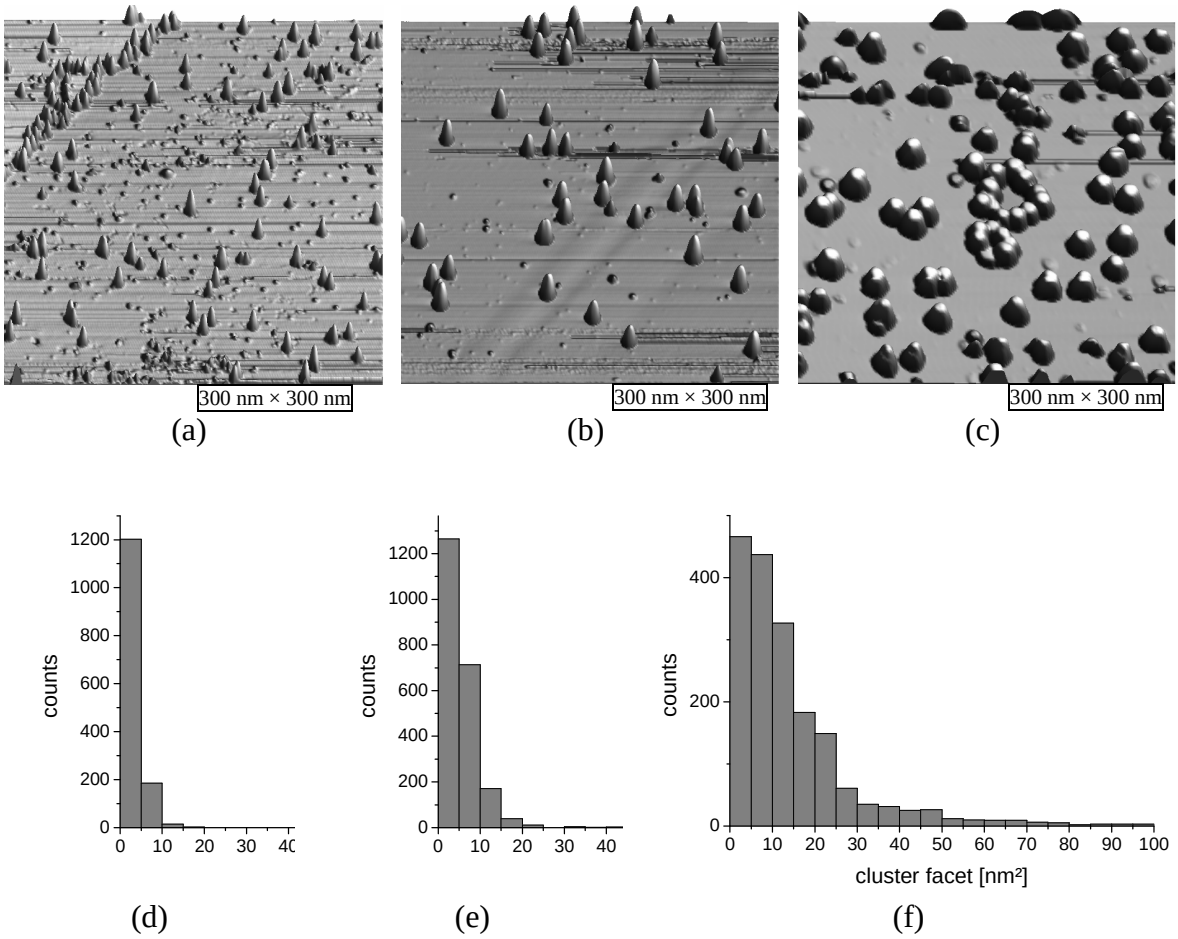

FIGURE 5-44: STM images on the top show the shape of the silver clusters after room temperature deposition of (a) 0.07 ML, (b) 0.27 ML and (c) 1.05 ML silver. The histograms on the bottom show the facet distribution of the silver clusters for (d) 0.07 ML, (e) 0.27 ML and (f) 1.05 ML silver.

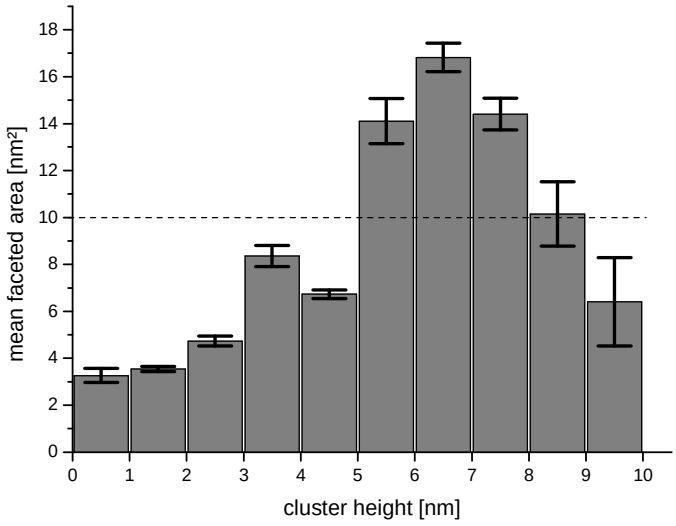

FIGURE 5-45: Dependence of the mean faceted area on the cluster height for all deposition steps. The faceted area increases with the height up to a height between 6 and 7 nm. Then it decreases for higher clusters. The dashed line marks the smallest facet detectable A_{min}.

5.4.2.3 Cluster stability

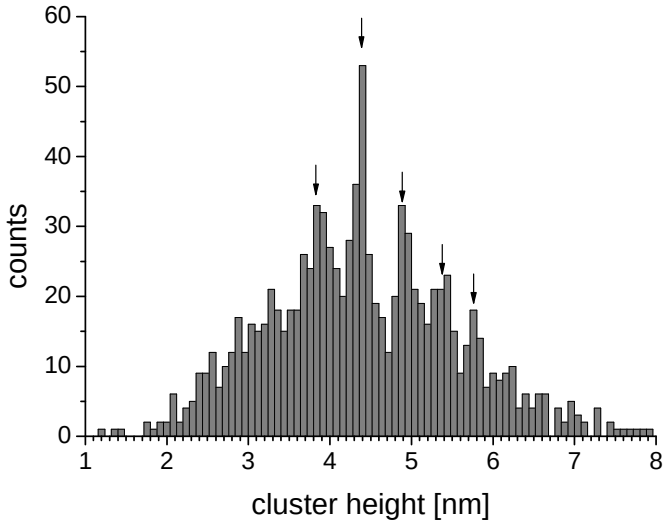

FIGURE 5-46: Height distribution of silver clusters after deposition of 0.4 ML silver at room temperature on SAMPLE 1. The sample was transferred to the LT-system for STM measurements after a short air contact and transport in a desiccator. The histogram indicates prominent peaks. The statistically relevant peaks are marked with arrows.

The silver clusters grown on SAMPLE 1 which were transferred in air after deposition of 0.4 ML silver can be compared to the results of the last sections. This can be used to figure out whether the clusters were contaminated by the short air contact. The cluster heights globally exhibit a Gaussian distribution (figure 5-46). The maximum is about 4.3 nm. The same height was observed for clean silver clusters but for a coverage of 0.27 ML.

The temperature difference is not large enough to cause this difference. Another explanation is the change of the cluster composition. The clusters may be contaminated, e.g. with oxygen or sulphur. Thus the cluster shape and its dimensions have been changed. In this case the measured cluster heights become smaller.

Similar to clean silver clusters the height distribution of these clusters exhibits a peak fine-structure. The most prominent peaks selected with the same assumption as explained in 5.4.2.1 are marked with arrows. The peak pitch evaluated with equation 15 amounts to 0.48 nm. This value equals to about 2 ML of bulk silver. That may be another indication for the contamination of the silver clusters.

5.4.3 Lead clusters

Lead is a very reactive metal with a melting point at 327 °C [115]. At low temperatures superconductivity is observed [156]. The deposition at various conditions especially at different temperatures leads to very different lead structures. In the present study the morphology of lead clusters is in the center of interest. The relative strong interaction between graphite and lead clusters simplifies the production of patterned nano-structures. To understand the growth behavior of these clusters they are investigated in respect of their height and facet. The change of the cluster shape is discussed in the following subsections.

5.4.3.1 Cluster height

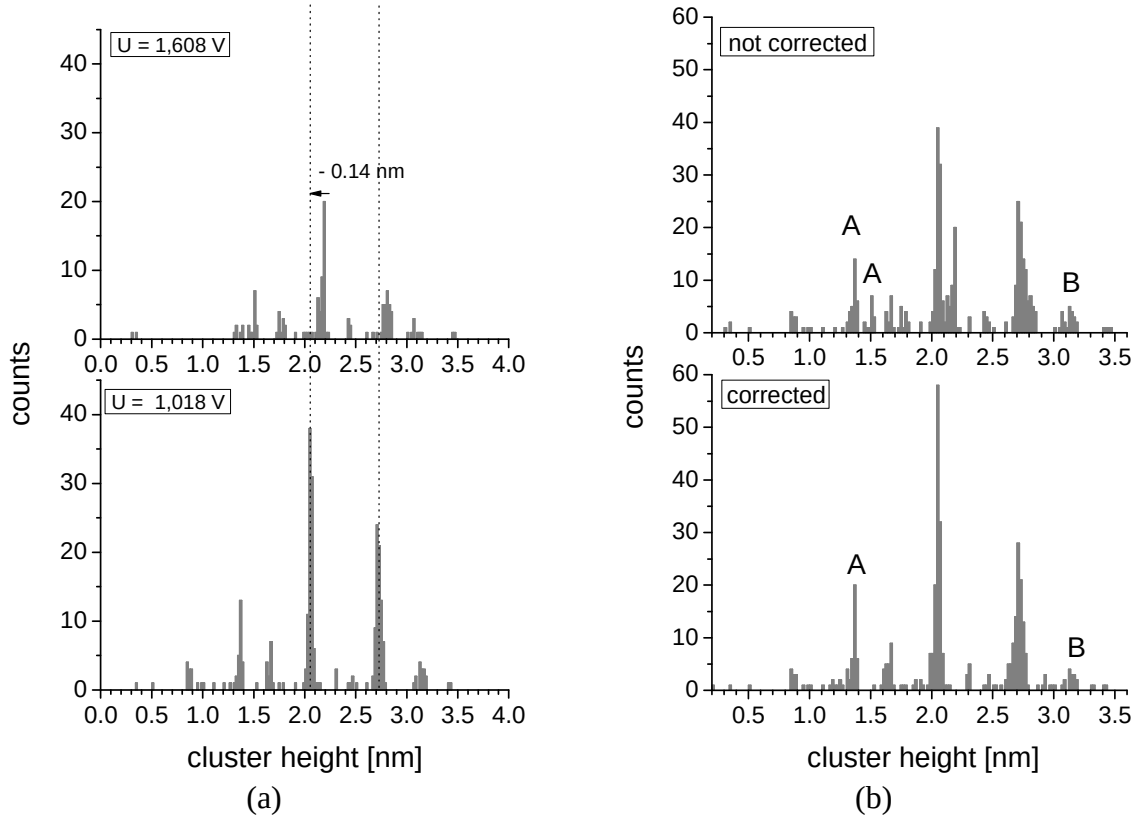

FIGURE 5-47: (a) Cluster height distribution after deposition of 0.28 ML lead on SAMPLE A2 for two different gap voltages. The change of voltage causes a shift in the cluster height. This is visible in the peaks, especially for the 2.1 nm peak. It is shifted about 0.14 nm. (b) The change in the cluster heights results in a peak splitting as shown in the upper histogram. As a result of the correction of peak positions well separated narrow peaks are obtained as shown in the bottom histogram.

"Height Corrections"

In order to get acceptable STM results it is unavoidable to change the tunneling parameters, especially the gap voltage and the feed back current. This is often necessary because the tip shape changes during the STM measurement and only with other parameters the measurement becomes possible. Earlier experiments have shown that the measurement of cluster heights in STM depends on the gap voltage between tip and sample. In reference [157] the cluster heights of two individual clusters were measured for different gap voltages. A systematic decrease of the cluster height by about 0.4 nm was observed for gap voltages up to 4 V. For a high accuracy in the distribution it is therefore necessary to have the same tunneling parameters for all measurements. Often this is not possible.

However, sometimes it is possible to correct the gap voltage induced shift. This is only feasible if the shift can be clearly identified as a consequence of the voltage change. For example the height distribution of one sample is shown in figure 5-47a. For a gap voltage of 1.608 V a peak can be identified at 2.19 nm, which shifts to 2.05 nm for 1.018 V. The whole distribution is shown in the upper histogram in figure 5-47b. A correction of the cluster heights measured with 1.608 V results in clear narrow peaks (lower histogram in figure 5-47b). This correction method is used for the histograms in figures 5-48b, 5-48c and 5-49a.

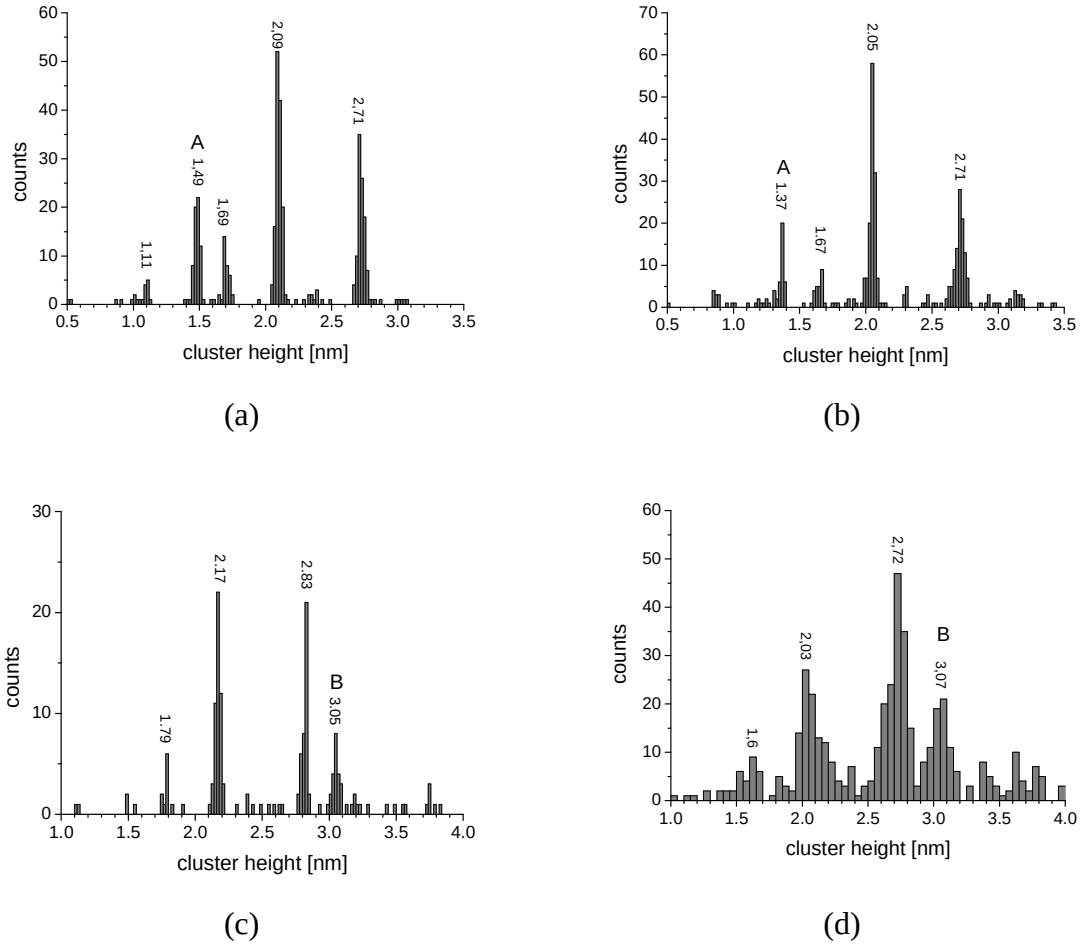

FIGURE 5-48: Height distribution of lead clusters grown on SAMPLE A2. The total deposition coverage of lead amounts to approximately (a) 0.14 ML, (b) 0.28 ML, (c) 0.42 ML and (d) 0.56 ML. The deposition temperature is about 40° C. Different bin sizes are chosen due to different measurement qualities.

One may assume that all histograms can be corrected in that way but some requirements have to be complied. For this, well identifiable features have to exist which can be used as reference. That is fulfilled for lead clusters which exhibit a clearly visible peak structure in the height distribution. But often a correction is not possible because the peaks are not visible due to poor statistics. Furthermore a systematic dependence of the cluster height on the gap voltage was not visible in all STM images. That indicates that also the tip shape influences the height measurement. That means, the cluster height can be shifted at the same gap voltage if the tip shape has been changed, e.g. after tip-preparation or collision with a surface structure.

"Clusters on Ar Sputtered Samples"

Figure 5-48 shows height distributions of lead clusters grown on a sample, which was structured with argon ions and oxidized. Each histogram corresponds to a certain coverage of lead. The mean cluster heights amount to 2.06, 2.19, 2.43 and 2.55 nm for 0.14, 0.28, 0.42 and 0.56 ML lead, respectively. Note that the cluster heights in histogram (c) are shifted about 0.12 nm to higher values. Two most prominent peaks are observable in all histograms at approximately 2.05 and 2.71 nm. The count rate at 2.05 nm is larger than at 2.71 nm for the first deposition steps but becomes smaller for the last deposition steps.

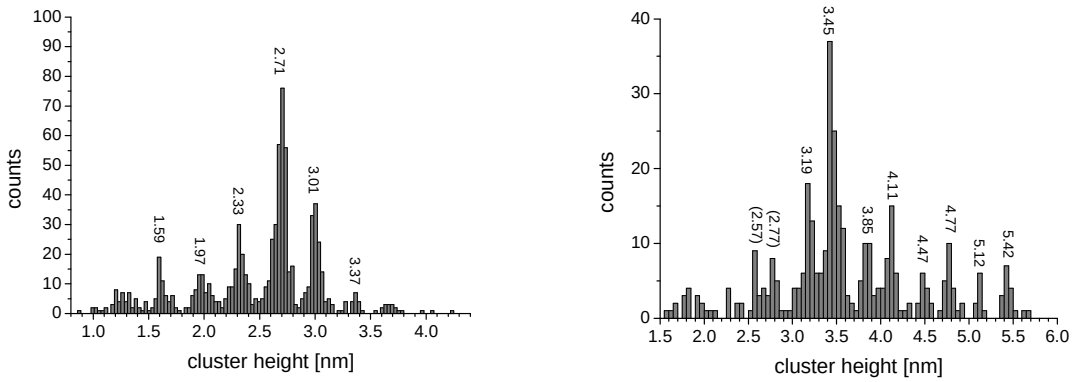

(a) (b)

FIGURE 5-49: Height distribution of lead clusters on SAMPLE 10 after room temperature deposition of (a) 0.14 ML and (b) 1.36 ML (total coverage of 1.5 ML) lead. The sample is annealed at 100°C for about one hour.

Another interesting feature in the histograms is that two peaks are shifted independently from other peaks. They are labeled with A and B in the histograms in figure 5-48. Peak A is located at 1.49 nm in histogram a and at 1.37 nm in histogram b. The difference is equal to the correction value of 0.14 nm. Peak B is located at 3.05 nm in the histograms c and d although other peaks in these histograms are shifted. The shifts in the height distribution seem to depend on the cluster height. In this case one can distinguish between two groups of cluster heights. This effect contributes to a broadening of the peaks especially in the summarized histograms.

"Clusters on FIB Structured Samples"

Two other samples are investigated in respect of the height distribution. Both samples were pre-structured with FIB. The coverage for both samples is 0.14 ML lead. That is comparable to the first deposition step of the sample discussed above.

The cluster height distribution for SAMPLE 10 is shown in figure 5-49a. The sample was annealed at 100° C after the deposition. The mean cluster height is 2.49 nm. This is comparable with the highest coverage for SAMPLE A2 (0.58 ML). That may be caused by a lower deposition temperature and by the annealing process. The subsequent annealing seems not to cause a noticeable desorption of the lead material. The Gaussian distribution of the clusters is here clearer observable. This may originate from Ostwald ripening (see page 55).

The height distribution of the lead clusters on SAMPLE 11 is shown in figure 5-50. This time the lead atoms were evaporated at 55 °C and the sample was not annealed after the deposition. The mean cluster height is 2.18 nm. This is comparable to a deposition coverage of 0.28 ML for SAMPLE A2 despite the nearly identical preparation. That may be caused by a higher nano-pit density. Four peaks with nearly equal counts can be identified which are similar to the most prominent peaks for SAMPLE A2 and SAMPLE 10 (with an overall shift of 0.04 nm). The height distribution seems to deviate from a Gaussian distribution. That is unusual for self organization growth processes.

To observe the peak evolution for higher clusters the total coverage of lead on SAMPLE 10 was enhanced to 1.5 ML (figure 5-49b). The sample was annealed again at 100°C. The result is a mean cluster height about 3.59 nm. The most prominent peak is located at 3.45 nm. The counts of most of the peaks are too small for a detailed analysis but one can see that the peak structure continues for higher clusters.

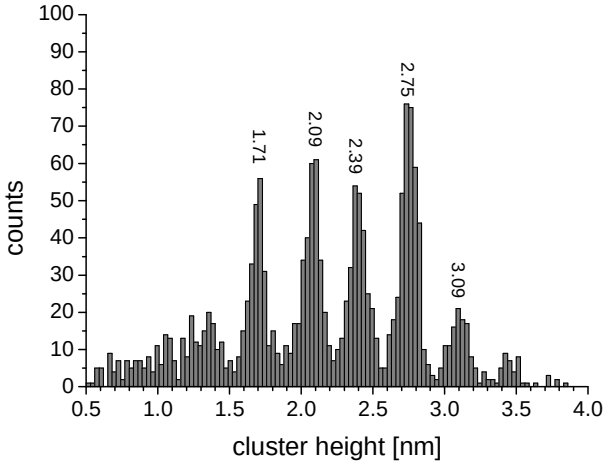

FIGURE 5-50: Height distribution of lead clusters grown on SAMPLE 11. The deposition coverage is 0.14 ML and the deposition temperature is 55°C. 4 peaks with nearly equal counts are visible between 1.5 and 3 nm. The mean peak pitch is 0.35 nm.

"Summarized Histograms"

The histograms are summarized for SAMPLE A2 and SAMPLE 10 in figure 5-51a and b. The single histograms are shifted in such a way that the most prominent peaks have the same position. The histogram in figure 5-48d is left out due to the broadened distribution. Since the total cluster count in each histogram is different, the mean cluster height in the summarized histograms is not relevant.

The most obvious feature is the missing peak at 2.33 nm in figure 5-51a. The deposition conditions such as equipment, temperature or deposition rate are always the same. Thus it can be concluded that it is a special property of the HOPG sample or the preparation procedure of the nano-pits. The specification of the HOPG substrate properties is not simple and very time consuming. All substrates are cut from a large HOPG sheet. However the HOPG surface for each tape-cleaving can be different.

Another possible reason is the nature of the produced nano-pits. SAMPLE A2 exhibited a high nano-pit density and the nano-pits had a narrow size distribution. In contrast the samples structured with FIB exhibited a broad distribution of nano-pit width and depth (c.f. figure 5-3, page 33). In these samples a lot of weak- or non-oxidized defects were also observed. This growth behavior is caused by the distribution of the defects with a high local ion intensity. Also the interaction cross section of the argon and gallium ions may be different. That may influence the cluster growth. Furthermore the role of the gallium atoms which remain in the inner layers are not clear.

The sum of all histograms for all three samples results in the histogram shown in figure 5-51c. Every second peak between 1.6 and 3 nm has fewer (more) counts primarily caused by SAMPLE A2. However the other two samples exhibit weakly similar effects. In figure 5-50 the peaks at 1.71 and 2.39 nm have fewer counts than the peaks at 2.09 and 2.75 nm. For SAMPLE 10 this effect is not visible because of the annealing process. A similar behavior can be observed in figure 5-49b for larger clusters and was also observed in other studies for lead layers [158]. The peaks between 1.6 and 3.5 nm are more relevant for a detailed analysis here.

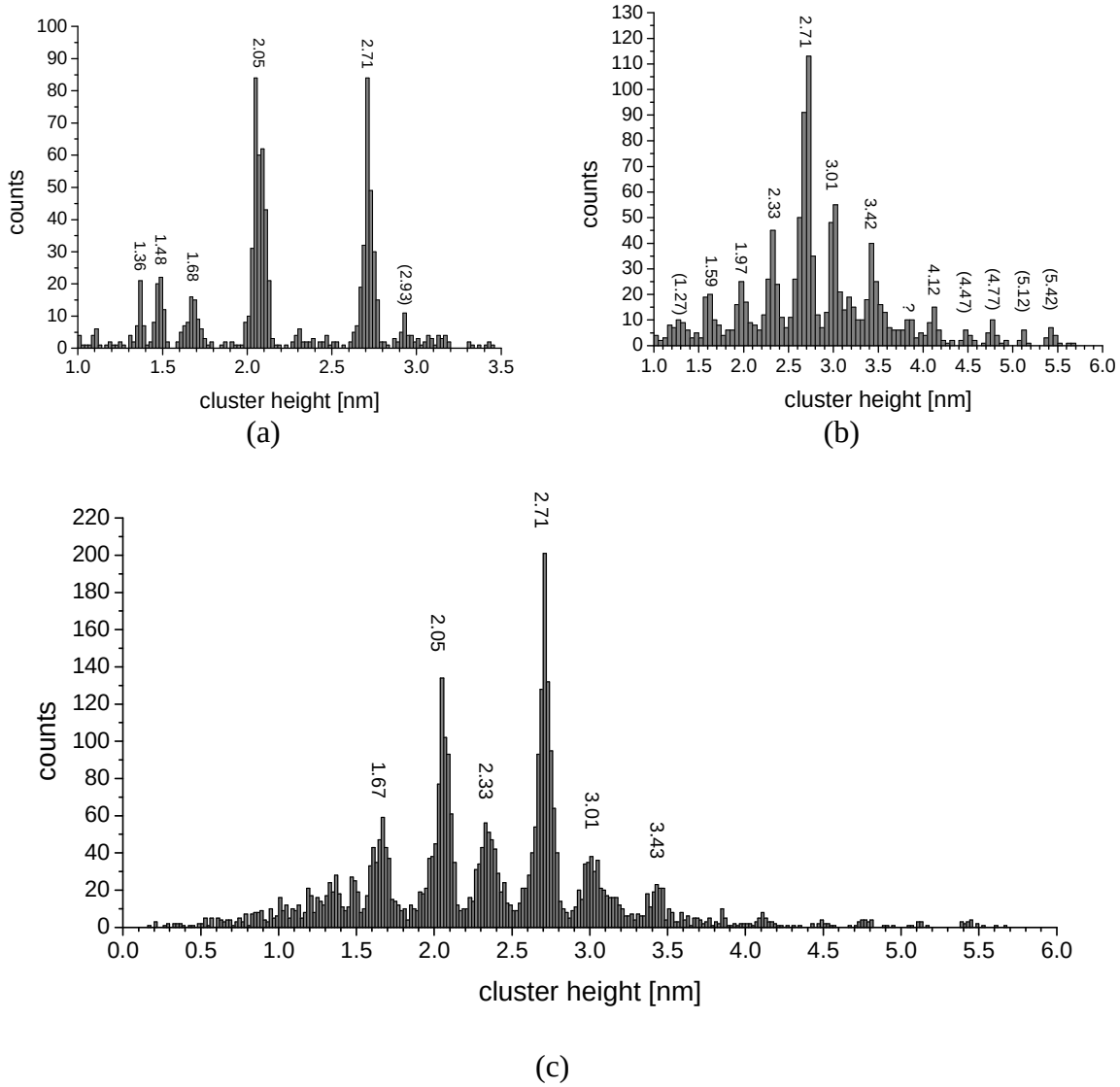

FIGURE 5-51: (a) Height distribution of lead clusters on SAMPLE A2 for the first three deposition steps. (b) Height distribution of lead clusters on SAMPLE 10 for both deposition steps. (c) The total height distribution of all three samples (SAMPLE A2, SAMPLE 10 and SAMPLE 11)

"Odd-Even Effect"

The cluster height values of the mentioned peaks are plotted versus the peak number in figure 5-52a. The fitted line has a slope of 0.345 nm. An interesting point is the deviation of the measured data from the fitted line which represents the cluster heights for equal peak pitch. In most of the histograms the peak pitch is not exactly equal. That effect is clarified in figure 5-52b where the fitted line is subtracted from the peak position. It shows a zigzag progression. Every second peak is higher (smaller) than the fitted line.

This *odd-even oscillation* can be explained with quantum well states (QWS). This effect is treated in detail in reference [159] for thin freestanding Pb(111) layers. The energy distances of the QW-states decrease for thicker lead layers (figure 5-53). The distance of the highest occupied state to the Fermi level is not always equal; it oscillates with counts of atomic layers (odd-even oscillation). This behavior is also reflected to surface energy and work function. In contact to the surface this behavior changes slightly but the oscillation is always present (see reference [160] for Pb layers on Si). The progression of the quantum

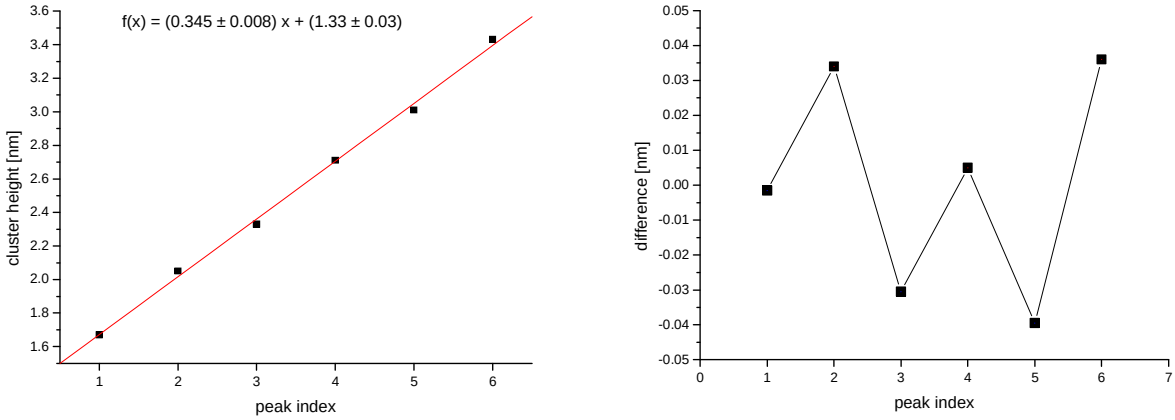

(a) (b)

FIGURE 5-52: **(a) Cluster height versus peak index for five most prominent peaks which are marked in figure 5-51c. The fitted line yields a slope of 0.345 nm which is equal to the peak pitch. The offset is nearly equal to 4 × 0.345 nm (1.38 nm). (b) The difference between the measured heights and the fitted line exhibits a zigzag evolution.**

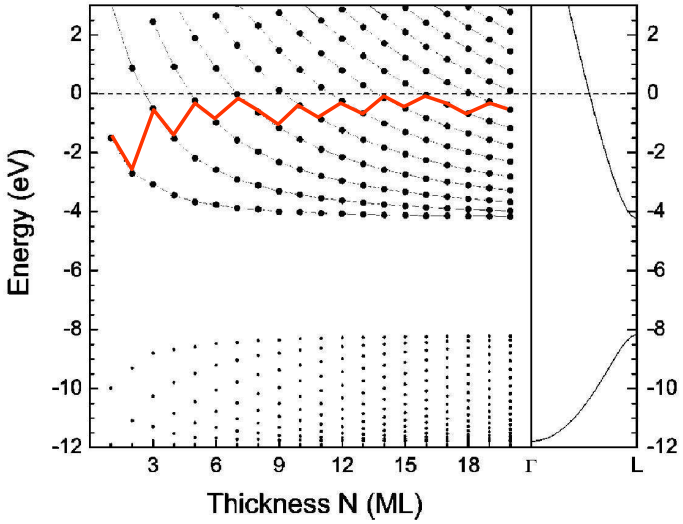

FIGURE 5-53: **Quantum well-states of a thin Pb(111) film as a function of thickness (taken from [159]). The energy at the Fermi level is set to zero.**

well states with the thickness of lead layers influences the tunneling current in the STM measurement. Altfeder et al. have investigated a lead layer on silicon step edges with STM and STS [161]. They observed in an STM measurement that the surface of a lead island is structured in a sequence of bands depending on the local island thickness.

In our STM measurements a positive sample bias is used, i.e. electrons tunnel from the occupied states of the STM tip into the unoccupied states of the sample (cf. figure 3-12a). In a simple model the tunneling into states which are nearer to the vacuum level E_v involves a smaller barrier. Hence, the smaller the energy distance between an unoccupied state of the sample and the Fermi level of the tip is (with $E < E_{F,tip} = E_{F,sample} + eV$) the higher is the probability of the tunneling effect which results in a higher tunneling current. Thus the odd-even oscillation is reflected in the tunneling current.

The odd-even oscillation is also correlated with the favored cluster heights. As mentioned above the odd-even oscillation also appears for surface energy. The clusters with lower surface energy should be more stable and thus more favored. Thus every second cluster height is more present, which is observable in the histograms as peak with more counts.

5.4.3.2 Cluster facet

"Clusters on Ar Sputtered Samples"

The formation of facets on lead clusters is observed on most of the samples. But they do not always have the same facet shape. Figure 5-54 shows the formation of cluster facets for four equal deposition steps. The deposition temperature was 40 °C (close to room temperature). Many clusters have already a small facet at the first evaporation step. Histogram (e) indicates that 47% have a larger facet than A_{min} which is defined in 5.4.2.2 as 'smallest facet detectable'. This is visible in the histogram as well as in the corresponding STM image. The cut 0.135 nm from the highest point of clusters with facets > A_{min} indicates a hexagonal shape. For 0.28 ML lead 98% and for 0.42 ML lead 93% of the clusters are faceted.

For the highest lead coverage of 0.56 ML 73% overtop the value A_{min} although in the STM image all clusters seem to be faceted. That is because many clusters are not imaged well in this measurement run. The interaction with the STM tip caused a motion or damage of the clusters and their facet. As result some clusters are not imaged completely. That effect appears in histogram (h) in the form of a peak between 0 and 5 nm². However the cluster facets indicate a clear hexagonal shape for this coverage.

"Clusters on FIB Structured Samples"

In another experiment the clusters were grown at room temperature but the sample was annealed at 100°C, afterwards. The corresponding results are shown in figure 5-55 for 0.14 and 1.36 ML lead. In the first deposition step the clusters do not form facets, although in histogram (c) there are many clusters with a facet > A_{min}. Actually in this case the facet measurement is modified by the tip influence. The top of each cluster has a double structure in a very small distance which together are erroneously identified as one facet. This effect can be observed for all clusters, but it can not be corrected in the analysis. It doubles the value of the faceted area if the analysis method in section 3.2.4 is used. Thus the value A_{min} has to be increased to 20 nm² for this measurement (that effect is not observed for the higher coverage). With this only 8% of the clusters indicate a small facet although the clusters are on average higher than the clusters in figure 5-54a.

For the higher coverage the clusters predominantly form a triangular facet after the annealing process. This shape can be explained by the crystalline structure. In a model which proceeds on a truncated octahedron for faceted clusters the side facets are (111) and (100) alternately (cf. [105]). Since the cluster facet is a (111) facet and the transition from (111) to (111) is more favored than from (111) to (100), every second side is larger in the equilibrium case. Thus the facet shape seems to be triangular. In the histogram in figure 5-55d 99% of the clusters have facets > A_{min}.

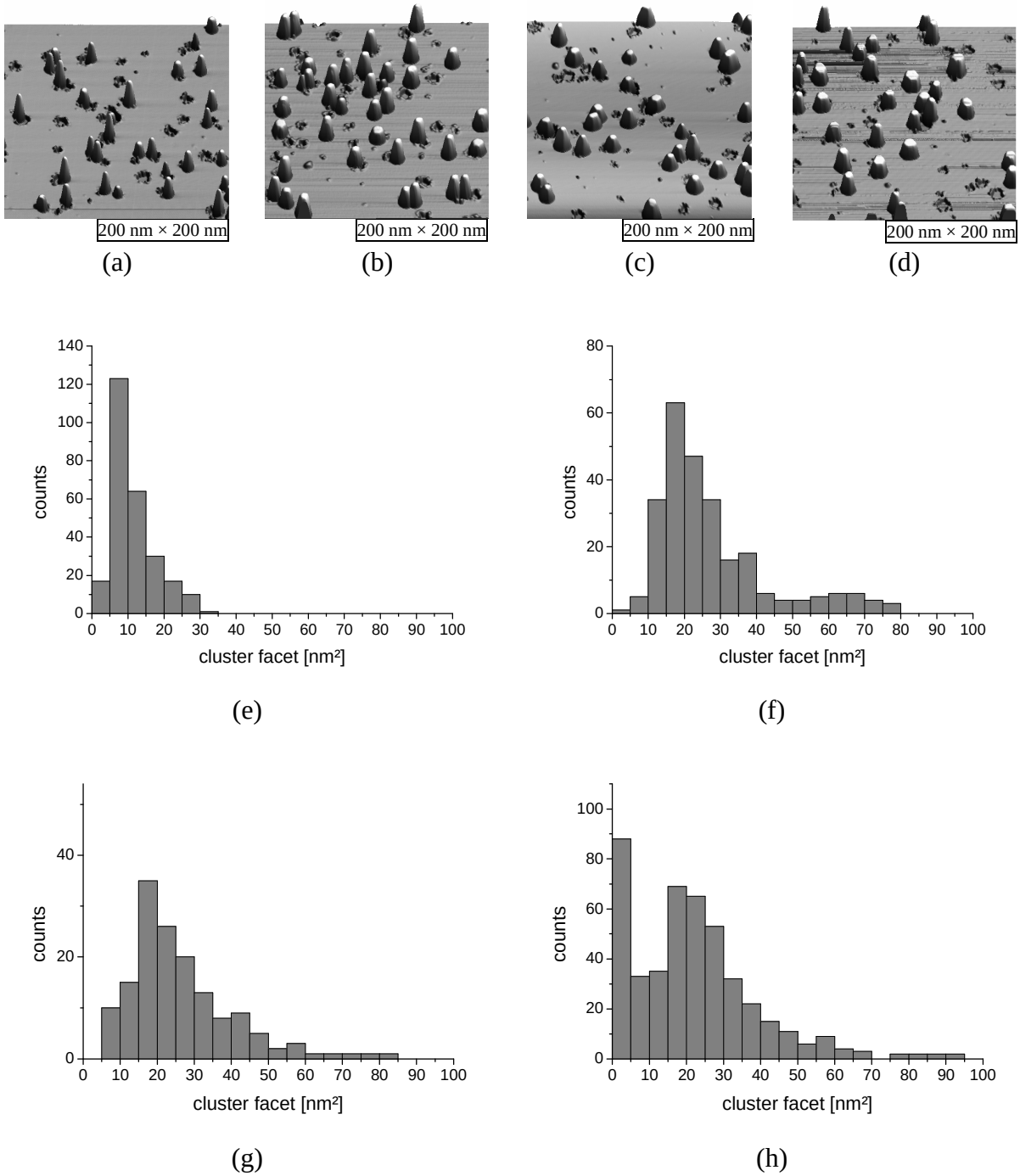

FIGURE 5-54: (a-d) STM images for 0.14 ML, 0.28 ML, 0.42 ML and 0.56 ML lead on SAMPLE A2. The images show the successive formation of cluster facets. The corresponding distribution is shown in histograms (e-h). For the first deposition steps small cluster facets are already observable. For the highest coverage large hexagonal facets are formed.

"Height Dependence"

In figure 5-56 the dependence of cluster facet on the cluster height is shown for both samples. The facet of lead clusters is formed for clusters higher than 0.5 nm. For annealed clusters the facet is not formed below 1 nm. The decrease of facets for higher clusters is caused by the limitation of the deposited material. Thus the facet of the highest clusters can not grow. The facets of clusters with a height between 0.5 and 2.5 nm are larger for the not annealed sample.

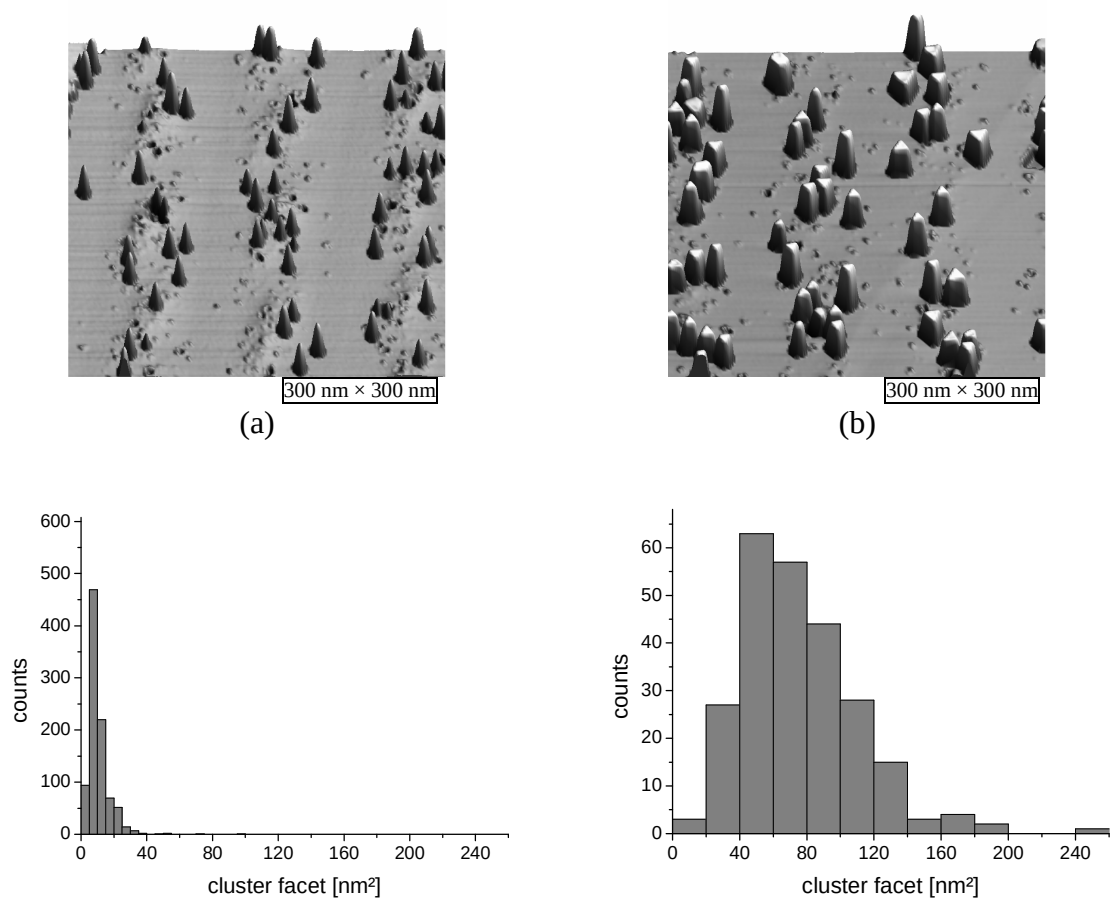

FIGURE 5-55: (a-b) STM images after deposition of 0.14 and 1.36 ML lead on SAMPLE 10 and the subsequent annealing. In the first deposition case the clusters are mostly not faceted. After the second deposition large triangular like facets are formed. The corresponding facet distributions are shown in histograms (c-d).

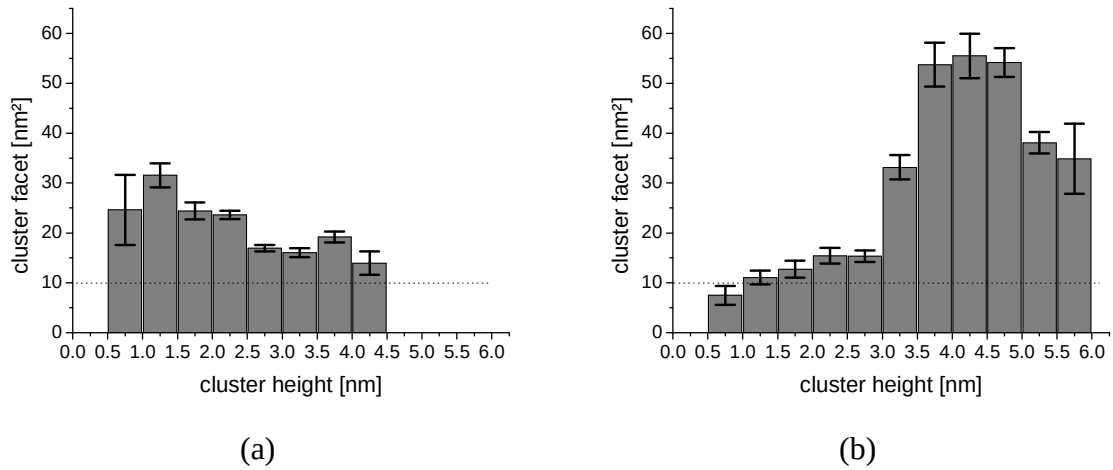

FIGURE 5-56: Dependence of the mean faceted area on the cluster height for all deposition steps on (a) SAMPLE A2 and (b) SAMPLE 10. The faceted area increases with the height. The dashed line marks the smallest facet detectable A_{min}. In contrast to silver the lead clusters form facets very early.

5.4.3.3 STS measurements

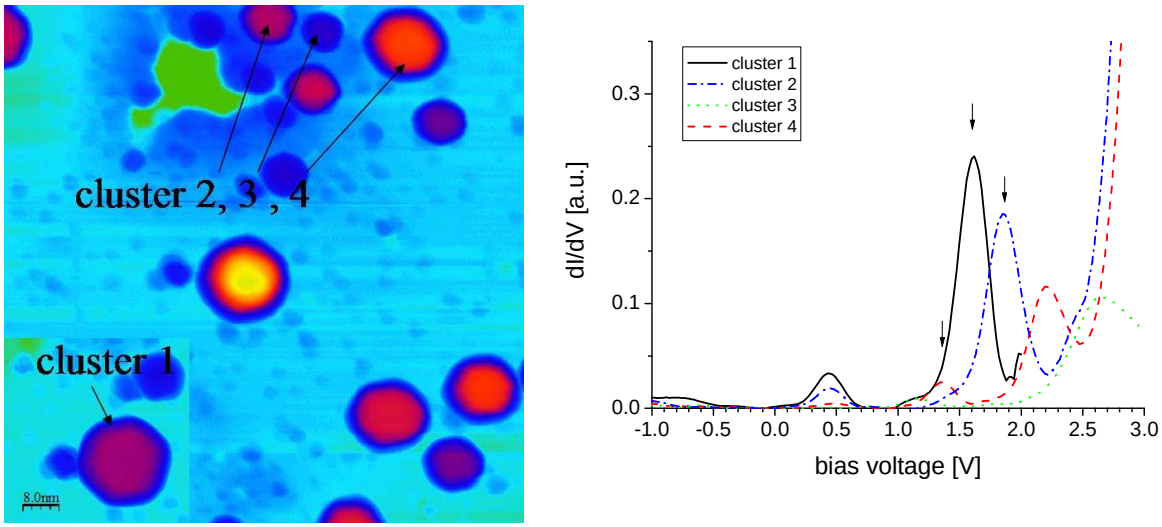

(a) (b)

FIGURE 5-57: (a) STM images of lead clusters grown on SAMPLE 3. The heights of clusters 1 to 4 are 3.5, 2.7, 2.1 and 4.9 nm, respectively. Clusters 1 and 4 have a large facet whereas clusters 2 and 3 are not clearly faceted. (b) Corresponding STS-spectra for the labeled clusters. The set point is *I* = 26 pA at *U* = 1 V.

In references [159-161] the effect of quantum well states is investigated for lead layers with various thicknesses. The quantum well states are confined in one dimension between layer surface and substrate. The question arises whether this effect is also observable for lead clusters. In this case the problem is extended to three dimensions. Thus the quantum well states can also appear between the side facets or in many other variations. However in practice two directions can be investigated: the vertical direction given by the cluster height and the lateral direction given by the cluster width. The cluster width in STM measurements can only be evaluated from the cluster facet.

A first set of STS measurements should reveal the quantum well states and their dependence on the cluster size. In figure 5-57 STS measurements for four clusters with different heights are displayed. The STS measurements have been performed at 77 K. Only the unoccupied states can be observed clearly. The peaks in *dI/dV* spectra represent the energies of the quantum well states. The influence of the cluster facet is not visible in these spectra. But the cluster height influences the peak location. The clusters 1, 2 and 4 will be discussed in the following. The first peak in positive range is located at about +0.5 V and is equal for all clusters even though very weak for cluster 4. In contrast the second peak appears at different voltages (marked with arrows in figure 5-57b). For higher clusters it appears at lower voltages. The peak about 2.2 V for cluster 4 belongs to the third state above the Fermi level. The peaks in the spectrum of cluster 3 can not be allocated. The peak at 2.7 V may belong to the second unoccupied state.

These spectra yield a first indication for height influenced quantum well states. In order to get an idea of this dependency 43 clusters were investigated with STS. In figure 5-58a the peak locations are plotted versus the cluster height. In this figure two states can clearly be identified for clusters higher than 3 nm. The first state exhibits a horizontal trend at 0.5 V and the second state a linear decrease from 2 to 1 V. One may identify a third state which also exhibits a linear decrease from 3 to 2 V. Clusters smaller than 3 nm do not exhibit a visible trend in the peak structure.

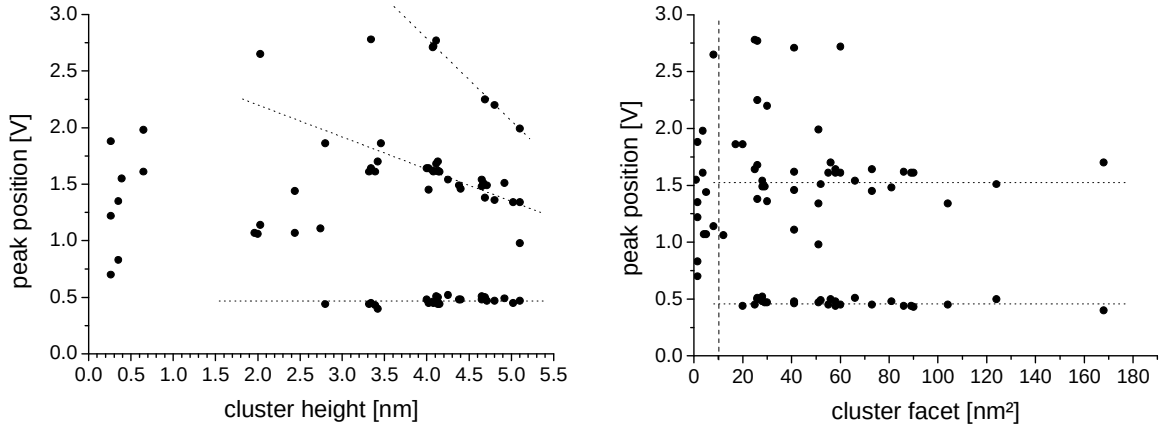

(a) (b)

FIGURE 5-58: Peak positions of lead clusters on SAMPLE 3 are plotted (a) versus the cluster height and (b) versus the cluster facet. The doted lines in (a) indicate the trend of the peak positions versus cluster height. The horizontal line in (b) correspond to the mean peak positions in (a) and the dashed vertical line marks the smallest facet detectable A_{min}.

In figure 5-58b the dependency on the cluster facet is displayed. The peaks do not show any dependency on the facet size. That is not only visible for the first QWS but also for the second one. The distribution around the doted line is caused by the height dependence of the states. The third state is not really visible here. This independency does not mean that there are no quantum well states in the lateral direction but rather that they can not be measured with STS. That may originate from the measurement configuration in which the gap voltage is applied in vertical direction and the tunneling current flows in the same direction. Behind the dashed vertical line (at A_{min}) the two QWS can not be identified. The existence of cluster facets seems to be essential for the measurement of quantum well states.

5.4.3.4 Cluster stability

"Scanning & Tunneling"

The influence of the tunneling process on the cluster shape is presented for one single cluster observed in STM. The faceted lead cluster was formed after room temperature deposition of 0.8 ML (figure 5-59a). On the top of the cluster STM measurements were performed with tunneling parameters typical for STM measurements with atomic resolution. The gap voltage was decreased to 0.3 V and the feedback was set at about 100 pA. Thus the gap between the STM tip and cluster was decreased and the interaction increased. The result is shown in figure 5-59b. The cluster becomes higher while other structures on the surface do not change. The line profiles in figure 5-59c show that the cluster height is increased from 3.5 to 6.5 nm.

Since no material from the surroundings was transported to the cluster the width should be decreased correspondingly. That can roughly be observed in the line profiles but the tip influence does not allow a detailed analysis. The changed cluster does not exhibit a facet. Furthermore in the STM images an enhancement of the image quality can be observed. That indicates that tip and cluster exchanged material which led to a sharpening of the STM tip. However it is supposed that not enough material was exchanged to cause the cluster enlargement.

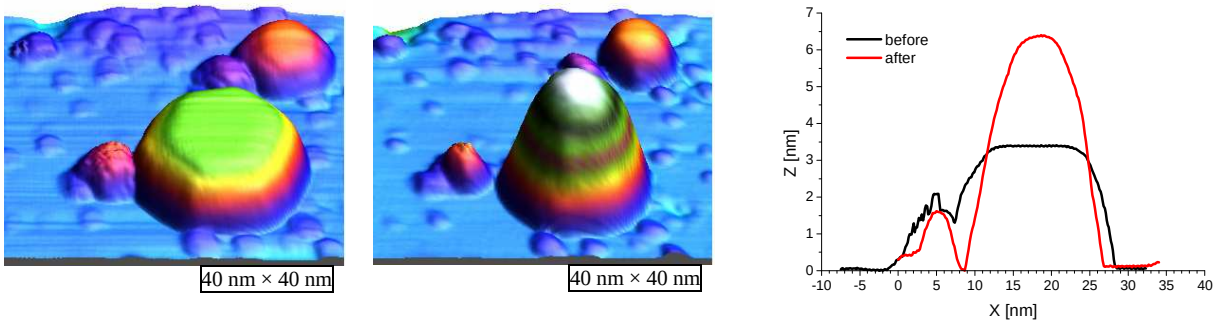

FIGURE 5-59: (a) A lead cluster on SAMPLE 3 exhibiting a large hexagonal facet. (b) The same cluster which has changed its shape after scanning on the facet with a gap voltage of 0.3 V and a feedback set of 100 nA. (c) Line profiles of both clusters. The cluster height is increased from 3.5 nm to 6.5 nm after scanning with the mentioned parameters.

"Annealing & UPS"

In another experiment the sample was annealed at 150°C (figure 5-60a). The height distribution shows an increase of the mean cluster height about 1 nm. In contrast the cluster density did not obviously change. It amounts to 1075/µm² before annealing and 950/µm² after it. That corresponds to a decrease of the cluster density of 10%, neglecting the statistical error. But the height increase is about 36%. Also the cluster facets obviously shrunk. That is comparable with the results in figure 5-54a (not annealed) and figure 5-55a (annealed) and in the corresponding facet distributions. This behavior is comparable with the change of the cluster shape after tip interaction.

During UPS measurements a typical operating pressure is between 10^{-7} and 10^{-8} mbar (mostly helium). It might be higher close to the sample. The height distributions (before and after UPS measurement) show that this is not enough to change the cluster shape (figure 5-60b).

"Air Contact"

Additionally the lead clusters are investigated with respect to stability in ambient conditions. The STM image in figure 5-61 shows lead clusters after storage for 7.5 hours in a nitrogen atmosphere in the load-lock of the LT-system. The STM measurement could only be performed at high gap voltages. The clusters are contaminated and seem to have no metallic character anymore. The clusters exhibit neither a facet nor a spherical shape. It is rather jagged. The clusters may have reacted with oxygen or sulfur contaminations in the nitrogen atmosphere. Hence, the lead clusters can not be transferred in a nitrogen atmosphere.

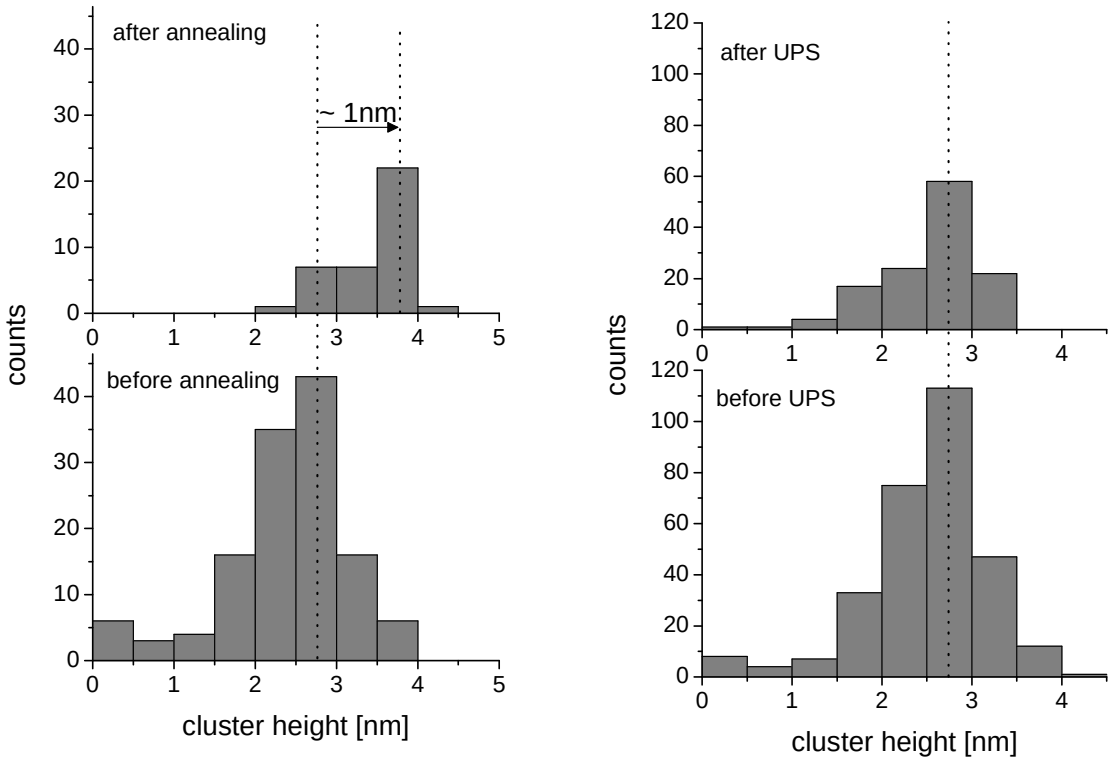

(a) (b)

FIGURE 5-60: **(a) Distribution of cluster heights shows the change of the cluster heights after annealing the sample at 150°C. The mean cluster height is shifted about 1 nm to higher values. (b) Height distributions before and after measurement with UPS, which is performed in a helium atmosphere with a pressure between 10^{-7} and 10^{-8} mbar. No changes in the height distribution are observable. The sample used is SAMPLE A2.**

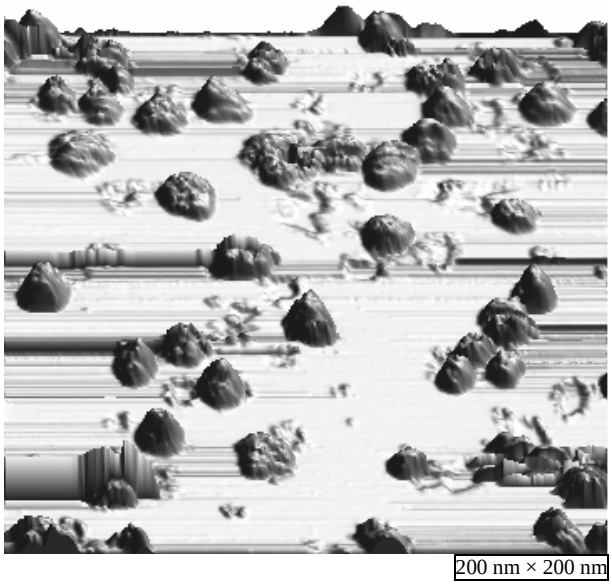

FIGURE 5-61: **Contaminated lead clusters on SAMPLE A2. The sample was transferred into a nitrogen atmosphere for 7.5 hours before STM measurement. The gap voltage was 3.8 V and the feedback set 25 pA.**

5.4.4 Discussion

The investigation of silver and lead clusters has shown several differences in respect of the cluster height, cluster facet and their stability. For a quantitative comparison of the cluster heights with the height of the atomic layer in bulk we have to use an exact calibration on a nm scale considering errors caused by the calibration of the STM apparatus [162]. The calibration was performed by growing C_{60} multilayers on HOPG at LN_2 temperature (77 K). The expected theoretical monolayer height of C_{60} can be evaluated from the lattice constant a_{C60} = 1.405 nm [163]. It leads to d_{C60} = 0.81 nm for the (111)-orientation. The experimental value is evaluated from a height histogram of an STM image with a good image quality as presented in figure 5-62. The peak distances were 0.91 nm. Thus the structures are imaged 11% higher.

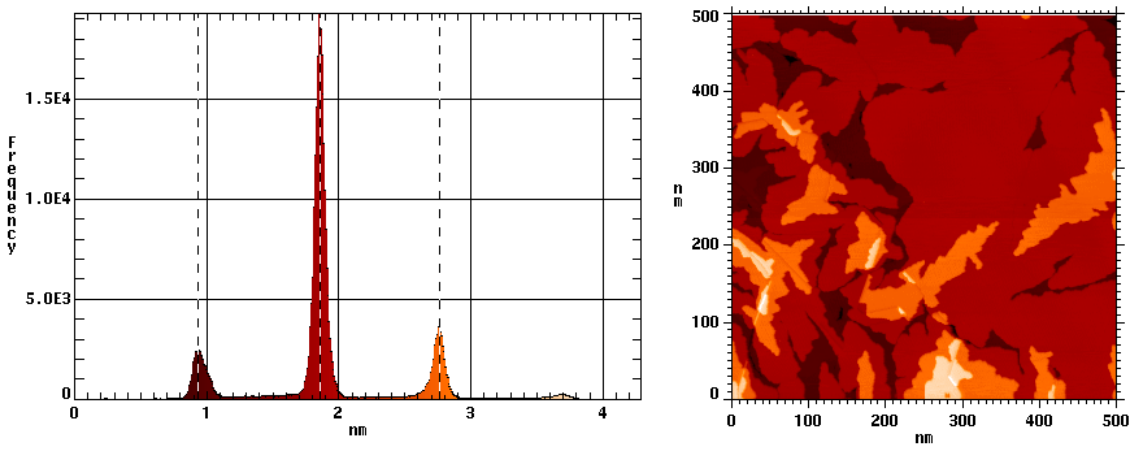

FIGURE 5-62: Histogram (left) and STM image (right) of C_{60} islands on HOPG.

With this calibration the mean peak distances can be corrected which leads for silver clusters to 0.231 nm and for lead clusters to 0.307 nm. The theoretical thickness of an atomic layer in (111)-orientation in bulk can be evaluated from the fcc-structure and the lattice constant. The lattice-constant for Ag is 0.409 nm and for Pb 0.495 nm [6,115]. So the theoretical thickness of a (111) atomic layer is 0.236 nm for Ag and 0.286 nm for Pb. The measured peak distances correspond with the bulk values of the layer thickness within the measurement inaccuracy of about 5% relative error [162] or 0.05 nm as absolute error of the histogram (bin size). Considering this one can say that all clusters have grown layer by layer but the lead clusters indicate that every second atomic layer is more stable. This behavior is associated with the odd-even-oscillation as discussed above.

The reason that this effect occurs for Pb and not for Ag is the different growth behavior of Ag and Pb clusters. The diffusion of Pb atoms occurs at lower temperatures and Pb forms facets more easily. Thus the Pb atoms can reorganize within the clusters and between them and form clusters with smaller surface energies, which is influenced by the odd-even-oscillation. In contrast the Ag atoms do not reorganize and the cluster shape does not change its original form. In this case the odd-even-oscillation of the QWS is not reflected in the height distribution.

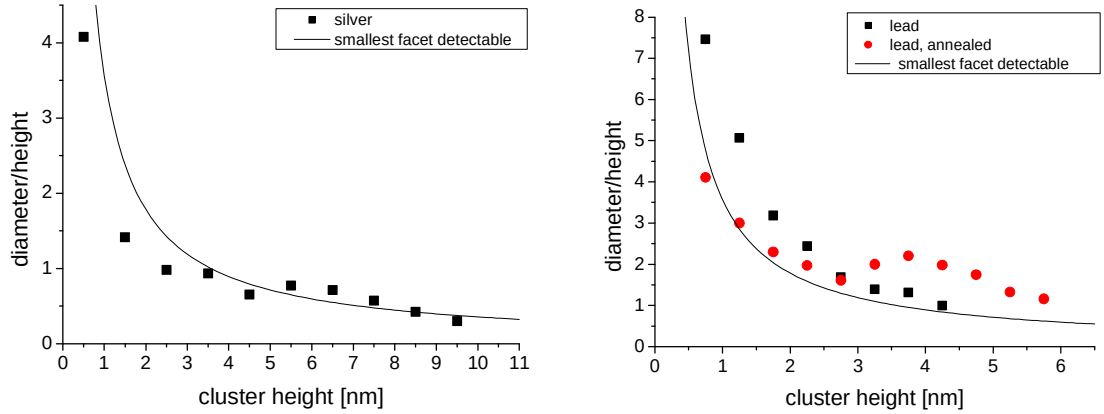

(a) (b)

FIGURE 5-63: Plots of the diameter of the cluster facets versus the cluster height for (a) silver and (b) lead clusters. It is also plotted for annealed clusters in the case of lead (red circles). The plots are evaluated from figure 5-45 and figure 5-56. The black line marks the smallest detectable facet of 10 nm².

For lead clusters the smallest cluster height with a facet is about 1 nm whereas it is 5 nm for silver clusters. In figure 5-63 the ratio facet diameter height is shown for silver, lead and annealed lead clusters evaluated from:

$$\frac{d}{h} = \frac{\sqrt{4A/\pi}}{h} \tag{16}$$

where A is the faceted area. For the smallest facet detectable of A_{min} = 10 nm² (see page 5.4.2.2) the d/h-curve is drawn in figure 5-63. In the case of silver clusters the measurement data points are below this curve for clusters smaller than 5 nm and close to the curve for higher clusters (figure 5-63a). That means the cluster shape is nearly spherical even for faceted clusters. In contrast, for lead clusters the measured d/h is higher than the curve (figure 5-63b black squares). For higher clusters the measurement data points approach to the curve. This emerges because the facets are not completely formed due to the limitation of the deposited lead material.

The annealing process moves the data points closer to the curve for clusters smaller than 3 nm (figure 5-63b red circles). In this case the clusters have a nearly spherical shape. But for higher clusters the distance to the curve is distinctly larger. The facets of these clusters are probably more stable.

The difference between the shapes of silver and lead clusters can be explained by the different interaction strength between the cluster and the graphite surface. The silver clusters exhibit a small interaction with the substrate. That is noticeable during STM measurements where the silver clusters can be moved easily by the STM tip. As a result of the weak interaction the clusters are quasi free and can build a spherical shape which has the smallest possible surface energy. In contrast the lead clusters seem to have a stronger interaction with the substrate. Thus they do not form a spherical shape. Only after annealing or tip interaction the clusters are restructured to the spherical shape.

Another difference is the stability concerning a transfer in nitrogen or air. Lead clusters are contaminated already for a storage in a nitrogen atmosphere. With this the lead clusters can not be examined in ex-situ experiments. Silver clusters are contaminated, too, but the contamination is smaller even for a transfer at ambient air for longer time. For silver clusters the contamination only becomes visible in the height distribution where the layer height is increased to 0.42 nm (including the calibration correction). The higher reactivity of the lead clusters is comparable to the bulk behavior of silver and lead.

6 Monte Carlo Simulations

Many phenomena observed in experiments can be understood either by theoretical treatments or by simulations. Especially the *Monte Carlo* method (MC) is a statistical method for simulation of problems which are too complex for a detailed treatment. In this method the real variables or processes are represented by random numbers. The name Monte Carlo, coming from the Monte Carlo Casino in Monaco, was used first by Metropolis inspired by interest of his coauthor Ulam in poker [164]. Actually the method of random numbers was used before by Enrico Fermi in 1930 for calculation of neutron diffusion processes. It was the central method for simulations within the Manhattan Project (in World War II). The MC method is especially suitable for simulation of dynamic events in physics, such as diffusion processes in fluids or solids (*random walk*). It is used here to simulate first the impact of gallium ions and then the oxidation process.

6.1 Ion impact

The measurements have shown that the exposed structures are wider than the resolution of the FIB tool. The origin of this effect is mainly the creation of defect cascades. Most important for broadening in the oxidation process are defects on the surface which are caused by atom recoils. That results in defects in the surroundings of the main pattern structure for lower ion doses or in broadening of the exposed structure for higher ion doses. To understand these effects simulations of the ion impacts into the surface are required. Furthermore the penetration depth of the ions which is discussed in 5.3.1.2 can be understood in connection with the corresponding simulations. The simulations are performed with the program TRIM (*Transport Range of Ions in Matter*) which is often used for Monte Carlo simulations of ion impacts into a modifiable target [165].

6.1.1 About TRIM

The super-program of TRIM is called SRIM (*The Stopping and Range of Ions in Matter*) which provides other tools for ion implementations. A full description of the calculation method used in TRIM is in reference [166]. In the TRIM input window the parameters of the simulation, the target and the ion specifications can be modified. The simulation provides results about the ion path in the target, target damage, sputtering, ionization and phonon production in a three dimensional distribution. During the simulation all atom cascades are saved into different files which can be used for a detailed analysis. The ion is specified by its atomic mass, energy and the angle of incidence. The atoms in the target are specified by their atomic mass, density, displacement energy E_d, lattice binding energy E_b, and surface binding energy E_s. Additionally the ions lose energy by interaction with the electron shells of the target atoms. That is given by the *stopping power* which depends on the ion, target atoms and ion energy. The stopping power is investigated in many studies for different materials [167].

After collision the incident atom 1 has energy E_1 and the stationary atom 2 has energy E_2. A displacement occurs if $E_2 > E_d$ and a vacancy occurs if also $E_1 > E_d$. A *vacancy* is the hole left behind when a recoil atom moves from its original site. If a moving atom strikes a target atom and has not enough energy to move onwards, it replaces the target atom. After collision the energy E_2 is reduced by E_b. If $E_2 < E_d$ then atom 2 has not enough energy and it vibrates back to its original site, releasing E_2 as phonons. If atom 2 leave the surface and $E_2 > E_s$ then atom 2 is sputtered. These are the main procedures occurring during a collision. For more details about the used *Kinchin-Pease analytic method* see references [168,169]. The occurrence of a collision is based on a Monte Carlo simulation. The crystalline structure of the target is not considered in the collision process. However these simulations provide very good estimations.

6.1.2 Simulation results

"Energy Dependence"

The simulations presented here are comparable with Gierak´s study [72]. They were performed for 3000 gallium ions striking on a graphite surface at the same position $x = y = 0$. The graphite target is predefined in TRIM. The density is 2.253 g/cm^3, the atomic weight is 12 u and the energies are E_d = 28 eV, E_b = 3 eV, E_s = 7.47 eV. Additionally TRIM provides a special 'bond correction' about 0.868 for graphite [167].

The results of the simulations for five ion energies are displayed in figure 6-1. The ion traces are colored red. The bright green color marks the trace of recoil atoms and the dark green the collision position. Since the TRIM software stacks the ion tracks in the image the red lines are not clearly visible. The recoils appear down to 15 nm for 5 keV and 70 nm for 35 keV. The lateral extension of this region is approx. 20 nm for an ion energy of 5 keV and approx. 60 nm for 35 keV. It is remarkable that the shape of this region is roughly shaped like a rectangle for all ion energies. This volume will completely oxidize. Consequently, the measured STM image shows roughly the shape of the defected volume like a cylinder (excepting the broadening caused by the tip shape). In other experimental setups the ion implantation could also cause a spherical defected volume which is narrow on the surface (e.g. cf. figure 6-2). The STM image of these samples would also result in a cylinder like shape, too, different to the real shape (cf. figure 3-11). The simulations show that this is not the case for impingement of gallium ion on graphite.

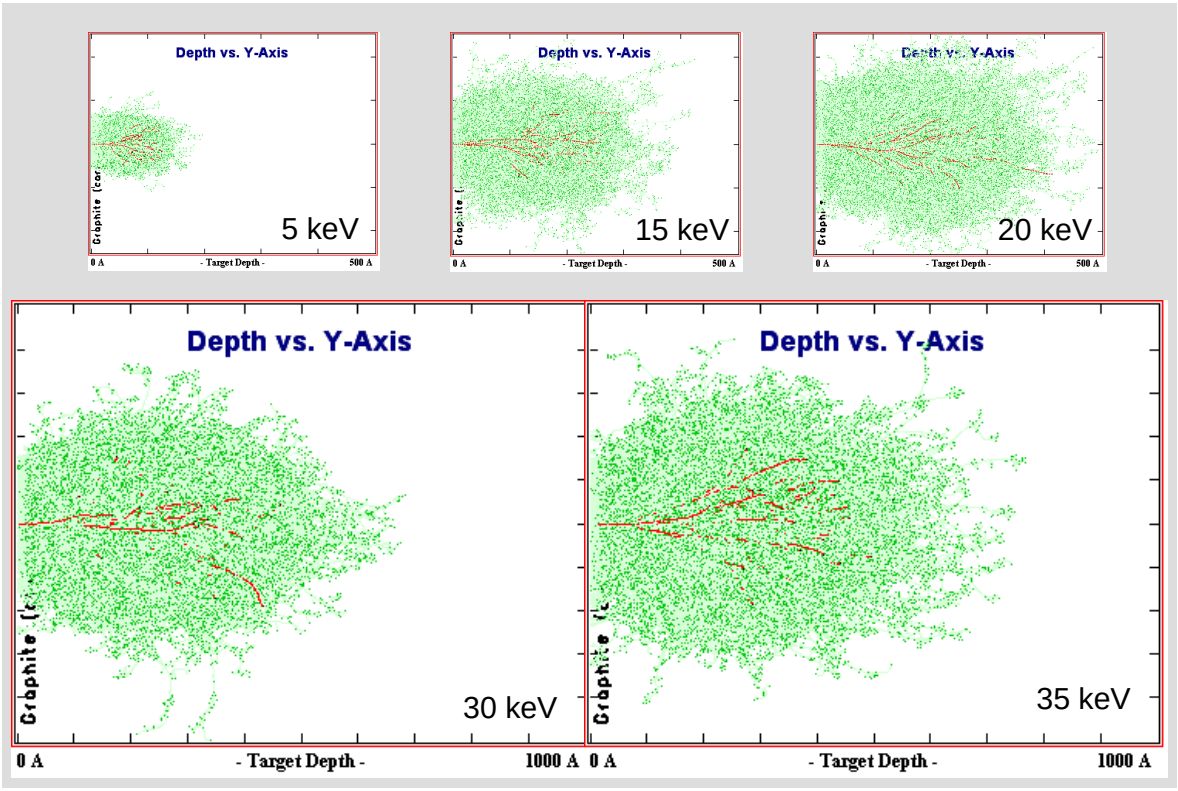

FIGURE 6-1: **Calculated results from TRIM for five ion energies. The red dots are collisions between the ions and target atoms. The green dots are collisions between recoiling atoms and other target atoms.**

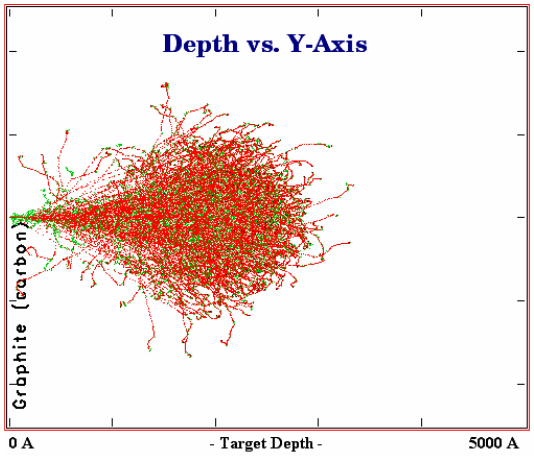

FIGURE 6-2: **Calculated results from TRIM for 1000 helium ions with an energy of 35 keV into a graphite substrate.**

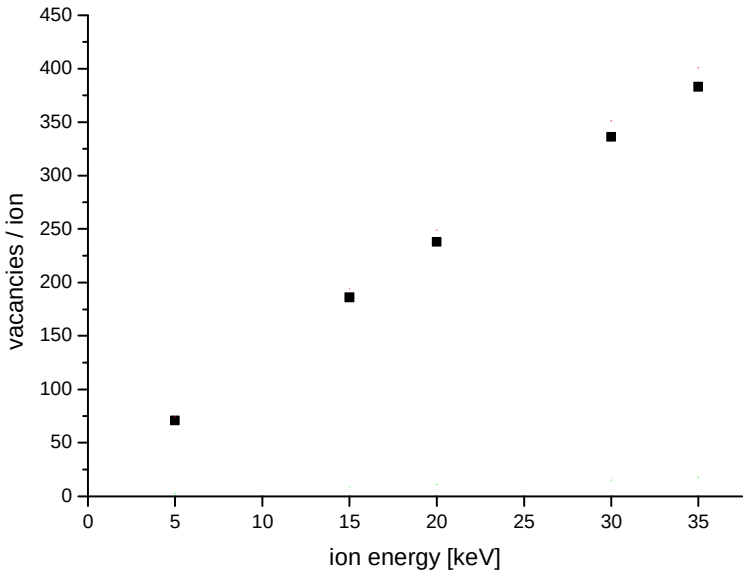

FIGURE 6-3: Total target vacancy per ion is plotted versus the ion energy.

The number of target vacancies increases roughly linear dependent on the ion energy (figure 6-3). The ions with higher energy can transfer more energy to the recoiling atom and initiate a larger cascade.

The histograms in figure 6-4 display the vacancy distribution versus the target depth in the graphite substrate for two energies. The maximum lays at 4.5 nm for 5 keV and shifts to 18 nm for 35 keV. The FWHM amounts to 6 nm for 5 keV and becomes wider to a value of 26 nm for 35 keV.

"Influence of the Beam Diameter"

The lateral distribution of the target vacancies is displayed in figure 6-5 for 30 and 35 keV. This time the TRIM simulation was performed for a Gaussian distribution of gallium ions. The Gaussian distribution is described with:

$$f(x,y) = \frac{1}{2\pi\sigma^2}\exp\left(-\left[\frac{(x-\mu_x)^2+(y-\mu_y)^2}{2\sigma^2}\right]\right) \tag{17}$$

where σ is the standard deviation and μ_i the mean value of the variable i which is set to zero. The FWHM is fixed at 8 nm to have a comparison to Gierak´s study. With the values of *x* and *y* the impact position of every gallium ion is calculated and forwarded to TRIM.

In figure 6-5 the vacancies are distributed within a depth of ca. 30 nm. Gierak et al. have achieved a mean in-depth free path of 22.7 nm for 37200 gallium ions with an ion energy of 30 keV [72]. These values are appreciably smaller than the experimental result for the pit depth which was about 50 nm. In order to understand the correlation between simulation and experiment the limit of the vacancy density should be defined in the following with respect to the oxidation process.

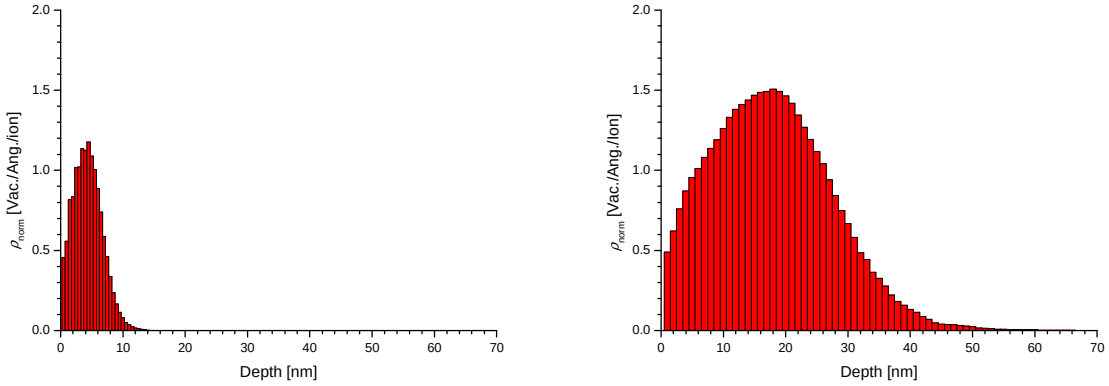

(a) (b)

FIGURE 6-4: Distribution of the target vacancies for an ion energy of (a) 5 keV and (b) 35 keV.

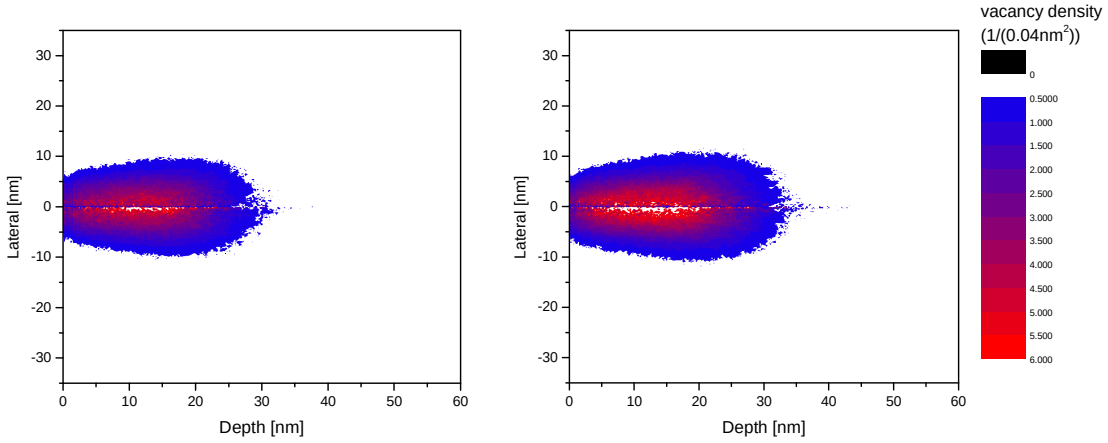

(a) (b)

FIGURE 6-5: Density of target vacancies for (a) 30 keV and (b) 35 keV. Red regions are the regions with the highest vacancy density. The white region in the middle is a result of poor statistics.

"Prediction of the Cavity Depth"

To compare the TRIM simulations with the experimental results for the oxidation of nano-cavities it has to be estimated which defect density is needed to oxidize a complete graphite layer. In a simple approximation a nano-pit is regarded as a cuboid with the side length of a and the depth of d_{HOPG} = 0.335 nm (the graphite layer distance). If the oxidized layer is imagined as a matrix of these cuboid nano-pits the density of the nano-pits is given by:

$$\rho_{limit} = \frac{1}{a^2 d_{HOPG}} \tag{18}$$

This value is equal to the density of defects which is needed to oxidize the complete layer if one nano-pit emerges for one defect. This value has to be compared to the defect density normalized with the ion counts and the depth difference as used in the TRIM software:

$$\rho_{\text{norm}} = \frac{1}{N_{\text{ion}}} \times \frac{\Delta N_{\text{Vac}}}{\Delta z} \tag{19}$$

where N_{Vac} is the number of vacancies and z the target depth. Correspondingly, ρ_{limit} has to be normalized as follows:

$$\rho_{\text{norm}} = \frac{\rho_{\text{limit}} \times A_{\text{point}}}{N_{\text{ion}}} \tag{20}$$

where A_{point} is the impact area for the incident ions. It is approximately 14500 nm² for SAMPLE 1 [103]. N_{ion} represents the number of incident ions, it is equal to 3000. The highest uncertainly in this model is made by a and A_{point}. In table 6-1 the value of ρ_{norm} for different reasonable values of a and A_{point} is calculated. The depth for which the vacancy distribution is equal to the vacancy density of ρ_{norm} corresponds to the maximal depth of the nano-cavity which would emerge after oxidation (cf. figure 6-4). It is obvious that the resulting depth corresponds to a very low vacancy density in the tail of the vacancy distribution. In figure 6-5 no vacancies are visible at this depth due to the used color scale.

The cavity depth for 5 representative values of ρ_{norm} in dependence on the ion energy is displayed in figure 6-6. It rises roughly linearly with the ion energy and ρ_{norm} defines the slope. However the cavity depth is not very sensitive to ρ_{norm} due to the exponential decay of the vacancy density in the tail of the distribution. For a value about 0.025 Å^{-1} the simulated depth is near to the measured depth of the STM experiments (cf. 5.3.1.2). This value is marked in table 6-1 with a dashed blue line.

a [nm]	A_{point} [nm²]			
	10000	13000	16000	19000
3	0.109	0.142	0.174	0.207
4	0.061	0.080	0.098	0.116
5	0.039	0.051	0.063	0.075
6	0.027	0.035	0.044	0.052
7	0.020	0.026	0.032	0.038
8	0.015	0.020	0.025	0.029
9	0.012	0.016	0.019	0.023
10	0.010	0.013	0.016	0.019

TABLE 6-1: **Calculated values of ρ_{norm} given in 1/Å using formula 20 for a vacancy density which is needed for a complete layer oxidation. It is calculated for different values of a and A_{point}.**

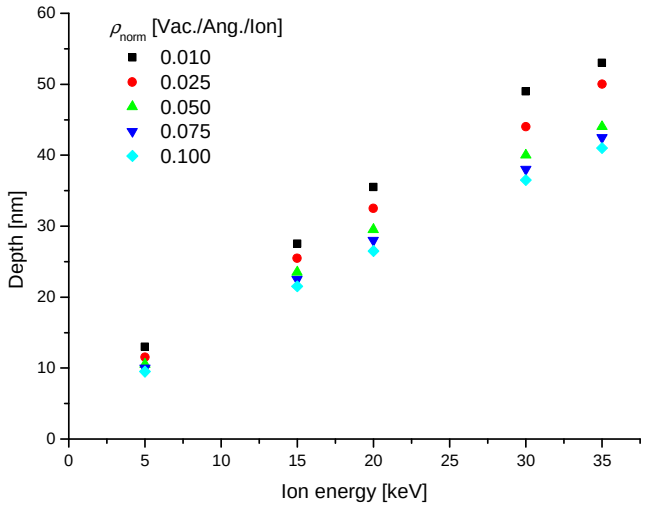

FIGURE 6-6: **The depth extracted from vacancy distributions for five chosen values of the vacancy density plotted versus the ion energy. For ρ_{norm} = 0.025 Å^{-1} the depth is near to the measured one.**

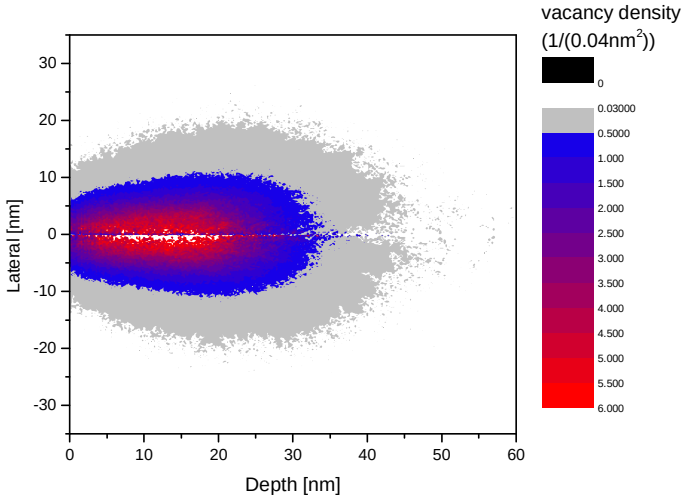

FIGURE 6-7: **Density of target vacancies for 35 keV (cf. figure 6-5b). The color range is extended with gray which represents the areas with a low vacancy density.**

For comparison of the lateral dimension of the pit with experiments the color range in the figure 6-5b is extended for lower vacancy densities (figure 6-7). It shows that the lateral distribution amounts to 20 nm at the surface and to 40 nm in a depth between 10 and 30 nm. The experimental result for the pit diameters with optimal focus (cf. figure 5-32) was 20-30 nm and therefore comparable with these values. Also the shape of the defected volume becomes more visible. It deviates more from a rectangle. With this the STM image would not exactly show the real shape of the pit (cf. figure 3-11).

6.2 Oxidation

The oxidation process was simulated in several studies before. Stevens et al. performed simulations for single pits to investigate the growth of hexagonal and circular pits [125]. Another group simulated the growth of multilayer pits [124]. In this study they could create nano-pits and simulate their growth with time.

However these simulations do not describe the oxidation process for defects in a given pattern. That is performed here with a program written in C++ for windows operated systems. The algorithm is explained in section 6.2.1. The correlation of the used parameters to the experimental parameters is treated in section 6.2.2. The physical meaning of the simulation parameters is discussed in section 6.2.3. Finally some results with focus on nano-pit groups are presented in section 6.2.4.

6.2.1 Algorithm

The basic algorithm is the following. An oxygen atom adsorbs on a random position on the surface and performs a random walk. If it hits a defect, e.g. a vacancy on the surface the oxidation happens with the *oxidation probability* p_{ox}. If the oxidation is not accomplished the random walk continues until it hits a defect again or its path length is equal the *diffusion length before desorption* l_o given in nm. In the latter case the oxygen atom will desorb. With this the simulation process mainly depends on three parameters l_o, p_{ox} and the density of the adsorbed O-atoms ρ_o given in 1/nm² (called *atom density* in the following).

The flow chart of the simulation program is shown in figure 6-8. At program start a two dimensional graphene sheet is created. The graphene structure is converted to a Cartesian coordinate system with the method depicted in figure 6-9a. Then the initial defects are created. In this step the program provides many defect types like single defects, defect lattices, random defects, Gaussian distributed defects etc. Afterwards the oxidation process begins for N_o oxygen atoms calculated from ρ_o and the sheet size A_{sheet}. In this process the oxygen atom starts at a random position and moves over the graphite atomic bonds as illustrated in figure 6-9a with arrows. The direction of the movement is calculated from random numbers. Thus the oxygen atom performs a random walk as illustrated in figure 6-9b. In the next step the program checks whether the atom arrived at a step between a vacancy and a surface atom. In this case the program performs the oxidation process with the given probability for the mentioned surface atom. Otherwise it will go on with the random walk. This process cycle runs until the O atom reacts or the diffusion length is achieved. Thus the program uses three random numbers. These are the start position of the oxygen atom, the movement direction and the oxidation probability test number.

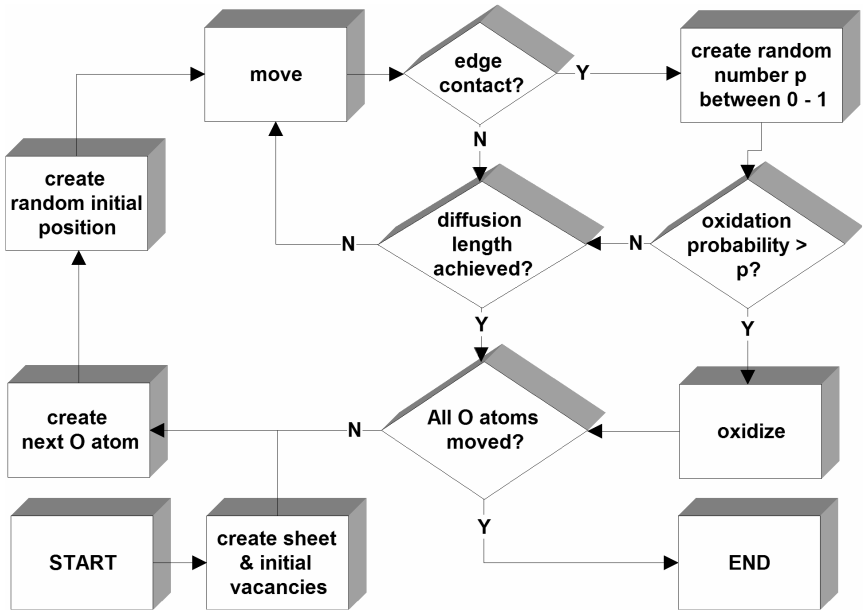

FIGURE 6-8: **Schematic illustration of the program structure for simulation of the oxidation process.**

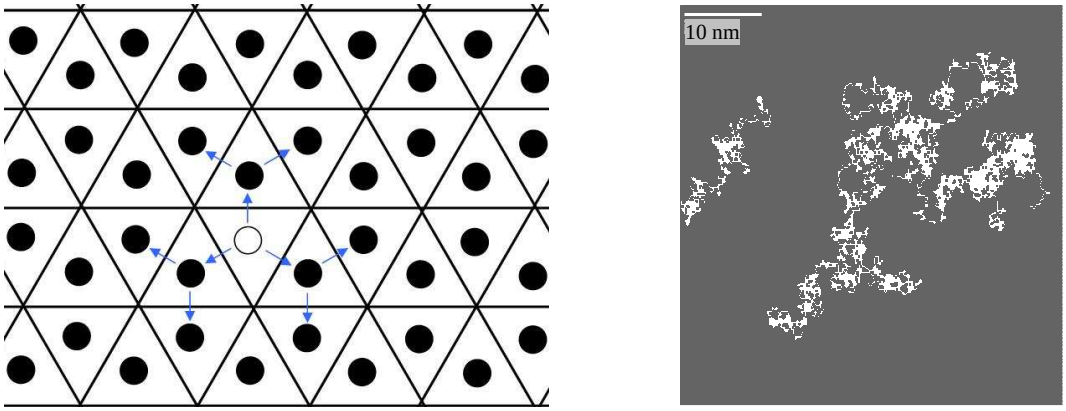

(a) (b)

FIGURE 6-9: **(a) The HOPG lattice is transformed to a lattice of two types of triangles representing the two atomic basis. This reflects directly the HOPG lattice. The white circle represents the start point of the O-atom. It moves along the carbon bonds. That is shown with arrows. (b) The simulated random walk for 5 oxygen atoms with a diffusion length of l_o = 500 nm.**

6.2.2 Characterization

The parameters l_o, p_{ox} and ρ_o create a three dimensional parameter space. It is not simple to find the matching parameters which correspond to the oxidation process in the experiments. Hence in this section the parameters are tested for their influence on the oxidation process. At the end the matching parameters for the sample oxidation as used in the experiments should be estimated.

In order to visualize the influence of the oxidation probability p_{ox}, l_o and ρ_o are hold constant and p_{ox} is varied. The simulation results are shown in figure 6-10. For $p_{ox} < 0.05$ the pit is more or less round. For $p_{ox} > 0.05$ the pit begins to build a dendritic shape which becomes clearly visible for $p_{ox} = 0.2$. This shape of growth is similar to structures observed for metal atoms deposited at low temperatures [170]. The oxidized area and its perimeter

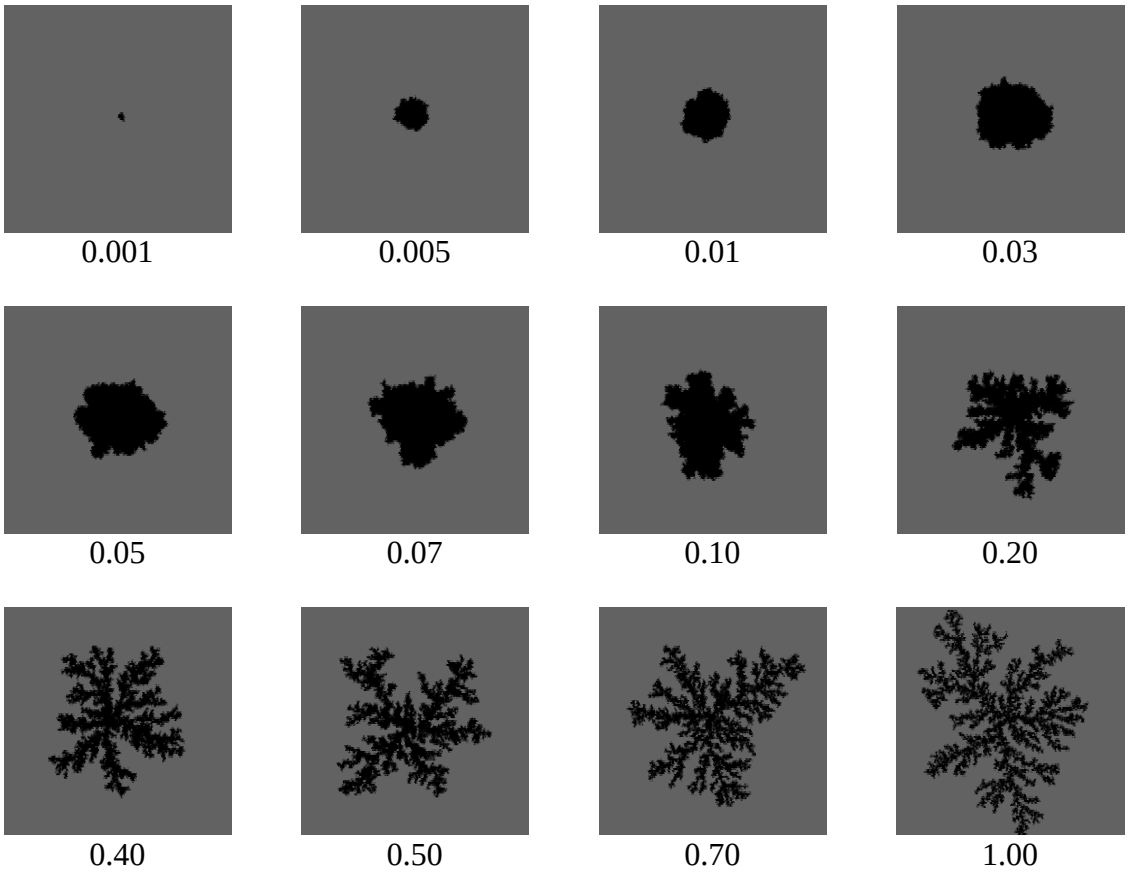

FIGURE 6-10: Simulated pit shape for different oxidation probabilities. The simulation parameters are: ρ_o = 5/nm², l_o = 6.7 µm, A_{sheet} = 100 nm × 100 nm. Image sizes are 50 nm × 50 nm.

are plotted in figure 6-11. The value of the oxidized area reflects the number of reacted oxygen atoms. The saturation is reached at $p_{ox} = 1$ where 34% of the oxygen atoms have reacted with the surface. The perimeter of the pit increases linearly.

In figure 6-12 the perimeter P is plotted versus the area A. The simulation results exhibit an overall deviation from the curve for an ideal cycle (described with equation 21 for $n = 1$). This is caused by the pit borders which are not smooth. It exhibits a zigzag structure which results in a larger pit perimeter (described by the equation 21). It is evaluated from a fit for simulations with two oxidation probabilities $p_{ox} = 0.003$ and 0.03 which both yielded pits with nearly round shapes (see figure 6-13) and result both in a correction factor $n = 2.3$. The corrected curve is added in figure 6-12 with a doted red line. It fits very well the simulation results for $A < 250$ nm². At this point the deviation from the round shape begins. The corresponding oxidation probability is $p_{ox} = 0.05$. That is the limit value for the growth of dendritic structures. All pits with $p_{ox} < 0.05$ have a round shape which corresponds to the experimental results. For most of the following simulations the oxidation probability is set to $p_{ox} = 0.03$ (see next section for a detailed discussion).

$$A = n \cdot 2\sqrt{\pi \cdot P} \tag{21}$$

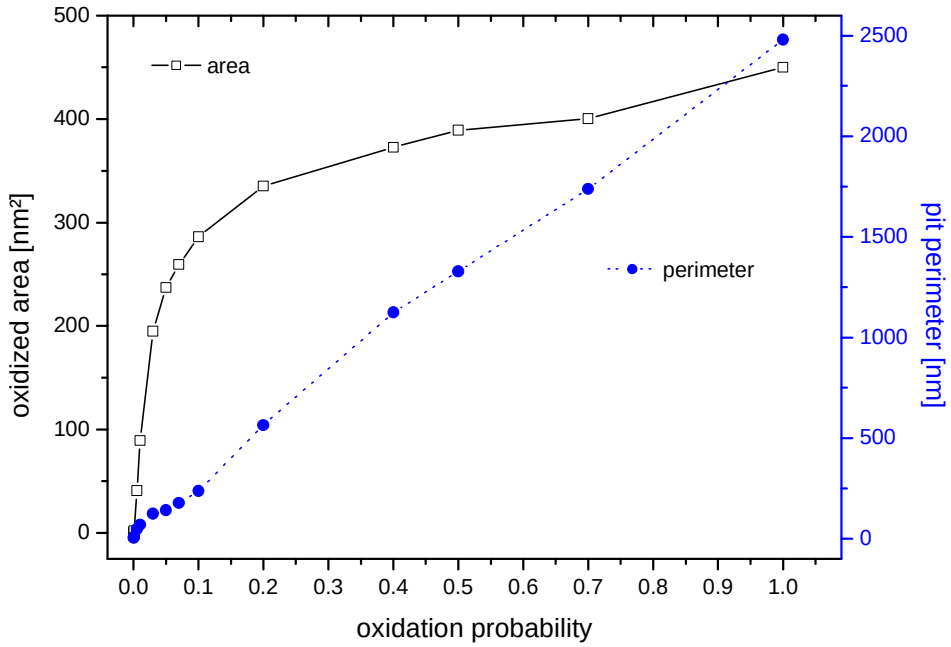

FIGURE 6-11: Oxidized area and pit perimeter are plotted versus the oxidation probability for the simulations shown in figure 6-10.

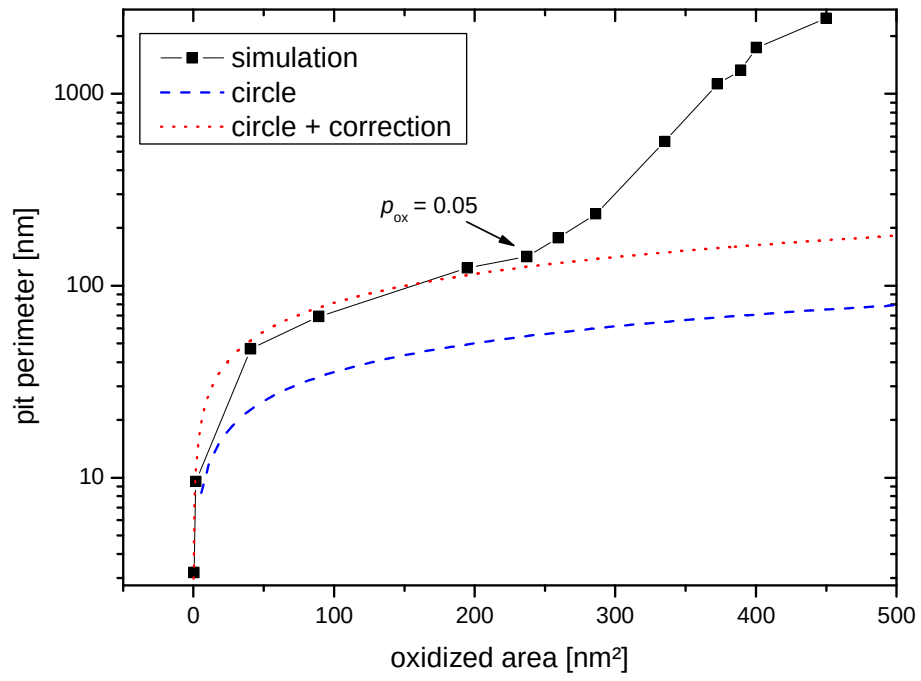

FIGURE 6-12: Pit perimeter plotted versus the oxidized area for simulations presented in figure 6-10.

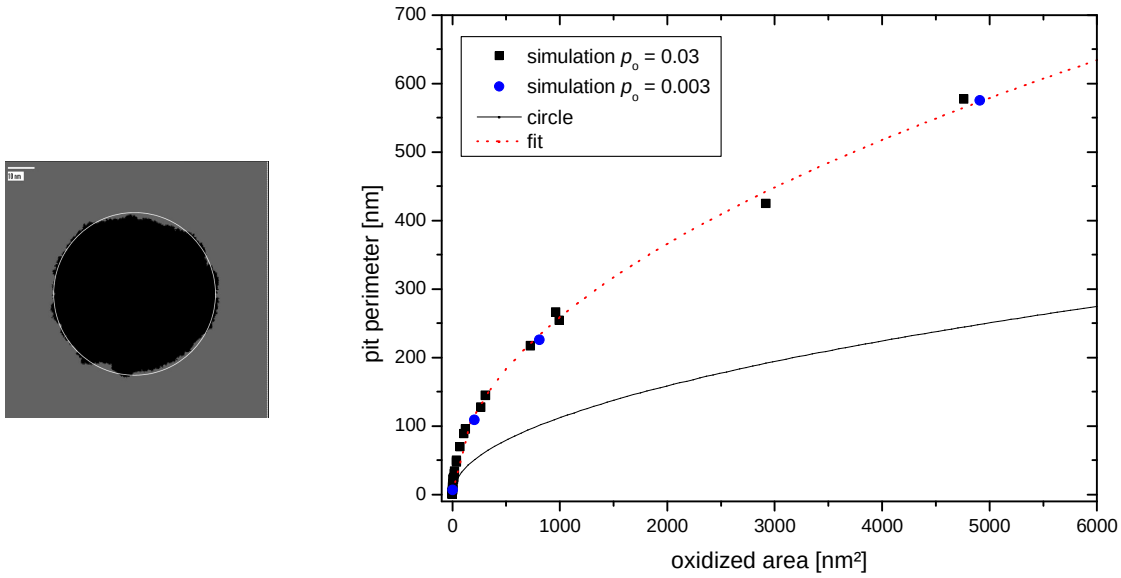

(a) (b)

FIGURE 6-13: **(a) A nearly round pit with a perimeter of 425 nm. The white circle has a perimeter of 193 nm. (b) The pit diameter is plotted versus the oxidized area for simulations with two oxidation probabilities of 0.03 and 0.003 which lead to nearly circular pits. The black solid line represents a perfectly circular pit shape based on formula 21 for n = 1. The doted red line is the fit with the formula 21. It yields a correction factor of n = 2.3.**

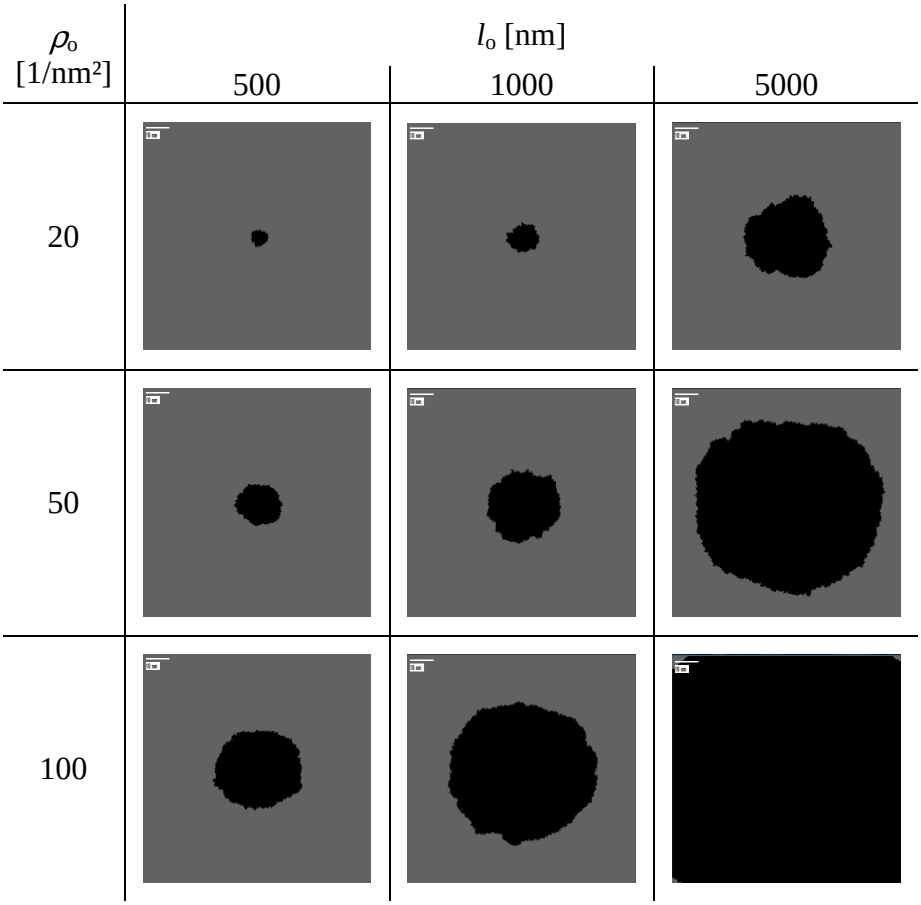

FIGURE 6-14: **Simulated pit shape for different values of atom density and diffusion length. Other simulation parameters are: A_{sheet} = 100 nm × 100 nm, p_{ox} = 0.03**

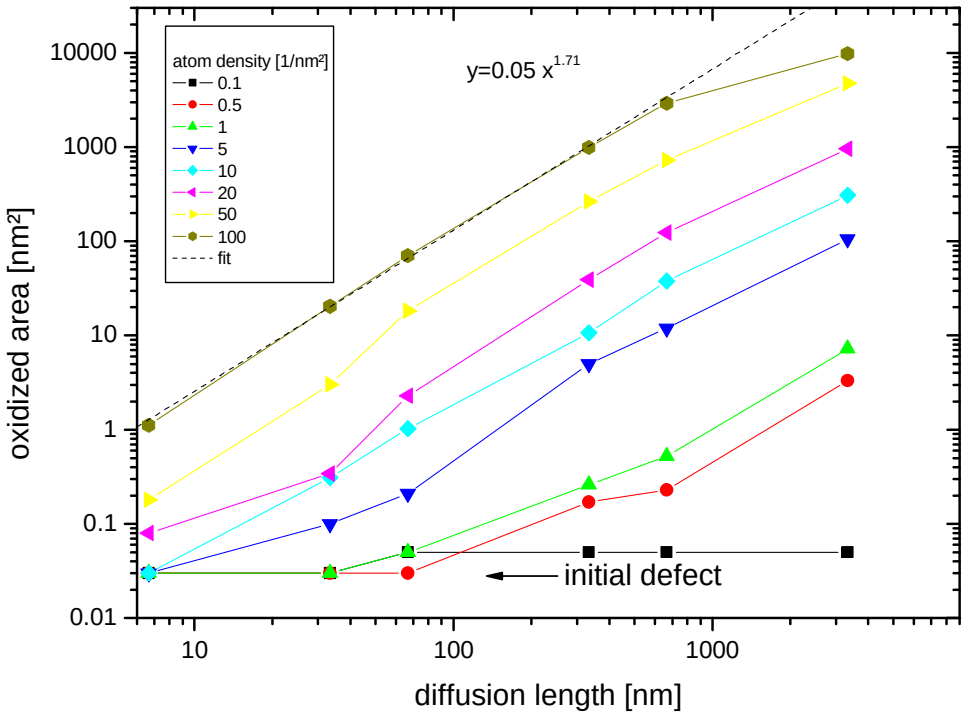

FIGURE 6-15: Dependence of the oxidized area on the diffusion length l_o for the simulations presented in figure 6-14. The arrow marks the initial defect, and therefore the lower limit for the oxidation area.

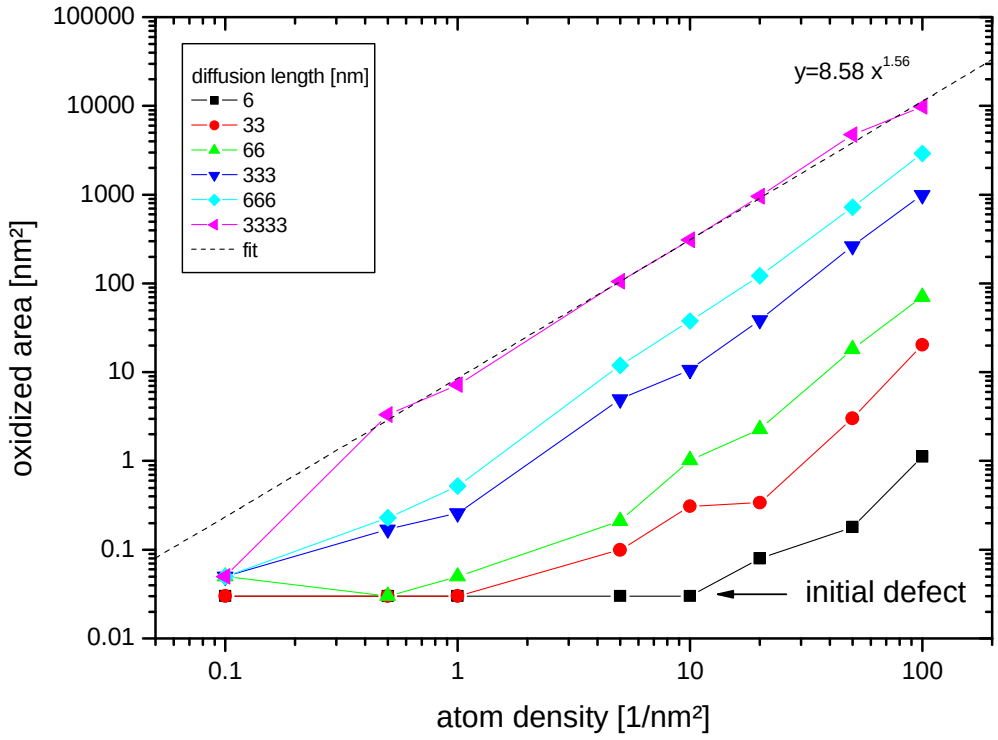

FIGURE 6-16: Dependence of the oxidized area on the oxygen atom density ρ_o for the simulations presented in figure 6-14. The arrow marks the initial defect.

In figure 6-14 different simulation results are shown for different values of l_o and ρ_o. The main effect is the change of the pit size. The shape of the pits is round for all parameter sets. It is well visible that the same pit shape and size can be achieved with different values of these two parameters. The plots in figure 6-15 and figure 6-16 show the increase of the pit area with l_o and ρ_o. The curve shape can be described by:

$$A(l_o, \rho_o) = A_0 \times \left(\rho_o \times \mathrm{nm}^2\right)^{\alpha} \left(\frac{l_o}{\mathrm{nm}}\right)^{\beta} \tag{22}$$

Fits with this function yield the following values:

$$\begin{aligned} A_0 &\approx 2 \cdot 10^{-5}\, nm^2 \\ \alpha &\approx 1.61 \pm 0.04 \\ \beta &\approx 1.76 \pm 0.07 \end{aligned} \tag{23}$$

They describe the growth behavior best for small l_o and large ρ_o for a constant oxidation probability of p_{ox} = 0.03. With this function the pit diameter can be roughly predicted.

In order to find the matching parameters for an oxidation process as performed in the experiments the properties of the oxidized samples are considered in the following. Experiments which exhibited a reasonable shape and density of the nano-pits have shown that the mean pit diameter should be between 5 and 10 nanometers. The mean distance between the nano-pits for a reasonable pit density is about 20 nm. A first estimation for the simulation parameters could be achieved by formula 22.

Since the defect oxidation is influenced by neighbored defects the best parameters should be estimated with a pattern of defects with a pitch of 20 nm as shown in figure 6-17a and b for two different parameter pairs, calling *parameter set A* and *parameter set B* (table 6-2). In the first case the diffusion length of the oxygen atom is very large, in the other case the density of the oxygen atoms is very high. Both parameter sets result in the same pit shape with diameters about 10 nm.

	parameter set	
	A	B
p_{ox}	0.03	0.03
l_o	10000 nm	50 nm
ρ_o	5 / nm²	100 / nm²

TABLE 6-2: Oxidation parameters for parameter set A and B.

For comparison the same simulation is performed for single defects. They represent the case of a very low defect density. For parameter set A the nano-pit is larger than in the lattice pattern (figure 6-17c). In contrast for parameter set B there is no difference between the single pit and the pit pattern concerning the pit shape (figure 6-17d). That is an important effect which noticeably influences the oxidation process. This becomes visible by comparison with an STM image as shown in figure 6-18a. In this image there are about 107 nano-pits. Assuming that every nano-pit is caused by a single defect the defect density

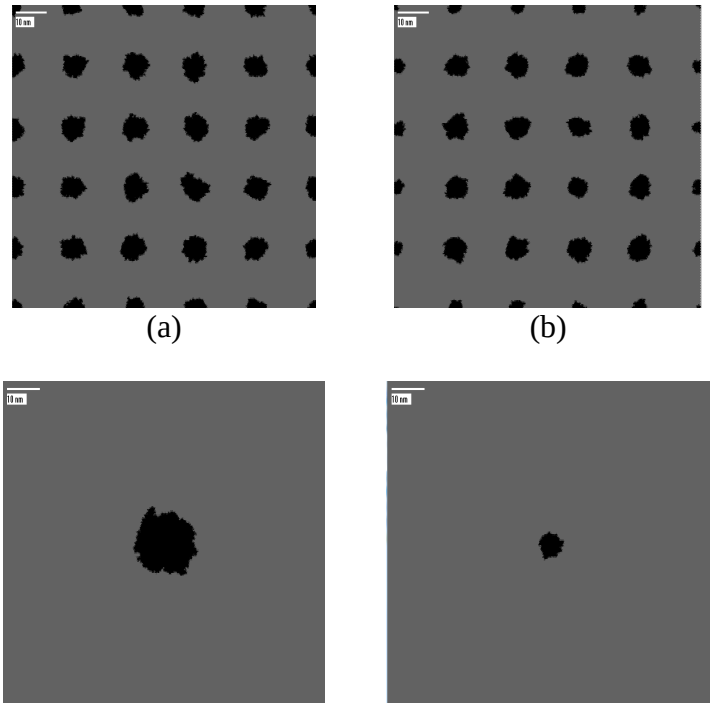

FIGURE 6-17: Simulation results for oxidation of a defect pattern with distances of 20 nm and of a single defect. The oxidation probability is p_{ox} = 0.03. Other simulation parameters are (a,c) l_o = 10000 nm, ρ_o = 5/nm² (parameter set A), (b,d) l_o = 50 nm, ρ_o = 100/nm² (parameter set B). The image sizes are equal to A_{sheet} = 100 nm × 100 nm.

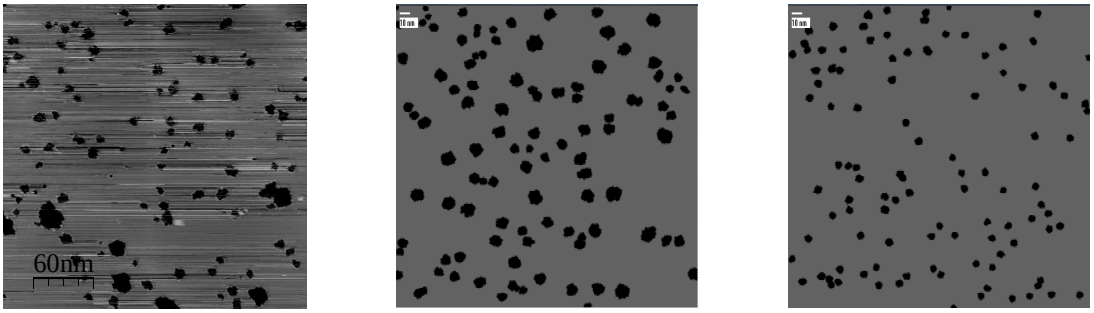

FIGURE 6-18: (a) STM measurement of nano-pits grown on SAMPLE A2. There are 107 pits on an area of 300 × 300 nm². That results in a defect density of 1190/µm². (b) Simulation results with parameter set A. (c) Simulation results with parameter set B.

would be about 1190/µm². With this defect density two simulations were performed with parameter sets A and B. The defects are distributed at random positions to hold the simulation comparable with the STM measurement (figure 6-18b and c). The distribution of the diameters of the grown nano-pits is shown in figure 6-19. The STM image exhibits a pit distribution with a maximum between 5 and 10 nm. Also the simulation with the parameter set A exhibits a pit distribution but with a maximum about 10 nm. In contrast the simulation with parameter set B does not really exhibit a size distribution of the pits. The pit diameter is sharply defined. This would not change even if the defect density varies. The simulation with the parameter set A corresponds better to the experiment. These parameters are used as standard parameters for the following simulations.

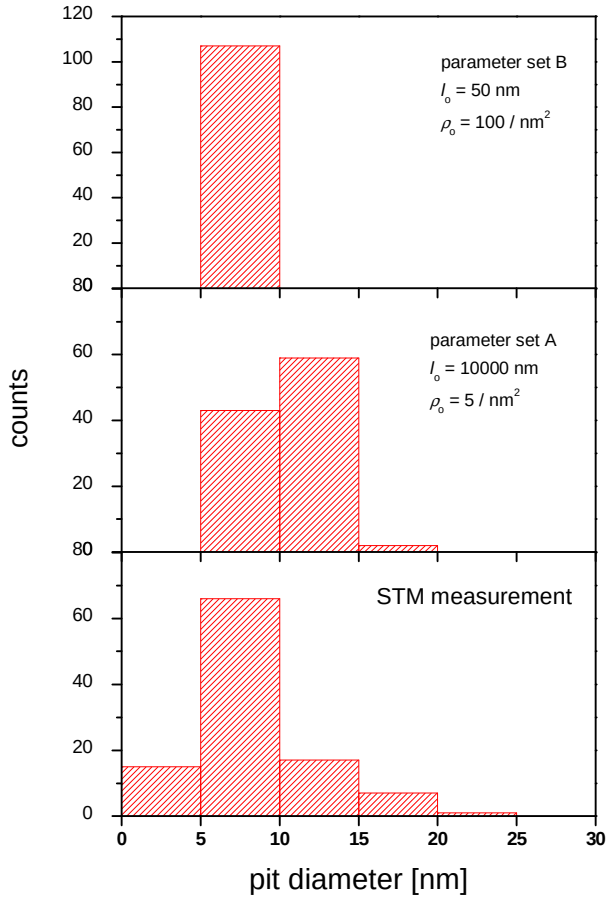

FIGURE 6-19: Distribution of the pit diameters in the images in figure 5-16.

6.2.3 The physical background

The parameters l_o, p_{ox} and ρ_o used for the simulation process are not physical values. Furthermore the oxidation process is strongly simplified. In the simulation oxygen atoms (O) are first physisorped on the surface. In reality oxygen molecules (O_2) are adsorbed on the surface with the sticking probability η as discussed in section 2.4. Since carbon atoms can react only with one oxygen atom the oxygen molecule has to be dissociated into two oxygen atoms. This process is explained in section 2.4 with two types of the carbon oxidation. There is a certain difference between O_2 adsorption and O diffusion. The O_2 molecule has a weak interaction with the surface as compared to O atoms. The O_2 molecule adsorbs on the surface but it does not perform a large diffusion. If it does not find a reaction partner it desorbs after a few diffusion steps. In this process the oxidation mainly occurs by the large number of the adsorbed oxygen molecules. In contrast the rate of the O atoms is very low because it occurs only after dissociation of the O_2 molecules. However the binding energy of an oxygen atom with the graphite substrate is very high [54,171]. Consequently the oxygen atoms remain and diffuse for a long time on the surface.

The diffusion process is determined by the *diffusion time* t_{diff} and the *diffusion velocity* v_{diff}. But the simulation process is time independent. Thus the diffusion length l_{diff} (differs from the simulation variable l_o) represents both parameters in the simulation process. They are linked with the equation:

$$l_{diff} = v_{diff} \times t_{diff} \qquad (24)$$

In the simulation the diffusion process is a random walk of the O atoms. In real process the atom jumps between discrete positions determined by the lattice structure of the substrate (e.g. between the surface atoms). This action is interrupted by vibration of the adatom at these positions [172]. Thus the diffusion time contains also the vibration time. Experimentally the diffusion process is described with the *diffusivity D* given in cm^2s^{-1} (for oxygen diffusion see references [173,174]):

$$D = D_0 \exp\left(-\frac{E_{diff}}{k_B T}\right) \tag{25}$$

where E_{diff} is the activation energy. However the estimation of the diffusion length from this value is very difficult.

The number of the incident O_2 can be evaluated from:

$$\dot{\rho}_{O_2} = \frac{\Delta N_{O_2}}{\Delta A \Delta t} = \frac{1}{4} n_{O_2} \left\langle v_{O_2} \right\rangle \tag{26}$$

n_{O2} is the density and $\langle v_{O2} \rangle$ the mean velocity of the oxygen molecules which can be described by the Maxwell-Boltzmann-distribution:

$$\left\langle v_{O_2} \right\rangle = \sqrt{\frac{8 k_B T}{\pi \times m_{O_2}}} \tag{27}$$

where $k_B = 1.38 \times 10^{-23}$ J/K is the Boltzmann constant and m_{O2} the mass of the oxygen molecule. With the equation of state for an ideal gas:

$$p_{O_2} = n_{O_2} k_B T \tag{28}$$

follows:

$$\dot{\rho}_{O_2} = \frac{p_{O_2}}{\sqrt{2\pi \times m_{O_2} k_B T}} \tag{29}$$

$$\rho_{O_2} = \dot{\rho}_{O_2} \times \Delta t_{ox} \tag{30}$$

With the oxygen pressure $p_{O2} = 0.02$ bar (2% × 1 bar), oxidation temperature $T = T_{ox} =$ 540 °C and $m_{O2} = 2 \times 16$ u (1 u = 1.66×10^{-27} kg) one gets $\dot{\rho}_{O_2} =$ 330 $nm^{-2}s^{-1}$. That results for $\Delta t_{ox} = 200$ minutes in $\rho_{O2} = 4 \times 10^6$ nm^{-2}.

In order to estimate the oxidation probability a nano-pit with the diameter of 10 nm is assumed. To oxidize an area of 100 nm^2 approximately 3800 O atoms are needed. For a pit distance of 20 nm the density of reacted atoms amounts to 10/nm^2. With the estimated ρ_{O2} a reaction rate of O_2 of ca. 5×10^{-5} can be calculated. This value contains the sticking probability of O_2 molecules and the reaction probability of O atoms with carbon atoms. Compared to the simulation parameter set A this value is very small and the value of ρ_{O2} very high. However the density of oxygen atoms which contribute to the oxidation process could be much smaller than ρ_{O2}. On the other hand a higher reaction rate with a lower number of oxygen atoms may reflect nearly the experiment situation since most of the O_2

molecules would desorb at such low reaction rates. With this assumption these molecules are neglected at the simulation start which noticeably decreases duration of the simulation.

Therefore the oxidation parameters have the following meanings. The density of adsorbed oxygen atoms ρ_o is proportional to the oxygen pressure and oxidation time (cf. equation 29 and 30). At a constant pressure it is a value for oxidation time. The diffusion length l_o is defined by interaction between the oxygen atom and the surface carbon atoms which is a function of the temperature. The diffusion length is kept fixed at l_o = 10 µm, as obtained from the comparison with the experiment (cf. page 104). The oxidation probability p_{ox} is assumed to be dependent on the oxidation temperature. This correlation is unknown. It is supposed that it is not a linear function. However the range of the oxidation probability is limited, because at higher temperatures the oxidation of graphite would not only occur at defects and step edges but also directly at the surface. Hence, such dendritic structures as shown in figure 6-10 probably can not be realized in experiments. Shortly the oxidation parameters can be described with these three formulas:

$$\rho_o \propto \Delta t_{ox} \tag{31}$$

$$l_o \approx \text{const} \tag{32}$$

$$p_{ox} = f(T) \tag{33}$$

For simplicity ρ_o and p_{ox} are identified in parts of the following section directly with the oxidation time and temperature, respectively.

6.2.4 Simulation results

6.2.4.1 Oxidation process

With the simulation of the oxidation process some general trends of the oxidation process can be visualized. Some effects are already discussed in section 6.2.2 as temperature influence and oxidation time (including in p_{ox} or ρ_o, respectively).

A question is which area the oxygen atom can reach by its random walk. In order to describe this, the capture diameter is defined as the mean value between maximal position differences in horizontal and vertical directions. Its dependence on the diffusion length is shown in figure 6-20. It is proportional to the square root of l_o. For l_o = 10000 nm as used in parameter set A the diameter of the random walk would be about 70 nm. Thus the maximal capture diameter of a defect is about 140 nm. That is comparable with the value determined from experiments (see 5.2.1.2).

Another interesting aspect is the oxidation time. According to formula 9 the diameter of the nano-pits should grow linear with time. On the other hand formula 22 deduced from simulations says that this dependency is not exactly linear. The dependence of the pit diameter (determined by formula 34) on the oxidation time is visualized in figure 6-21. The dependency is only linear for a long oxidation time, which is much higher than the time used in parameter set A which represents the experiment (doted vertical line in figure 6-21b). Within this shorter oxidation time the pit growth is not linear with regard to the time. This could be caused by the ratio of the diffusion length and the pit diameter.

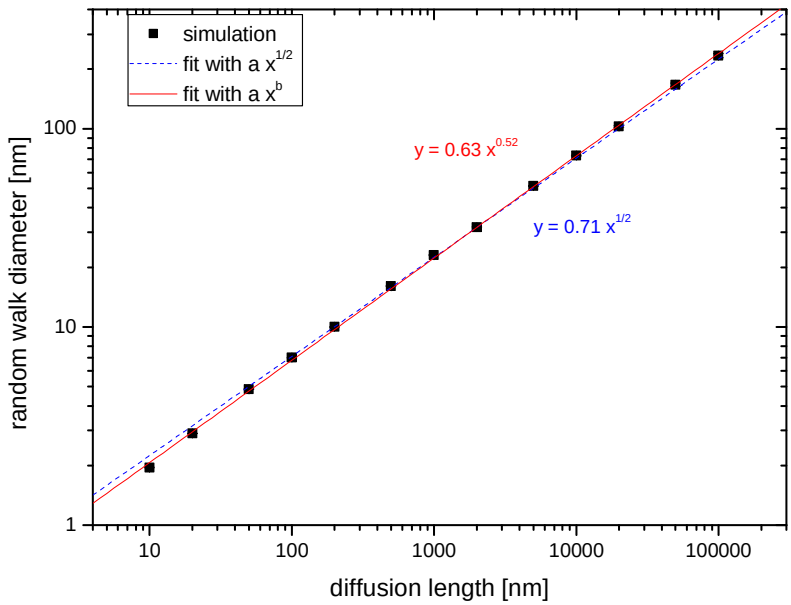

FIGURE 6-20: The mean diameter of the random walk in dependence on the diffusion length. It is evaluated from the mean value between maximal position differences in horizontal and vertical directions.

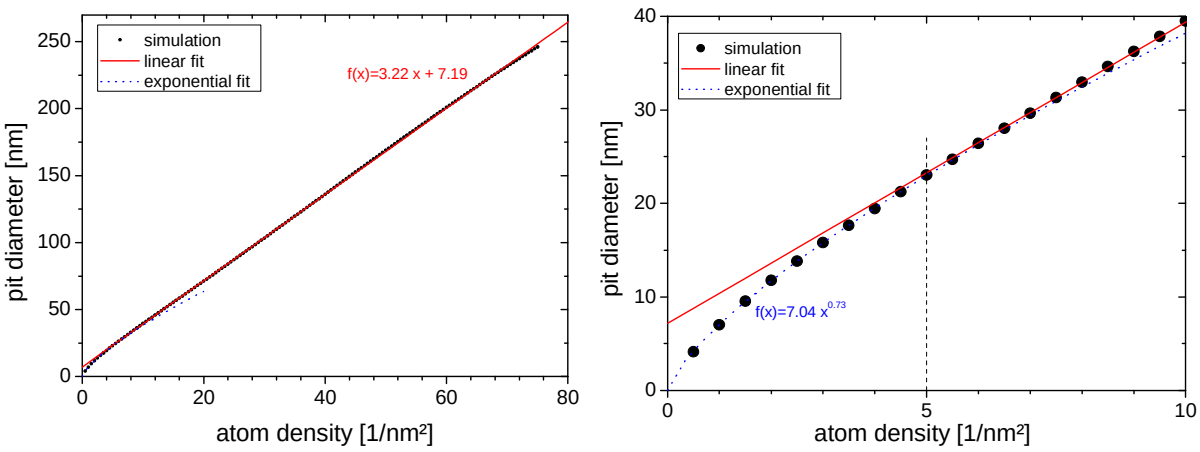

(a) (b)

FIGURE 6-21: Time dependence of the oxidation process. (a) For a long time and (b) for a shorter time (inset of (a)). The doted vertical line marks the value used in parameter set A.

$$d = \sqrt{\frac{4A}{\pi}} \tag{34}$$

For a short time scale the pit diameter can be fitted ~ $\rho_0^{0.73}$ which roughly corresponds to the area ~ $\rho_0^{1.56}$ (cf. figure 6-16). However this effect is not easy to study in experiment since other effects like thermalization time after inserting of the sample into the oven play a more important role.

6.2.4.2 Random defects

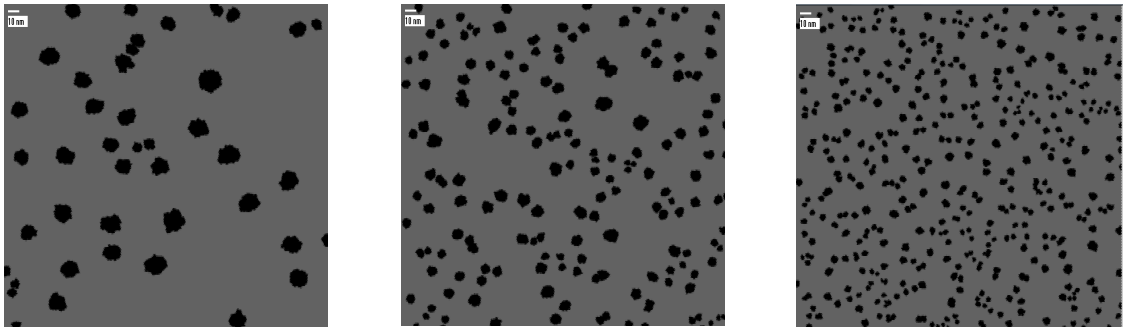

500 /µm² 2000 /µm² 5000 /µm²

FIGURE 6-22: Simulation results for oxidation of defects distributed at random positions for different defect densities. Parameter set A and A_{sheet} = 300 nm × 300 nm are used for these simulations.

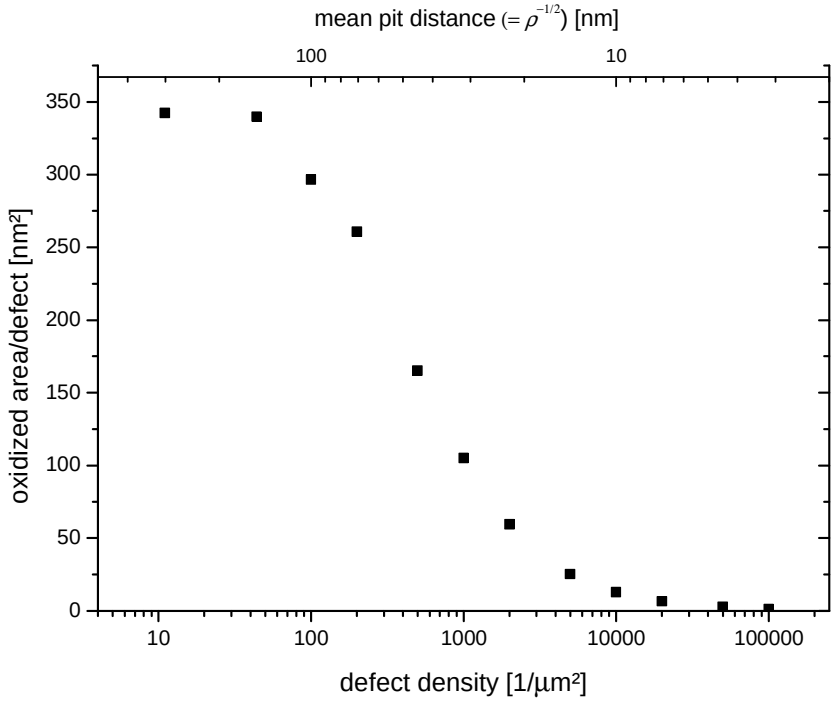

FIGURE 6-23: The mean pit size versus the defect density as a result of simulations.

Nano-pits produced by sputtering with argon ions are distributed at random positions on the surface. For comparison the defects in the following simulations are also put at random positions. Some selected simulation results are shown in figure 6-22. A low defect density would result in growth of pits which are unaffected by other defects (cf. figure 6-17c). Hence, they would grow to a maximal size.

For higher defect densities the defects would influence each other. The higher the defect density is the smaller are the pits. This is visible in figure 6-23. Note that the abscissa is logarithmic. For nano-pits with a diameter between 5 and 10 nm a defect density about 1000/µm² is reasonable. This is of course not a result of the simulation, since the

estimation of parameter set A is based on this defect density. However this diagram can be used to produce nano-pits with other sizes by changing the defect density.

An aspect neglected in the simulations is the oxidation of multilayer pits which grow faster. Especially for a high defect density the growth of multilayer pits becomes more probable. Therefore the pit size would become larger for a high defect density in figure 6-23 due to the formation of multilayer pits.

In section 5.2.1.2 the capture diameter d_{ca} was determined from experiments (≈ 150 nm). That can be compared with the simulation results in figure 6-23. For high pit distances the oxidized area/defect remains constant and becomes for distances < 100 nm smaller. This value corresponds to d_{ca}. It is roughly comparable with the value obtained from experiment considering the high inaccuracy.

6.2.4.3 Defect groups

For samples prepared with FIB the defects are produced as a pattern of points. Every point contains a group of defects. The number of defects is determined by the ion dose. It can be determined from SAMPLE 9 which is oxidized at a lower temperature. Thus the defects become visible but do not coalesce to nano-pits. STM measurements for two defect groups structured with different ion doses are shown in figure 6-24. For simulations a Gaussian distribution of defects is assumed. The width of the distribution is determined from the STM measurements. It is fixed at 30 nm for the following simulations.

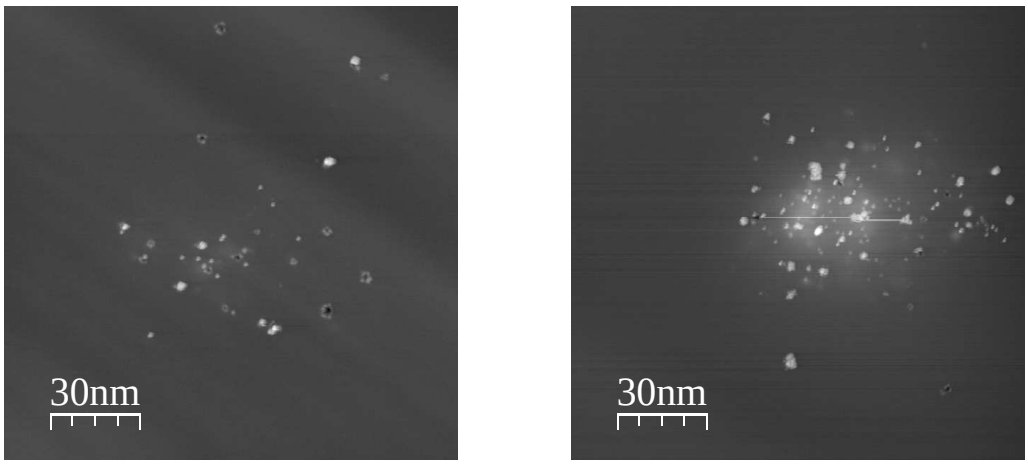

(a) (b)

FIGURE 6-24: Two defect groups (points) on SAMPLE 9 (a) exposed with a dot dose of 1.4×10^{-5} pAs, including 30 defects and (b) exposed with a dot dose of 7×10^{-5} pAs, including 120 defects.

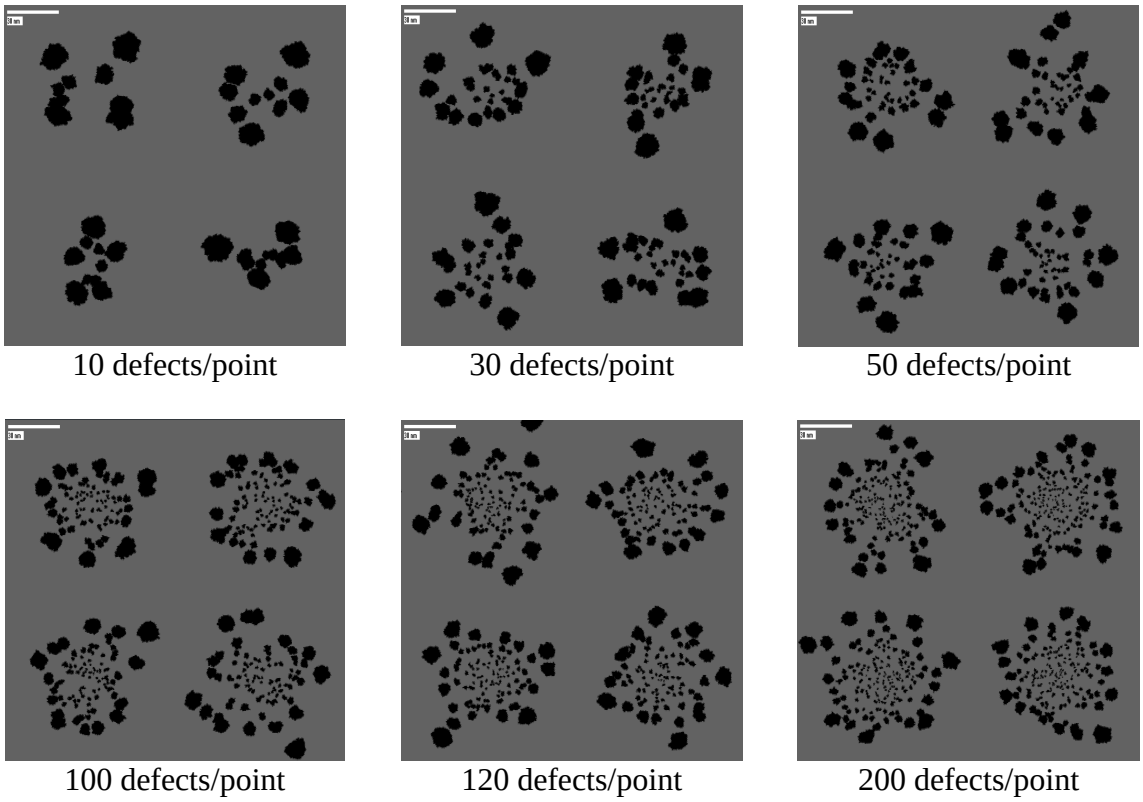

FIGURE 6-25: Simulation results for a lattice of defect groups with different defect densities. The point distance is 100 nm. The image size shown here is 200 nm × 200 nm. The simulation area is A_{sheet} = 350 nm × 350 nm including more defect groups at the borders.

"Ion Dose Dependence"

The influence of the ion dose on the pit structure is shown in figure 6-25. In the case of a low defect intensity the defects are comparable with the random positioned nano-pits. For higher defect densities the nano-pits are separated into two types. The first type is localized in the inner region of the defect group. These defects are only weakly oxidized. In the STM images the defects would not really be visible as pits, but as bright spots. The second type is localized at the border region of the defect group. These defects are well oxidized and build a ring around the defect group. These distribution of nano-pits make the production of single patterned clusters (grown at the nano-pits) difficult.

"Temperature Dependence"

The oxidation process can be tuned with the oxidation temperature. For the following simulation the defect density was fixed at 120 defects/point since the corresponding ion dose (cf. figure 6-24b) was used for most of the experiments. The simulation results are shown in figure 6-26. One can see that the shape of the defect group changes from the 'flower shape' (with large pits surrounding smaller ones) to equally sized nano-pits at p_{ox} = 0.003. For smaller p_{ox} the main mechanism for nano-pit formation is the coalescence of smaller pits in the inner region. Thus the emerged nano-pits are localized in the center of the spot. However the oxidation rate is too low for the production of larger pits. In order to obtain larger pits the oxidation time has been doubled. The simulation result is shown in figure 6-27. In this image the coalescence shows some statistical variations. In the case of the point at the bottom left side the smaller pits show less coalescence and are more equally distributed than for the other three.

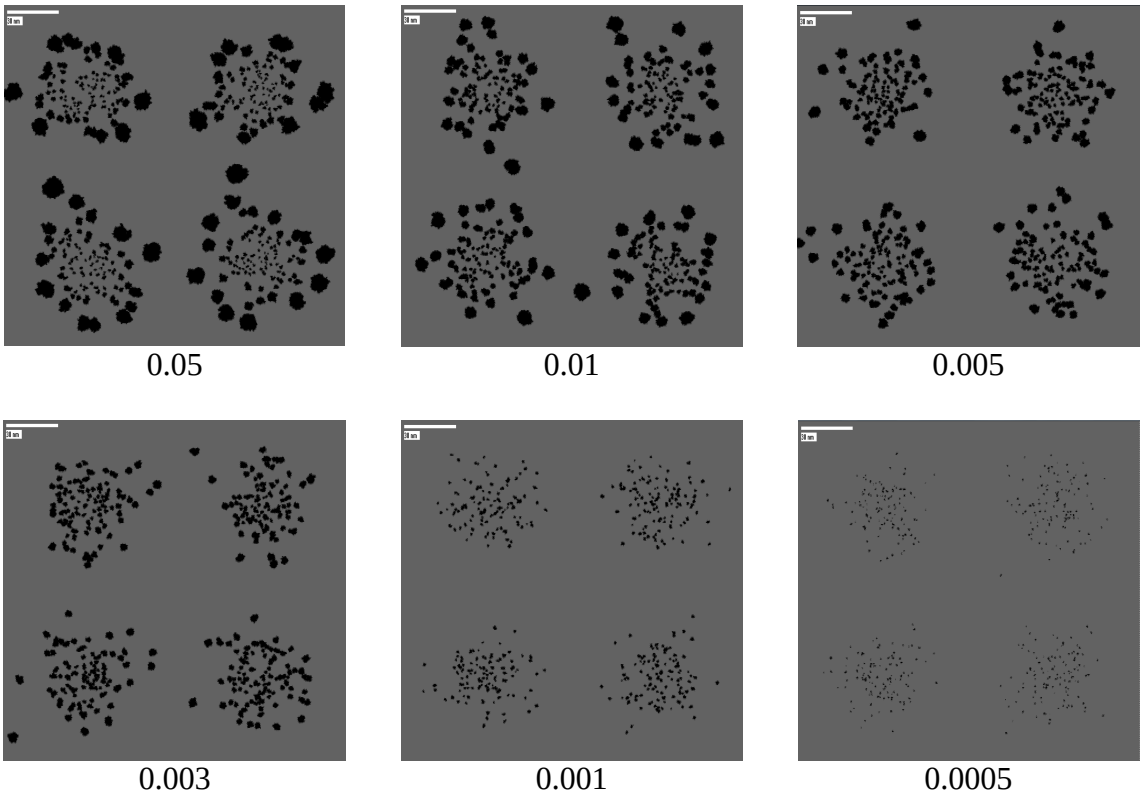

FIGURE 6-26: Simulation results of the oxidation of defect groups with different oxidation probabilities p_{ox} which represents the oxidation temperature.

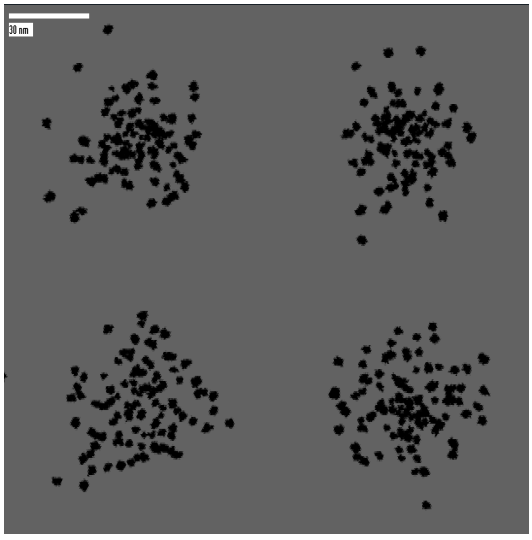

FIGURE 6-27: Simulation result for a reduced oxidation probability of p_{ox} = 0.001 and a higher oxidation time with ρ_0 = 10/nm².

This method was used for growth of single cluster patterns on SAMPLE 9. With the help of Ostwald ripening single clusters were produced in a regular pattern in distances of 100 nm from each other. However one may tune the ion dose and temperature at the same time to reduce the distance even more.

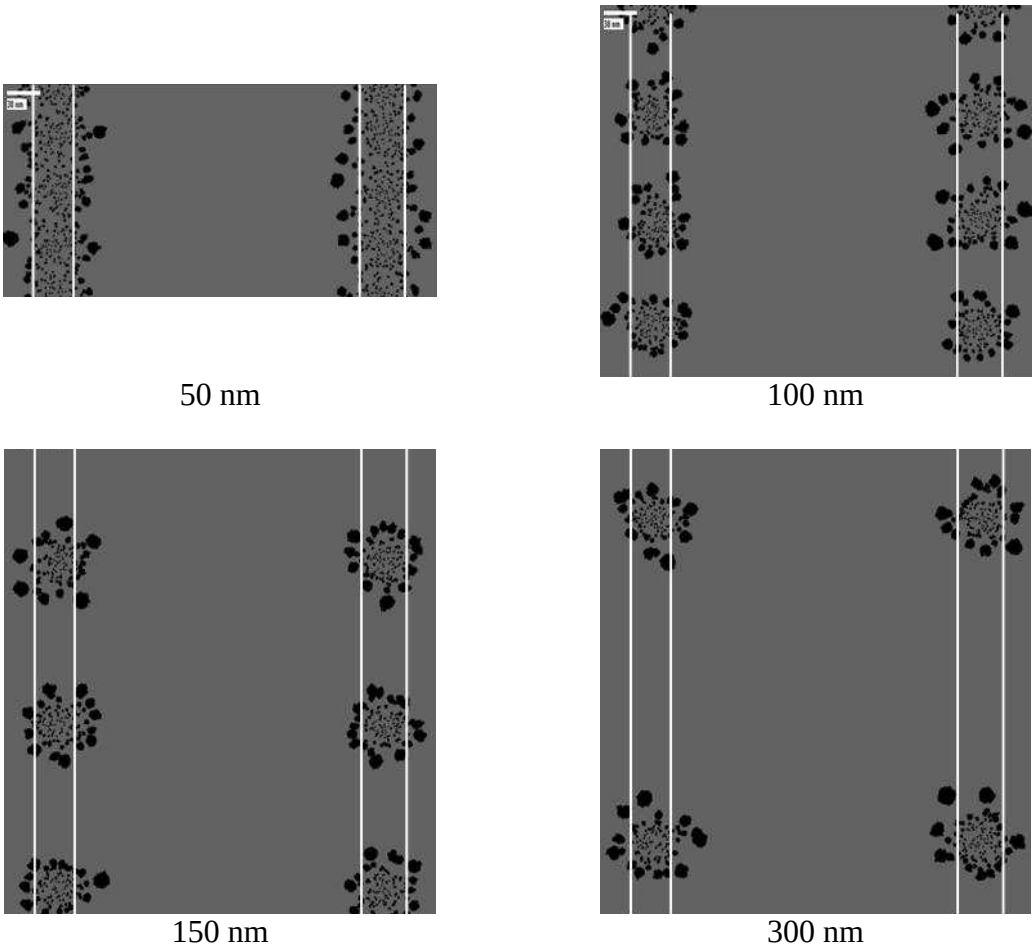

FIGURE 6-28: Simulation results for different point to point distances. The distance in the vertical direction is kept constant. The white lines should detach the influence in the horizontal direction for better visualization. The simulation parameters are the same as the parameter set A. The sheet size in the horizontal direction is 1000 nm and in vertical direction chosen in a way that 4 points fit into the simulation sheet. The images are cut out of the simulated area with a size of 400 nm in horizontal direction.

"Distance Dependence"

The influence of the capture diameter d_{ca} and the Gaussian distribution of defects on each point can be also visualized in simulations. For this the point to point distance in the horizontal direction is kept constant at 300 nm and the vertical distance is varied. Thus the simulation can be compared with the experiment in section 5.2.1.2 (in particular figure 5-5a). Some selected results are shown in figure 6-28. The effect becomes visible if only the influence in the vertical direction is considered (within the white lines). For a distance of 50 nm the points are coalesced and there are only defects within the white line. For a distance of 100 nm small nano-pits emerge in this region. They become larger for higher point distances. In the case of 300 nm there are some very large pits at the border regions.

The neglected multilayer oxidation would change the image. A high defect density benefits the emergence of multilayer pits in the center of the defect distribution, which oxidize faster. This leads to larger pits in the center, so the 'flower shape' does not appear in experiments.

7 Summary

"Nano-pits & Clusters"

In the present work the localized defect production with FIB on an HOPG surface has been combined with an oxidation process. The shape of the structure by variation of the ion dose was examined in a first experiment. The resulting structures were divided into three groups (cf. [1]).

For the **first group** structured with low ion doses (< 10^3 ions/point) 'nano-pits' with a depth of 1 HOPG layer were observed. These nano-pits could be produced in rows and in a square lattice of points. In another experiment they were arranged in a coded pattern (finding pattern). After metal deposition clusters were produced in a pattern of rows with a width about 50 nm. With optimized oxidation parameters single clusters were produced in a square pattern with a 100 nm pitch. To our knowledge this is the first example for the fabrication of single metal clusters in a given pattern by nano-structuring of a surface and Ostwald ripening. Furthermore the nano-pits were used for fabrication of lead layers with a thickness of one atomic layer.

The **second group** (10^3-10^5 ions/point) indicated the transition from nano-pits to nano-cavities. In these dose regions the structures exhibited a hill shape including multilayer pits.

"Nano-Cavities & Islands"

The **third group** structured with high ion doses (> 10^5 ions/point) exhibited 'nano-cavities' with a depth of several 10 nm. These nano-cavities have a nearly constant depth independent from the ion dose. This depth corresponds to the penetration depth of the gallium ions into the HOPG substrate. It amounts to approximately 50 nm for an ion energy of 35 keV. The depth was measured by exposure with a defocused ion beam for the production of broad structures. With an optimized beam focus nano-cavities with diameters down to 20 nm were produced in a square pattern with 50 nm pitch. An interesting application of nano-cavities is the fabrication of graphene devices. That was demonstrated in a first experiment for two exemplary structures. Furthermore it was demonstrated that larger metal islands grow in a pattern given by the nano-cavities.

"Simulations"

The measurements were compared with the corresponding simulations. A simulation of the impingement of gallium ions into a graphite substrate was performed with the TRIM-software. The penetration depth of the gallium ions was estimated evaluating the defect density. With this the penetration depth for different ion energies was predicted to be roughly a linear function of the ion energy. For a Gaussian distribution a width of the oxidized nano-cavities about 20 nm was evaluated, comparable with the experiment.

The oxidation process of nano-pits was simulated in a self-developed program. This program can be used in future to test the pattern and the preparation parameters before performing the real experiment. The program was used for random defects as well as for patterns of defects. It yields an explanation for the modified nano-pit production at reduced temperatures. The results are comparable with experiment. Furthermore the nano-pit growth could be simulated for different temperatures, point distances and defect densities.

"Cluster Properties"

The observed features in the STM measurements concerning the clusters were treated in a separate section. A first feature was the peak structure in the height distribution. The analysis showed that the peaks are induced by the layer by layer growth of the clusters. The lead clusters exhibited an odd-even oscillation in the height distribution. That could be explained with quantum well states in lead layers. The facet analysis showed that lead clusters form a facet at a height about 1 nm whereas silver clusters form a facet for cluster heights larger than 5 nm. Silver as well as lead clusters are modified after air contact but the modification is more severe for lead clusters than for silver. Changes of the shape of lead clusters were also observed during annealing and after STM tip interaction.

8 Outlook

During the experiments in the present study a number of new perspectives arose which could be the matter for further investigations.

"Clusters & Nano-wires"

One point in the present study was the fabrication of 'finding patterns'. In future these patterns may be used to investigate the same clusters during different preparation steps. For example the growth of the clusters can be observed by dividing the metal deposition into several steps and performing STM measurements between them. Another application are before-after investigations, for example to explain what happens to the lead clusters by annealing. That experiment could answer whether the clusters restructure or coalesce.

Another application of nano-pits is the production of nanometer sized metallic wires (*nano-wires*). Two possible ways are based on nano-pits patterned in rows. One way is to vary the nano-pit density and evaporate metal on the substrate. The question is whether the growing nano-particles can build a coherent structure by using the (adhesive) influence of the nano-pits. Another way is to proceed the oxidation process until the nano-pits coalesce and an elongated pit emerges. The nano-wires may grow within these *nano-grooves* after metal deposition. Further experiments should reveal the producibility of these structures.

"Nano-cavities & Graphene Structures"

The depth of the nano-cavities was investigated for an ion energy of 35 keV. For other energies the depth was predicted with simulations. In future the depth should be also obtained from experiments and compared with the simulation results.

There are a lot of possible applications for nano-cavities. One application is the fabrication of nano-particles within the nano-cavities. Another application as demonstrated in this work is the fabrication of graphene devices. Open questions are, e.g., the conductivity of these structures, the development of a method for transfer of a layer to other substrates and possibly the investigation of ballistic transport phenomena.

"Other Substrates"

The HOPG-substrate is experimentally simple to handle, but no versatile material for industrial applications because it is soft and can easily be deformed and it exhibits a non-negligible conductivity. A substrate often used in the industry is silicon. For this the oxidation process has to be replaced by another etching process, e.g. chemical etching or plasma etching (cf. [175-177]). For production of nano-pits with atomic depth substrates with lamellar structure are needed such as mica or molybdenum disulfide (cf. [178-180]).

"The Simulation Program"

The simulation program can be developed further. The present simulations considered only one graphene layer. It should be extended to more graphene layers since the oxidation of multilayer pits differs from the monolayer pits. For this purpose the defects should be produced in a separate program for a three dimensional substrate. Another possible extension is the simulation of the metal deposition process (including Ostwald ripening) to predict the best parameters for growth process such as ion dose or temperature. This would be helpful, e.g., for production of single clusters in a pattern.

9 References

"Publications"

[1] F. Ghaleh, R. Köster, H. Hövel, L. Bruchhaus, S. Bauerdick, J. Thiel, R. Jede
Controlled fabrication of nanopit patterns on a graphite surface using focused ion beams and oxidation
Journal of Applied Physics **104**, 044301 (2007)

Abstract:

We produced nanopits on a highly oriented pyrolytic graphite substrate arranged in a given pattern with a combination of focused ion beam (FIB) irradiation and an oxidation process. The FIB irradiation was carried out using a dedicated FIB nanofabrication tool [J. Gierak *et al.*, Appl. Phys. A: Mater. Sci. Process. **A80**, 187 (2005)]. After oxidation of the sample surface, defects produced by single ions were imaged as one monolayer deep nanopits with scanning tunneling microscopy. The penetration depth of the ions could be measured by oxidation of the defective volume produced on points irradiated with high ion doses. An array of well separated nanopits with a periodicity of 50 nm could be produced.

[2] M. Rohmer, F. Ghaleh, M. Aeschlimann, M. Bauer, H. Hövel
Mapping the femtosecond dynamics of supported clusters with nanometer resolution
The European Physical Journal D **45**, 491 (2007)

Abstract:

In this paper we present a combined STM, SEM and time-resolved PEEM study of silver clusters on a nano-patterned HOPG-substrate, exhibiting areas of different defect type and defect densities. The areas show small but distinct differences in the femtosecond dynamics associated with electronic excitations in the clusters. We assign these differences to variations in the cluster size distribution and variations in the cluster-substrate interaction as governed by the bonding to the different defect types.

"References"

[3] W. P. Halperin
Quantum sized effects in metal particles
Rev. Mod. Phys. **58**, 533 (1986)

[4] W. A. de Herr
The physics of simple metal clusters: experimental aspects and simple models
Rev. Mod. Phys. **65**, 611 (1993)

[5] K. H. Meiwes-Broer
Metal Clusters at Surfaces
Springer, Berlin, Heidelberg (2000)

[6] Ch. Kittel
Introduction to solid state physics
Oldenbourg Verlag (1998)

[7] J. Goodisman
Thomas-Fermi-Dirac-jellium model of the metal surface: Change of surface potential with charge
J. Chem. Phys. **86**, 882 (1987)

[8] J. L. Martins, J. Buttet, R. Car
Electronic and structural properties of sodium clusters
Phys. Rev. B **31**, 1804 (1985)

[9] B. K. Rao, P. Jena, M. Manninen, R. M. Nieminen
Spontaneous Fragmentation of Multiply Charged Metal Clusters
Phys. Rev. Lett. **58**, 1188 (1987)

[10] L. A. Peyser, T. H. Lee, R. M. Dickson
Mechanism of Ag_n Nanoclusters Photoproduction from Silver Oxide Films
J. Phys. Chem. B **106**, 7725 (2002)

[11] T. Gleitsmann, B. Stegemann, T. M. Bernhardt
Femtosecond-laser-activated fluorescence from silver oxide nanoparticles
Appl. Phys. Lett. **84**, 4050 (2004)

[12] V. Rapain, J.-P. Jamet, N. Vernier, M. Bauer, J. Ferré, C. Chappert, J. Gierak, D. Mailly
Magnetic interactions in dot arrays with prependicular anisotropy
J. Appl. Phys. **95**, 2614 (2004)

[13] C. Binns, F. Sirotti, H. Cruguel, S. H. Baker, P. Prieto, J. D. Bellier, S. C. Thornton
Static and dynamic magnetic behaviour of iron nanoclusters on magnetic substrates
J. Phys. Condens. Matter **15**, 4287 (2003)

[14] L. C. Sampaio, R. Hyndman, F. S. de Menezes, J. P. Jamet, P. Meyer, J. Gierak, C. Chappert, V. Mathet, J. Ferré
Power-law relaxation decay in two-dimensional arrays of magnetic dots interacting by long-range dipole-dipole interactions
Phys. Rev. B **64**, 184440 (2001)

[15] H. Hövel, I. Barke
Large noble metal clusters: electron confinement and band structure effects
New J. Phys. **5**, 31 (2003)

[16] H. Hövel
Clusters on surfaces: high-resolution spectroscopy at low temperatures
Appl. Phys. A **72**, 295 (2001)

[17] P. J. Berlowitz, C. H. F. Peden, D. W. Goodman
Kinetics of carbon monoxide oxidation on single-crystal palladium, platinum, and iridium
J. Phys. Chem. **92**, 5213 (1988)

[18] W. X. Li, C. Stamfl, M. Scheffler
Why is a Noble Metal Catalytically Active? The Role of the O-Ag Interaction in the Function of Silver as an Oxidation Catalyst
Phys. Rev. Lett. **90**, 256102 (2003)

[19] Y. D. Kim, M. Fischer, G. Ganteför
Origin of unusual catalytic activities of Au-based catalysts
Chem. Phys. Lett. **377**, 170 (2003)

[20] H. Häkkinen, M. Moseler, O. Kostko, M. Astruc Hoffmann, N. Morgner, B. v. Issendorff
Symmetry and structure of noble metal nanoparticles and the role of relativity
Phys. Rev. Lett. **93**, 093401 (2004)

[21] M. Astruc Hoffmann, G. Wrigge, B. v. Issendorff
Photoelectron spectroscopy of Al32000: Observation of 'Coulomb Staircase' in a free cluster
Phys. Rev. B **66**, 041404 (2002)

[22] H. Haberland, T.Hippler, J. Donges, O. Kostko, M. Schnidt, B. v. Issendorff
Melting of Sodium Clusters: where do the Magic Numbers come from
Phys. Rev. Lett. **94**, 035701 (2005)

[23] O. C. Wells
Scanning electron microscopy
McGraw-Hill Book Company (1974)

[24] R. K. Matta
High-resolution electron-beam exposure of photoresists
Electrochem. Technol. **5**, 382 (1967)

[25] T. Sun, R. F. M. Thornley
Luminescent electron-sensitive resist
J. Electrochem. Soc. **5**, 363 (1967)

[26] M. Schmidt, M. Eich, U. Huebner, R. Boucher
Electro-optically tunable photonic crystals
Appl. Phys. Lett. **87**, 121110 (2005)

[27] B. J. Y. Tan, C. H. Sow, T. S. Koh, K. C. Chin, A. T. S. Wee, C. K. Ong
Fabrication of Size Tunable Gold Nanoparticles Array with Nanosphere Lithography, Reactive Ion Etching, and Thermal Annealing
J. Phys. Chem. B **109**, 11100 (2005)

[28] T. Kraus, L. Malaquin, H. Schmid, W. Riess, N. D. Spencer, H. Wolf
Nanoparticle printing with single-particle resolution
Nature Nanotechnology **2**, 570 (2007)

[29] T. Mühl
Scanning-tunneling-microscopy-based nanolithography of diamond-like carbon films
Appl. Phys. Lett. **85**, 5727 (2004)

[30] S. W. Hla, K. F. Braun, K. H. Rieder
Single-atom manipulation mechanics during a quantum corral construction
Phys. Rev. B **67**, 201402 (2003)

[31] N. Oyabu, Y. Sugimoto, M. Abe, O. Custance, S. Morita
Lateral manipulation of single atoms at semiconductor surfaces using atomic force microscopy
Nanotechnology **16**, S112 (2005)

[32] K. Kanaya, K. Shimizu, Y. Ishikawa
Scattering effects in ion beam exposure of photoresist polymer films
Brit. J. Appl. Phys. **1**, 1657 (1968)

[33] S. Matsui, Y. Ochiai
Focused ion beam applications to solid state devices
Nanotechnology **7**, 247 (1996)

[34] A. Hannour, L. Bardotti, B. Prével, E. Bernstein, P. Mélinon, A. Perez, J. Gierak, E. Bourhis, D. Mailly
2D arrays of CoPt nanoclusters assemblies
Surf. Sci. **594**, 1 (2005)

[35] L.Bardotti, B. Prével, P. Jensen, M. Treilleux, P. Mélinon, A. Perez, J. Gierak, G. Faini, D. Mailly
Organizing nanoclusters on functionalized surfaces
Appl. Surf. Sci. **191**, 205 (2002)

[36] T. Mitsui, D. Stein, Y. R. Kim, D. Hoogerheide, J. A. Golovchenko
Nanoscale Volcanoes: Accretion of Matter at Ion-Sculpted Nanopores
Phys. Rev. Lett. **96**, 036102 (2006)

[37] M. I. Katsnelson
Graphene: carbon in two dimensions
Materials Today **10**, 20 (2007)

[38] A. H. Castro Neto, F. Guinea, N. M. R. Peres, K. S. Novoselov, A. K. Geim:
The electronic properties of graphene
arXiv.org/0709.1163v2 (2008)

[39] A. H. Castro Neto, F. Guinea, N. M. R. Peres
Drawing conclusions from graphene
Physics World **19**, 33 (2006)

[40] P. R. Wallace
The Band Theory of Graphite
Phys. Rev. **71**, 622 (1947)

[41] K. S. Novoselov, A. K. Geim, S. V. Morozov, D. Jiang, M. I. Katsnelson, I. V. Grigorieva, S. V. Dubonos
Tow-dimensional gas of massless Dirac fermions in graphen
Nature **438**, 197 (2005)

[42] A. K. Geim, K. S. Novoselov
The rise of graphene
nature materials **6**, 183 (2007)

[43] S. V. Morozov, K. S. Novoselov, M. I. Katsnelson, F. Schedin, D. C. Elias, J. A. Jaszczak, A. K. Geim
Giant Intrinsic Carrier Mobilities in Graphene and Its Bilayer
Phys. Rev. Lett. **100**, 016602 (2008)

[44] J. H. Chen, C. Jang, S. Xiao, M. Ishigami, M. S. Fuhrer
Intrinsic and extrinsic performance limits of graphene devices on SiO_2
Nature Nanotechnology **3**, 206 (2008)

[45] K. S. Novosolev, A. K. Geim, S. V. Morozov, D. Jiang, Y. Zhang, S. V. Dubonos, I. V. Grigorieva, A. A. Firsov
Electric Field Effect in Atomically Thin Carbon Films
Science **306**, 666 (2004)

[46] K. V. Emtsev, F. Speck, Th. Seyller, L. Ley, J. D. Riley
Interaction, growth, and ordering of epitaxial graphene on Si{0001} surfaces: A comparative photoelectron spectroscopy study
Phys. Rev. B **77**, 155303 (2008)

[47] E. McCann
Asymmetry gap in the electronic band structure of bilayer graphene
Phys. Rev. B **74**, 161403 (2006)

[48] J. C. Charlier, P. C. Eklund, J. Zhu, A. C. Ferrari
Electron and Phonon Properties of Graphene: Their Relationship with carbon Nanotubes
Carbon Nanotubes, Topics Appl. Phys. **111**, 673 (2008)

[49] B. Partoens, F. M. Peeters
From graphene to graphite: Electronic structure around the K point
Phys. Rev. B **74**, 075404 (2006)

[50] S. Banerjee, M. Sardar, N. Gayathri, A. K. Tyagi, Baldev Raj
Conductivity landscape of highly oriented pyrolytic graphite surfaces containing ribbons and edges
Phys. Rev. B **72**, 075418 (2005)

[51] T. Ohta, A. Bostwick, T. Seyller, K. Horn, E. Rotenberg
Controlling the Electronic Structure of bilayer Graphene
Science **313**, 951 (2006)

[52] X. Chu, L. D. Schmidt
Reaction of NO, O_2, H_2O, and CO_2 with the basal plane of graphite
Surface Science **268**, 325 (1992)

[53] A. J. Bennett, B. McCarrol, R. P. Messmer
Molecular Orbital Approach to Chemisorption II. Atomic H, C, N, O, and F on Graphite
Phys. Rev. B **3**, 1397 (1971)

[54] D. R. Olander, W. Siekhaus, R. Jones, J. A. Schwarz
Reactions of Modulated Beam with Pyrolytic Graphite. I. Oxidation of the Basal Plane
J. Chem. Phys. **57**, 408 (1972)

[55] G. Blyholder, J. S. Binford, H. Eyring
A Kinetic Theory for the Oxidation of Carbonized Filaments
J. Phys. Chem. **62**, 263 (1958)

[56] R. H. Jones, D. R. Olander, W. J. Siekhaus, J. A. Schwarz
Investigation of Gas-Solid Reactions by Modulated Molecular Beam Mass Spectrometry
J. Vac. Sci. Technol. **9**, 1429 (1972)

[57] J. Nagle, R. F. Strickland-Constable
Oxidation of carbon between 1000 °C and 2000 °C
Proceeding of the Fifth Conference on Carbon, vol. **1**, Pergamon Press, Oxford, 154 (1962)

[58] J. R. Walls, R. F. Strickland-Constable
Oxidation of carbon between 1000–2400 °C
Carbon **1**, 333 (1964)

[59] NanoFIB project 2001
EC growth project Contract No. G5RD-CT2000-0034
Project homepage: www.nanofib.com

[60] R. G. Forbes
Understanding how the liquid-metal ion source works
Vacuum, **48**, 85 (1997)

[61] W. Gilbert
De Magnete
Book 2, London (1600)
Translation by P. F. Mottelay, Dover, New York (1958)

[62] G. I. Taylor
Disintegration of Water Drops in an Electric Field
Proc. Roy. Soc. Lond. A **280**, 383 (1964)

[63] V. E. Krohn, G. R. Ringo
Ion source of high brightness using liquid metal
Appl. Phys. Letters **27**, 479 (1975)

[64] J. F. Mahoney, A. Y. Yahiku, H. L. Daley, R. D. Moore, J. Perel
Electrodynamics Ion Source
J. Appl. Phys. **40**, 5101 (1969)

[65] A. E. Bell, L. W. Swanson
The Influence of Substrate Geometry on the Emission Properties of a Liquid Metal Ion Source
Appl. Phys. A **41**, 335 (1986)

[66] R. G. Forbes
Field evaporation theory: a review of basic ideas
Appl. Surface Science **87**, 1 (1995)

[67] E. W. Müller
Field Desorption
Phys. Rev. **102**, 618 (1956)

[68] V. E. Krohn
Electrohydrodynamic capillary source of ions and charged droplets
J. Appl. Phys. **45**, 1144 (1973)

[69] L. W. Swanson, G. A. Schwind, A. E. Bell
Measurement of the energy distribution of gallium liquid metal ion source
J. Appl. Phys. **51**, 3453 (1980)

[70] G. D. Alton, P. M. Read
The emittence characteristics of a gallium liquid-metal ion source
J. Appl. Phys. **66**, 1018 (1989)

[71] J.J. Van Es, J. Gierak, R.G. Forbes, V.G. Suvorov, T. Van den Berghe, Ph. Dubuisson, I. Monnet, A. Septier
An improved gallium liquid metal ion source geometry for nanotechnology
Microelectronic Engineering **73**, 132 (2004)

[72] J. Gierak, D. Mailly, P. Hawkes, R. Jede, L. Bruchhaus, L. Bardotti, B. Prével, P. Mélinon, A. Perez, R. Hyndman, J.-P. Jamet, J. Ferré, A. Mougin, C. Chappert, V. Mathet, P. Warin, J. Chapman
Exploration of the ultimate patterning potential achievable with high resolution focused ion beams
Appl. Phys. A **80**, 187 (2005)

[73] R. L. Seliger, J. W. Ward, V. Wang, R. L. Kubena
A high-intensity ion probe with submicrometer spot size
Appl. Phys. Lett. **34**, 310 (1978)

[74] P. Kitslaar, M. Strassner, I. Sagnes, E. Bourhis, X. Lafosse, C. Ulysse, C. David, R. Jede, L. Bruchhaus, J. Gierak
Towards the creation of quantum dots using FIB technology
Microelectronic Engineering **83**, 811 (2006)

[75] J. Gierak, E. Bourhis, R. Jede, L. Bruchhaus, B. Beaumont, P. Gibart
FIB technology applied to the improvement of the crystal quality of GaN and to the fabrication of organised arrays of quantum dots
Microelectronic Engineering **73**, 610 (2004)

[76] G. Ben Assayag, P. Sudraud, J. Gierak, D. Remiens, L. Menigaux, L. Dugrand
Focused ion beam machining of mirror facets of a monolithicaly integrated GaAs/GaAlAs double heterojunction (DH) laser and its optical waveguide
Microelectronic Engineering **11**, 413 (1990)

[77] Hompage of Raith GmbH
http://www.raith.com

[78] J. Gierak, A. Septier, C. Vieu
Design and realization of a very high-resolution FIB nanofabrication instrument
Nucl. Instrum. Methods Phys. Res. A **427**, 91 (1999)

[79] A. L. Biance, J. Gierak, É. Bourhis, A. Madouri, X. Lafosse, G. Patriarche, G. Oukhaled, C. Ulysse, J. C. Galas, Y. Chen, L. Auvray
Focused Ion Beam sculped membranes for nanoscience tooling
Microelectronic Engineering **83**, 1474 (2006)

[80] J. Gierak, E. Cambril, M. Schneider, C. David, D. Mailly, J. Flicstein, G. Schmid
Very high-resolution focused ion beam nanolithography improvement: A new three dimensional patterning capacibility
J. Vac. Sci. Technol. B **17**, 3132 (1999)

[81] R. Hyndman, P. Warin, J. Gierak, J. Ferré, J. N. Chapman, J. P. Jamet, V. Mathet, C. Chappert
Modification of Co/Pt multilayers by gallium irradiation-Part 1: The effect on structural and magnetic properties
J. Appl. Phys. **90**, 3843 (2001)

[82] P. Warin, R. Hyndman, J. Gierak, J. N. Chapman, J. Ferré, J. P. Jamet, V. Mathet, C. Chappert
Modification of Co/Pt multilayers by gallium irradiation-Part 2: The effect of patterning using a highly focused ion beam
J. Appl. Phys. **90**, 3850 (2001)

[83] C. Vieu, J. Gierak, H. Launois, T. Aign, P. Meyer, J. P. Jamet, J. Ferré, C. Chappert, T. Devolder, V. Mathet
Modification of magnetic properties of Pt/Co/Pt thin layers by focused gallium ion beam irradiation
J. Appl. Phys. **91**, 3103 (2002)

[84] R. Hyndman, A. Mougin, L. C. Sampaio, J. Ferré, J. P. Jamet, P. Meyer, V. Mathet, C. Chappert, D. Mailly, J. Gierak
Magnetization reversal in weakly coupled magnetic patterns
J. Magn. Magn. Mater. **240**, 34 (2002)

[85] S. Duffe (former: Krause)
Massenselektierte Cluster deponiert auf Oberflächen
diploma thesis, Univ. Dortmund (2006)

[86] G. Binnig, H. Rohrer, Ch. Gerber, and E. Weibel
Surface Studies by Scanning Tunneling Microscopy
Phys. Rev. Lett. **49**, 57 (1982)

[87] G. Binnig and H. Rohrer
Scanning Tunneling Microscopy
Hel. Phys. Acta **55**, 726 (1982)

[88] K. von Bergmann, S. Heinze, M. Bode, G. Bihlmayer, S. Bügel, R. Wiesendanger
Complex magnetism of the Fe monolayer on Ir(111)
New J. Phys. **9**, 396 (2007)

[89] M. Wilms, M. Kruft, G. Bermes, K. Wandelt
A new and aophisticated electrochemical scanning tunneling microscope design fort he investigation of potentiodynamic processes
Rev. Sci. Instrum. **70**, 3641 (1999)

[90] T. Tansel, O. M. Magnussen
Video STM Studies of Adsorbate Diffusion at Electrochemical Interfaces
Phys. Rev. Lett. **96**, 026101 (2006)

[91] T. Mayer Kuckuk
Kernphysik
Teubner-Verlag, Stuttgart (1985)

[92] E. U. Condon, R. W. Gurney
Wave mechanics and radioactive disintegration
Nature **122**, 439 (1928)

[93] R. W. Gurney, E. U. Condon
Quantum Mechanics and Radioactive Disintegration
Phys. Rev. **33**, 127 (1929)

[94] H.-J. Güntherodt, R. Wiesendanger
Scanning Tunneling Microscopy I
Springer, Berlin, Heidelberg, New York (1994).

[95] J. Tersoff und D. R. Hamann
Theory and Application for the Scanning Tunneling Microscope
Phys. Rev. Lett. **50**, 1998 (1983)

[96] J. Bardeen
Tunneling from a Many-Particle Point of View
Phys. Rev. Lett. **6**, 57 (1961)

[97] P. Sautet
Atomic adsorbate identification with the STM: a theoretical approach
Surface Science **374**, 406 (1997)

[98] I. S. Tilinin, M. K. Rose, J. C. Dunphy, M. Salmeron, M. A. Van Hove
Identification of adatoms on metal surfaces by STM; experiment and theory
Surface Schience **418**, 511 (1998)

[99] Omicron Nanotechnology
http://www.omicron.de

[100] T. Becker, H. Hövel, M. Tschudy, B. Reihl
Applications qith a new Low-Temperature UHV STM at 5 K
Appl. Phys. A **66**, S27 (1998)

[101] T. Irawan
Morphologie und elektronische Struktur von Edelmetallclustern hergestellt durch gestreutes Wachstum auf HOPG
diploma thesis, Univ. Dortmund (2003)

[102] B. Sieben
Rastertunnelmikroskopie an Clustersystemen
diploma thesis, Univ. Dortmund (2007)

[103] R. Köster
Nanostrukturen auf Graphit erzeugt mit fokussierten Ionenstrahlen (FIB): Wachstum von Silber- und Gold-Clustern
diploma thesis, Univ. Dortmund (2006)

[104] N. Grönhagen
Wachstum von Nanostrukturen auf strukturiertem Graphit
diploma thesis, TU Dortmund (2008)

[105] T. Irawan, I. Barke, H. Hövel
Size-dependent morphology of gold clusters grown on nanostructured graphite
Appl. Phys. A **80**, 929 (2005)

[106] I. Horcas, R. Fernandez, J.M. Gomez-Rodriguez, J. Colchero, J. Gomez-Herrero, and A.M. Baro
wsxm: A software for scanning probe microscopy and a tool for nanotechnology
Rev. Sci. Inst. **78**, 013705 (2007)

[107] http://www.nanotec.es

[108] J. Tersoff, D. R. Hamann
Theory of the Scanning Tunneling Microscope
Phys. Rev. B **31**, 805 (1985)

[109] H. Henzler, W. Göpel
Oberflächenphysik des Festkörpers
Teubner Verlag, Stuttgart (1991)

[110] C. N. Bergland, W. E. Spicer
Photoemission Studies of Copper and Silver: Theory
Phys. Rev. **136**, A1030 (1964)

[111] B. Grimm
Tunnelspektroskopie und Photoemission bei tiefen Temperaturen an Edelgas-Modellsystemen und Nanostrukturen
PHD thesis, univ. Dortmund (2000)

[112] W. Swiech, G. H. Fecher, Ch. Ziethen, O. Schmidt, G. Schönhense, K. Grzelakowski, C. M. Schneider, R. Frömter, H. P. Oepen, J. Kirschner
Recent progress in photoemission microscopy with emphasis on chemical and magnetic sensitivity
J. Electron Spectroscopy Rel. Phenom. **84**, 171 (1997)

[113] homepage of AG Aeschlimann at TU Kaiserslautern
http://www.physik.uni-kl.de/aeschlimann

[114] P. Trucano, R. Chen
Structure of graphite by neutron diffraction
Nature **13**, 136 (1975)

[115] http://www.webelements.com

[116] G. R. Hennig
Determination of Lattice Vacancies in Graphite
J. Chem Phys. **40**, 2877 (1964)

[117] R. T. Yang, C. Wong
Kinetics and mechanism of oxidation of basal plane on graphite
J. Chem. Phys. **75**, 4471 (1981)

[118] H. Chang, A. J. Bard
Scanning Tunneling Microscopy Studies of Carbon-Oxygen Reactions on Highly Oriented Pyrolytic Graphite
J. Am. Chem. Soc. **113**, 5588 (1991)

[119] X. Chu, L. D. Schmidt
Gasification of Graphite Studied by Scanning Tunneling Microscopy
Carbon **29**, 1251 (1991)

[120] E. L. Evans, R. J. M. Griffiths, J. M. Thomas
Kinetics of Single-Layer Graphite Oxidation: Evaluation by Electron Microscopy
Science **171**, 174 (1971)

[121] J. R. Hahn
Promoted graphite ocidation in the presence of Cs trapped between basal planes
Surface Science **423**, L216 (1999)

[122] A. Tracz, G. Wegner, J. R. Rabe
Kinetics of Surface Roughening via Pit Growth during the Oxidation of the Basal Plane of Graphite. 1. Experiments
Langmuir **9**, 3033 (1993)

[123] F. Stevens, L. A. Kolodny, T. P. Beebe
Kinetics of Graphite Oxidation: Monolayer and Multilayer Etch Pits in HOPG studied by STM
J. Phys. Chem. B **102**, 10799 (1998)

[124] T. Pakula, A. Tracz, G. Wegner, J. P. Rabe
Kinetics of surface roughening via pit growth during the oxidation of the basal plane of graphite. II. Theory and simulation
J. Chem. Phys. **99**, 8162 (1993)

[125] F. Stevens, T. P. Beebe
Computer modelling of graphite oxidation: differences between monolayer and multilayer etching
Computers & Chemistry **23**, 175 (1999)

[126] D. L. Patrik, V. J. Cee, T. P. Beebe
"Molecule Corrals" for Studies of Monolayer Organic Films
Science **265**, 231 (1994)

[127] J. D. McBride, B. V. Tassell, R. C. Jachmann, T. P. Beebe
Molecule Corrals as Templates for the Formation of Metal and Silicon Nanostructures
J. Phys. Chem. B **105**, 3972 (2001)

[128] H. Hövel, Th. Becker, A. Bettac, B. Reihl, M. Tschudy, E. J. Williams
Controlled Cluster condensation into performed nanometer-sized pits
J. Appl. Phys. **81**, 154 (1997)

[129] J. R. Hahn, H. Kang, S. Song, J. C. Jeon
Observation of charge enhancement induced by graphite atomic vacancy: A comparative STM and AFM study
Phys. Rev. B **53**, R1725 (1996)

[130] Y. J. Zhu, A. Schnieders, J.D. Alexander, T. P. Beebe
Pit-Templated Synthesis and Oxygen Adsorption properties of Gold Nanostructures on Highly Oriented Pyrolytic Graphie
Langmuir **18**, 5728 (2002)

[131] F. Ghaleh
Messungen mit Photoelektronen Spektroskopie an Metallclustern auf Edelgasschichten
diploma thesis, Univ. Dortmund (2005)

[132] Y.-J. Zhu, T. A. Hansen, S. Ammermann, J. D. McBride, T. P. Beebe
Nanometer-Size Monolayer and Multilayer Molecule Corrals on HOPG: A Depth-Resolved Mechanistic Study by STM
J. Phys. Chem. B **105**, 7632 (2001)

[133] G. Bräuchle, S. Richard-Schneider, D. Illig, J. Rockenberger, R. D. Beck, M. M. Kappes
Etching nanometer sized holes of variable depth from carbon cluster impact induced defects on graphite surfaces
Appl. Phys. Lett. **67**, 52 (1995)

[134] L. Seminara, P. Convers, R. Monot, W. Harbich
Implantation of size-selected silver clusters into graphite
Eur. Phys. J. D **29**, 49 (2004)

[135] L. L. Wang, X. C. Ma, Y. Qi, P. Jiang, J. F. Jia, Q. K. Xue, J. Jiao, X. H. Bao
Controlled growth of uniform silver clusters on HOPG
Ultramicroscopy **105**, 1 (2005)

[136] M. Wutz, H. Adam, W. Walcher
Theorie und Praxis der Vakuumtechnik
or in english
Theory and practice of vacuum technology
Verlag Vieweg, Braunschweig/Wiesbaden (1992)

[137] R. Anton, P. Kreutzer
In situ TEM evaluation of the growth kinetics of Au particles on highly oriented pyrolithic graphite at elevated temperatures
Phys. Rev. B **61**, 16077 (2000)

[138] J. A. Venables
Rate Equation Approaches to Thin Film Nucleation Kinetics
Phil. Mag. **27**, 697 (1973)

[139] G. Bräuchle, S. Richard-Schneider, D. Illig, J. Rockenberger, R. D. Beck, M. M. Kappes
Etching nanometer sized holes of variable depth from carbon cluster impact induced defects on graphite surfaces
Appl. Phys. Lett. **67**, 52 (1995)

[140] R. Anton, I. Schneidereit
In situ TEM investigations of dendritic growth of Au particles on HOPG
Phys. Rev. B **58**, 13874 (1998)

[141] M. Munzinger, C. Wiemann, M. Rohmer, L.Guo, M. Aeschlimann, M. Bauer
The lateral photoemission distribution from a defined cluster/substrate system as probed by photoemission electron microscopy
New J. Phys. **7**, 68 (2005)

[142] M. Rohmer, C. Wiemann, M. Munzinger, L. Guo, M. Aeschlimann, M. Bauer
Local correlation of photoemission electron microscopy and STM at a defined cluster substrate system
Appl. Phys. A **82**, 87 (2006)

[143] O. Pfennigstorf, A. Petkova, Z. Kallassy, M. Henzler
Conductivity of ultrathin Pb films during growth on Si(111) at low temperatures
Eur. Phys. J. B **30**, 111 (2002)

[144] O. Pfennigstorf, K. Lang, H. L. Günter, M. Henzler
Electronic transport in ultrathin epitaxial Pb films on Si(111) surfaces
Appl Surf. Science **162**, 537 (2000)

[145] I. Vilfan, M. Henzler, O. Pfenningstorf, H. Pfnür
Anomalous thickness dependence of the Hall effect in ultrathin Pb layers on Si(111)
Phys. Rev. B **66**, 241306 (2002)

[146] W. Ostwald
Lehrbuch der Allgemeinen Chemie
vol. 2, part 1 (1896)

[147] Y. Zhu, J. D. McBride, T. A. Hansen, T. P. Beebe
Controlled Production of Molecule Corrals Using Cesium Ion Bombardment: A TOPF-SIMS, XPS, and STM study
J. Phys. Chem. B **105**, 2010 (2001)

[148] A. Böttcher, M. Heil, N. Stürzl, S. S. Jester, S. Malik, F. Pérez-Willard, P. Brenner, D. Gerthsen, M. Kappes
Nanostructuring the graphite basal plane by focused ion beam patterning and oxygen etching
Nanotechnology **17**, 5889 (2006)

[149] X. Liang, Z. Fu, S. Y. Chou
Graphene Transistors Fabricated via Transfer-Printing In Device Active-Areas on Large Wafer
Nano Letters **7**, 3840 (2007)

[150] M. Knop, U. Wieser, U. Kunze, D. Reuter, A. D. Wieck
Ballistic rectification in an asymmetric mesoscopic cross junction
Appl. Phys. Lett. **88**, 082110 (2006)

[151] M. Knop, M. Richter, R. Maßmann, U. Wieser, U. Kunze, D. Reuter, C. Riedesel, A. D. Wieck
Preparation of electron waveguide devices on GaAs/AlGaAs using negative-tone resist calixarene
Semicond. Sci. Technol. **20**, 814 (2005)

[152] J. Akola, H. P. Heiskanen, M. Manninen
Edge-dependent selection rules in magic triangular graphene flakes
Phys. Rev. B **77**, 193410 (2008)

[153] H. Heiskanen, M. Manninen, J. Akola
Electronic structure of triangular, hexagonal and round graphene flakes near the Fermi level
Phys. Rev B, to be published

[154] Böttcher et al.
Nanostructuring of the HOPG surface
Verhandl. DPG (VI) 43, O 4.3 (2008)

[155] H. Hövel, I. Barke
Morphology and electronic structure of gold clusters on graphite: scanning-tunneling techniques and photoemission
Progress in Surface Science **81**, 53 (2006)

[156] K. Hattori, T. Iimori, K. Komori
Development of UHV-STM/STS at 2 K
Thin Solid Films **281-282**, 644 (1996)

[157] I. Barke
Morphology and Electronic Structure of Gold Clusters on Graphite
PhD thesis, Univ. Dortmund (2004)

[158] Y. Jia, B. Wu, H. H. Weitering, Zh. Zhang
Quantum size effects in Pb films from first principles: The role of the substrate
Phys. Rev. B **74**, 035433 (2006)

[159] C. M. Wei, M. Y. Chou
Theroy of quantum size effects in thin Pb(111) films
Phys. Rev. B **66**, 233408 (2002)

[160] H. Hong, C. M. Wie, M. Y. Chou, Z. Wu, L. Basile, H. Chen, M. Holt, T. C. Chiang
Alternating Layer and Island Growth of Pb on Si by spontaneous Quantum Phase Separation
Phys. Rev. Lett. **90**, 076104 (2003)

[161] I. B. Altfeder, K. A. Matveev, D. M. Chen
Electron Fringes on a Quantum Wedge
Phys. Rev. Lett. **78**, 2815 (1997)

[162] L. E. C. van de Leemput, P. H. H. Rongon, B. H. Timmerman, H. van Kempen
Calibration and characterization of piezoelectric elements as used in scanning tunneling microscopy
Rev. Sci. Instrum. **62**, 989 (1991)

[163] S. Liu, Y.-J. Lu, M. M. Kappes, J. A. Ibers
The Structure of the C_{60} Molecule: X-Ray Crystal Structure Determination of a Twin at 110 K
Science **254**, 408 (1991)

[164] N. Metropolis, S. Ulam
The Monte Carlo Method
J. Am. Statistical Ass. **44**, 335 (1949)

[165] J. Ziegler
www.srim.org

[166] J. Ziegler, J. P. Biersack, U. Littmark
The Stopping and Range of Ions in Solids
Pergamon Press, New York (1985)

[167] J. F. Ziegler, J. M. Manoyan
The stopping of ions in compounds
Nuc. Inst. Meth. B **35**, 215 (1988)

[168] G. B. Kinchin, R. S. Pease
The displacement of Atoms in Solids by Radiation
Rep. Prog. Phys. **18**, 1 (1955)

[169] P. Sigmund
A note on integral equations of the kinchin-pease type
Rad. Eff. **1**, 15 (1969)

[170] H. Brune, H. Röder, K. Bromann, K. Kern, J. Jacobsen, P. Stoltze, K. Jacobsen, J. Norskov
Anisotropic corner diffusion as origin for dendritic growth on hexagonal substrates
Surf. Sci. **349**, L115 (1996)

[171] B. I. Bull, M. H. Hall, W. E. Garner
The Reaction between Carbon and Oxygen at Low Pressure and Room Temperature
J. Chem. Soc., 837 (1931)

[172] G. Antczak, G. Ehrlich
Jump processes in surface diffusion
Surf. Sci. Rep. **62**, 39 (2007)

[173] D. Morkes, M. Ondrejcek, I. Ulrych, Z. Chvoj, H. Conrad, V. Cháb
Surface diffusion of oxygen on a Ge{100}(2 × 1) surface studied by laser-induced thermal desorption (LITD)
Surface Science **352**, 607 (1996)

[174] J. C. Yang, M. Yeadon, B. Kolasa, M. Gibson
Oxygen surface diffusion in three dimensional Cu_2O growth on Cu(001) thin films
Appl. Phys. Lett. **70**, 3522 (1997)

[175] W. Moon, T. Yoshinobu, H. Iwasaki
Fabrication of Nanopit Arrays on Si(111)
Jpn. J. Appl. Phys. **38**, 483 (1999)

[176] D. Y. Choi, J. H. Lee, D. S. Kim, S. T. Jung
Formation of plasma induced surface damage in silica glass etching for optical waveguides
J. Appl. Phys. **95**, 8400 (2004)

[177] L. P. Allen, Z. Insepov, D. B. Fenner, C. Santeufemio, W. Brooks, K. S. Jones, I. Yamada
Craters on silicon surfaces created by gas cluster ion impacts
J. Appl. Phys. **92**, 3671 (2002)

[178] N. M. D. Brown, Z. H. Liu
The etching of natural alpha-recoil tracks in mica with an argon RF-plasma discharge and their imaging via atomic force microscopy
Appl. Surf. Science **93**, 89 (1996)

[179] R. V. Coleman, Q. Xue, Y. Gong, P. B. Price
Atomic force microscope study of etched tracks of low-energy heavy ions in mica
Surface Science **297**, 359 (1993)

[180] G. L. Montet
The detection of vacancies in molybdenite
Appl. Phys. Lett. **11**, 223 (1967)

10 Glossary

A

activation energy 107
active sites of graphite 8
AFM 5
aperture 11
aperture changer 12
area dose 13
area line mode 14
area meander mode 14
armchair edge 5
atom corral 5
atom density 98
atomic force microscope 5

B

ballistic electronic devices 63
ballistic transport 6, 63
basics 3
binding energy
    lattice 92
    surface 92
blanker 10
bond types
    π-bond 5
    σ-bond 5
bottom-up approach 3

C

calibration constant 27
capture area 33
capture diameter 33
circular model of oxidation 33
cluster 1
    fabrication 27
cluster facet
    lead 81
    silver 72
cluster height
    lead 75
    silver 71
cluster imaging 19
cluster physics 1
cluster stability
    lead 85
    silver 74
Clusterizer 20
condenser 10
constant-current-mode 17
constant-height-mode 17
coordinate system
    global 13
    local 13

D

data analyzing 19
dendritic shape 99
density of states 17
developer 4
diffusion length
    metall atoms 27
    oxygen atom 98
diffusion time 106
diffusion velocity 106
diffusivity 107
Dirac point 6
direct Gaussian beam vector scan 14
displacement energy 92
DOS 17
dose factor 13
dot dose 13
dwell time 13

E

EC-STM 16
EFM 18
electrochemical STM 16
emission current 27

etch-decoration TEM....24
evaporator with integral flux monitor....18
exfoliation....7
experimental equipment....9
exposure modes....14
exposure procedure....12
extractor....10

F

FBMS....13
feedback loop....17
fewer graphene layers....7
FIB....5, 9
  model of FIB-column....37
field evaporation....10
field of view....12
finding patterns....39
flux monitor....27
focus....13
focused ion beam....9
focused ion beams....5
free beam experiments....4
fullerene....5

G

GDSII....12
graphene....5
  nano-structures....63
graphite....5

H

honey comb lattice....5
HOPG....23

I

inverted patterning....67
ion current....11, 13
ion dose....13
ionLiNE....11
island....31, 67

J

Jellium-Model....4

K

Kinchin-Pease analytic method....92

L

large clusters....3
laser interferometer....11
LDOS....21
lead clusters
  rows....50
  single cluster patterns....53
lead layers....47
line dose....13
Liquid Metal Ion Source....9
LMIS....9
load-lock....19
local density of states....21
LT-System....17

M

mask....4
massless electrons....6
maximal penetration depth....29, 61
MC....91
mean velocity of oxygen molecules....107
mesa-structure....63
metal clusters....4
micro clusters....3
micro crystallites....3
molecule corrals....24
Monte Carlo....91
multilayer pits....25

N

nano tube....5
nano-cavity....25, 59
Nano-FIB....11
  applications....12
nano-grooves....117
nano-pit....25
  fabrication....24
  growth....24
nano-pit groups....32
nano-pit rows....31
nano-wires....117
negative resist....4
nucleation center....27

O

odd-even effect....79
odd-even oscillation....*See* odd-even effect
Ostwald-ripening....55
oxidation....8
  simulation program....98
oxidation probability....98

P

parameter set A and B....104
pattern generator....11
patterning....4
PEEM....22
  results....43
penetration depth....61
photo emission electron microscope....22
piezoceramic elements....17
pit imaging....20
point....14

point area dose 14
point dose 14
probe diameter 11

Q

quantum well states 79
QWS ..... *See* quantum well states

R

Raith GmbH 2
random walk 98
resist layer 4
RT-System 18

S

Sample 1 ..... 30, 42, 60, 63, 68, 74
Sample 10 ..... 77, 83
Sample 11 78
Sample 2 ..... 32, 61
Sample 3 ..... 37, 61, 84
Sample 4 34
Sample 5 40
Sample 6 45
Sample 7 46
Sample 8 ..... 48, 51
Sample 9 ..... 47, 54
Sample A1 71
Sample A2 ..... 75, 82, 87
scanning 10
scanning electron microscope 4
scanning probe microscopy 1
scanning tunneling microscope 5, 16
scanning tunneling spectroscopy 21
secondary electron detector 11
SEM 4
set point 17
settling time 15
sheet size 98
small clusters 3
smallest facet detectable 72
SPM 1
SP-STM 16
SRIM 92
stage 11
stamp 4
step size 13
sticking probability 8
stigmator 10
STM 5, 16
  band model 16
stopping power 92
STS 21
  results 84

T

Taylor-angle 9
Taylor-Gilbert-cone 9
TEM 10
The Stopping and Range of Ions in Matter 92
tight binding approximation 6
top-down approach 3
transmission electron microscopy 10
Transport Range of Ions in Matter 91
TRIM 91
tunneling current 16
tunneling effect 16
two-side model 8

U

ultra high vacuum 16
ultraviolet photoemission spectroscopy 18
UPS 18

V

vacancy 92
video STM 16

W

wave guide cross junctions 63
WD 12
working distance 12
write field alignment 13
writefield 13
WSxM 20

Z

zero-gap semiconductor 6
zigzag edge 5

11 Acknowledgements

An dieser Stelle möchte ich mich herzlich bei allen bedanken, die zur Entstehung und dem erfolgreichen Abschluss dieser Arbeit beigetragen haben.

Herrn Prof. Dr. Metin Tolan danke ich für die Möglichkeit meine Arbeit an seinem Lehrstuhl durchführen zu dürfen und für die angenehme Atmosphäre in seiner Arbeitsgruppe, in der ich gerne gearbeitet habe.

Ein ganz besonderer Dank geht an Priv. Doz. Dr. Heinz Hövel für die hervorragende Betreuung meiner Arbeit, der mit viel Geduld alle meine Fragen beantwortete und mit vielen Tipps und Diskussionen die Anfertigung dieser Arbeit unterstützte. Er hat mir auch immer bei privaten Problemen geholfen und ich könnte viel von ihm lernen. Letztendlich bin ich sehr froh darüber, in seiner Arbeitsgruppe gearbeitet zu haben.

Herrn Prof. Dr. Manfred Bayer danke ich für das Interesse an meiner Arbeit und die Übernahme des Koreferats.

Ich möchte mich auch bei Herrn Dr. Ralf Jede und bei Herrn Dr. Jürgen Thiel, die Verantwortlichen für die Firma Raith GmbH und dieses Projekt, bedanken. Durch die finanzielle Unterstützung und die Bereitstellung eines FIB-Apparates ist diese Arbeit erst möglich geworden. Ich möchte mich auch bei Dr. Guido Bösker bedanken, der die ersten Kontakte hergestellt hat.

Ein besonderer Dank geht an Dipl. Ing. Lars Bruchhaus, der mich bei der Strukturierung der Proben mit FIB unterstützt hat und immer bereit für Diskussionen war. Mit Hilfe seiner Schulung in den Techniken der Lithographie konnte ich die Probenbelichtungen durchführen.

Ich möchte mich auch bei Dr. Sven Bauerdick, der bei der Entwicklung des FIB-apparates beteiligt war, bedanken. Er hat mir ebenfalls bei den Belichtungen und bei meinen Aufgaben in der Firma geholfen. Dr. Ryo Mimura, der auch die FIB-Anlage mitentwickelt hat, danke ich für viele Diskussionen.

Ich bedanke mich auch bei Dipl. Phys. Robert Köster für die tolle Zeit während seiner Diplomarbeit in diesem Projekt. Er hat mir bei der Herstellung und Charakterisierung der ersten Proben sehr geholfen und einen wesentlichen Teil beim Aufbau des RT-Systems beigetragen.

Ich bedanke mich auch bei Dipl. Phys. Niklas Grönhagen, der mit seiner Diplomarbeit das Projekt in dem letzten Jahr sehr weit gebracht hat. Viele der Analysen sind erst mit seinem Programm „Clusterizer“ möglich geworden. Er hat auch einen wesentlichen Teil zur Erklärung der Clusterhöhen geleistet. Ich werde bestimmt die tollen Diskussionen mit ihm vermissen.

Ich möchte mich auch bei Dipl. Phys. Benedikt Sieben bedanken, der ebenfalls beim Aufbau des RT-systems mitgewirkt hat.

Und ich bedanke mich bei Dipl. Phys. Stefanie Duffe für die tolle Zusammenarbeit im Labor and für das Korrekturlesen bedanken. Ich wünsche ihr viel Erfolg für die letzten Monate ihrer Promotion.

Weiterhin möchte ich mich bei der Rest der STM Gruppe, Lukas Patryarcha, Ben Wortmann, Sabrina Hennes und bei den ehemaligen Mitglieder der STM Gruppe, Torsten Richter, Markus Bieletzki und Thomas Irawan, bedanken.

Ich möchte mich auch bei meinen ehemaligen Bürokollegen, Eugen Gaus für die spannende Diskussionen und Robert Fendt für C++ Tipps, bedanken. Ich bedanke mich auch bei der gesamten Gruppe der experimentellen Physik I für die tolle Arbeitsatmosphäre.

Ich bedanke mich auch bei Dipl. Phys. Martin Rohmer für die Durchführung der PEEM-Messungen und bei Prof. Dr. Michael Bauer und Prof. Dr. Martin Aeschlimann für die Ermöglichung dieser Zusammenarbeit.

Den Mitarbeitern des Konstruktionsbüros und der mechanischen Werkstatt danke ich für das Mitwirken beim Aufbau des RT-systems. Ferner bedanke ich mich bei Herrn Widinski für das bereitstellen des flüssigen Stickstoffs.

Den Mitarbeitern der mechanischen Werkstatt von Raith, insbesondere Herrn Carsten Plümpe, danke ich für deren Hilfe beim Anfertigen meiner Aufgaben in der Firma.

Meiner Familie danke ich für ihre Unterstützung während des Studiums und dafür, dass sie immer mein wissenschaftliches Interesse gefördert haben. Besonders möchte ich meiner Frau Marziyeh und meiner Tochter Samansa danken. Sie haben mir Tag für Tag neue Kraft gegeben und mir die Dissertationszeit sehr erleichtert.